Doctoral Dissertation
博士論文

Physics and Chemistry in the Beginning of Low-Mass Star Formation

(最初期形成過程における低質量原始星天体の物理・化学構造)

A Dissertation Submitted for the Degree of Doctor of Philosophy
December 2021

令和 3 年 12 月 博士（理学）申請

Department of Physics, Graduate School of Science,
The University of Tokyo

東京大学大学院理学系研究科 物理学専攻

Yuki Okoda
大小田　結貴

Abstract

Exploring the beginning of star/planet formation is of crucial importance from the perspective of thorough understandings of star and planet formation and eventually of the origin of the solar system, because it strongly affects the subsequent evolution of the protostar and the formation of planetary systems. For the last decade, our understandings of low-mass protostar formation have made a significant progress thanks to the advances of radio astronomical observations including the advent of Atacama Large Millimeter/Submillimeter Array (ALMA). Nevertheless, for the earliest stage, some important questions are still left behind. How does the youngest protostar grow? When does the disk formation start and how does the disk structure evolve as the growth of the protostar? How is the chemical diversity in the disk/envelope structure and what molecules are inherited from interstellar clouds to planetary systems? Since the earliest stage of protostar formation is poorly understood and is likely very complex, the observational approach is essential to address these questions. To disentangle the complex physical and chemical structures, distributions of various molecular lines need to be delineated at a high angular resolution. In this thesis, we study the three low-mass Class 0 protostellar sources, IRAS 15398−3359, B335, and L483, by molecular line observations with ALMA.

We find that a rotationally supported disk with the radius of 40 au has already been formed around the protostar of IRAS 15398−3359 which is as young as a few thousand years after the birth. The protostellar mass is evaluated to be $0.007^{+0.004}_{-0.003}$ $M_\odot$ on the assumption of a Keplerian rotation. The mass is much lower than that of typical low-mass protostars (0.1 $M_\odot$), and this protostar is surrounded by enough amount of gas (0.5-1.2 $M_\odot$) which will accrete onto the protostar. These facts support the youth of the protostar. We evaluate the disk mass from the dust continuum emission, and find that it is comparable to the protostellar mass. Hence, our results suggest the coevolution of disks and stars.

Furthermore, we investigate the physical structures of IRAS 15398−3359 over a larger scale ($\sim$50-10^3 au). We find a past outflow activity, based on the detection of shock tracer lines (SiO, CH_3OH, and SO) and their velocity structure. The direction of this outflow is almost perpendicular to that of the primary outflow reported previously. Hence, we propose the outflow reorientation as the protostar evolution. This can be caused by the temporal change in the angular momentum axis of accreting gas clumps. The accretion of fluid elements that have various angular momenta can occur in such a very low-mass protostar. This picture is further strengthened by the detection of the third outflow feature in this source.

In B335, we investigate the temperature distribution near the protostar at a very high resolution of $\sim$3 au. We find that a local temperature rise at a certain radius in the outer envelope by using multi-line analyses of the four molecular species ($HCOOH$, NH_2CHO, CH_2DOH, and CH_3OH). Namely, the temperature does not monotonously decrease with the increasing distance from the protostar. We propose the accretion shock as the heating mechanism for the local temperature rise.

To understand the molecular distributions around the protostars systematically, we introduce Principal Component Analysis (PCA). This is the first attempt to ap-

ply PCA for the chemical structure of protostellar sources. We conduct a PCA for 2-dimensional data (moment 0 maps) of IRAS 15398−3359 to validate its effectiveness. PCA successfully classifies and extracts the features of the molecular-line distributions without any preconception. Furthermore, we also perform PCA for the 3-dimensional data (cube data: distribution and velocity) of L483 and B335 which are rich in complex organic molecules (COMs). Some systematic trends of the molecular distributions are extracted by PCA. The distributions of the nitrogen-bearing species are more compact than those of the oxygen-bearing ones. HCOOH exceptionally shows the same trend as the nitrogen-bearing species such as NH_2CHO and HNCO. Although the differentiation between the nitrogen-bearing and the oxygen-bearing molecules as well as the peculiar behavior of HCOOH has been implied in other sources, they are quite qualitative. In this thesis, a clear difference is presented along with the temperature distribution. As a result, it is found that the different distributions cannot simply be interpreted by the different desorption temperature of molecules. Hence, we need to reconsider the formation processes of organic molecules in the early stage of protostellar evolution.

Above all, this thesis presents active and dynamic features of the beginning of low-mass star formation both for physics and chemistry. This result greatly contributes to a basic understanding of the physical and chemical evolution to planetary systems and their diversity.

Contents

Chapter 1
Introduction

In 2009, NASA's Kepler Space Telescope ('Kepler') was launched, and extensive searches for planets outside our solar system (exoplanets) by the transit method started. 'Kepler' traveled around the Sun for 9 years to survey exoplanets and to estimate how many stars are in/near habitable zones. Finally, more than 4000 exoplanet candidates were discovered[1], and more than a half of them were identified as exoplanets which have extraordinary mass and orbit in view of the solar system[2]. In some cases, the rotation axis of an exoplanet is misaligned from that of a central star: a planet even moving to the opposite direction with respect to the spin of the star is found (Albrecht et al., 2013; Xue et al., 2014; Winn & Fabrycky, 2015). Such diversity raises important questions about what its origin is and whether the solar system is a common occurrence in the Universe or not. Although the diversity of exoplanets could be caused after the formation of the planetary system, it may originate from the birth place of stars. This is my original motivation of this thesis work.

A low-mass protostar is a newly born star deeply embedded in a thick parent cloud, whose typical mass is lower than a few solar mass. Its formation process had long been attracting the interest of researchers in relation to the origin of the solar system. Extensive observational studies of low-mass protostars became possible in the 1980's thanks to Infrared Astronomical Satellite (*IRAS*). *IRAS* conducted a whole sky survey at the wavelengths of 12, 25, 60, and 100 μm for the first time and identified a lot of low-mass protostars in molecular cloud cores so far found in radio observations (Myers & Benson, 1983; Myers et al., 1983; Beichman et al., 1986; Benson & Myers, 1989). Infrared observations with *IRAS* in combination with radio observations successfully presented a frame-work of the formation and evolution of low-mass stars. However, it was difficult to study the initial stages of star formation, because such infant sources are cold and deeply embedded in parent cores. Furthermore, it was also difficult to study the disk formation around the protostar, because the disks are too tiny ($\lesssim$10-100 au) to be resolved by the telescope available in those days. Hence, high-resolution observations with radio wavelength are strongly awaited. Since the start of the early science operation of Atacama Large Millimeter/Submillimeter Array (ALMA) in 2011, observations for the disk/envelope system around young protostars have become possible. The ob-

---

[1] https://exoplanets.nasa.gov
[2] NASA, 2018, NASA Retires the Kepler Space Telescope

servational technology in the radio wavelength is getting improved and improved, and the structures around protostars can now be resolved in detail at a few 10 au scale or smaller. Moreover, the chemical composition of protostellar sources on the disk scale is being revealed.

In recent years, the exploration of comets and small solar system bodies has also made a great advance. Rosetta satellite explored the comet 67P/Churyumov-Gerasimenko in detail (e.g., Goesmann et al., 2015; Calmonte et al., 2016; Altwegg et al., 2019; Rubin et al., 2019). Some molecules detected in 67P are also found to be abundant in low-mass Class 0 protostellar sources with ALMA (Drozdovskaya et al., 2018, 2019). Thus, chemical composition around young protostars would provide us with novel information about molecules in the early solar system.

We can now study physics and chemistry in the earliest stage of low-mass star formation by high resolution and high sensitivity observations with ALMA. Such studies will eventually contribute to the understanding of the origin of the solar system.

1.1 Physics in Low-Mass Protostar Formation

Stars are formed in molecular cloud cores by gravitational contraction. Although the formation processes of high-mass stars (>8 $M_\odot$) are still controversial, those of low-mass stars (a few $M_\odot$) are relatively well understood particularly for the single star case. In this section, the physical conditions (temperature and density) of the interstellar clouds and the outline of the low-mass star formation processes are briefly described.
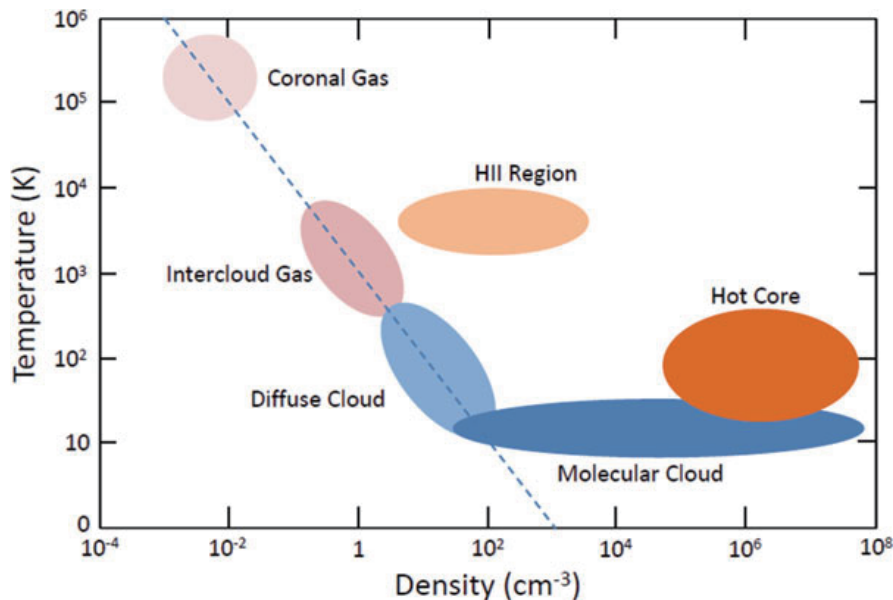
Figure 1.1: Temperature-density diagram of interstellar clouds taken from Yamamoto (2017). The dashed-line represents the constant-pressure line.

1.1.1 Physical Condition of Interstellar Clouds

The distribution of interstellar matter is not uniform in our Galaxy. Clouds consisting of diffuse gas and dust are formed everywhere, which are called 'interstellar clouds'. Figure 1.1 shows the temperature-density diagram of interstellar clouds. Clouds on the straight dashed line in Figure 1.1, coronal gas, intercloud gas, diffuse clouds, and part of molecular clouds, are in pressure equilibrium. HII regions around high-mass stars, where most hydrogen atoms are ionized as H^+ in the relatively dense condition by stellar radiation, are out of the line. Molecular clouds and hot cores are as well.

Protostars are formed in molecular clouds, having a high density ($\gtrsim 10^4$ cm^{-3}) and the low temperature ($\sim$10 K), where molecular hydrogen is dominant (e.g., Benson & Myers, 1989; Onishi et al., 2002; Inutsuka, 2012). Because of the high-density condition and high visual extinction, the interstellar ultraviolet (UV) radiation is well shielded in the central part of molecular clouds. Hence, molecules are not destroyed by the UV radiation and can survive for a long time (See Subsection 1.1.2). Thus, molecular clouds provide a good environment for the production of various molecules in the gas phase and on dust grains. Hence, we can study star-formation activities by observing spectral lines of molecules.

1.1.2 Formation of Low-Mass Stars

Theoretical works for low-mass star formation had extensively been conducted prior to observations, which constituted basic our understandings (e.g., Hayashi, 1961; Larson, 1969; Stahler et al., 1980). Observational studies had also been conducted since 1970's thanks to developments of infrared and radio astronomy (e.g., Benson & Myers, 1989; Ward-Thompson et al., 2000; Caselli et al., 2002a; Furuya et al., 2006; Evans et al., 2009; Sakai et al., 2009; Bjerkeli et al., 2016a). After the Atacama Large Millimeter/submillimeter Array (ALMA) started its early operation in 2011, young protostars in the embedded stages (Class 0/I) have been observed at unprecedented angular resolution and sensitivity, and their surprising features have been revealed. We here describe the outline of low-mass star formation processes inferred from observational results with ALMA and numerical simulations from its birth to the T-Tauri star phase just before reaching the main sequence. The processes are classified into the three major steps shown in Figure 1.2. The left panels of Figure 1.2 show a schematic picture of low-mass star formation. The right ones are examples of the corresponding ALMA images taken from Caselli et al. (2019), Okoda et al. (2020), and Carrasco-González et al. (2019) from the top in order. Here, we describe the three steps one by one.

Stege 1. Starless core phase

This phase corresponds to the last stage of prestellar evolution. Dense cores of molecular clouds on a 0.1 pc ($\sim$20,000 au) scale have a typical density and temperature of 10^5 cm^{-3} and 10 K, respectively (e.g., Myers & Benson, 1983; Myers et al., 1983; Benson & Myers, 1989; Bergin & Tafalla, 2007). A typical mass is a few $M_\odot$. A

central part of the dense core gradually contracts by self-gravity. While the gravitational energy is released in this process, the temperature of the central part almost remains constant or even slightly decreases down to 7-8 K. Such an isothermal collapse originates from the efficient radiation cooling through rotational line emission of CO and thermal emission of dust particles. The free-fall time is evaluated to be ~10^5 yr for the H$_2$ density of 10^4 cm^{-3} by using the following equation:

$$t_{\mathrm{ff}} = \left(\frac{3\pi}{32G\rho}\right)^{\frac{1}{2}} = 3.4 \times 10^5 \left(\frac{10^4}{n(\mathrm{H_2})}\right)^{\frac{1}{2}}, \quad (1.1)$$

where G is the gravitational constant, ρ the mass density, and $n(\mathrm{H_2})$ the number density of H$_2$ per cm^3. However, the actual timescale for the starless core phase can be longer due to the support by turbulent motions and magnetic field effects. Indeed, Evans et al. (2009) reported it to be (5±3)×10^5 yr by combining the statistical studies of starless cores with radio observations and a huge survey of infrared sources with Spitzer telescope, where the lifetime of the T-Tauri star (10^7 yr) is used as the reference. A top-right panel of Figure 1.2 shows the 1.3 mm continuum image of the famous starless core, L1544, observed with ALMA (Caselli et al., 2019), as an example. Since the molecules except for H$_2$ tends to be frozen out on dust grains in the cold condition of the starless core, the dust emission is the best tracer to characterize the physical condition (Caselli et al., 1999). Based on the high-resolution observational image of L1544 and simulations, they investigated its density structure in detail.

Stege 2. Protostar phase

When the H$_2$ density of the central core becomes higher than 10^{11} cm^{-3}, the isothermal collapse ends. The dust emission becomes opaque in such a high-density core. This causes reabsorption of photons emitted from the central part within the cloud, so that the temperature there starts to rise. This opaque core is called as 'first hydrostatic core' (first core) (e.g., Larson, 1969). Since the first core is too tiny (≲10 au) and its timescale is very short (~100 yr), it was thought to be difficult to find it observationally. Nevertheless, high resolution and high sensitivity observations with ALMA now enabled us to observe the first core candidates, such as L1451-mm and Chamaeleon-MMS1 (Busch et al., 2020; Maureira et al., 2020b).

The evolution from the first core to the second collapse is characterized by the central density and the temperature. Figure 1.3 shows the evolution of the central density and the temperature of the cloud, which was obtained from a radiation hydrodynamical calculation (Masunaga & Inutsuka, 2000; Inutsuka, 2012). γ_{eff} indicates the effective ratio of specific heats and can be used to specify the evolutional stage of the central core. In the first core stage, the temperature is so low that most H$_2$ molecules are in the ground rotational state (J =0). In this case, the H$_2$ molecule can be regarded as an atom in its internal degree of freedom (no rotation), and the gas behaves as the atomic gas. Hence, γ_{eff} equals 5/3 for the adiabatic process in the first core stage.

As the radiation cooling efficiency decreases, the temperature of the central part
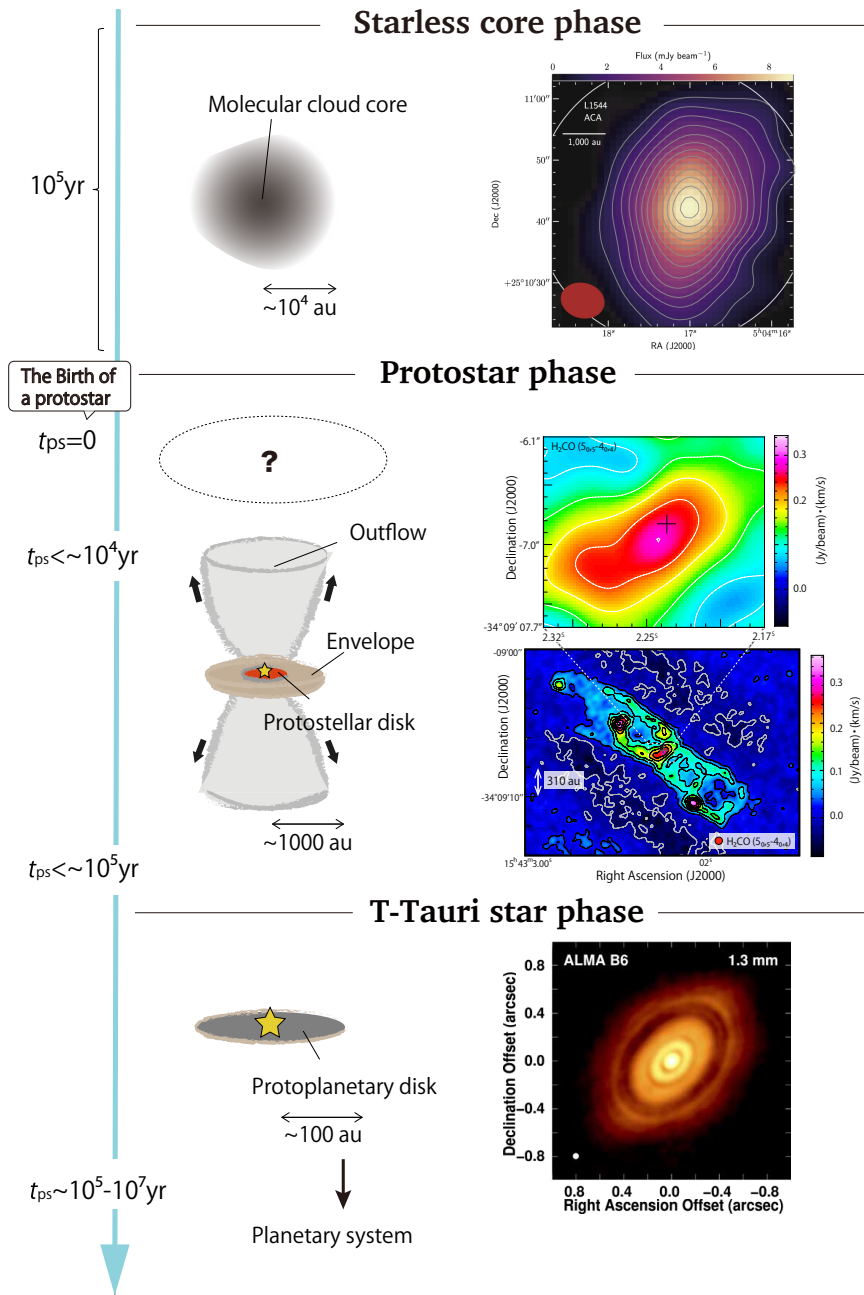
Figure 1.2: (Left): Schematic illustration of low-mass star formation. (Right): ALMA observational results for each stage taken from Caselli et al. (2019) for L1544, Okoda et al. (2020) for IRAS 15398−3359, and Carrasco-González et al. (2019) for HL Tau, from the top in order. 1 au corresponds to the distance between the earth and the Sun (1.496×10^{11} m).

becomes higher and higher, approaching to ~1500 K. As increasing temperature, excitation of the rotational levels becomes possible, and hence, $\gamma_{\rm eff}$ gradually decreases to the diatomic molecular case ($\gamma_{\rm eff}$=7/5) as the evolution (Figure 1.3). The H$_2$ molecules start to dissociate thermally at the high temperature (~1500 K), resulting in promoting the gravitational contraction (the second collapse). The huge energy is consumed for the dissociation process of the H$_2$ molecules. This point is defined as the birth of the protostar, and after this phase is called 'second core',
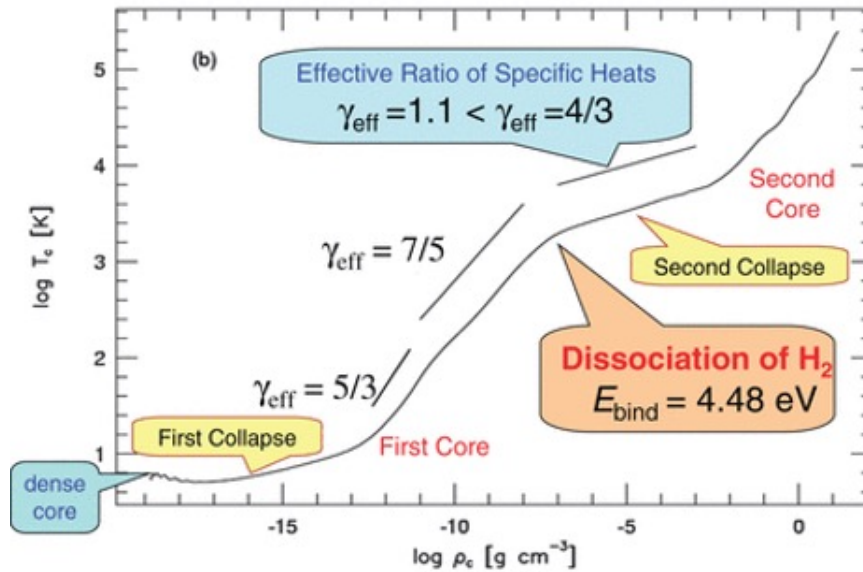
Figure 1.3: The relation between the temperature and the density at the center of a gravitationally collapsing cloud. The slope, indicating the effective ratio of specific heats (γ_{eff}) can be used to specify the evolutional stage. Taken from Inutsuka (2012).

where γ_{eff} is about 1.1 (Figure 1.3). This means that the second collapse is close to the isothermal process (γ_{eff}=1).

A newly born protostar is further growing by the gas accretion onto it, and the gravitational energy is released. Characteristic structures such as outflows, infalling-rotating envelopes, and disks associated with protostars mainly grow in this main accretion phase. Low velocity ($\sim$10 km s^{-1}) molecular outflow and high velocity jet ($\sim$100 km s^{-1}) play a role to extract the angular momentum of the accreting gas around the protostar, which accelerate the growth of the protostar. They are usually launched along the direction perpendicular to the disk/envelope system, although some cases are not. Thus, outflows are deeply related to the formation of the disk/envelope systems (See Subsection 1.1.4).

The evolutional stages of low-mass protostellar sources and young stellar objects have often been classified phenomenologically, based on the shape of the infrared Spectral Energy Distribution (SED)(e.g., Lada & Wilking, 1984). Figure 1.4 depicts a schematic picture of SED. At first, the protostellar stage was classified into three classes: Class I, Class II, and Class III. Later, Andre et al. (1993) added another class, Class 0, for the younger protostellar stage (See also André, 1994; Bachiller, 1996; Evans et al., 2009; Dunham et al., 2015). It is distinguished from Class I by using the bolometric temperature of sources (T_{bol}). T_{bol} of 70 K or lower is used to define the Class 0 stage, although this criterion is quite arbitrary. Class 0 and Class I both correspond to the protostar stage described in this section. Since the protostar is deeply embedded in the core, the stellar emission is not seen, and the SEDs for Class 0 and Class I originate from the thermal emission of dust heated by the protostar. The disk/envelope structures and the outflows around such embedded stars are observed with ALMA in detail (See Subsection 1.1.4). On the other

hand, Class II and Class III correspond to the T-Tauri star phase described in the next part.

Stege 3. T-Tauri star phase

Class II and Class III correspond to the T-Tauri stage (classical T-Tauri stage) and the late T-Tauri stage (weak-line T-Tauri stage), respectively. A young stellar object in these stages is called a T-Tauri star. The accretion of gas and dust onto the protostar is almost finished. This is because most of the surrounding gas around a T-Tauri star has already been dissipated by protostellar activities such as outflows in the Class I stage. Hence, the SED of Class II and III resembles the blackbody shown by the dashed line in Figure 1.4. The central temperature of a star increases due to quasi-static contraction, and the star is evolved toward a main-sequence star. The thermal energy of the central part of the star produced by the contraction is transferred to the stellar surface by convention (Hayashi phase; Hayashi, 1961, 1966), and then by radiation (Hayashi phase; Henyey et al., 1955). A small disk structure remaining around a protostar is called as a protoplanetary disk where a planetary system is formed (e.g., Williams & Cieza, 2011; Johansen & Lambrechts, 2017). A protostellar disk formed in the protostar phase is thought to be a precursor of a protoplanetary disk. Although accretion of matter from the protoplanetary disk onto the star still continues in the T-Tauri stage and causes UV and X-ray flares, such dynamical phenomena almost disappear in the late T-Tauri stage (e.g., Feigelson & Montmerle, 1999).
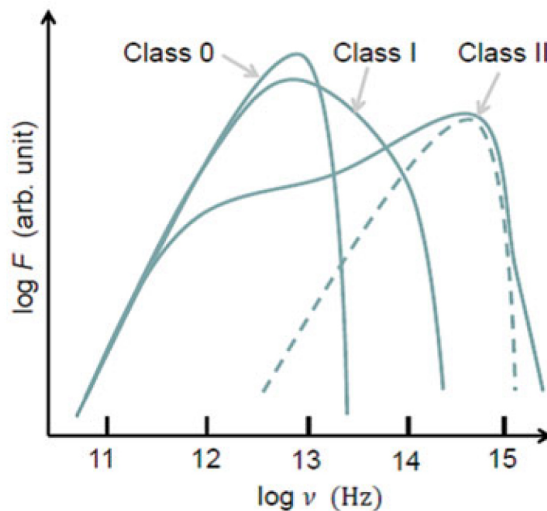
Figure 1.4: Schematic illustration of SED for the Class 0, I, and II sources. The dashed line represents the stellar blackbody. Taken from Yamamoto (2017).

The outline of low-mass star formation has been established as described above. However, we have to say that our understanding of its details is far from complete. In particular, observational studies about the beginning of low-mass star formation are very sparse, and hence, we need to accelerate studies of the early Class

0 protostellar sources with ALMA. On the other hand, comparison with theoretical simulations for the low-mass star formation is also important to interpret the observational results. In the next section, such theoretical works are briefly summarized.

1.1.3 Theoretical Works for Low-Mass Star Formation

Prior to observational studies, theoretical works for star formation had made a significant progress since the late 1960's (Larson, 1969; Penston, 1969). 'First core' was first proposed by Larson (1969), where the initial mass and radius of the core were calculated to be ~0.01 $M_\odot$ and ~4 au, respectively. Subsequently, Masunaga et al. (1998) performed the radiative hydrodynamic simulations to study formation and evolution of the first core. Although their work assumes a parent core without rotation, the evolution of a rotating molecular cloud core was later studied by Saigo & Tomisaka (2006). As well, the calculation of the evolution from molecular cloud cores to protostellar disks was reported by Inutsuka et al. (2010). They used resistive magnetohydrodynamical (MHD) simulations and showed that part of a first core transforms into a protostellar disk with a Keplerian motion. The protostellar disk is thought to evolve into a protoplanetary disk in the end.

When and how the disk structure forms in the protostar evolution is an important issue not only for observational studies but also for numerical simulations. In the early works, the formation of disk/envelope systems in the early stage of star formation (Class 0/I) was not successful in the simulations, because most of the angular momentum is removed away by magnetic fields (Mellon & Li, 2009; Li et al., 2013). Since the disk/envelope structures around Class 0/I protostars had been suggested observationally, based on the SED (e.g., Enoch et al., 2009), the above results were puzzling. Nonideal MHD simulations led us to solve this issue, which considers 'ohmic dissipation', 'ambipolar diffusion', and 'the Hall effect'. The magnetic field in a disk forming region is weakened by 'ohmic dissipation' and 'ambipolar diffusion' (Wurster et al., 2014, 2016), whereas the configuration of magnetic field lines is changed by 'the Hall effect' (Tsukamoto et al., 2015a,b). Finally, the nonideal MHD simulations successfully indicate the disk formation in the early stage (Dapp & Basu, 2010; Machida et al., 2011b; Dapp et al., 2012; Tomida et al., 2015; Masson et al., 2016; Tsukamoto et al., 2015a,b, 2018; Wurster & Li, 2018; Kawasaki et al., 2021). Figures 1.5(a) and (b) show the growing disk structure and the launching outflow from a protostar in the collapsing cloud core, respectively (Machida et al., 2011b). They calculated the long-term evolution until the end of the main accretion phase with a sink cell of 1 au by considering 'ohmic dissipation'. A sink cell ($r_{\rm sink}$) has often been used in MHD simulations to avoid the calculation of the densest part, which allow us to study the longer evolution (e.g., Machida & Hosokawa, 2013a). Since an outflow/jet begins is launched at a few 100 yr or later after protostar formation, a long calculation is essential to study the evolution. Tsukamoto et al. (2015a) pointed out that a disk size depends on the relative directions between the magnetic field and the rotation axis of the disk. If these directions are parallel or anti-parallel, a small disk (<1 au) or a large disk (> 20 au) are formed at the early stage, respectively.

In recent years, a long-term evolution of a few thousand years after the birth of a
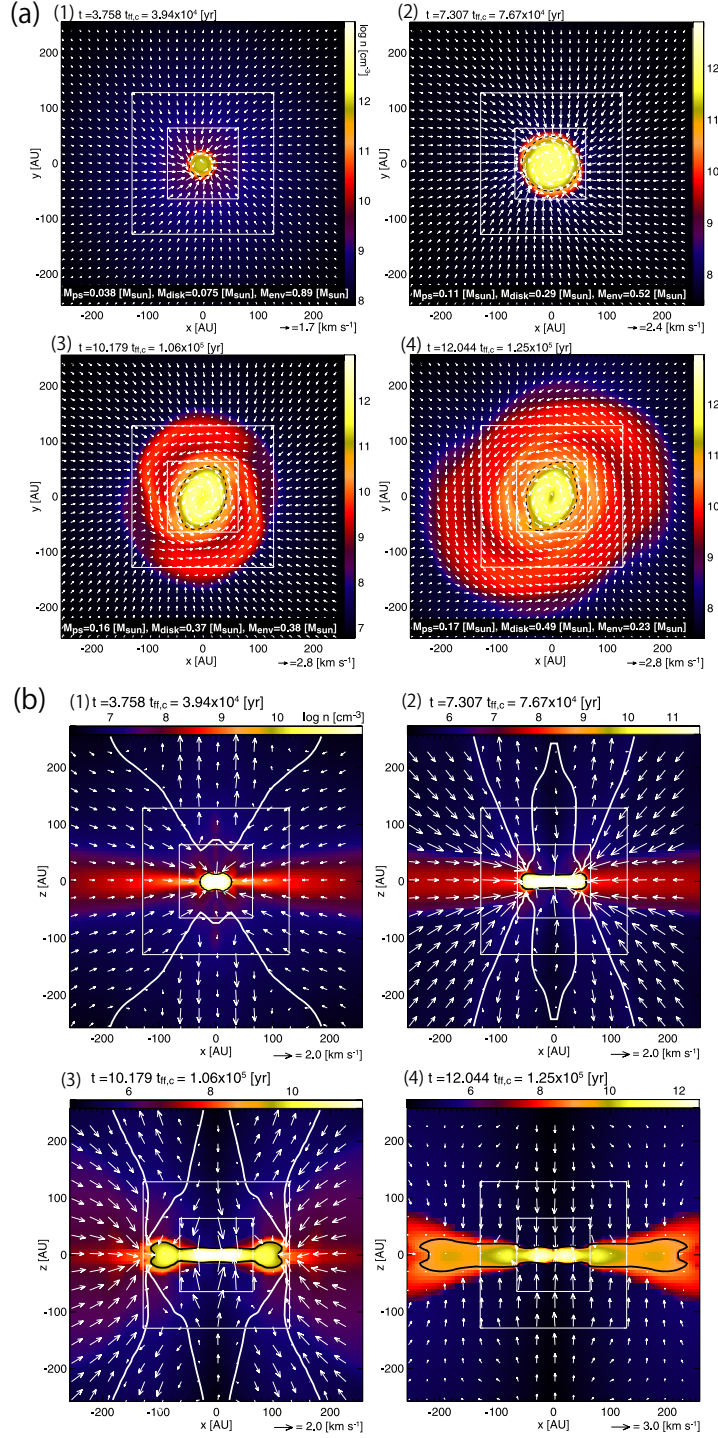
Figure 1.5: The time evolution of a disk structure (a) and an outflow (b). The center position corresponds to a protostar position. The elapsed time is denoted on the upper left on each panel. t and $t_{ff,c}$ indicate the calculation time and the initial free-fall time, respectively. Density distribution and velocity vectors are shown in colors and arrows. (a) The face-on view of the disk structure growing as the time evolution. (b) The edge-on view showing the outflow evolution. White lines show the boundary between outflowing gas and inflowing gas. Taken from Machida et al. (2011b).

protostar can be studied even without a sink. The sink cell (r_{sink}) is usually set to be 0.1-10 au or larger. Although r_{sink} is a convenient tool for a long-term calculation, the inside of r_{sink} cannot be resolved. The size of r_{sink} is often comparable to the disk size observed at a high resolution, and hence, it is hard to compare the simulations using a sink cell to the observations directly. Thanks to the improvement of calculation techniques and the enhancement of the computing power, simulations without a sink have been making rapid progress of theoretical understandings for outflows/jets as well as disk formation (e.g., Machida & Basu, 2019; Hirano et al., 2020). Machida & Basu (2019) recently investigated an episodic accretion onto a central protostar by simulations. In their work, an episodic accretion causes an episodic gas ejection from the inner edge of the circumstellar disk, which corresponds to the high-velocity jet. The jet velocity increases as increasing the protostellar mass, and exceeds ~100 km s^{-1}. In contrast, the outflow is driven from the outer edge of the circumstellar disk with a low velocity of ~10 km s^{-1}. Their results are qualitatively consistent with the ALMA observational results (e.g., Ohashi et al., 2014; Aso et al., 2015; Bjerkeli et al., 2016c; Zhang et al., 2018; Oya et al., 2018, 2021).

Owing to numerical simulations for the last two decades, star formation scenario looks settled at least for a single star case. On the other hand, interesting phenomena which had not been expected theoretically have recently been discovered around young protostars with ALMA. Although comparison between observations and simulations is crucially important, the results in simulations depend on the various parameters for the initial conditions assumed a priori. Hence, thorough observations are still indispensable for understanding the real features of young protostellar sources.

1.1.4 ALMA Observational Results for Protostars

Before the ALMA era, the highest resolution for radio observations of the thermal emission of molecules and dust was ~ 1″ (100 au for the source distance of 100 pc) even with the interferometers such as Northern Extended Millimeter Array (NOEMA) [3] and Submillimeter Array (SMA). Hence, the disk/envelope system around low-mass protostars, whose size is typically less than 100 au, was difficult to be resolved in most cases (e.g., Sakai et al., 2010; Saruwatari et al., 2011; Yen et al., 2013).

Thanks to the high resolution and high sensitivity of ALMA, disk/envelope structures on a few 10 au scale were able to be explored in young protostellar sources (Class 0/I: e.g., Lindberg et al., 2014; Ohashi et al., 2014; Oya et al., 2014, 2016, 2017; Sakai et al., 2014a,b; Yen et al., 2017). The kinematics of the inner disks and the outer envelopes was resolved with the high spatial and velocity resolution observations (~a few 10 au and < 1 km s^{-1}, respectively). Figure 1.6 shows a rotation profile along the disk/envelope direction observed in the low-mass protostellar source L1527 by Ohashi et al. (2014). The rotation profile shows a power-law index of -1.16±0.13 outside the radius of 54 au (Figure 1.6(b)). This index is close to that expected for the infalling motion conserving the angular momentum (the index of

---

[3]Plateau de Bure Interferometer (PdBI) was renamed as NOEMA in 2014.
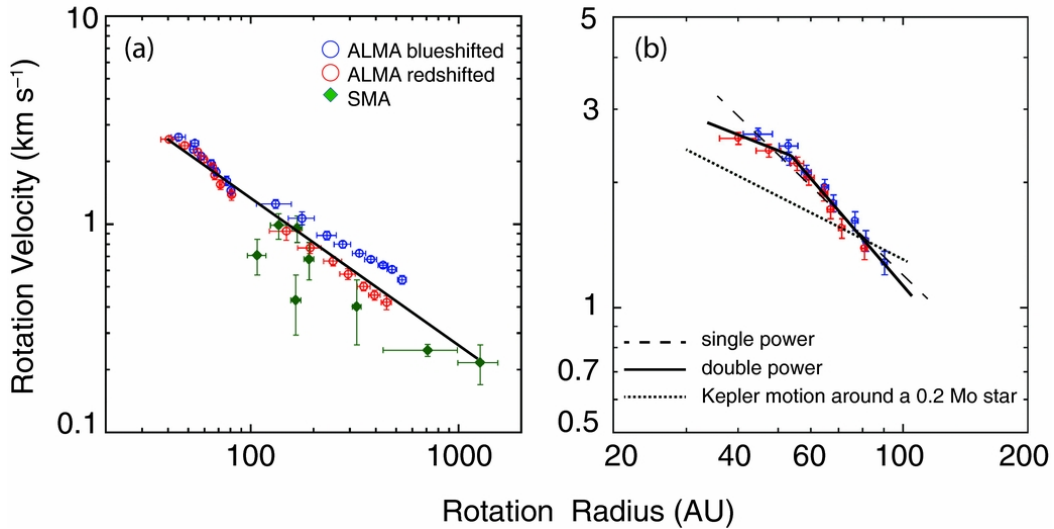
Figure 1.6: Rotation profile along the disk/envelope direction observed for L1527. (a) The $C^{18}O$ data of the blueshifted and redshifted components observed with ALMA are plotted in blue and red marks, respectively. The green marks show the SMA measurements reported by Yen et al. (2013). The solid line shows the result of the least-square fitting to all the data points, including both the SMA and the ALMA measurements. (b) Only the ALMA data points within 100 au are plotted. The power lows of $r^{-0.41\pm0.24}$ and $r^{-1.16\pm0.13}$ can be seen inside and outside the knee point of 54 au, respectively. Taken from Ohashi et al. (2014).

-1). On the other hand, the rotation profile within 54 au has a power-law index of -0.41±0.24, which is close to that expected for the Keplerian motion (the index of -0.5) (Figure 1.6(b)). Based on this result, they discuss the transition from the infalling-rotating envelope to the disk. Similar studies are also reported for TMC-1A (Aso et al., 2015) and L1489 (Sai et al., 2020).

On the other hand, position-velocity (PV) diagrams have often been used for the analysis of velocity structures. Figures 1.7(a) and (b) show the PV diagrams along the disk/envelope direction and the outflow direction, respectively, observed for the low-mass protostellar source, IRAS 16293−2422 Source A (Oya et al., 2016). The black and blue contours indicate the models of a Keplerian motion and an infalling-rotating motion, respectively. Based on the model fitting, they reported that the observed H_2CS emission in colors trace both the Keplerian disk and the infalling-rotating envelope. From these structures, the protostellar mass was evaluated to be 0.5-1.0 $M_\odot$. Such an approach to disentangling the disk and the envelope is also reported for other sources (e.g., Sakai et al., 2014a,b, 2016; Oya et al., 2017; Okoda et al., 2018; Imai et al., 2019), and is used in this thesis as well.

High-resolution observations including ALMA also contributed to the identification of binary/multiple systems for various protostellar sources including young protostars (e.g., Tobin et al., 2016b, 2018, 2020; Maury et al., 2019). For instance, the Karl G. Jansky Very Large Array (VLA) survey was conducted for 94 protostars in the Perseus molecular cloud to identify multiple sources. As a result, more than half of the Class 0 protostars are found to be binary or multiple systems (Tobin et al., 2016b). The formation of binary/multiple systems is also an important issue
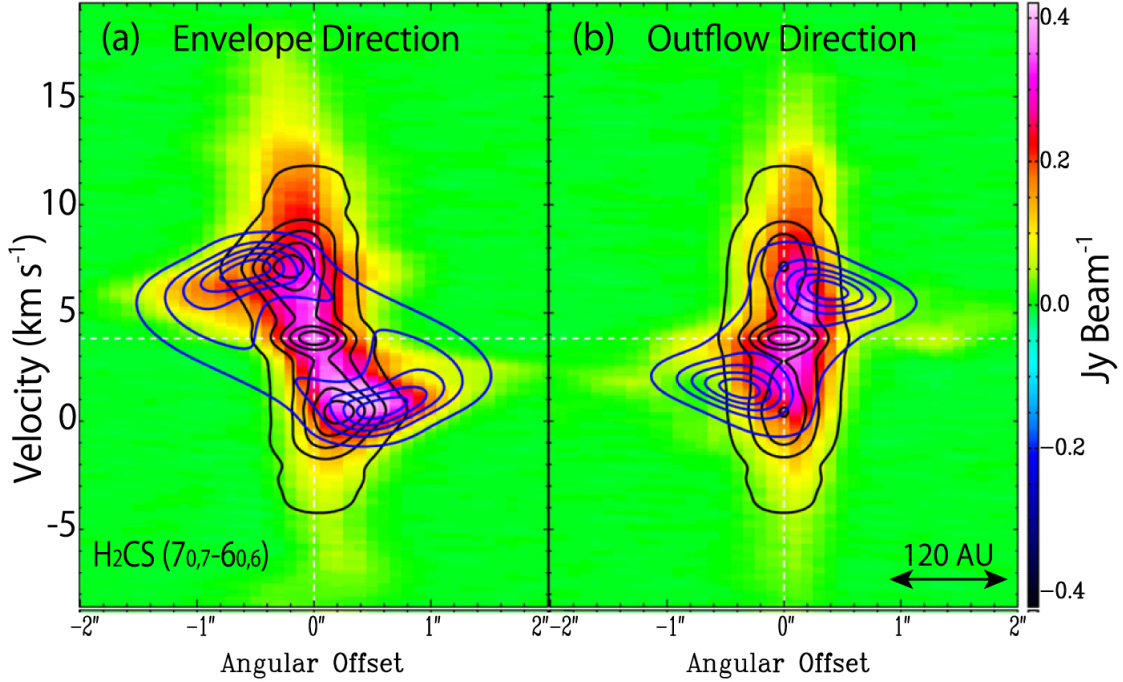
Figure 1.7: Velocity structures of the disk/envelope system in the H_2CS emission (Color). The black and blue contours indicate the models of a Keplerian motion and an infalling-rotating motion, respectively. Taken from Oya et al. (2016).

in star-formation studies. Class 0 protostellar sources are usually difficult to be identified as binary/multiple systems with the mid and far-infrared observations, because they are deeply embedded in molecular cloud cores. Although the radio observations of the multiplicity of Class 0 sources were reported, the separations are relatively large (>100-1000 au; Looney et al., 2000; Chen et al., 2013; Tobin et al., 2015a). ALMA enables us to resolve the separations of even a few au. (Tobin et al., 2016b) indeed the binary sources with the separation of <30 au.

Observations with a high spatial dynamic range are important for through understandings of star formation, and it is now possible with ALMA. The angular resolution of ALMA now reaches 0."01 (a few au), which enables us to study the disk/envelope system around young protostars including the binary/multiple structures in detail (Takakuwa et al., 2017; Yen et al., 2017; Sakai et al., 2019; Sai et al., 2020; Oya & Yamamoto, 2020; Zamponi et al., 2021). At the same time, an outflow launched from a first core candidate (Busch et al., 2020), the interaction with parent cores and a young protostar (Tokuda et al., 2014; Favre et al., 2020; Pineda et al., 2020) were found at a large scale (∼100-1000 au).

As described in Subsection 1.1.2, an outflow plays an important role in the growth of the central star and the disk/envelope system. Oya et al. (2018) studied the outflow of the low-mass protostellar source L483, and found that the outflow is rotating around its axis. Figure 1.8 shows the position-velocity diagrams of the CS ($J = 5−4$) emission along the axes perpendicular to the outflow axis at various offsets

17
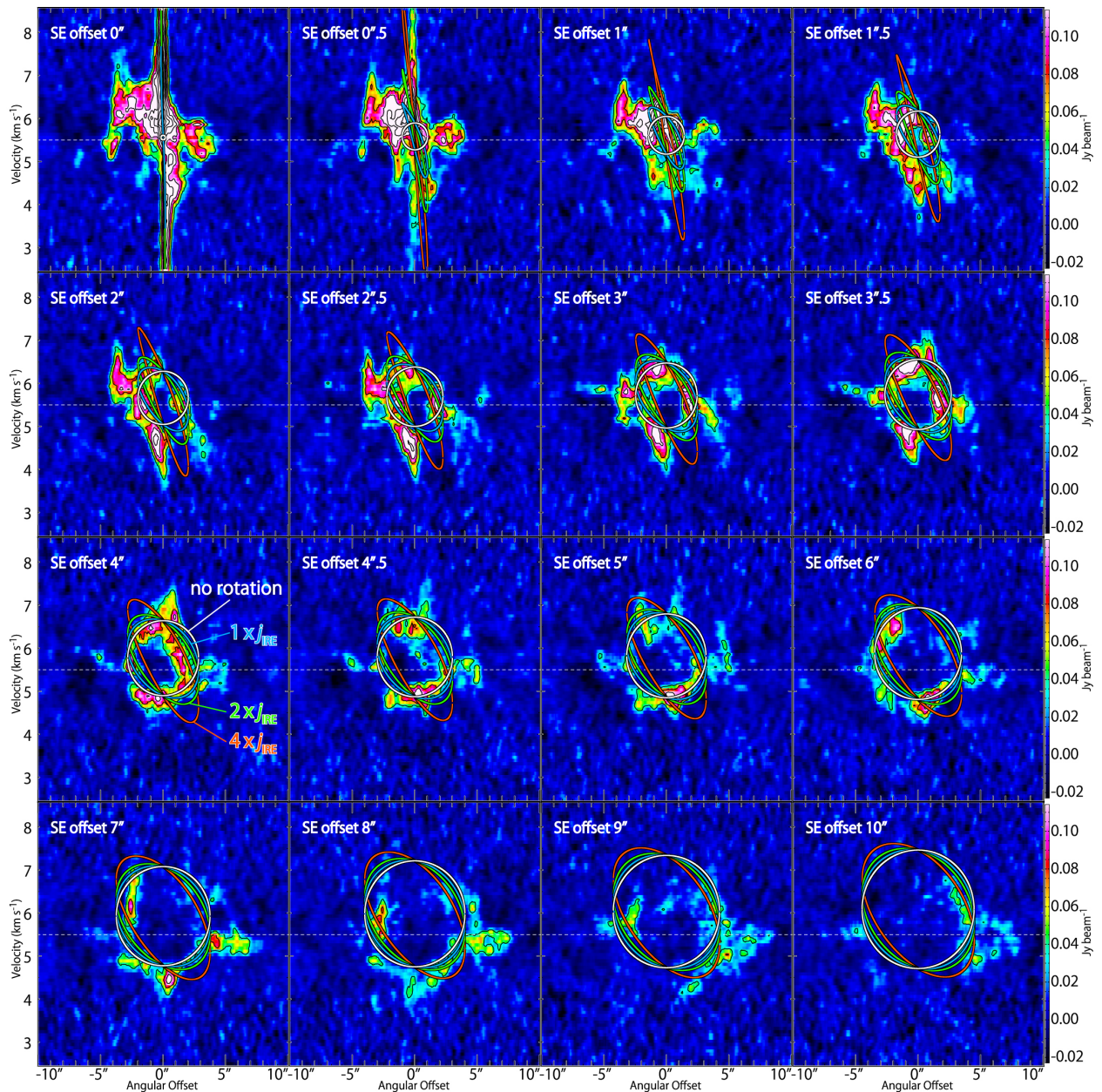
Figure 1.8: Position-Velocity (PV) diagrams of the CS emission along the axes perpendicular to the outflow axis at various offsets from the protostar position (Color). The offsets are denoted in the upper-left corner of each panel. White, blue, green, and red elliptic lines represent the results of the outflow model, where the specific angular momentum of the gas in the outflow is 0, 7.9×10^{-4}, 15.8×10^{-4}, and 31.6×10^{-4} km s^{-1} pc, respectively. Note that the specific angular momentum of the infalling-rotating envelope is 7.9×10^{-4} km s^{-1} pc. The specific angular momentum of the gas is assumed to be conserved in each outflow model. Taken from Oya et al. (2018).

from the protostar position. The emission feature in the maps is better explained by the model with outflow rotation than by that without rotation. Such an outflow rotation has also been found in a few other sources (Zhang et al., 2018; Oya et al., 2021; Ohashi et al., 2022). From the rotation velocity, the specific angular
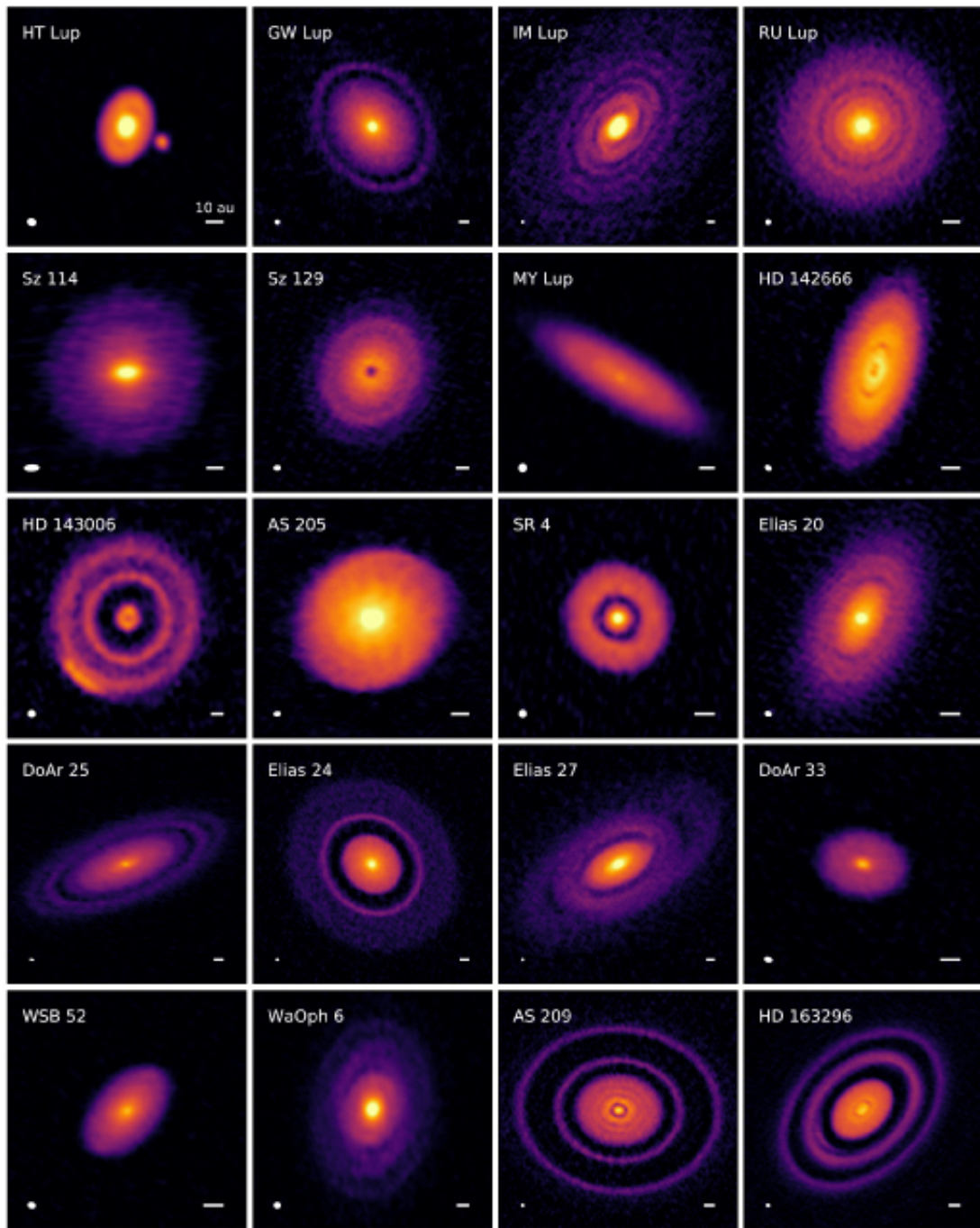
Figure 1.9: Images of 20 protoplanetary disks observed at 240 GHz (1.25 mm) continuum in the DSHARP project. The substructures such as rings, gaps, arc-like features, and spiral arms are seen. Taken from Andrews et al. (2018).

momentum is derived and compared with that of the disk/envelope system. The result of L483 indicates that the outflow can contribute to the extraction of the angular momentum from the disk/envelope gas and accelerate the mass accretion onto the protostar. Furthermore, the low-outflow activity and the compact detached disk structure are observed with ALMA toward a young object which is expected in the evolution from starless core to protostar (Tokuda et al., 2016, 2017), although it had ever been thought that outflows and disk structures are formed after the birth

of protostars.

On the other hand, substantial progress has been made in observations of protoplanetary disks in the late stage of star formation. The ALMA Large Program DSHARP (Disk Substructures at High Angular Resolution Project), was carried out at a resolution of ~0."035 au (~5 au) to delineate substructures of 20 nearby protoplanetary disks. DHARP successfully presented the diversity of protoplanetary disks. Figure 1.9 shows the 20 protoplanetary disk images reported by Andrews et al. (2018). Most samples show concentric bright rings and dark gaps. Some have spiral patterns (e.g., IM Lup, Elias 27, and WaOph 6), and others have small arc-like features (e.g., HD 143006 and HD 163296). The origins of such substructures are still controversial. Nevertheless, the existence of the wide diversity is interesting, and it may originate from earlier stages.

1.2 Chemistry in Low-Mass Protostar

Interstellar Molecules

To date, the existence of 241 interstellar molecules in space has been reported (McGuire, 2021). Figure 1.10 shows part of molecules found in interstellar clouds. They are mainly discovered in radio wavelength by observing their rotational transitions. Non-polar species such as H_2, CO_2, and C_2H_2 are detected by UV/visible and infrared observations. Besides the fundamental molecules such as H_2, CO, and HCN, we can find the following three characteristics among these molecules. First, there are molecular ions such as H_3^+, HCO^+, and N_2H^+. This fact indicates that interstellar clouds are essentially weakly ionized plasma. Second, there are various carbon-chain molecules such as HC_5N and C_4H, which are highly unsaturated organic molecules. Since carbon-chain molecules are almost absent in the terrestrial conditions, their rich existence in some sources is surprising from a viewpoint of chemistry. Third, complex organic molecules (COMs) such as $HCOOCH_3$ and C_2H_5CN exist. They are mainly found in star-forming regions (e.g., Caselli & Ceccarelli, 2012; van Dishoeck et al., 2013). Recently, larger molecules such as indene (C_9H_8: Cernicharo et al., 2021) and ethanolamine ($NH_2CH_2CH_2OH$: Rivilla et al., 2021) have been detected. Indeed, the molecular evolution in interstellar space is more complex than ever thought. Note that fullerenes (C_{60} and C_{70}) were also detected through infrared observations (Cami et al., 2010).

Here, a brief history of the discovery of interstellar molecules is presented. McKellar (1940) first revealed the existence of molecules in interstellar clouds through detection of the absorption lines of CN and CH in the visible region. Soon after that, CH^+ was found in interstellar clouds by Douglas & Herzberg (1941). After the discovery of the emissions from atomic hydrogen (HI) at 1.42 GHz (21 cm) in interstellar clouds (Muller & Oort, 1951; Ewen & Purcell, 1951), the absorption line of OH at the wavelength of 18 cm was found as the first interstellar molecule identified with radio astronomical observations (Weinreb et al., 1963). Although the above discoveries had not received much attention from astronomers, the first detection of NH_3 in interstellar clouds (Cheung et al., 1968) made them realize the importance of molecules in space. Subsequently, H_2O (Cheung et al., 1969), H_2CO

(Snyder et al., 1969), HCN (Snyder & Buhl, 1971), and CO (Wilson et al., 1970) were detected in interstellar clouds. CO has widely been used for the study of molecular clouds and star formation.

Complex organic molecules (COMs) and carbon-chain molecules were discovered in the 1970's. While they are found in various sources, carbon-chain molecules tend to be abundant in cold starless clouds, and COMs are mainly found in hot cores of star-forming regions. For instance, the spectral line survey was conducted toward the cold dark cloud TMC-1 with the 45 m radio telescope of Nobeyama Radio Observatory (NRO) by Kaifu et al. (2004), and various carbon-chain molecules such as C_6H, CCS, C_3S, CCO, C_3O, HNCCC, HCCNC, HC_3NH^+, HCCCHO, and cyclic C_3H (c-C_3H) were discovered. On the other hand, COMs were first found in high-mass star-forming regions such as Orion KL and Sgr B2 (e.g., Blake et al., 1987; Turner, 1991). About 10 years later, Cazaux et al. (2003) detected them toward the low-mass protostellar source, IRAS 16293−2422. Today, such a hot and dense region around low-mass protostars is called as 'hot corino' (e.g., Caselli & Ceccarelli, 2012; van Dishoeck et al., 2013).

The density and the temperature, where molecules appear in the gas phase, depend on molecules. Similarities and differences among the molecular distributions reflect such physical conditions, and they can trace specific physical structures such as parent cores, outflows, and disk/envelopes in protostellar sources.

Simple neutral molecules
H_2, CH, CN, CO, HCl, NH, NO, NS, OH, PN, SO, SiO, SiS, CS, HF, O_2, SH, CH_2, HCN, HCO, H_2O, H_2S, HNC, HNO, N_2O, OCS, SO_2, CO_2, NH_2, HO_2, NH_3, H_2CO, H_2CS, CH_3, H_2O_2, CH_4
Ionic species
(Cation)
CH^+, CO^+, SO^+, CF^+, OH^+, SH^+, HCl^+, ArH^+, HCO^+, HCS^+, HOC^+, N_2H^+, H_3^+, H_2O^+, H_2Cl^+, OH_3^+, $HCNH^+$, HCO_2^+, C_3H^+, H_2COH^+, NH_4^+, H_2NCO^+, HC_3NH^+
(Anion)
C_4H^-, C_6H^-, C_8H^-
Carbon-chain molecules and their isomers
C_2, C_3, C_2H, C_2O, C_2S, c-C_3H, l-C_3H, C_3N, C_3O, C_3S, C_2H_2, C_5, C_4H, l-C_3H_2, c-C_3H_2, HC_3N, HCCNC, HNC_3, C_5H, l-C_4H_2, C_5N, C_6H, CH_3CCH, HC_5N, CH_3C_3N, C_6H_2, CH_2CCHCN, CH_3C_4H, HC_7N, CH_3C_5N, HC_9N, CH_3C_6H, $HC_{11}N$
Complex organic molecules
HCOOH, CH_2CO, CH_3CN, CH_3NC, CH_3OH, CH_3SH, HC_2CHO, c-C_3H_2O, CH_2CNH, HNCHCN, CH_2CHCN, CH_3CHO, CH_3NH_2, c-C_2H_4O, H_2CCHOH, $HCOOCH_3$, CH_3COOH, CH_2OHCHO, CH_2CHCHO, NH_2CH_2CN, CH_3CHNH, CH_3CH_2CN, $(CH_3)_2O$, CH_3CH_2OH, CH_3CONH_2, C_3H_6, CH_3CH_2SH, $(CH_3)_2CO$, $(CH_2OH)_2$, CH_3CH_2CHO, C_2H_5OCHO, CH_3OCOCH_3, $C_2H_5OCH_3$, n-C_3H_7CN
Other molecules
FeO, HNCO, HNCS, H_2CN, HCNO, HOCN, HSCN, CH_2CN, H_2CNH, NH_2CN, HCOCN, HNCNH, CH_3O, NH_2CHO

Figure 1.10: Examples of molecules found in interstellar clouds. Taken from Yamamoto (2017).

1.2.1   Formation of Molecules

There are two ways for molecular formation: the gas-phase reaction and the grain-surface reaction (see Yamamoto, 2017; Garrod & Widicus Weaver, 2013). In both cases, ionization by cosmic rays and/or UV radiation initiate the chemical reactions. In the gas phase, exothermic binary reactions to produce plural products mainly occurs in cold condition. Because of this reason, the hydrogenation by H atom is not efficient, so that unsaturated organic molecules such as carbon-chain molecules (e.g., HC_5N, C_4H) are preferentially produced through ion-molecule reactions and neutral-neutral reactions.

On the other hand, the hydrogenation by H atom is the dominant process on dust grains, because the grain surface can act as a third body to absorb the excess reaction energy. Hence, saturated organic molecules are preferentially produced. For instance, the successive reactions of CO with H produce CH_3OH as (e.g., Hasegawa et al., 1992; Watanabe & Kouchi, 2002; Hama & Watanabe, 2013):

$$CO \rightarrow HCO \rightarrow H_2CO \rightarrow CH_3O\ (CH_2OH) \rightarrow CH_3OH.$$
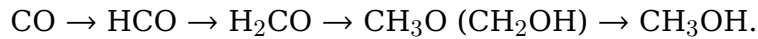
Larger COMs are thought to be produced on dust grains from CH_3OH and other intermediate species in the above reaction. However, the details of the formation routes are still controversial. The molecules thus formed stay on dust grains in the cold condition. When the temperature is raised by the protostellar heating and/or shocks, these molecules are liberated from dust grains to the gas phase. Then, we can identify them by observations. For instance, COMs are thought to be liberated at 100 K or higher (e.g., Charnley et al., 1992; Caselli et al., 1993; Oya et al., 2019), where the ice mantle of dust grains containing COMs are sublimated.

To simulate the chemical processes in molecular clouds and star forming regions, chemical network calculations have extensively been conducted (Herbst & Leung, 1989; Hasegawa et al., 1992; Garrod & Herbst, 2006; Herbst & van Dishoeck, 2009; Aikawa et al., 2008). In these calculations, all the potential reactions in the gas phase and on dust grains are considered, and their rate equations are solved as differential equations to trace the temporal variation of molecular abundances, where the gas-grain interaction is also taken into account. The current model includes more than 500 chemical species and more than 10000 chemical reactions. Chemical model calculations considering the physical evolution are also reported. Aikawa et al. (2008, 2012, 2020) conducted the gas-grain chemical network calculations in a collapsing cloud and revealed the molecular evolution from the starless core to the hot core/hot corino. Figure 1.11 shows their result of the formation of various organic species (Aikawa et al., 2012). The organic species are evaporated into the gas phase from near the protostar as time goes by.

1.2.2   Chemical Diversity of Protostellar Sources

Chemical diversity in the disk/envelope system of low-mass protostellar sources was recognized in the 2000's with single-dish observations (e.g., Cazaux et al., 2003; Sakai et al., 2008). Following the discovery of hot corino in IRAS 16293−2422 (Cazaux et al., 2003), hot corinos were also found in some other sources (e.g.,
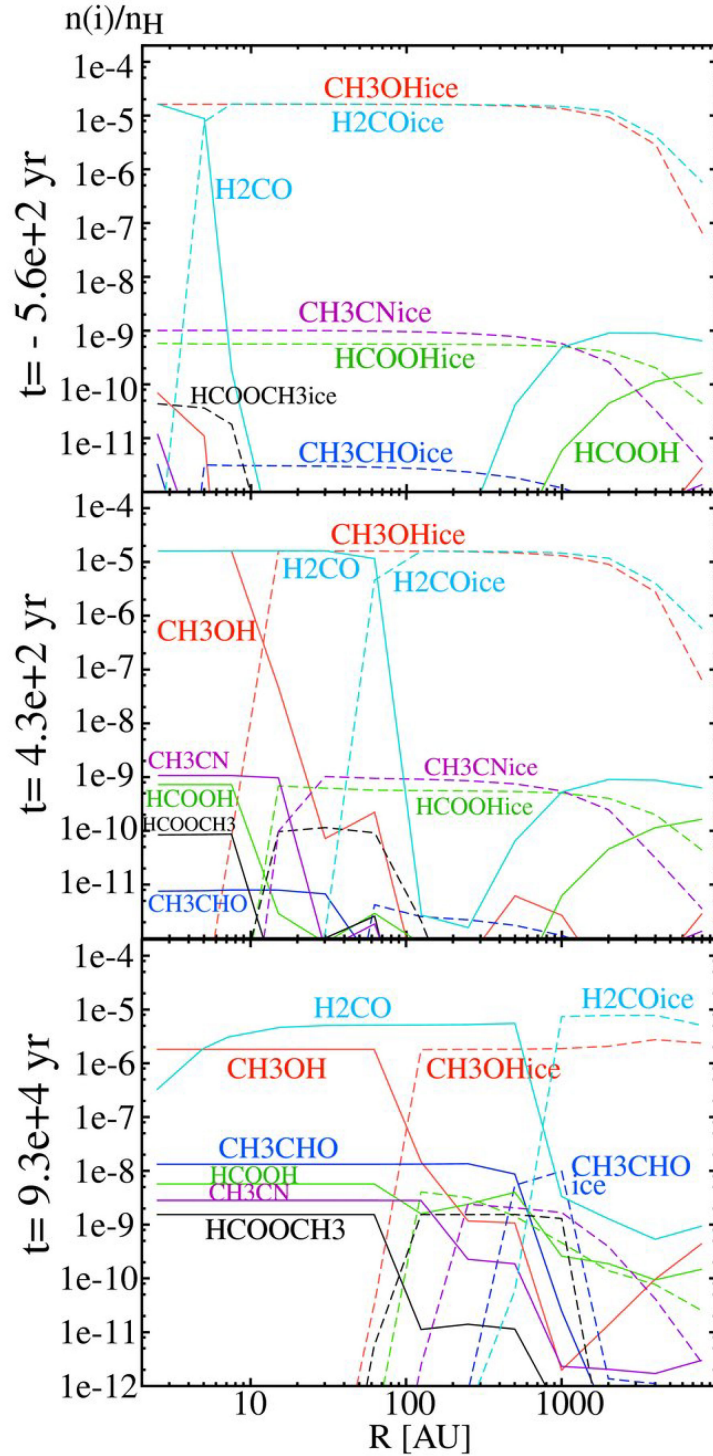
Figure 1.11: Abundance of organic species relative to H as a function of the radius of the core. The timescales from the birth of the protostar are written in the left side of each panel. Taken from Aikawa et al. (2012).

NGC1333 IRAS 2A, IRAS 4A, and IRAS 4B; Maury et al., 2014; Bottinelli et al., 2004a; Sakai et al., 2006). While COMs are abundant in these sources, carbon-chain molecules are found to be deficient. On the other hand, Sakai et al. (2008)

found the protostellar source rich in carbon-chain molecules. That is the Class 0 protostellar source, L1527, in Taurus molecular cloud. This source is identified as the first Warm Carbon-Chain Chemistry (WCCC) source. In L1527, many kinds of carbon-chain molecules (e.g., C_4H_2, c-C_3H_2, C_4H, C_5H, CH_3CCH, HC_7N, and HC_9N) were found to be associated with the protostar, while COMs specific to the hot corino chemistry are not found. Furthermore, Sakai et al. (2009) found similar chemical features in the Class 0 protostellar source, IRAS 15398−3359, in Lupus-1 molecular cloud. Then, IRAS 15398−3359 was recognized as the second WCCC source. Figure 1.12 shows the molecular line emissions observed toward L1527 and NGC1333 IRAS 4A observed with the IRAM Large Program, Astrochemical Surveys At IRAM (ASAI) (Lefloch et al., 2018). As shown in Figure 1.12, CH_2DOH and CH_3CHO are not detected in L1527, although the c-C_3H lines of the carbon-chain related molecule are clearly seen. In contrast, the emission of CH_2DOH and CH_3CHO are bright and the c-C_3H emission is very weak in IRAS 4A.

Although hot corino chemistry in L1527 and IRAS 15398−3359 has not been reported, some sources were recently recognized as a hybrid source with ALMA observations: that is the WCCC source containing hot corino nature (e.g., B335 and L483; Imai et al., 2016; Oya et al., 2017). In hybrid sources, while carbon-chain species are abundant on a 100-1000 au scale, molecules characteristics to hot corino chemistry, $HCOOCH_3$, NH_2CHO, and $HNCO$, can be seen on a 10-100 au scale. Namely, WCCC and hot corino chemistry coexist on different scales. Now, this hybrid chemistry is thought to be 'standard' chemical structure of low-mass protostellar sources. This picture is consistent with the prediction by the chemical model by Aikawa et al. (2008). On the other hand, hot corino sources and WCCC sources can be recognized as distinct cases. Thus, high-resolution observations with ALMA contributed to reveal the standard chemical feature through the discovery of the hybrid sources.
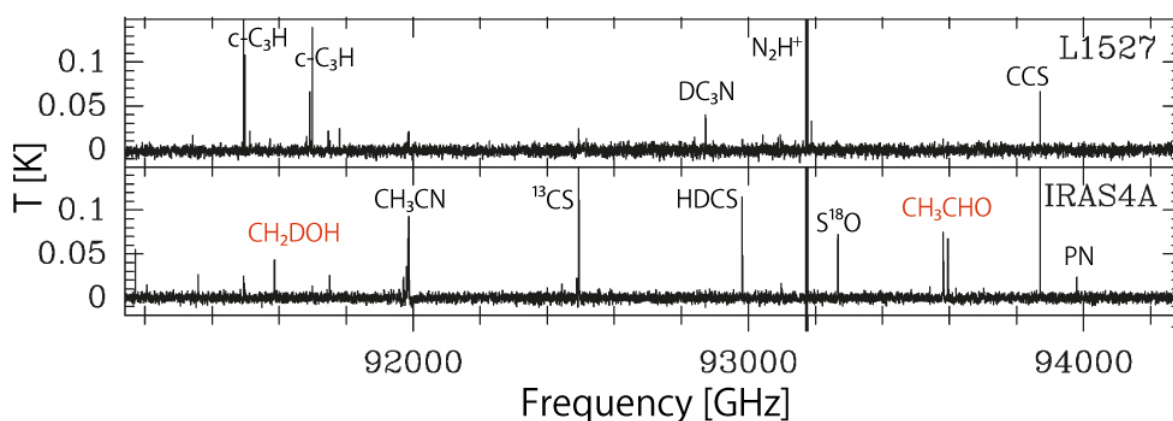
Figure 1.12: Spectral lines toward L1527 and NGC1333 IRAS 4A with the IRAM Large Program, Astrochemical Surveys At IRAM (ASAI). Taken from Lefloch et al. (2018).

To explain such chemical diversity, Sakai & Yamamoto (2013) proposed that the timescale of the prestellar core phase is related to the chemical processes of carbon-chain species and COMs. When the timescale is longer, more CO molecules

can deplete onto dust grains. CO molecules have enough time to form CH_3OH, H_2CO, and COMs through hydrogenation reactions by the H atom and radical reactions on grain surfaces. In this case, COMs would be detected in the protostellar phase, when they appear in the gas phase through the evaporation from dust grain mantles at the temperature higher than 100 K (e.g., Charnley et al., 1992; Caselli et al., 1993). When the timescale is not enough for the CO formation in the gas phase, WCCC appears. The C atom can be depleted onto dust grain, and CH_4 is formed by hydrogenation. Finally, CH_4 molecules evaporated from dust grain mantles in a warm region triggers the gas-phase chemical reactions to produce carbon-chain molecule. Thus, the difference of the timescale of the prestellar core phase makes the difference of the chemical composition of dust grain mantles, and eventually causes the chemical diversity.

In order to explore the chemical evolution in protostellar sources, we need to know how the molecular species are distributed around the protostar: namely we should investigate the chemical differentiation within the source in detail. It has been revealed with ALMA observations that the molecular distribution is related to the internal structures of disk/envelope systems. For WCCC sources (e.g., L1527 and IRAS 15398−3359), SO and CH_3OH are enhanced at the rotating disk structure and the centrifugal barrier. They are thought to be liberated into the gas phase from grain mantles in the above components, where the temperature increases due to the protostar radiation and the accretion shock caused by the infalling gas. In contrast to these species, c-C_3H_2 and CCH are abundant only in the outer envelope (Sakai et al., 2014a,b; Okoda et al., 2018). These species are depleted on dust grains in the dense part of the disk or are destroyed due to photodissociation by protostellar radiation. On the other hand, for hot corino chemistry sources and hybrid sources (e.g., L483 and B335), COMs are rich in the centrifugal barrier and its inside (Oya et al., 2016, 2017). These volatile species come out from grain mantle due to the high temperature.
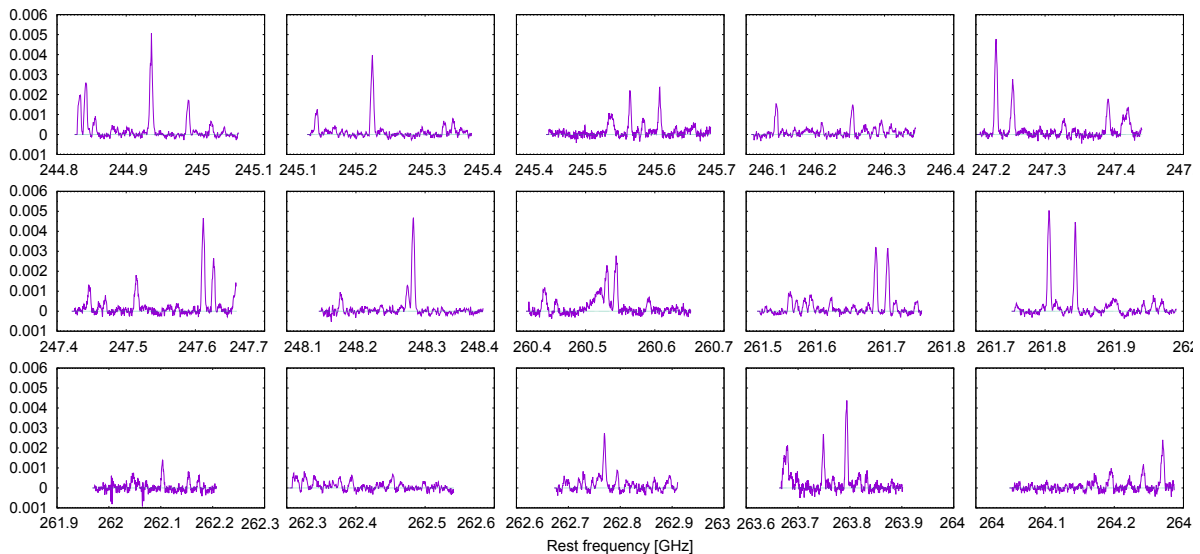
Figure 1.13: Part of our observation toward the low-mass Class 0 protostellar source, B335, with ALMA. A lot of molecular lines are detected.

Now, we can detect many molecular lines even in a single observation with ALMA. As an example, Figure 1.13 shows the spectrum observed toward the Class 0 protostellar source, B335. We can identify almost 100 lines including weak ones. Although they should be fully used for the analysis of chemical differentiation, it is practically difficult to characterize them including the velocity structures by eye. To overcome this situation, a sophisticated analysis method can be useful for classification of the molecular lines. Such an approach to the molecular distribution has been reported for a prestellar core. Spezzano et al. (2017) applied the Principal Component Analysis (PCA) to the molecular line distributions observed in the prestellar core L1544 and classified them into 4 groups. Here, they only used the moment 0 maps for PCA and did not involve the velocity structure. This method is very useful for the studies of chemical differentiation and should be applied to protostellar sources.

An outflow gas launched from a protostar often interacts with the ambient gas, which makes a 'shocked region'. L1157-B1 is a famous outflow shocked region, and has been studied extensively since the 1990's (e.g., Mikami et al., 1992; Bachiller, & Pérez Gutiérrez, 1997). Figure 1.14(a) shows the outflow of L1157, where the outflow impact on the ambient gas occurs in the southern part (B1 and B2). Mikami et al. (1992) detected the SiO emission in this source and suggested that SiO is liberated into the gas phase in the shock region through grain destruction processes. Bachiller, & Pérez Gutiérrez (1997) studied the L1157 shocked region by using several molecular lines such as SiO, CH_3OH, SO, and H_2CO. The middle and right panels of Figure 1.14(b) show the spectral line profiles of the observed molecular lines. These molecular lines show the broad line widths specific to the shock region ($\sim$10 km s^{-1}). Since then, SiO has frequently been used as a shock tracer (e.g., Gueth et al., 1998; Codella et al., 1999; López-Sepulcre et al., 2016). Most of silicon exists in dust grain cores as silicate compounds (e.g., $Mg_{2x}Fe_{2-2x}SiO_4$, $Mg_xFe_{1-x}SiO_3$). Grain cores are thermally destroyed or sputtered by collisions at high-temperature conditions. This happens, when the temperature suddenly increases up to a few 1000 K at the shock velocity of 10 km s^{-1}.

Based on the conversion of the kinetic energy of the gas to the thermal energy, the maximum temperature is given as:

$$T = \frac{5}{36k_B}\mu v^2 = 3830 \left(\frac{v}{10 \text{ km s}^{-1}}\right)^2 \text{ K} \qquad (1.2)$$

k_B is Bolzmann constant, μ the mean mass of colliding particles (H_2 and He), and v the velocity of the gas. After the collision, the gas rapidly cools down, and hence, we usually observe shock regions having a temperature of $\sim$50-100 K. In fact, L1157-B1 shows the temperature of $\sim$80 K (Bachiller et al., 1993). After cooling, molecules thus liberated into the gas phase will eventually be re-depleted onto dust grains. The depletion timescale (t_d) depends on the H_2 density ($n(H_2)$), and is roughly given as (e.g., Yamamoto, 2017):

$$t_d \sim \frac{3 \times 10^9}{n(H_2)} \text{ yr.} \qquad (1.3)$$

For the H_2 density of 10^5 cm^{-3}, the liberated molecules can stay in the gas phase
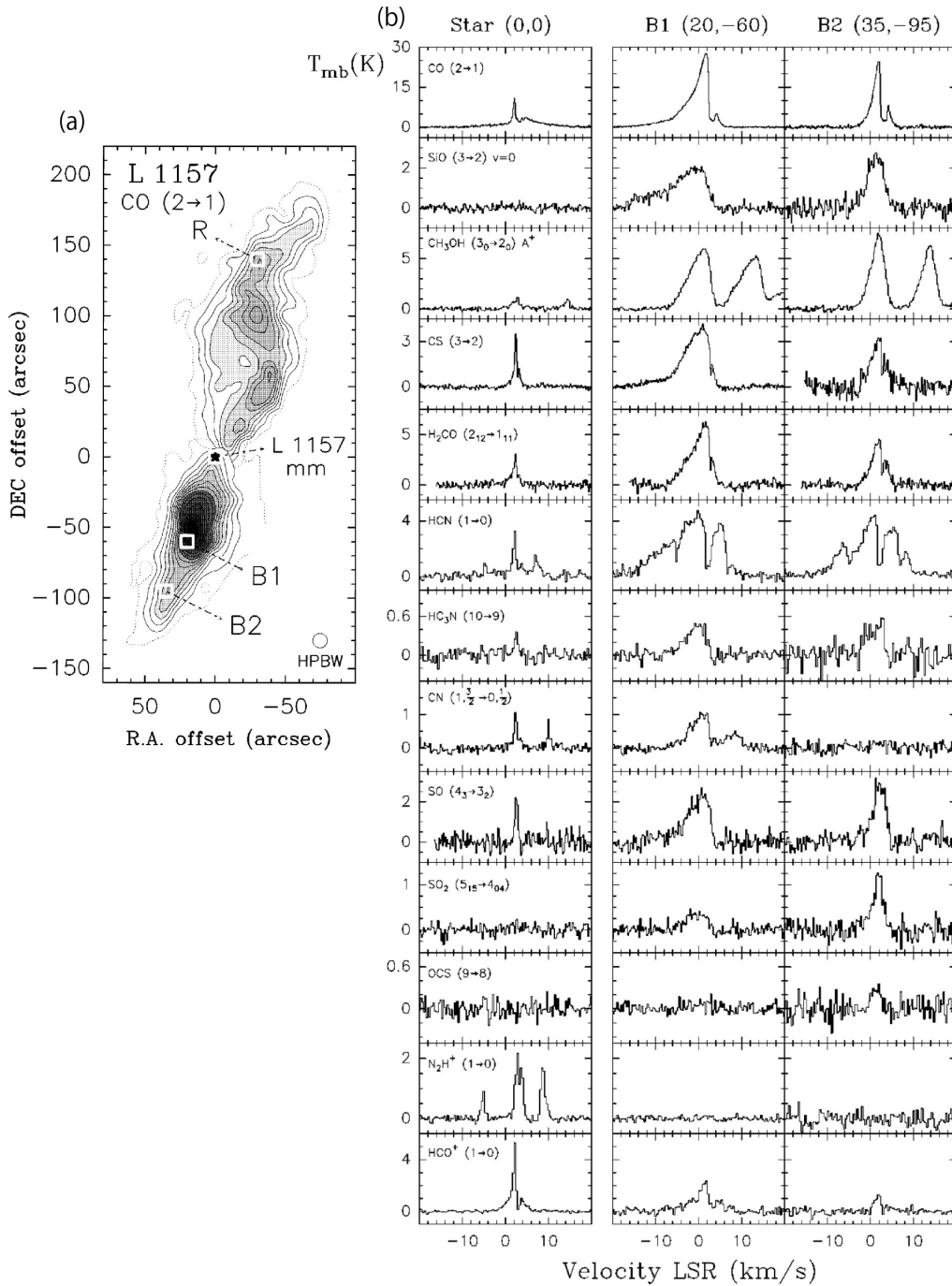
Figure 1.14: (a) Distribution of the CO (J =2−1) line emission. It traces the outflow structure launched from L1157, where the shock regions are caused in the south (B1 and B2). (b) Molecular line profiles toward the protostar position (left), the shocked region B1 (middle), and the shocked region B2 (right) of L1157. Molecular lines are denoted in the upper-left corner of the left panels. Broad and blueshifted line profiles in B1 and B2 indicate the shock by the blue-shifted lobe of the outflow. Taken from Bachiller, & Pérez Gutiérrez (1997).

for 10^4 yr after the cooling.

It is worth noticing that some organic molecular lines were also detected in the shocked region. They come out from grain mantle due to the high temperature. The

first detection of the organic molecular lines such as HCOOCH$_3$, CH$_3$CN, HCOOH, and C$_2$H$_5$OH in L1157-B1 was reported by Arce et al. (2008) and Sugimura et al. (2011). Furthermore, Yamaguchi et al. (2012) detected the phosphorus-containing molecule (PN) in the same source with 45 m telescope of NRO, in addition to the organic molecular lines such as NH$_2$CHO and CH$_3$CHO.

In short, molecular distributions can be used as an important tools to study various physical structures of star-forming regions. They are also useful to explore the chemical processes occurring there. In order to fully understand the protostellar evolution, we need to focus on both physics and chemistry.

1.3 This Thesis

1.3.1 Aims of This Thesis

As described above, disk/envelope systems of nearby low-mass protostellar sources are now able to be spatially resolved with ALMA, and the structure and kinematics for some sources have been investigated in detail. In addition to the physical structures, chemical structures have also been delineated, and they are found to have significant diversity among sources. One may think that the low-mass star formation has already been understood reasonably. However, this is not correct. As mentioned in Subsection 1.1.2, the very early stage of protostellar evolution, in particular, the transition phase from the first core stage to the main accretion stage is not well revealed observationally. In this relation, it is not clear when the disk structure is formed around the protostar, and whether the initial disk structure is a remnant of the first core as suggested by theoretical simulation (Inutsuka et al., 2010). These issues need to be addressed to understand the physical diversity of star formation. Since the early phase is just like a bridge between the interstellar gas and the stellar system, its detailed understanding allows us to investigate how the initial condition of a parent core affects the protostellar system newly born in it. To step forward toward this direction, we need to find the protostellar source in the earliest evolutionary stage and characterize it. This is one of the main aims of this thesis.

Another aspect of the protostellar evolution is what kind of molecules are inherited from interstellar clouds to planetary systems. For this purpose, it is important to study chemical compositions and their distributions in very young sources. We can now detect many spectral lines of various molecular species at a high spatial resolution. Hence, we can answer the above question partly. A new difficulty is how to classify the molecular distribution objectively. For this purpose, we here introduce a sophisticated analysis method using PCA. We confirm the validity of this method in the chemical analysis of the protostellar sources, and the results are discussed in relation to physical structures and chemical processes proposed so far. This is another main aim of this thesis.

1.3.2   Outline of This Thesis

This thesis mainly consists of 2 parts, the physics part and the chemistry part. After this introduction (Chapter 1) and the brief descriptions of interferometers (Chapter 2), 3 chapters for the physics part are described (Chapters 3, 4, and 5). Chapters 3 and 4 present the kinematics of the disk structure and the outflow around the very young protostar IRAS 15398−3359, respectively. Chapter 5 deals with the temperature distribution around the hot core of B335. The chemistry part is composed of 4 chapters (Chapters 6, 7, 8, and 9). The basic description of PCA is given in Chapter 6. The applications of PCAs to the observational data are presented in Chapters 7 and 8. Our discussion for organic molecules based on the results of PCAs for cube data is described in Chapter 9. Chapter 10 concludes the thesis and presents some future prospects.

Chapter 2
Observation Equipment

The ALMA (Atacama Large Millimeter/Submillimeter Array) data are used for this thesis work to study young low-mass protostellar sources. In this chapter, we describe basic principle of interferometers and the analysis of the ALMA data.

2.1 Principles of Interferometers

2.1.1 Coordinate System

We define a coordinate system for the two antennas (Antenna 1 and Antenna 2) and an observed source, as shown in Figure 2.1, to explain the basic principles of interferometers. Here, $\vec{s}$ is a unit vector from the earth to the observed source, whereas $\vec{l}$ and $\vec{m}$ correspond to the directions of x-axis and y-axis, respectively. 'Baseline vector' is defined as $\vec{D}$, which is a vector from Antenna 1 to Antenna 2. If an interferometer consists of n antennas, the number of $\vec{D}$ is $n(n-1)$. When we observe the radiation from the source with the two antennas, the mutual time delay between the antennas is caused. This is called as 'geometrical delay' and is described by using the speed of light (c) as:

$$\tau_g = -\frac{1}{c}(\vec{D} \cdot \vec{s}),\tag{2.1}$$

where the delay is defined to be relative to Antenna 1.

2.1.2 Point Source

In the case of the monochromatic radiation from a point source at the frequency of ν_0, the amplitude of the radiation is represented as:

$$E(t) = E_0 \exp{(2\pi i\nu_0 t)},\tag{2.2}$$

where E_0 is the peak amplitude. Hence, the signals observed by the two antennas are given as:

$$\widetilde{E}_1(t) = a_1 E(t), \ \widetilde{E}_2(t) = a_2 E(t - \tau_g),\tag{2.3}$$
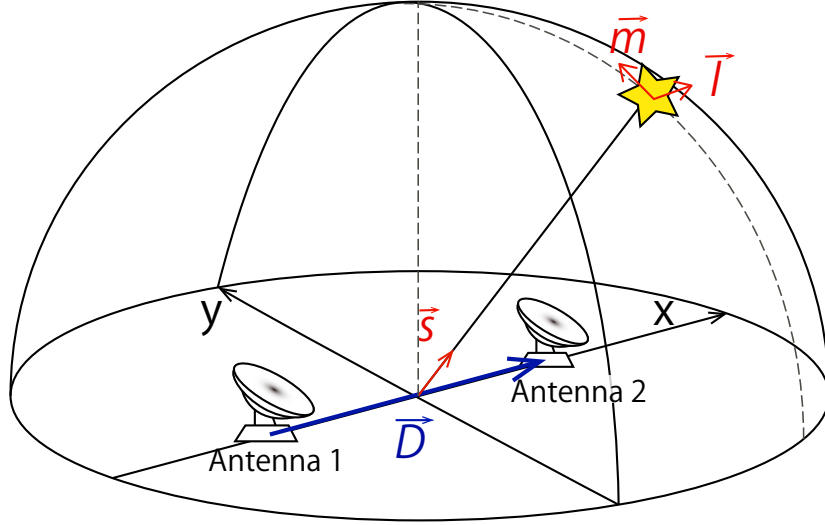
Figure 2.1: Coordinate system for the two antennas and an observed source.

by considering the geometrical delay, where a_1 and a_2 represent the complex gain of Antenna 1 and 2, respectively. Correlation function $C(\tau)$ between these two signals can be obtained as follows:

$$C(\tau) = \lim_{T \to \infty} \frac{1}{T} \int_{-T/2}^{T/2} \widetilde{E}_1(t - \tau_i)\widetilde{E}_2^*(t - \tau) \, dt \tag{2.4}$$

$$= \lim_{T \to \infty} \frac{1}{T} \int_{-T/2}^{T/2} a_1 a_2^* |E_0|^2 \exp\left(2\pi i \nu_0((t - \tau_i) - (t - \tau_g - \tau))\right) dt \tag{2.5}$$

$$= a_1 a_2^* |E_0|^2 \exp\left(2\pi i \nu_0(\tau + \tau_g - \tau_i)\right). \tag{2.6}$$

Here, we introduce τ_i for an artificial correction of the mutual delay, which is applied to $E_1(t)$. $C(\tau)$ is the output data from the correlator (Figure 2.2). Then, a Fourier transformation is applied to $C(\tau)$ to obtain the cross power spectrum $\hat{C}(\nu)$ (visibility data) as:

$$\hat{C}(\nu) = \int_{-\infty}^{\infty} d\tau \, C(\tau) \exp(-2\pi i \nu t) \tag{2.7}$$

$$= a_1 a_2^* |E_0|^2 \delta(\nu_0 - \nu) \exp\left(2\pi i \nu_0(\tau_g - \tau_i)\right). \tag{2.8}$$

If τ_i is adjusted as τ_g to compensate the geometrical delay, the phase of $\hat{C}(\nu)$ equals to 0. Then $\hat{C}(\nu)$ is simply proportional to a delta function with the peak at $\nu = \nu_0$.

Assumption of the monochromatic radiation is too ideal, and such radiation never exists in reality. Hence, we have to employ a concept of the quasi-monochromatic radiation by involving the time-dependent complex amplitude of the radiation, $a_m(t)$
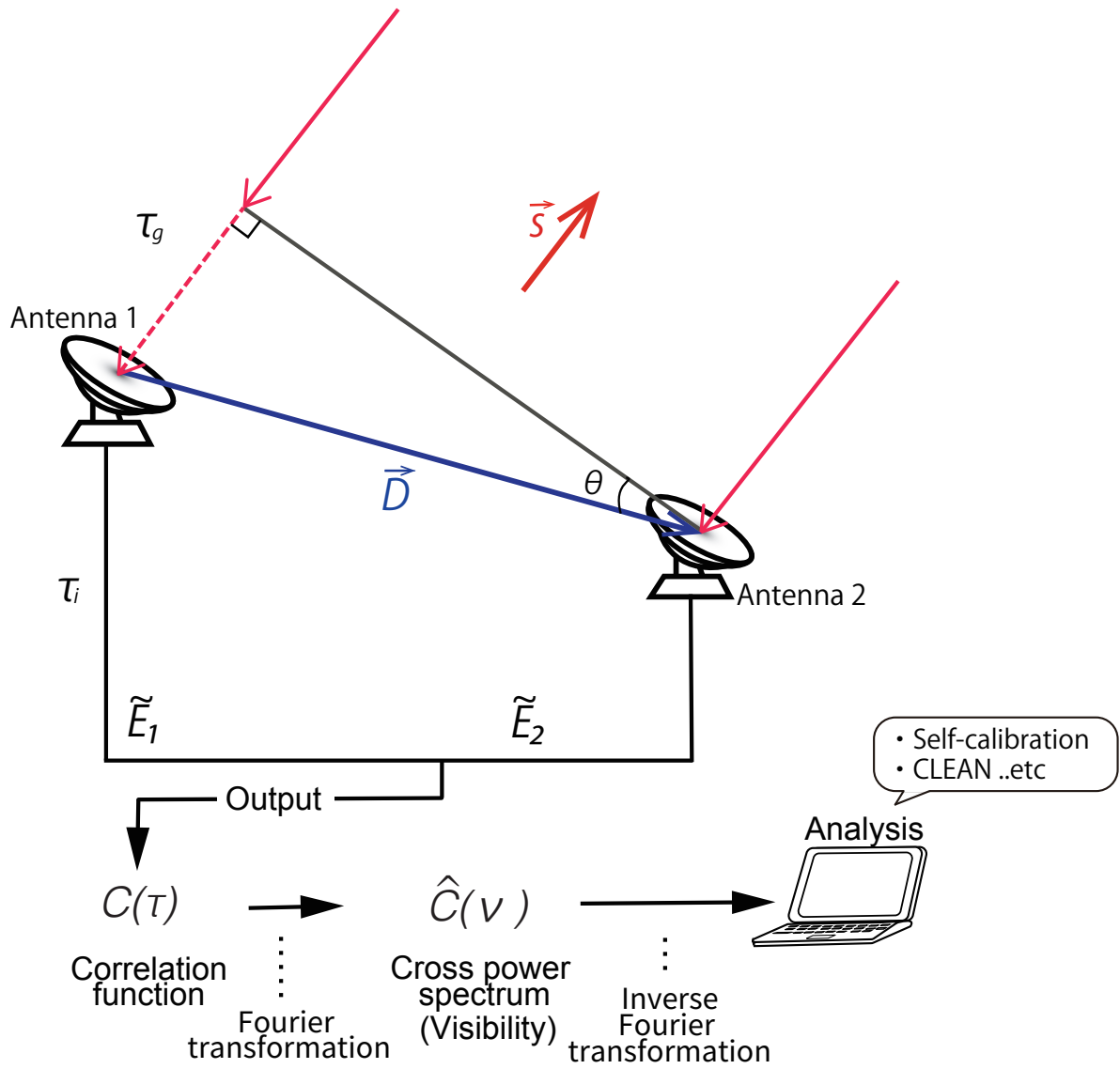
Figure 2.2: Signals and geometrical delay for two antennas.

,and then, the signal is represented as:

$$E(t) = \int_{-\infty}^{\infty} \hat{E}(\nu) \exp\left(2\pi i \nu t\right) \, d\nu \tag{2.9}$$

$$= a_m(t) \exp\left(2\pi i \nu_0 t\right). \tag{2.10}$$

This means that the amplitude and the phase are slowly modulated by $a_m(t)$, and the spectrum has a narrow width around the center frequency ν_0. The signals of antennas and the correlation function are then given as:

$$\widetilde{E}_1(t) = a_1 a_m(t) \exp\left(2\pi i \nu_0 t\right), \quad \widetilde{E}_2(t) = a_2 a_m(t - \tau_g) \exp\left(2\pi i \nu_0 (t - \tau_g)\right), \tag{2.11}$$

and

$$C(\tau) = \lim_{T \to \infty} \frac{1}{T} \int_{-T/2}^{T/2} \widetilde{E}_1(t - \tau_i) \widetilde{E}_2^*(t - \tau) \, dt \tag{2.12}$$

$$= \lim_{T \to \infty} \frac{1}{T} \int_{-T/2}^{T/2} a_1 a_2^* a_m(t - \tau_i) a_m^*(t - \tau_g - \tau) \exp\left(2\pi i \nu_0 (\tau + \tau_g - \tau_i)\right) dt. \tag{2.13}$$

By assuming that the variation of $a_m(t)$ is much slower than $(\tau + \tau_g - \tau_i)$, the following equations hold:

$$\lim_{T \to \infty} \frac{1}{T} \int_{-T/2}^{T/2} a_m(t - \tau_i) a_m^*(t - \tau_g - \tau) \tag{2.14}$$

$$= < a_m(t) a_m^*(t) >_T \tag{2.15}$$

$$= |E_0|^2. \tag{2.16}$$

Hence, we have the correlation function as:

$$C(\tau) = a_1 a_2^* < a_m(t) a_m^*(t) >_T \ \exp\left(2\pi i \nu_0 (\tau + \tau_g - \tau_i)\right). \tag{2.17}$$

The cross power spectrum is obtained as:

$$\hat{C}(\nu) = \int_{-\infty}^{\infty} d\tau \, C(\tau) \exp\left(-2\pi i \nu t\right) \tag{2.18}$$

$$= a_1 a_2^* < a_m(t) a_m^*(t) >_T \delta(\nu_0 - \nu) \exp\left(2\pi i \nu_0 (\tau_g - \tau_i)\right). \tag{2.19}$$

The phase of $\hat{C}(\nu)$ equals to 0 when τ_i is taken to be τ_g correctly. Thus, we can deal with any radiation by assuming the quasi-monochromatic radiation.

2.1.3 Extended Source

Next, we consider a source extended only along the x-axis ($\vec{l}$). For an angular offset of Δl from the center position of the source, the phase of $\hat{C}(\nu)$ ($\phi = 2\pi\nu(\tau_g - \tau_i)$) changes by $\Delta\phi$ as:

$$\Delta\phi = -\frac{\partial\phi}{\partial l}\Delta l \tag{2.20}$$

$$= -2\pi\nu \frac{\partial\tau_g}{\partial l}\Delta l \tag{2.21}$$

$$= -\frac{2\pi\nu}{c} \frac{\partial(\vec{D} \cdot \vec{s})}{\partial l}\Delta l \tag{2.22}$$

$$= \frac{2\pi}{\lambda} D \cos\theta \, \Delta l, \tag{2.23}$$

where θ corresponds to the angle shown in Figure 2.1. Here, 'fringe frequency' (u) is defined as:

$$u \equiv \frac{D \cos \theta}{\lambda}. \tag{2.24}$$

Then, the phase change is:

$$\Delta\phi = 2\pi u \Delta l. \tag{2.25}$$

The radiation of an extended source can be expressed by the superposition of the radiation from many point sources distributed continuously. For simplicity, we first focus on the positions l_1 and l_2 on the x-axis ($\vec{l}$), where the radiation spectra are $\hat{E}_1(\nu)$ and $\hat{E}_2(\nu)$, respectively. In this case, the intensity of an extended source is given as:

$$I(\nu, l) = |\hat{E}_1(\nu)|^2 \delta(l - l_1) + |\hat{E}_2(\nu)|^2 \delta(l - l_2). \tag{2.26}$$

We further assume that the delay correction (τ_i) is correctly applied for the geometrical delay (τ_g). Then, the phases of $\hat{C}(\nu)$ are written as:

$$\phi_1 = 2\pi\nu\tau_{g1} = 2\pi u l_1, \quad \phi_2 = 2\pi\nu\tau_{g2} = 2\pi u l_2, \tag{2.27}$$

where τ_{g1} and τ_{g2} are the geometrical delay between l_1 or l_2 and the source center, respectively. Since the radiation from the two point sources does not interface from each other for the quasi-monochromatic wave. (Born & Wolf, 1959), the correlation function $C(\tau)$ and the cross power spectrum $\hat{C}(\nu)$ are represented as follows:

$$C(\tau) = a_1 a_2^* \int_{-\infty}^{\infty} d\nu \left[|\hat{E}_1(\nu)|^2 \exp\left(2\pi i \nu(\tau + \tau_{g1})\right) + |\hat{E}_2(\nu)|^2 \exp\left(2\pi i \nu(\tau + \tau_{g2})\right) \right] \tag{2.28}$$

$$= a_1 a_2^* \int_{-\infty}^{\infty} d\nu \left[|\hat{E}_1(\nu)|^2 \exp\left(2\pi i u l_1\right) + |\hat{E}_2(\nu)|^2 \exp\left(2\pi i u l_2\right) \right] \exp\left(2\pi i \nu\tau\right), \tag{2.29}$$

and

$$\hat{C}(\nu) = \int_{-\infty}^{\infty} d\tau \, C(\tau) \exp\left(-2\pi i \nu t\right) \tag{2.30}$$

$$= a_1 a_2^* \int_{-\infty}^{\infty} d\tau \int_{-\infty}^{\infty} d\nu' \left[|\hat{E}_1(\nu')|^2 \exp\left(2\pi i \nu'\tau_{g1}\right) \right. \tag{2.31}$$

$$\left. + |\hat{E}_2(\nu)|^2 \exp\left(2\pi i \nu'\tau_{g2}\right) \right] \exp\left(2\pi i (\nu' - \nu)\tau\right) \tag{2.32}$$

$$= a_1 a_2^* \left[\left(|\hat{E}_1(\nu)|^2 \exp\left(2\pi i u l_1\right) + |\hat{E}_2(\nu)|^2 \exp\left(2\pi i u l_2\right)\right) \right]. \tag{2.33}$$

Based on the above derivation for the two point sources, the intensity from an extended source ($I(\nu, l)$) and the cross power spectrum $\hat{C}(\nu)$ are represented as:

$$I(v, l) = \sum_k |\hat{E}_k(v)|^2 \delta(l - l_k), \tag{2.34}$$

$$\hat{C}(v) = a_1 a_2^* \sum_k |\hat{E}_k(v)|^2 \exp(2\pi i u l_k). \tag{2.35}$$

In the case of a continuous source, the cross power spectrum $\hat{C}(v)$ is described by substituting the summation by integral as:

$$\hat{C}(v) = a_1 a_2^* \int_{all} dl \, |\hat{E}(v, l)|^2 \exp(2\pi i u l) \tag{2.36}$$

$$= a_1 a_2^* \int_{all} dl \, I(v, l) \exp(2\pi i u l). \tag{2.37}$$

The cross power spectrum $\hat{C}(v)$ is a function of the fringe frequency, u. This is called as 'complex visibility' and denoted as $V(v, u)$. This formulation can be expanded to the 2-dimensional distribution, where the complex visibility is a function of v, u, and v. Here, v is defined similarly as equation (2.24). In this case, the complex visibility $V(v, u, v)$ is denoted as:

$$V(v, u, v) = a_1 a_2^* \int_{-\infty}^{\infty} \int_{-\infty}^{\infty} dl \, dm \, I(v, l, m) \exp(2\pi i(ul + vm)), \tag{2.38}$$

This relation is called as 'van Cittert-Zernike theorem'. Namely, the complex visibility is a Fourier transformation of the intensity distribution of the source. By using this relation, the source image can be obtained from complex visibility data. This method is called as aperture synthesis.

2.1.4   Performance of Interferometer

In general, the angular resolution of a single-dish telescope (θ_{beam}) is determined by the diameter of the main reflector (D_{max}) and the observational wavelength (λ). Hence, θ_{beam} is frequency dependent even for the same telescope and is represented as:

$$\theta_{\mathrm{beam}} = \frac{k\lambda}{D_{\mathrm{max}}}, \tag{2.39}$$

where k is a constant value determined by the illumination pattern on the main reflector. θ_{beam} is also called as the beam size. The highest resolution is achieved, if all of the signals from the main reflector are fed into the receiver with uniform weights (Fraunhofer diffraction case). In this case, k equals to 1.02. As a drawback, the beam pattern has relatively high side lobes. We can reduce them by adjusting the illumination for the edge of the main reflector, resulting in k from 1.2 to 1.5. For interferometers, D_{max} corresponds to the longest projected baseline length (L_{max}).

The baseline length of ALMA can be as long as ~16 km s^{-1}, and hence, the highest resolution is ~0.″01 at the wavelength of 1 mm. As in the case of the single-dish telescope, the actual resolution depends on the weights for the baseline data.

On the other hand, the minimum baseline length of interferometers is limited by the diameter of the reflectors. Hence, the visibility data has a void around the origin of the u-v plane. This means the limit of the sensitivity for extended distributions larger than a certain scale, which is called as maximum recoverable scale (θ_{mrs}). It is given by using the shortest projected baseline length (L_{min}) as:

$$\theta_{\mathrm{mrs}} \fallingdotseq \frac{\lambda}{L_{\mathrm{min}}}. \tag{2.40}$$

As well, the field of view for observations (θ_{FOV}) is mainly determined by the beam size of the element antenna as:

$$\theta_{\mathrm{FOV}} \fallingdotseq \frac{\lambda}{D_{\mathrm{a}}}, \tag{2.41}$$

where D_{a} is the diameter of the element antenna. In ALMA observations, ACA (Atacama Compact Array) which consists of 4 12-m antennas and 12 7-m antennas is often used to fill the short (u,v) data, in order to reduce the resolve-out effect for extended sources. Mosaic observations with the total power observations are also employed to expand the field of view, where all of the correlations obtained from the observations toward the slightly different pointing directions are concatenated.

The observational noise level is usually presented as 'root mean square (rms)' (σ). It is defined as follows:

$$\sigma = \sqrt{\frac{\sum_i (x_i - \bar{x})^2}{N - 1}}, \tag{2.42}$$

where x_i represents the intensity at the position i without the source signal, N the total number of the positions. $\bar{x}$ is the average of them, which essentially equals to 0 for the ideal case.

2.2 ALMA

ALMA (Atacama Large Millimeter/Submillimeter Array) is a large radio interferometer telescope with state-of-the-art technologies (Figure 2.3), which is designed to observe all the millimeter and submillimeter wave windows from the ground (Figure 2.4). To minimize the absorption by water vapor and oxygen molecules contained in the atmosphere, it was constructed at the high altitude site (5000 m) with dry and thin air, Llano de Chajnantor, in the Atacama Desert, northern Chile. ALMA project is being conducted in the international cooperation with Chile, Europe (ESO), North America (AUI/NRAO), and East Asia including Japan (NAOJ). ALMA consists of the main array (50 12-m antennas) and ACA (4 12-m antennas and 12 7-m antennas). The early science operations started in 2011 by using only 16 antennas. Now, ALMA is in its full operation and achieves the resolution of 0.″01

for the baseline length extended up to ~16 km. Such a resolution is 10-100 times higher than that of other millimeter/submillimeter telescopes. The spectral (velocity) resolution is as narrow as ~0.008 km s^{-1}, and hence, we can analyze velocity structures of the gas around protostars in detail by using molecular lines.

Figure 2.3: ALMA (Atacama Large Millimeter/Submillimeter Array)

2.2.1 Observable Frequency

The millimeter/submillimeter wave of 84-950 GHz (~0.3-10 mm) is now observable, and it is divided into 8 frequency bands which correspond to the atmospheric windows (Figure 2.4). They are Band 3-Band 10, as listed in Table 2.1. The results of this thesis are based on the data observed in Band 6 and Band 7.

In the Band 3-Band 10 receivers, SIS (Superconductor-Insulator-Superconductor) mixers are employed as the frontend. The SIS mixer utilizes the photon-assisted tunneling of a Josephson junction in the frequency mixing, whose quantum theory is presented by Tucker & Feldman (1985). By using the Nb/AlOx/Nb junction, the receiver noise is as low as a few times the quantum noise ($h\nu/k$) even for the highest frequency band, Band 10 (e.g., Kojima et al., 2009). In addition, the ALMA receivers observe the two orthogonal polarization signals simultaneously. Furthermore, the Band 3-Band 8 receivers output the lower and upper sideband signals separately by using the two mixers for each polarization. Their instantaneous bandwidth for each sideband is 4 GHz (5.5 GHz for Band 6) so that we can cover 8 GHz in total by using both sidebands. Note that the Band 1 and Band 2 receivers are not ready for the operation at this moment. The Band 1 receiver is now under development.

ALMA has a large correlator system with high flexibilities for the spectral line observations as well as the continuum observation. At most, 16 spectral windows can be set within the instantaneous bandwidth. Correlator setups depend on the purpose of observations. In this thesis, we use one wideband and low-resolution
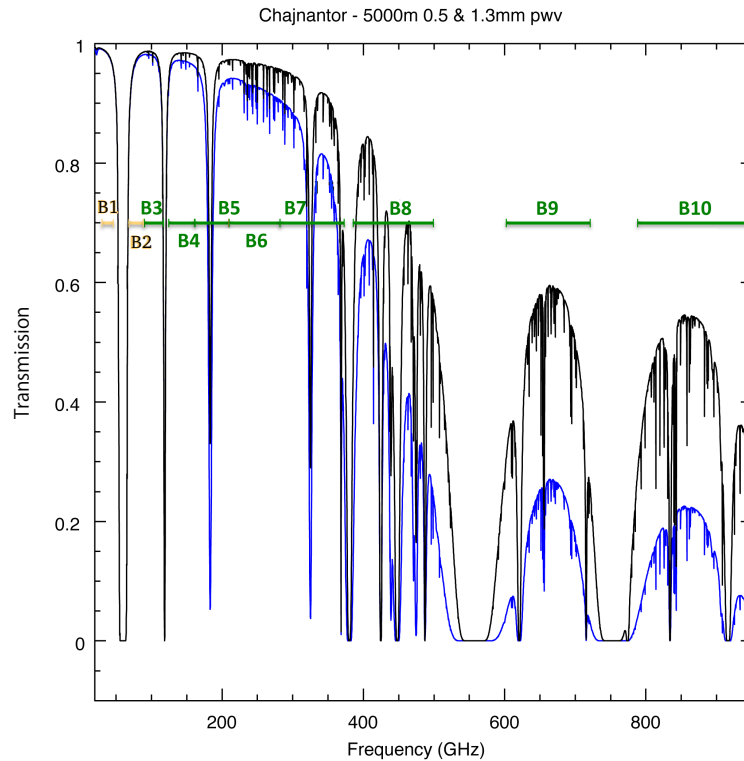
Figure 2.4: The transparency spectrum of the atmosphere above the ALMA site is shown. Blue and Black curves are the transparencies for 55 % and 25 % weather conditions, respectively, averaged over the year. This means that 55% of the time in a year is better than the blue line (corresponding to a precipitable water vapor (PWV) of 1.3 mm), and 1/4 (25 %) of the time is better than the black line (corresponding to 0.5 mm of PWV). The horizontal lines represent the frequency coverage of the ALMA receiver bands described in Subsection 2.2.1. Taken from Observing with ALMA-A Primer: Doc 8.1 (ver. 2 in 2021).

spectral window for the continuum observation and narrow and high-resolution spectral windows as many as possible for the spectral line observation. This correlator capability is ideal for observing many spectral lines simultaneously to study chemical compositions and their distributions.

In interferometric observations, the following calibrations are necessary: phase and amplitude calibration, bandpass calibration, and absolute flux calibration. Phase and amplitude calibrations and bandpass calibration are usually carried out by observing the bright continuum sources such as quasars near the target source. Absolute flux calibration is usually done by observing the satellites of the solar system planets. The accuracy of the absolute intensity scale is 10 %[1]. The above calibrations are carried out by the pipeline provided by ALMA. For better imaging, self-calibration, that is the phase and amplitude calibration by the target source itself, is sometimes applied, as mentioned later (Subsection 2.2.3).

---

[1]Lundgren, A. 2013, ALMA Cycle 2 Technical Handbook Version 1.1, ALMA
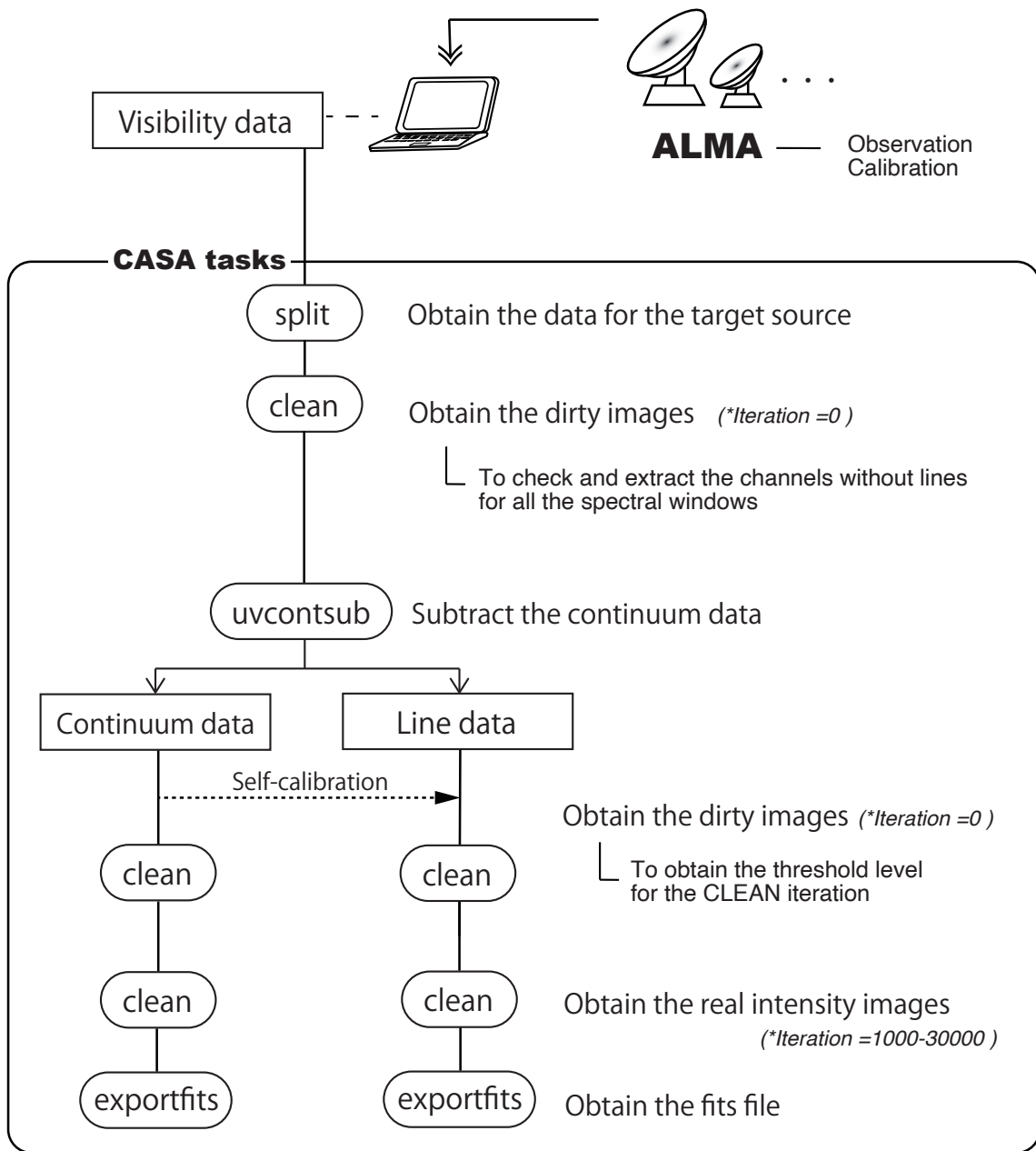
Figure 2.5: Flow of the analysis for the ALMA data after the delivery from ALMA. First, the CASA task, 'split' is applied to the visibility to obtain the visibility for the target source. Then, the dirty images are prepared to extract the frequency ranges seen in molecular line emissions. By subtracting the visibility data for the continuum from the original visibility by using the CASA task, 'uncontsub', the visibility data for the lines are obtained. The observed images are obtained by using the CLEAN algorithm (See Subsection 2.2.2).

2.2.2 CLEAN

A typical flow of the analysis for ALMA data is shown in Figure 2.5. In this thesis, we obtain the images through this process with the tasks in the application soft-

Table 2.1: ALMA Receiver Bands[a]

Band	Wavelength (mm)	Noise (K)	Frequency (GHz)	Produced by[b]	Receiver[c]	First light
1	6-8.5	26	35-50	TBD	HEMT	TBD
2	3.3-4.5	47	65-90	TBD	HEMT	TBD
3	2.6-3.6	60	84-116	HIA	SIS	2009
4	1.8-2.4	82	125-163	NAOJ	SIS	2013
5	1.4-1.8	105	163-211	OSO/NOVA	SIS	2016
6	1.1-1.4	136	211-275	NRAO	SIS	2009
7	0.8-1.1	219	275-373	IRAM	SIS	2009
8	0.6-0.8	292	385-500	NAOJ	SIS	2013
9	0.4-0.5	261	602-720	NOVA	SIS	2011
10	0.3-0.4	344	787-950	NAOJ	SIS	2012

[a] Taken from 'https://www.eso.org/public/teles-instr/alma/receiver-bands/' .
[b] HIA for Herzberg Astrophysics, NAOJ for National Astronomical Observatory of Japan, OSO for Onsala Space Observatory, NOVA for Nederlandse Onderzoekschool Voor Astronomie, NRAO for National Radio Astronomy Observatory, and IRAM for Institut de Radioastronomie Millimétrique.
[c] HEMT fot High-Electron-Mobility Transistor, SIS for Superconductor-Insulator-Superconductor

ware provided by ALMA (CASA: Common Astronomy Software Applications). In the analysis, we can derive the source images by the inverse Fourier transformation of the visibility with the CASA task, 'clean'. CLEAN is an imaging technique to subtract the effect of side lobes, which is essentially the process of deconvolution (Högbom, 1974). The intensity distribution ($I_{\rm obs}$) is assumed to be the superposition of the intensity for a position. We convolve it with the CLEAN beam which corresponds to the beam pattern approximated by Gaussian function, and obtain the better intensity distribution without the effect of the side lobes ($I^c_{\rm obs}$).

2.2.3 Self-Calibration

This procedure can be applied for the phase and the amplitude to refine these calibrations by using the data of the target source. The dust continuum data before the self-calibration are used for the first deconvolved model. From the second deconvolved model, the previous dust continuum data is used. In this thesis works, the intensity of the dust continuum of IRAS 15398−3359 for the data used in Chapters 3 and 7 is not bright enough for this procedure, and hence, we performed the phase self-calibration only for the data of IRAS 15398−3359 (Chapter 4), L483 (Chapter 8) and B335 (Chapters 5 and 8). The amplitude self-calibration is also applied for IRAS 15398−3359 (Chapter 4). Although self-calibration can be conducted as many iterations as the calibration is improved, we should check the refined images after each iteration. The dust continuum images of L483 before and after the self-calibration are shown in Figures 2.6 (a) and (b), respectively. The peak positions are not changed, which is (α_{2000}, δ_{2000})= ($18^{\rm h}17^{\rm m}29^{\rm s}.94$, $-4°39'39.''59$). These peak intensities are 10.8 mJy beam^{-1} and 15.3 mJy beam^{-1}, respectively, where the beam sizes are 0.''2×0.''1 for both images. The peak intensity after the self-calibration is ∼1.4 times higher than the original one, because the side lobe effects are reduced. The solutions obtained from the self-calibration procedure for the continuum are

applied to the spectral line data.
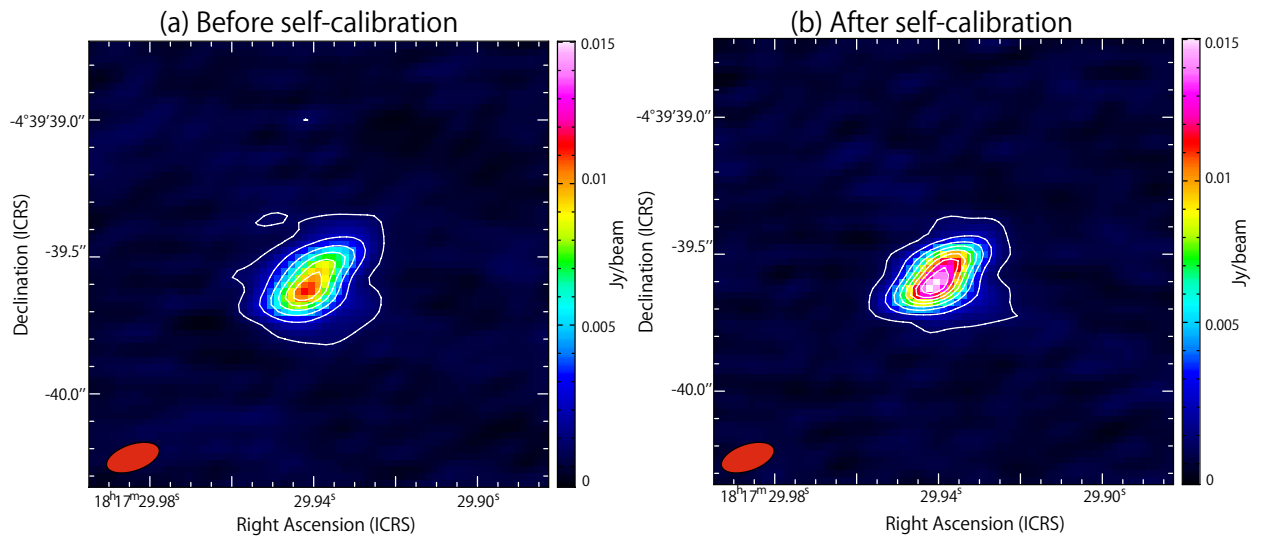
Figure 2.6: Dust continuum images of L483. Contour levels are 3σ from σ, where σ is 0.2 mJy beam^{-1}. Red ellipses in the bottom-left corner of each panel represent the beam size. (a) The self-calibration is not applied. The peak intensity is 10.84 mJy beam^{-1}. (b) The self-calibration is applied. The peak intensity is 15.30 mJy beam^{-1}. The beam size and σ are not changed through the self-calibration.

Part I

Physical Structure

Chapter 3
Very Low Mass Protostar: IRAS 15398-3359*

In this chapter, the disk/envelope structure for the low-mass Class 0 protostellar source, IRAS 15398−3359, is investigated to explore the beginning of disk formation. For this purpose, we have observed the CCH (N =3−2, J =7/2−5/2, F =4−3 and 3−2) and SO (J_N =7_6−6_5) emission at a 0.″2 angular resolution with ALMA (Atacama Large Millimeter/Submillimeter Array). Based on these molecular distributions, we comprehend the kinematics for the inner disk and the outer envelope structure separately. The inner disk detected in the SO emission most likely shows a Keplerian rotation, and the protostellar mass is estimated to be $0.007^{+0.004}_{-0.003}$ $M_\odot$. With this protostellar mass, the velocity structure of the CCH emission is explained by the model of the infalling-rotating envelope, where the radius of the centrifugal barrier is estimated to be 40 au from the comparison with the model. The disk mass evaluated from the dust continuum emission by assuming the dust temperature of 20 K−100 K is 0.1−0.9 times the stellar mass, resulting in the Toomre Q parameter of 0.4−5. Hence, the disk structure may be partly unstable. All these results suggest that a rotationally supported disk can be formed in the earliest stage of the protostellar evolution.

3.1   Introduction

A thorough understanding of disk formation is of fundamental importance in exploring the origin of the solar system, as described in Chapter 1. Although theoretical simulations have extensively been conducted for disk formation (e.g., Bate, 1998; Hueso & Guillot, 2005; Inutsuka et al., 2010; Machida et al., 2011a; Tsukamoto et al., 2017; Zhao et al., 2018), our understanding is far from complete. The existence of the disk structure has recently been suggested for protostars in the young stages (Class 0/I), thanks to high spatial resolution observations with interferometers including ALMA (e.g., Tobin et al., 2012; Yen et al., 2013, 2017; Brinch & Jørgensen, 2013; Murillo et al., 2013; Lindberg et al., 2014; Lee et al., 2014; Ohashi et al., 2014; Oya et al., 2016, 2017; Sakai et al., 2017). These results suggest that the disk structure is possibly formed at an earlier stage than previously thought. Hence, it is now more and more important to explore when the disk formation starts. It may

---

*The content of this chapter is published as: Okoda et al. (2018), ApJL, 864, L25

be related to the evolution of the first hydrostatic core (Inutsuka et al., 2010). In addition, the protostellar mass can be evaluated by analyzing the rotation motion, if the disk structure is observed in molecular lines. Thus, studies of disk kinematics make it possible to trace the amount of material that has been accreted onto the young star and thus follow its build up during the embedded protostellar stages.

IRAS 15398−3359 is a low-mass protostar in the Lupus 1 molecular cloud at a distance of d =156 pc (Dzib et al., 2018). Its bolometric temperature is 44 K (Jørgensen et al., 2013), typical of Class 0 protostars. A molecular outflow from this source was detected through single-dish observations of its CO emission (Tachihara et al., 1996; van Kempen et al., 2009). From a chemical point of view, IRAS 15398−3359 is a so-called warm carbon-chain chemistry (WCCC) source which is rich in various unsaturated carbon-chain molecules, such as CCH, C_4H, and CH_3CCH, present on scales of a few thousand au scale around the protostar (Sakai et al., 2009).

Past episodic accretion events was suggested for this source with ALMA observations. Jørgensen et al. (2013) conducted sub-arcsecond resolution observations, and found a ring structure of the $H^{13}CO^+$ (J =4−3) emission at scales of 150−200 au. This ring structure is thought to be formed by the destruction of HCO^+ through the gas-phase reaction with H_2O which has sublimated from the grains due to the enhanced protostellar luminosity caused by a recent accretion burst. Bjerkeli et al. (2016b) observed the HDO ($1_{0,1}-0_{0,0}$) emission, and found that it is localized at the cavity wall in the vicinity of the protostar. The extent of the emission is also consistent with the interpretation that a recent accretion burst has taken place. In addition, Bjerkeli et al. (2016a) found bullets with spacings consistent with the time-scale for relatively recent accretion bursts through the Submillimeter Array (SMA) observation.

High-resolution observations with ALMA toward this source have also been conducted to explore the outflow structure and the disk/envelope system. Oya et al. (2014) reported the distribution of the H_2CO ($5_{1,5}-4_{1,4}$) line at a high angular resolution of 0.″5 (∼80 au), and characterized a bipolar outflow extending along the northeast-southwest axis on a 2000 au scale. The analysis of the outflow structure indicates that it is oriented almost in the plane of the sky with an inclination angle of 70° with respect to the line of sight. This, in turn, suggests that the disk/envelope system is seen edge-on. This feature is further verified by CO observations with SMA (Bjerkeli et al., 2016a). Oya et al. (2014) derived an upper limit on the protostellar mass to be 0.09 $M_\odot$ from the velocity structure of the H_2CO emission around the protostar. In the envelope, they pointed out the possibility that a rotationally supported disk structure may have already been formed around the protostar based on the detection of high-velocity components of H_2CO associated with the protostar whose velocity shift is as high as ∼3 km s^{-1}. Later, Yen et al. (2017) found an upper limit of 0.01 $M_\odot$ for the protostellar mass, based on their observation of the $C^{18}O$ ($J = 2 - 1$) line (resolution of about 0.″5).

From these results, it seems likely that IRAS 15398−3359 has a very low protostellar mass. However, all values obtained so far are upper limits, and the mass has not been evaluated definitively. Thus, we need to confirm the existence of the disk component around the protostar suggested by Oya et al. (2014) and use it to measure the protostellar mass. With these motivations, we conducted the ALMA

observations at a higher angular resolution of 0.″2 ($\sim$ 30 au) to characterize the disk/envelope structure of IRAS 15398−3359.

3.2 Observation

Observations of IRAS 15398−3359 were carried out with ALMA in its Cycle 2 operation on 2015 July 20. Spectral lines of CCH and SO were observed with the Band 6 receiver at a frequency range from 261 to 263 GHz. The spectral line parameters are listed in Table 3.1. The N =4−3 lines of CCH used by Oya et al. (2014) do not clearly show the velocity structures because of mutual overlapping of the two hyperfine components, and hence, we here chose the N =3−2 lines having a larger separation of the hyperfine components. Forty-one antennas were used in the observations, where the baseline length ranged from 14.90 to 1559.16 m. The field center of the observations was (α_{2000}, δ_{2000})= ($15^{\mathrm{h}}43^{\mathrm{m}}02^{\mathrm{s}}.242$, $-34°09'06.″70$). The system temperature ranged from 60 to 100 K during the observation. The back-end correlator was set to a resolution of 61 kHz and a bandwidth of 59 MHz. This spectral resolution corresponds to a velocity resolution of 0.07 km s^{-1} at 250 GHz. The bandpass calibrator was J1517−2422. The data calibration was performed in the antenna-based manner, and the absolute calibration accuracy is 10 % (Lundgren , 2013), where the absolute flux density scale was derived from Titan. Images were prepared by using the CLEAN algorithm, where Briggs' weighting with a robustness parameter of 0.5 was employed. The continuum image was obtained by averaging line-free channels, and the line images were obtained after subtracting the continuum component directly from the visibilities. Self-calibration was not applied in this study, since the continuum emission is not bright enough. The primary beam (half-power beam) width was 23.″04. The total on-source time was 21.61 minutes. The synthesized-beam sizes are 0.″21×0.″15 (P.A. 58°) for the continuum image, 0.″36×0.″29 (P.A. 60°) for the CCH image, and 0.″22×0.″16 (P.A. 55°) for the SO image. The rms noise levels (σ) for the continuum emission, the CCH emission, and the SO emission are 0.12 mJy beam^{-1}, 4 mJy beam^{-1}, and 4 mJy beam^{-1}, respectively, for the channel width of 61 kHz.

Table 3.1: Parameters of the Observed Line

Molecule	Frequency (GHz)	$S\mu^2(D^2)$	$E_{\mathrm{u}}k^{-1}(\mathrm{K})$
CCH (N =3−2, J =7/2−5/2, F =4−3)	262.0042600	2.3	25
CCH (N =3−2, J =7/2−5/2, F =3−2)	262.0064820	1.7	25
SO (J_N =7_6−6_5)	261.8437210	16.4	47

3.3 Distribution

Figure 3.1(a) shows the moment 0 map of the CCH (N =3−2, J =7/2−5/2, F =4−3 and 3−2) lines, where the extended outflow cavity along the northeast-southwest axis (P.A. 220°) is clearly seen. This feature is essentially similar to those for the

CCH (N =4−3, J =7/2−5/2, F =4−3 and 3−2) lines reported by Jørgensen et al. (2013) and Oya et al. (2014). On 300 au scales in the vicinity of the protostar, the CCH emission is extended along the northwest-southeast axis. Figures 3.1(b) and (c) are blow-ups of the central part of panel (a). In Figure 3.1(b), the continuum map is superposed with contours on the CCH map. The coordinates of the peak position and its intensity are derived from a 2D Gaussian fit to the image : (α_{2000}, δ_{2000}) = ($15^h43^m02^s.2421\pm0.0002$, $−34°09'06.''805\pm0.001$). The position is consistent with previous reports (Jørgensen et al., 2013; Oya et al., 2014; Bjerkeli et al., 2016b). The peak intensity of 6.98±0.12 mJy beam^{-1} at 1.2 mm is also consistent with previous observations at 0.8 mm (19 mJy beam^{-1} with a beam size of about 0.''55×0.''37; P. A. −82°: Jørgensen et al., 2013) and 0.6 mm (36 mJy beam^{-1} with a beam size of about 0.''55×0.''37; P. A. −82°: Bjerkeli et al., 2016b) on the assumption of optically thin emission from dust with the opacity law $\kappa \propto \nu^\beta$ with $\beta \simeq 2$ typical for standard interstellar medium dust.

The CCH emission is weak at the continuum peak position, as shown in Figure 3.1(b). We define the line perpendicular to the outflow axis as the envelope direction (P.A. 130°; the arrow in Figure 3.1(b)), and prepare the intensity profiles of the CCH, SO, and 1.2 mm continuum emission along the line (Figure 3.2). Apparently, CCH shows a double peak in its intensity profile. The intensity peak of CCH appears on both sides at a distance of about 70 au from the continuum peak. Although this double-peaked feature was marginally reported in the CCH (N =4−3, J =7/2−5/2, F =4−3 and 3−2) emission by Jørgensen et al. (2013) and Oya et al. (2014), it is further confirmed in the present high-resolution observation.

In contrast to the CCH distribution, the SO distribution is concentrated in the vicinity of the protostar. Figure 3.1(c) shows the integrated intensity map of the SO (J_N =7_6−6_5) line in contours superposed on that of CCH in a color map. The peak position of the SO distribution almost coincides with the continuum peak. This feature is clearly seen in the intensity profile along the envelope direction, as shown in Figure 3.2, where the SO emission shows a single-peaked distribution between the two intensity peaks of CCH.

A similar difference between the CCH and SO distributions is reported for another Class 0 low-mass protostar, L1527. The gas distribution around the protostar of L1527, which is a prototypical WCCC source, was explored with ALMA by Sakai et al. (2014a,b). According to their results, CCH and c-C$_3$H$_2$ are distributed outside the centrifugal barrier of the infalling-rotating envelope, while SO resides at the centrifugal barrier and/or inside it. A centrifugal barrier stands for the perihelion of the ballistic motion of the infalling-rotating gas, where the gas cannot fall inward under the conservation laws of the energy and angular momentum. It has been proposed that the temperature is raised around the centrifugal barrier due to a weak accretion shock of the infalling gas, and SO is likely liberated from grain mantles and enhanced there (Sakai et al., 2014a,b; Aota et al., 2015; Miura et al., 2017). In contrast, CCH seems to be broken up by gas-phase reactions or depleted onto grain mantles inside the centrifugal barrier.
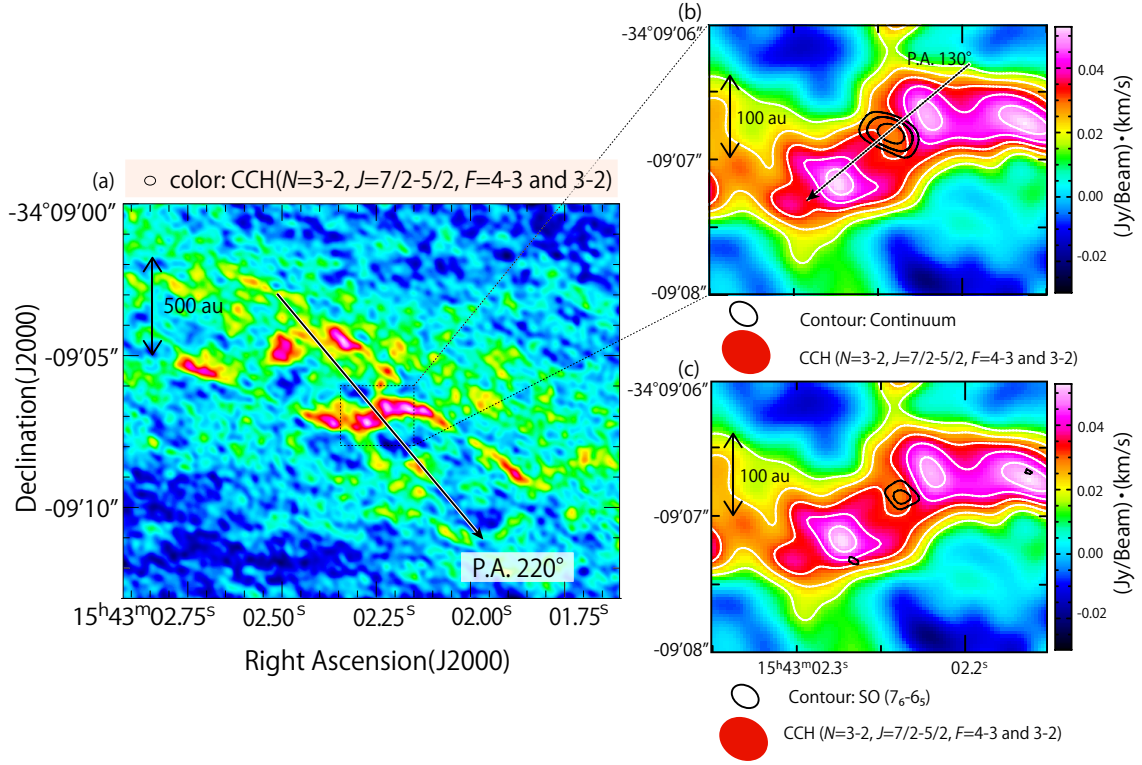
Figure 3.1: (a) The moment 0 map of the CCH (N =3−2, J =7/2−5/2, F =4−3 and 3−2) lines. The arrow represents the outflow axis (P.A. 220°). (b) The color map is a blow-up of the central part of panel (a). The black contours are the continuum map. Contour levels are 10σ, 20σ, and 40σ, where σ is 0.12 mJy beam^{-1}. The white contours are the moment 0 map of the CCH (N =3−2, J =7/2−5/2, F =4−3 and 3−2) lines. Contours levels are 2σ, 3σ, 4σ, 5σ, and 6σ, where σ is 8 mJy beam^{-1} km s^{-1}. The dotted arrow represents the envelope direction (P.A. 130°). (c) The color map is a blow-up of the central part of panel (a). The contours are the moment 0 map of the SO (J_N =7_6−6_5) line. Contour levels are 3σ and 4σ, where σ is 8 mJy beam^{-1} km s^{-1}. The black cross shows the continuum peak position. The ellipses depicted in front of the lines show the beam size.

3.4 Kinematics

3.4.1 Keplerian Motion

First, we investigate the kinematic structure of the SO emission, which is well concentrated around the protostar. Figure 3.3(a) shows the position-velocity (PV) diagram of the SO emission along the envelope direction (P.A. 130°) centered at the continuum peak. Red-shifted and blue-shifted components can be recognized in the southeastern and northwestern parts, respectively (Figure 3.3(a)). More importantly, the maximum velocity shift from the systemic velocity is as high as about 3 km s^{-1}. These components likely correspond to the high-velocity components marginally detected in the H_2CO emission (Oya et al., 2014). These results imply that SO traces the rotating disk structure around the protostar. The PV diagram along the line perpendicular to the envelope direction does not show a significant

47
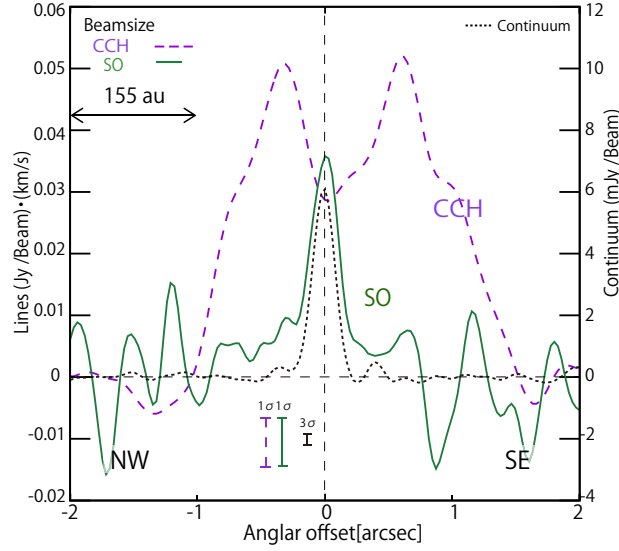
Figure 3.2: The intensity profiles of CCH (N =3−2, J =7/2−5/2, F =4−3 and 3−2) and SO (J_N =7_6−6_5) along the envelope direction shown by the dashed arrow in Figure 3.1(b). Their noise levels are described by σ, where σ is 8 mJy beam^{-1} km s^{-1}, on the bottom of this figure. The noise level of the continuum is described by 3σ, where σ is 0.12 mJy beam^{-1}. The abscissa is the angular offset from the continuum peak.

velocity gradient, indicating no infall and outflow motion (Figure 3.3(b)). Hence, the observed rotational motion is most likely the Keplerian rotation. In Figure 3.3(a), the blue contours represent the model of Keplerian rotation with a protostellar mass of 0.007 $M_\odot$. It seems to explain the velocity structure of the PV diagram observed for the SO emission reasonably well. Note that the intensity around the central position in the model is much stronger than that in the observed PV diagram. This is most likely due to self-absorption or absorption by the foreground gas, especially around the systemic velocity. In this study, we focus on the kinematic structure of the disk, and the effects of radiative transfer and self-absorption are not included in the model. On the other hand, the PV diagram cannot be explained by the infalling-rotating envelope, even if the radius of the centrifugal barrier is set to 1 au (almost the free-fall motion) (Figure 3.3(c)). The counter velocity components, which are red-shifted and blue-shifted for the northwestern and southeastern sides, respectively, appear in this model as opposed to the observed PV diagram.

Thus, the protostellar mass of this source is evaluated to be $0.007^{+0.004}_{-0.003}$ $M_\odot$ on the assumption of the Kepler rotation (Figure 3.3(d)). This very small mass is consistent with the upper limits reported so far: <0.09 $M_\odot$ (Oya et al., 2014); < 0.01 $M_\odot$ (Yen et al., 2017). Although IRAS 15398−3359 clearly has a very low protostellar mass, a rotating disk structure has already formed around the protostar. Note that, in the above analysis, we employ a systemic velocity of 5.5 km s^{-1}. This is slightly different from the value (5.0−5.3 km s^{-1}) reported in Oya et al. (2014) and Yen et al. (2017). This difference is discussed later.

The protostellar mass derived above is comparable to, or even smaller than, the mass of the first hydrostatic core expected from star formation theories (0.01-0.05

$M_\odot$: Penston, 1969; Larson, 1969; Masunaga et al., 1998; Saigo & Tomisaka, 2006). Since the protostellar mass is so small, the gravity of the system may not be well represented by a central force field. In fact, the dust mass evaluated from the 1.2 mm continuum data is between 0.006 and 0.001 $M_\odot$ for an assumed dust temperature of 20 K and 100 K, respectively, which are not much different from the protostellar mass. Here, we employ the mass absorption coefficient of 6.8×10^{-4} cm^2 g^{-1} at 1.2 mm (Ward-Thompson et al., 2000). Although the temperature of 100 K seems too high, it is adopted as the upper limit. Hence, the rotation motion may not be exactly Keplerian, and the mass of 0.007 $M_\odot$ might be an apparent value. Nevertheless, the small protostellar mass would not change drastically, even if such an effect is considered (Mestel, 1963). To explore this effect in more detail and to derive the protostellar mass definitively, we need higher sensitivity observations of SO and other molecules. Even if the motion can be approximated by the Keplerian motion, a caveat should be mentioned. With the current resolution, we cannot be sure whether the materials in the beam centered at the protostar have already accreted onto the star. In this case, the derived mass could be an upper limit to the mass of the prototstar.

To assess the stability of the disk, we evaluate the Toomre-Q parameter, $Q(r)$, (Toomre, 1964; Goldreich & Lynden-Bell, 1965) with the equations:

$$Q(r) = \frac{\kappa(r)c_{\mathrm{s}}}{\pi G \Sigma(r)}, \qquad (3.1)$$

and

$$\kappa(r) = \left[2\frac{V_{\mathrm{rot}}(r)}{r} \left(\frac{V_{\mathrm{rot}}(r)}{r} + \frac{dV_{\mathrm{rot}}}{dr} \right) \right]^{\frac{1}{2}}, \qquad (3.2)$$

where $\kappa(r)$ is epicyclic frequency, c_{s} the sound velocity, G gravitational constant, and we have: $\Sigma(\mathrm{r})$ the surface density of the dust continuum. By assuming the Keplerian motion,

$$\kappa(r) = \frac{V_{\mathrm{rot}}(r)}{r}. \qquad (3.3)$$

Toomre-Q parameter indicates the unstable disk when it is lower than 1. The derived Q parameter is 0.4 and 5 for temperatures of 20 K and 100 K, respectively. Thus, either the disk is relatively warm and of low mass, or it is in an unstable regime. Such an unstable part may be responsible for future accretion bursts.

3.4.2   Infalling-rotating Envelope

By using the protostellar mass estimated from the Keplerian motion, we examine whether the kinematic structure traced by the CCH emission is consistent with an infalling-rotating envelope. Figure 3.4(a) is the PV diagram of the CCH emission along the envelope direction, while Figure 3.4(b) shows that along the line perpendicular to the envelope direction. The black dashed lines are the model of the

49
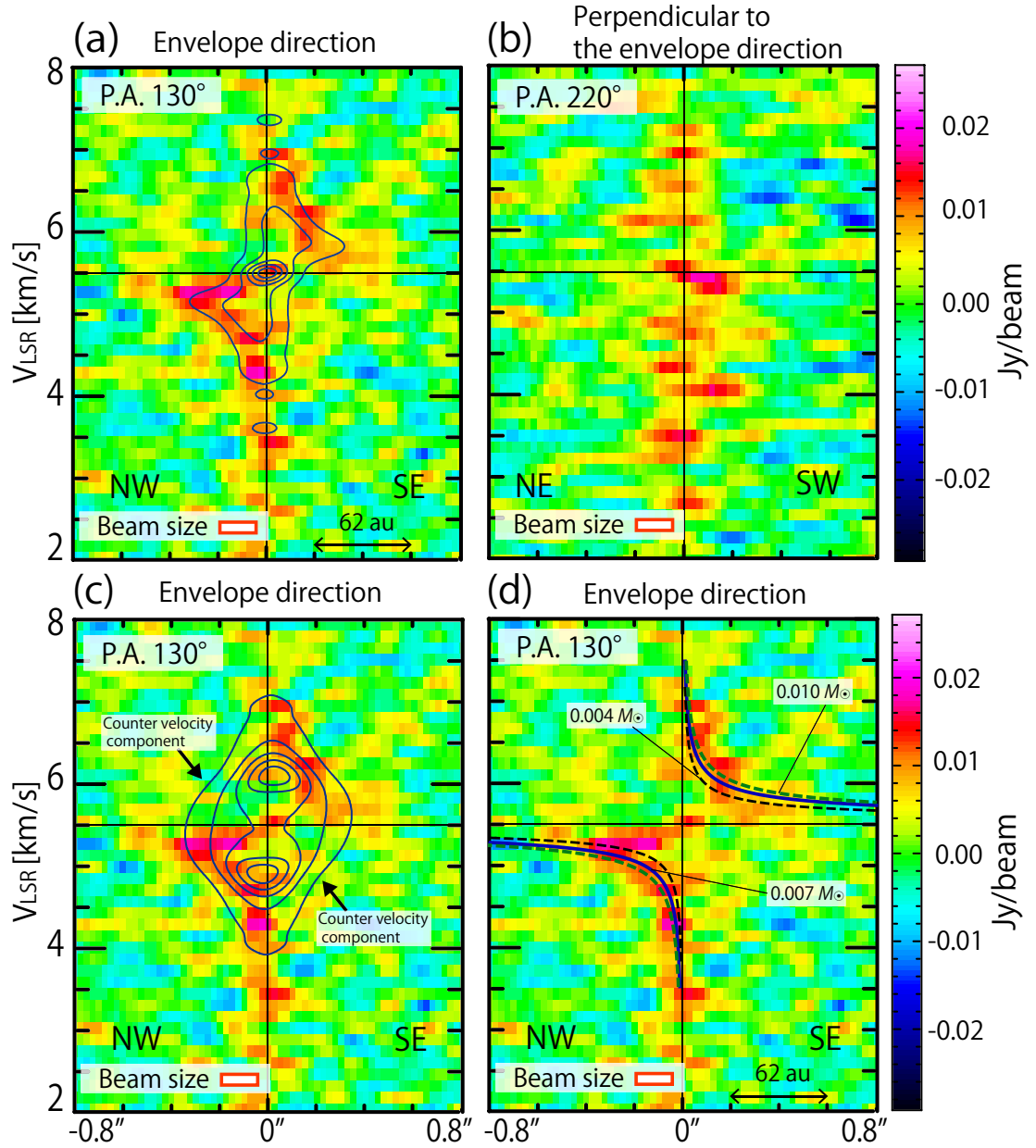
Figure 3.3: (a) The PV diagram of the SO ($J_N = 7_6 - 6_5$) emission along the envelope direction shown by the dashed arrow in Figure 1(b). The origin is the continuum peak position. The blue contours are the model of Keplerian rotation around the systemic velocity of 5.5 km s^{-1} with the protostellar mass of 0.007 $M_\odot$, the outer radius of 40 au, and the inclination angle of 70°(0° for a face-on configuration). (b) The PV diagram of the SO ($J_N = 7_6 - 6_5$) emission along the line perpendicular to the envelope direction centered at the continuum peak position. (c,d) The color maps are the PV diagrams of the SO ($J_N = 7_6 - 6_5$) emission along the envelope direction. The blue contours are the infalling-rotating envelope model with the protostellar mass of 0.007 $M_\odot$, the outer radius of 40 au, the radius of the centrifugal barrier of 1 au, and the inclination angle of 70°. The curves are the model of Keplerian rotation with the different protostellar mass assumed. Green, blue and black show the cases of 0.010, 0.007 and 0.004 $M_\odot$.

Keplerian rotation with the protostellar mass of 0.007 $M_\odot$. The Keplerian rotation model does not explain the velocity gradient along the line perpendicular to the envelope direction (Figure 3.4(b); dashed lines). The contours in Figures 3.4(a) and (b) are the results of the infalling-rotating envelope model (Oya et al., 2014) around the protostar with a protostellar mass of 0.007 $M_\odot$, where the radius of the centrifugal barrier is assumed to be at 40 au. The infalling-rotating motion seems to roughly explain the observed kinematic structure of CCH, although there is weak emission outside of the model in the observed PV diagrams probably due to contributions from the outflow cavity. It should be noted that, in the infalling-rotating envelope case, the systemic velocity of 5.3 km s^{-1}, which is similar to the previous report (Yen et al., 2017), gives a better fit. Hence, the envelope and the disk could have slightly different systemic velocities. This difference is small, but significant. It may originate from the small protostellar mass, because, in this case, the disk system and the envelope could have different centers of mass.

3.5   Co-evolution of Disks and Stars?

IRAS 15398−3359 is found to be a very low-mass protostar. A protostar with a mass as low as this source has never been reported. Nevertheless, we find that a rotating disk structure has already formed (Figure 3.3(a)). Although the radius of the centrifugal barrier is derived to be 40 au, SO could become abundant in front of the centrifugal barrier due to the accretion shock. Hence, its distribution up to a radius of about 60 au is reasonable. The Keplerian rotation model is mainly compared in the range of $r \lesssim 40$ au, and hence, the effect of the infalling-rotating components to the derivation of the protostellar mass can be ignored. Kristensen et al. (2012) and Jørgensen et al. (2013) reported envelope masses of 0.5 $M_\odot$ and 1.2 $M_\odot$, respectively, and hence, the protostar will grow further. Thus, the very low mass of the protostar means that it is in its infancy. In fact, the dynamical timescale of the outflow of this source is reported to be 10^2-10^3 yr (Oya et al., 2014; Bjerkeli et al., 2016a). The present results therefore mean that a rotating disk structure can be formed at a very infant stage of protostellar evolution.

Figures 3.5 (a) and (b) show the comparison of the protostellar masses with the bolometric luminosties and the disk masses, respectively. Red marks represent the result for IRAS 15398−3359 obtained in this study. Compared with some other low-mass protostars reported in previous works, the mass of IRAS 15398−3359 is the lowest, while its bolometric luminosity is moderate. This result indicates that the bolometric luminosity is not always a good indicator of the protostellar mass. On the other hand, the disk mass is the lowest among the sources in Figure 4(b). The disk mass seems to increase with increasing protostellar mass, although more systematic studies are necessary.

The mass accretion rate $\dot{M}_{\mathrm{acc}}$ averaged over the protostar life is estimated to be about ~7 × 10^{-6} $M_\odot$ yr^{-1} from the protostellar mass of 0.007 $M_\odot$ and the above dynamical timescale. On the other hand, the current mass accretion rate can also
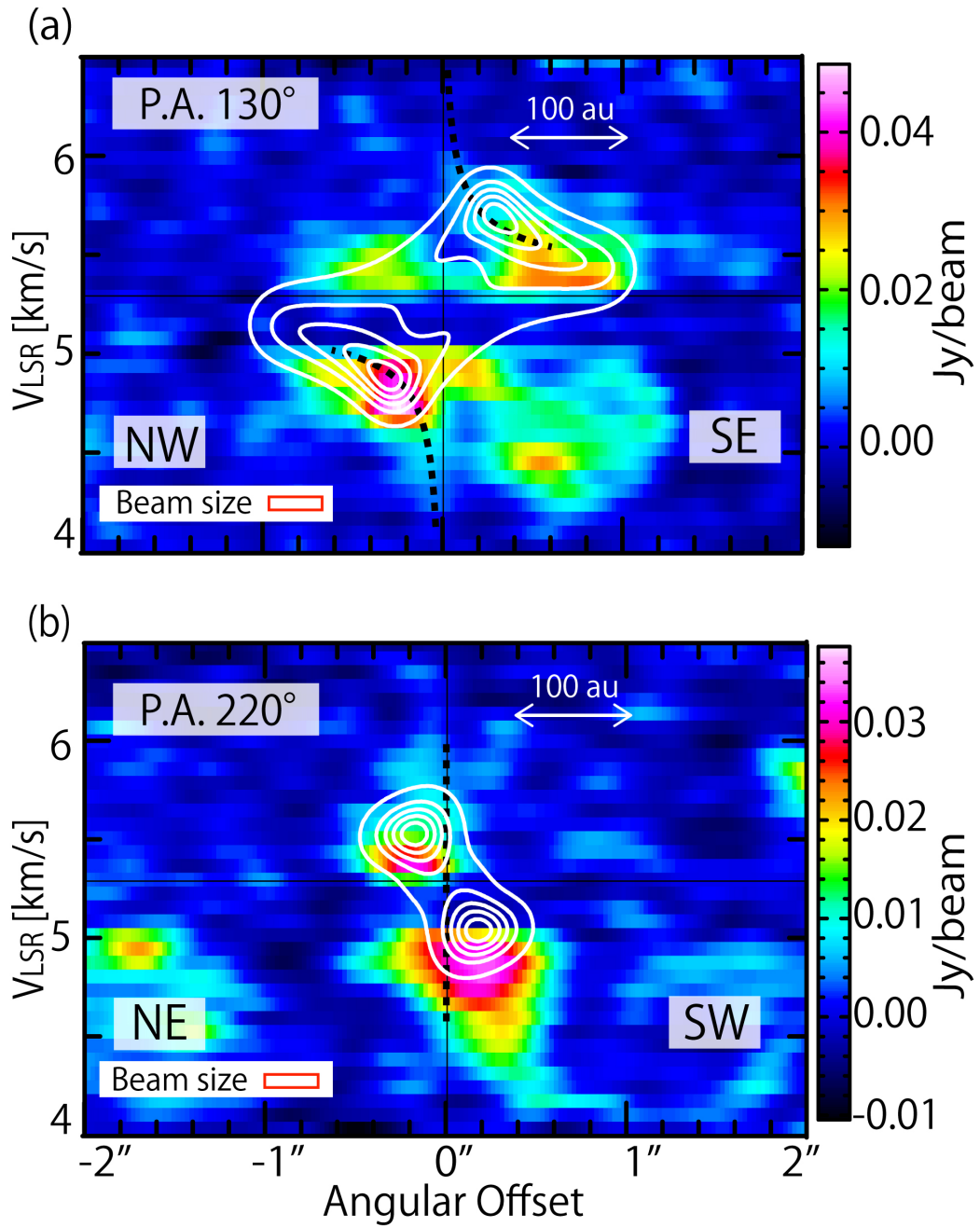
Figure 3.4: The PV diagrams of the CCH ($N = 3-2$, $J = 7/2-5/2$, $F = 4-3$) emission along the envelope direction (a), and along the line perpendicular to the envelope direction (b). The dashed lines show the model of Keplerian rotation with the protostellar mass of 0.007 $M_\odot$. The white contours are the results of the infalling-rotating envelope model with a protostellar mass of 0.007 $M_\odot$, the outer radius of 155 au, the radius of the centrifugal barrier of 40 au, and the inclination angle of 70°.
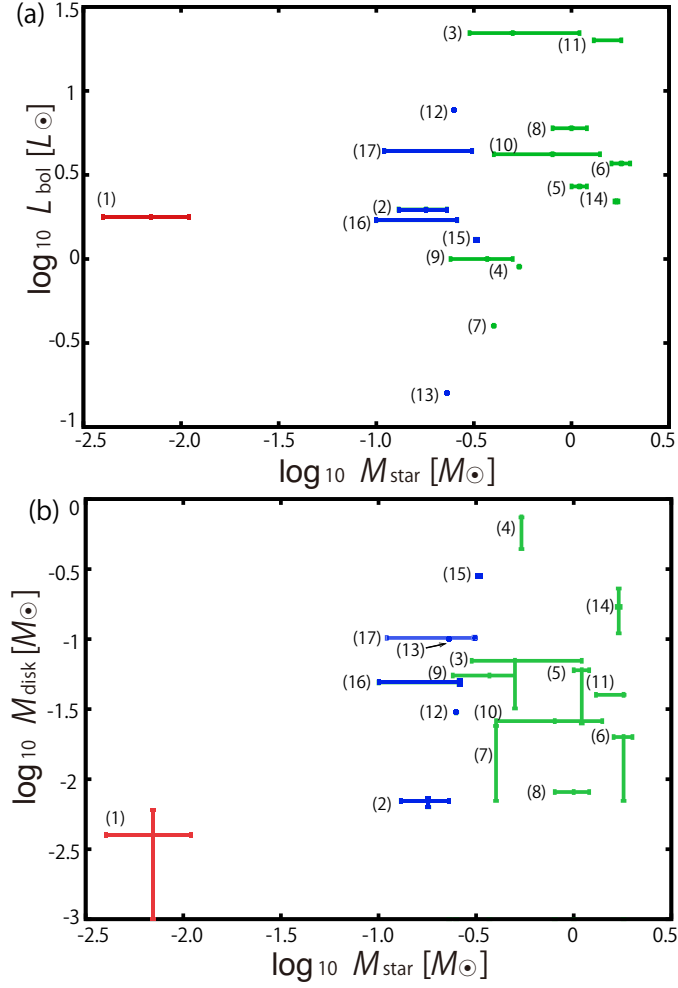
Figure 3.5: (a) Comparison between the protostellar masses and the bolometric luminosities. (b) Comparison between the protostellar masses and the disk masses. They are for the sample of protostars in previous studies listed below. Red marks with error bars represent IRAS 15398-3359 (this study). Blue and Green marks show the protostars of $T_{bol} < 70$ K (Class 0) and $T_{bol} > 70$ K (Class I), respectively. Error bars show the ranges of the mass. The sources used in the plots are as follows: (1)IRAS 15398-3359 (Jørgensen et al., 2013, this work) (2) L1527 IRS (Kristensen et al., 2012; Tobin et al., 2012; Sakai et al., 2014a) (3) L1551 IRS5 (4) TMC1 (5) TMC1A (6) L1489 IRS (7) L1536 (8) IRS 43 (9) IRS 63 (10) L1551NE (Chou et al., 2014) (11) HH111 (Lee, 2011; Lee et al., 2018) (12) HH212 (Lee et al., 2017) (13) Lupas3 MMS (Yen et al., 2017) (14) BHB07-11 (Alves et al., 2017; Yen et al., 2015a) (15) IRAS 03292+3039 (16) L1448 IRS2 (17) L1448C (Tobin et al., 2015b; Yen et al., 2015a). In some protostars, only the range of the protostellar mass and that of the disk mass are estimated. In this case, we employ the maximum range.

be estimated by using of the following relation (Palla & Stahler, 1991):

$$\dot{M}_{acc} = \frac{L R_{star}}{G M}, \tag{3.4}$$

where L is the luminosity and R_{star} the radius of the protostar. We evaluate the current accretion rate $\dot{M}_{acc}$ to be 2.1×10^{-5} $M_\odot$ yr^{-1} by using L of 1.8 $L_\odot$ (Jørgensen

et al., 2013) and R_{star} of 2.5 $R_\odot$ (e.g., Palla, 1999; Baraffe & Chabrier, 2010). It should be noted that we roughly employ the bolometric luminosity for L and the average radius of the protostar for R_{star}. The average and current accretion rates are almost within a range of canonical values 10^{-5}-10^{-6} $M_\odot$ yr^{-1} (Hartmann et al., 1997). It should be noted that the mass loss rate due to the outflow is reported to be (3.2-3.7) $\times 10^{-6}$ $M_\odot$ yr^{-1} (Yıldız et al., 2015) and 7×10^{-8} $M_\odot$ yr^{-1} (Bjerkeli et al., 2016a), which is comparable to or smaller than the above estimates of the accretion rate.

Although the very low mass of this protostar can naturally be interpreted as its infancy, the alternative possibility is that this protostar may evolve into a brown dwarf. A planetary system could be formed even around a brown dwarf, as predicted by theoretical models for the formation of Earth-like planets around a brown dwarf (Payne & Lodato, 2007). However, this interpretation may be not the case for this source, because the envelope mass around the protostar is as high as $0.5-1.2$ $M_\odot$ (Kristensen et al., 2012; Jørgensen et al., 2013). In any case, the observational characterization of very low-mass protostars is important for further understandings of the stellar and disk formation process and its diversity. More sensitive observations are awaited in this direction.

3.6   Summary

1. We have detected the SO and CCH emission with the high angular resolution observation of 0."2 (~30 au) with ALMA. The distributions of SO and CCH are compact and extended around the protostar, respectively.

2. The velocity structure of the SO emission is most likely a Keplerian motion, where the systemic velocity is 5.5 km s^{-1}. We estimate the protostellar mass to be $0.007^{+0.004}_{-0.003}$ $M_\odot$ on the assumption of Keplerian motion. On the other hand, we find that the CCH emission traces the infalling-rotating envelope. The systemic velocity shown by the velocity structure of CCH, 5.3 km s^{-1}, is consistent with the previous report, which is slightly different from that of the disk traced by SO.

3. The disk mass estimated from the dust continuum emission is between 0.006 and 0.001 $M_\odot$ by assuming the temperature of 20 K and 100 K, respectively. Toomre-Q, a parameter indicating the stability of the disk, is derived to be 0.4 and 5 for the above temperatures, respectively, meaning that the disk can have an unstable regime.

4. The envelope mass was reported to be 0.5 -1.2 $M_\odot$ previously, which is much higher than the protostellar mass and the disk mass that we estimate. Hence, our results suggest that this source can be a very low-mass protostar in the earliest stage of protostellar evolution. Even in such an infancy stage, the disk structure is found to have already been formed.

Chapter 4

Chaotic Environment of the Earliest Stage: Reorientation Outflow in IRAS 15398-3359[*]

In the previous chapter, our observational results show that IRAS 15398−3359 is a very low-mass protostellar source and is in the earliest evolutionary stage. We here focus on the environment at scales ranging from 50 au to 1800 au around the protostar. Based on observations of the ALMA Large Program FAUST (Fifty AU STudy of the chemistry in the disk/envelope system of Solar-like protostars[1]) toward IRAS 15398−3359, we find unexpected dynamical features at the above scales. We uncover a linear feature, visible in H_2CO, SO, and $C^{18}O$ line emission, which extends from the source along a direction almost perpendicular to the known active outflow. Shock tracer molecular lines, SO, SiO, and CH_3OH, further reveal an arc-like structure connected to the outer end of the linear feature and separated from the protostar by 1200 au. The velocity gradient along the linear structure is explained as an outflow motion, and hence, we interpret the arc-like structure as a relic shocked region produced by an outflow launched from IRAS 15398−3359. This result means a large reorientation of the outflow axis by about 90°. Furthermore, the third outflow structure on a 2' scale is identified in the archival CO and HCO^+ data. The origins of the reorientation are discussed in relation to turbulent motions within the protostellar core and episodic accretion events. These results provide a novel insight into the earliest stage of protostellar evolution.

4.1 Introduction

Recent millimeter/submillimeter-wave observations with ALMA have revealed the complex physical and chemical nature of low-mass protostellar systems during their earliest evolutionary stage. For instance, protostellar accretion bursts resulting in a large instantaneous increase in the protostellar luminosity and subsequent heating of the protostellar envelope have been suggested for Class 0 sources (Jørgensen et al., 2013; Bjerkeli et al., 2016b; Hsieh et al., 2018, 2019). Furthermore, complex structure, consisting of arc-like features and dense clumps, has been reported

---

[*]The content of this chapter is published as: Okoda et al. (2021), ApJ, 910, 11

[1]http:\slash\slashfaust-alma.riken.jp

around the very young protostellar core, L1521F (Tokuda et al., 2014; Favre et al., 2020), and for the first hydrostatic core candidate, Chamaeleon-MMS1 (Busch et al., 2020). Because the protostars are deeply embedded in their parent cores, interactions between a protostellar outflow and surrounding gas may contribute to such complicated morphologies. Thus, detailing these structures will provide us with an important clue to elucidating a dynamic feature in the earliest stage of protostellar evolution. Given these circumstances, it is increasingly important to explore carefully and in detail the earliest stage of star formation for specific sources.

As described in Chapter 3, IRAS 15398−3359 is a very low-mass protostellar source in the earliest evolutionary stage and is an ideal target to investigate the activity of an infant protostar. For this purpose, we employ the data acquired in the ALMA Large Program FAUST, which aims at revealing the physical and chemical structure of 13 nearby protostars (d =137-235 pc) including IRAS 15398−3359, at scales from a few 1000 au down to 50 au, by observing various molecular lines. In addition to lines of fundamental molecules (e.g., $C^{18}O$ and H_2CO) and complex organic molecules, some shock tracer molecules, such as SO, SiO, and CH_3OH, are included in this program to reveal possible interactions between the outflow and the ambient gas: these species are thought to be liberated from dust grains or to be produced in the gas phase within shocked regions. Taking advantage of the chemical diagnostic power of FAUST obtained by observing these shock tracer lines with high sensitivity, we have found a secondary outflow feature launched from IRAS 15398−3359.

4.2 Observations

Single field observations for IRAS 15398−3359 were conducted between October 2018 and January 2019 as part of the ALMA Large Program FAUST. The parameters of observations are summarized in Table 4.1. The molecular lines analyzed in the frequency range from 217 GHz to 220 GHz (Band 6) are listed in Table 4.2. We used the 12-m array data from the two different configurations (C43-5 and C43-2 for sparse and compact configurations, respectively) and the 7-m array data of ACA (Atacama Compact Array; Chapter 2), combining these visibility data in the UV plane. In total, the baseline lengths range from 7.43 m to 1310.74 m. The adopted field center was (α_{2000}, δ_{2000})= ($15^h43^m02^s.242$, $-34°09'06.''805$), which is close to the protostellar position. The backend correlator for the molecular line observations was set to a resolution of 122 kHz and a bandwidth of 62.5 MHz. The data were reduced in Common Astronomy Software Applications (CASA) 5.4.1 (McMullin et al., 2007) using a modified version of the ALMA calibration pipeline and an additional in-house calibration routine (Mollenbrock et al. in prep) to correct for the T_{sys} and spectral line data normalization[2]. Self-calibration was carried out using line-free continuum emission, for each configuration. The complex gain corrections derived from the self calibration were then applied to all channels in the data, and the continuum model derived from the self calibration was subtracted from the data to produce continuum-subtracted line data. A self-calibration tech-

---

[2]`https://help.almascience.org/index.php?/Knowledgebase/Article/View/419`

nique was also used to align both amplitudes and phases (i.e., positions) across the multiple configurations. Images were prepared by using the *tclean* task in CASA, where Briggs' weighting with a robustness parameter of 0.5 was employed. The primary beam correction was applied to all the images presented in this paper. Since the maximum recoverable scales are 12."8, any structures extended more than that size could be resolved-out. The root mean square (rms) noise levels for H_2CO, SiO, CH_3OH, and $C^{18}O$ and for SO are 2 mJy beam^{-1}channel^{-1} and 3 mJy beam^{-1}channel^{-1}, respectively. The original synthesized beam sizes are summarized in Table 4.2. The uncertainty in the absolute flux density scale is estimated to be 10 % (Francis et al., 2020).

Table 4.1: Observation Parameters[a]

Parameter	(C43-5)	(C43-2)	(7 m Array of ACA)
Observation date	2018 Oct 23	2019 Jan 06	2018 Oct 24, Oct 25
Time on Source (minute)	47.10	12.63	28.75, 28.77
Number of antennas	45	47	10
Primary beam width (″)	26.7	26.7	45.8
Total bandwidth (GHz)	0.059	0.059	0.062
Continuum bandwidth (GHz)	1.875	1.875	2.000
Proj. baseline range (m)	15.03–1310.74	12.66–425.02	7.43–46.74
Bandpass calibrator	J1427-4206	J1427-4206	J1229+0203, J1427-4206
Phase calibrator	J1626-2951	J1517-2422	J1517-2422
Flux calibrator	J1427-4206	J1427-4206	J1229+0203, J1427-4206
Pointing calibrator	J1650-2943, J1427-4206	J1427-4206	J1229+0203, J1427-4206, J1517-2422
Resolution(″×″(P.A.°))	0.338×0.280 (63.9)	1.140×0.921 (79.9)	8.210×4.780 (69.2)
Rms (mJy beam^{-1}channel^{-1})	1.8	4.4	24.0

[a] These observations are conducted with Band 6.

Table 4.2: List of Observed Lines [a]

Molecule	Transition	Frequency (GHz)	$S\mu^2(D^2)$	$E_u k^{-1}$(K)	Beam size
H_2CO[b]	$3_{0,3}-2_{0,2}$	218.2221920	16.308	21	0.″35×0.″30 (P.A. 69°)
SO[c]	$J_N = 6_5-5_4$	219.9494420	14.015	35	0.″35×0.″30 (P.A. 65°)
SiO[d]	5−4	217.1049190	47.993	31	0.″35×0.″30 (P.A. 68°)
CH_3OH[e]	$4_{2,3}-3_{1,2}$	218.4400630	13.905	45	0.″35×0.″29 (P.A. 69°)
$C^{18}O$[f]	2−1	219.5603541	0.024399	16	0.″35×0.″29 (P.A. 65°)

[a] Line parameters are taken from CDMS (Endres et al., 2016). The beam size for each line is obtained from the observations.

4.3 Primary Outflow in the Northeast to Southwest Direction

Figures 4.1(a) and 4.2(a) show the moment 0 maps of the H_2CO and SO line emission, respectively. The outflow structure along the northeast to southwest axis (P.A. 220°) is seen in the H_2CO emission, as reported previously (Oya et al., 2014; Bjerkeli et al., 2016a). We call this primary outflow. Contrastingly, the SO emission is concentrated around the protostar as described in Chapters 3 and 7 with little emission within the outflow except for a localized knot (Blob D in Chapter 7) seen in the southwestern lobe, which could be formed by an impact of the outflow on ambient gas. The CH_3OH and $C^{18}O$ line emission trace part of the outflow in Figures 4.2(b) and 4.2(c). The knot can also be seen in the CH_3OH emission (See also Chapter 7). Along with these previously known structures, we have found an additional spatial feature extending toward the southeast and northwest of IRAS 15398−3359.

4.4 A Possible Secondary Outflow

4.4.1 Arc-Like Structure in the Southeast Direction

Part of the H_2CO line emission and a majority of the SO line emission are extended in the southeastern direction (P.A. 140°), which is also close to the disk/envelope direction (P.A. 130°) of the IRAS 15398−3359 protostar reported by Oya et al. (2014), Yen et al. (2017), and Okoda et al. (2018). The H_2CO emission appears to bend toward the south about 8″ (∼1200 au) from the protostar. The moment 0 map of the SO emission shows an arc-like structure around the southeastern part (Figure 4.2(a)), where the northern tip of the arc corresponds to the bending point seen in the H_2CO emission. Although the arc-like structure is near the edge of the field of view for the ALMA 12 m data, it lies within the field of view of ACA data. Hence, the observed structure is real.

Along with the H_2CO and SO line emission, the SiO and CH_3OH line emission is found to trace the arc-like structure around the southeastern part. In contrast to the H_2CO and SO line emission, the SiO emission is not detected toward the protostar, and mainly traces the southeastern part of the arc-like structure (Figure

4.2(d)). These features are also apparent in the molecular line profiles (Figure 4.3) toward four positions within the arc-like structure and at the protostellar position, as indicated in Figures 4.1 and 4.2. The line width of the SiO emission is slightly broader at position D (0.9 km s^{-1}) than at positions A, B, and C (0.3–0.8 km s^{-1}). Faint emission from CH$_3$OH is also detected in part of the arc-like structure in addition to the previously observed outflow cavity wall (Figure 4.2(b)). While the CH$_3$OH emission looks faint in the moment 0 map, its spectrum is clearly detected in the arc-like structure, as revealed in Figure 4.3.

In Figure 4.4, we present the velocity channel maps of the H$_2$CO, SO, SiO, CH$_3$OH, and C^{18}O line emission from the 3.9 km s^{-1} panel to the 5.5 km s^{-1} panel, where the systemic velocity of the protostellar core is 5.2 km s^{-1} (Yen et al., 2017). The velocity channel maps reveal the arc-like structure. The CH$_3$OH emission is seen clearly in the velocity maps at 4.7 km s^{-1} and 5.1 km s^{-1}. On the other hand, the arc-like structure is not evident in the C^{18}O emission, as shown in the line profiles and the velocity channel maps (Figures 4.3 and 4.4 (e)). The C^{18}O emission usually traces cold and dense clumps of gas with relatively high column density. Although marginal emission may be detected around the southeastern extent in the map of 5.5 km s^{-1}, the low C^{18}O column density (calculated in Subsection 4.5.2) ensures that the arc-like structure is not part of an adjacent prestellar core.
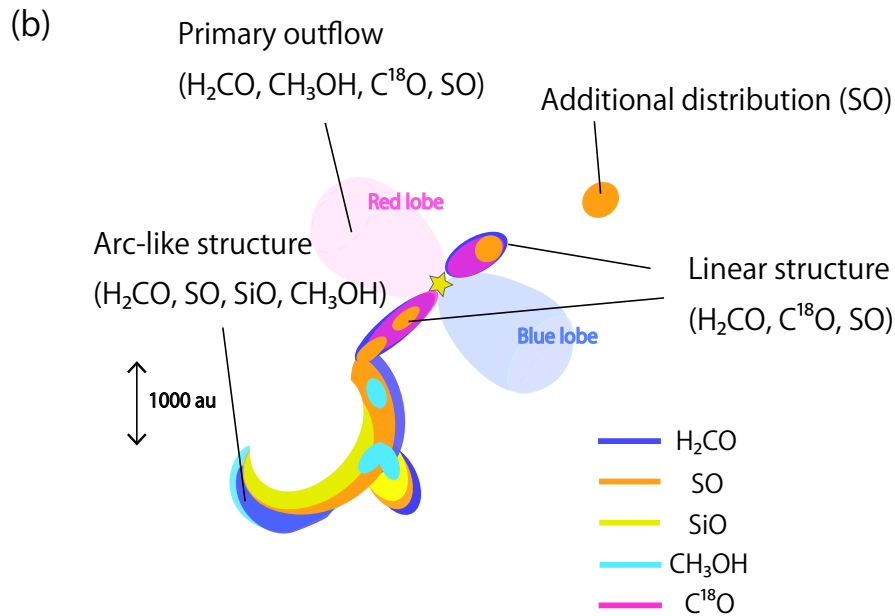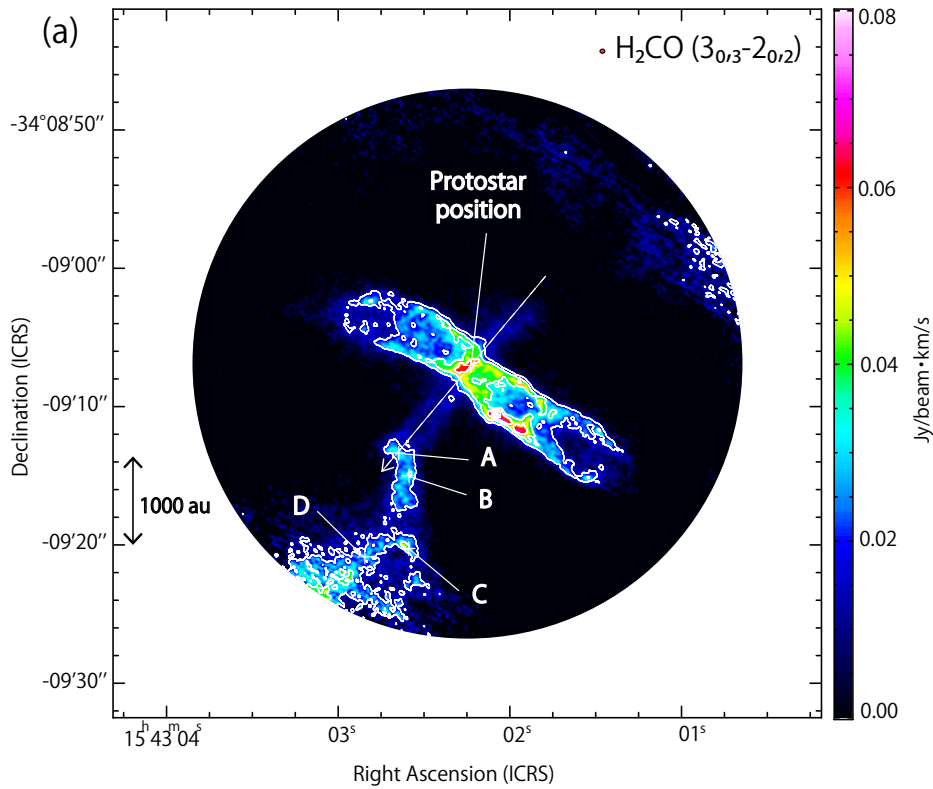
Figure 4.1: (a) Moment 0 map of the H_2CO line emission. Contour levels are every σ from 3σ, where σ is 6 mJy beam^{-1}km s^{-1}. The line intensities are integrated from 3.7 km s^{-1} to 5.7 km s^{-1} to focus on the arc-like feature and linear structure. White cross marks (protostar position and A-D) show the five locations where molecular line profiles are produced (See Figure 4.3). The circle at top-right represents the synthesized beam size. The dashed arrow represents the direction of the PV diagram of Figure 4.6. (b) Schematic picture of the molecular distributions.
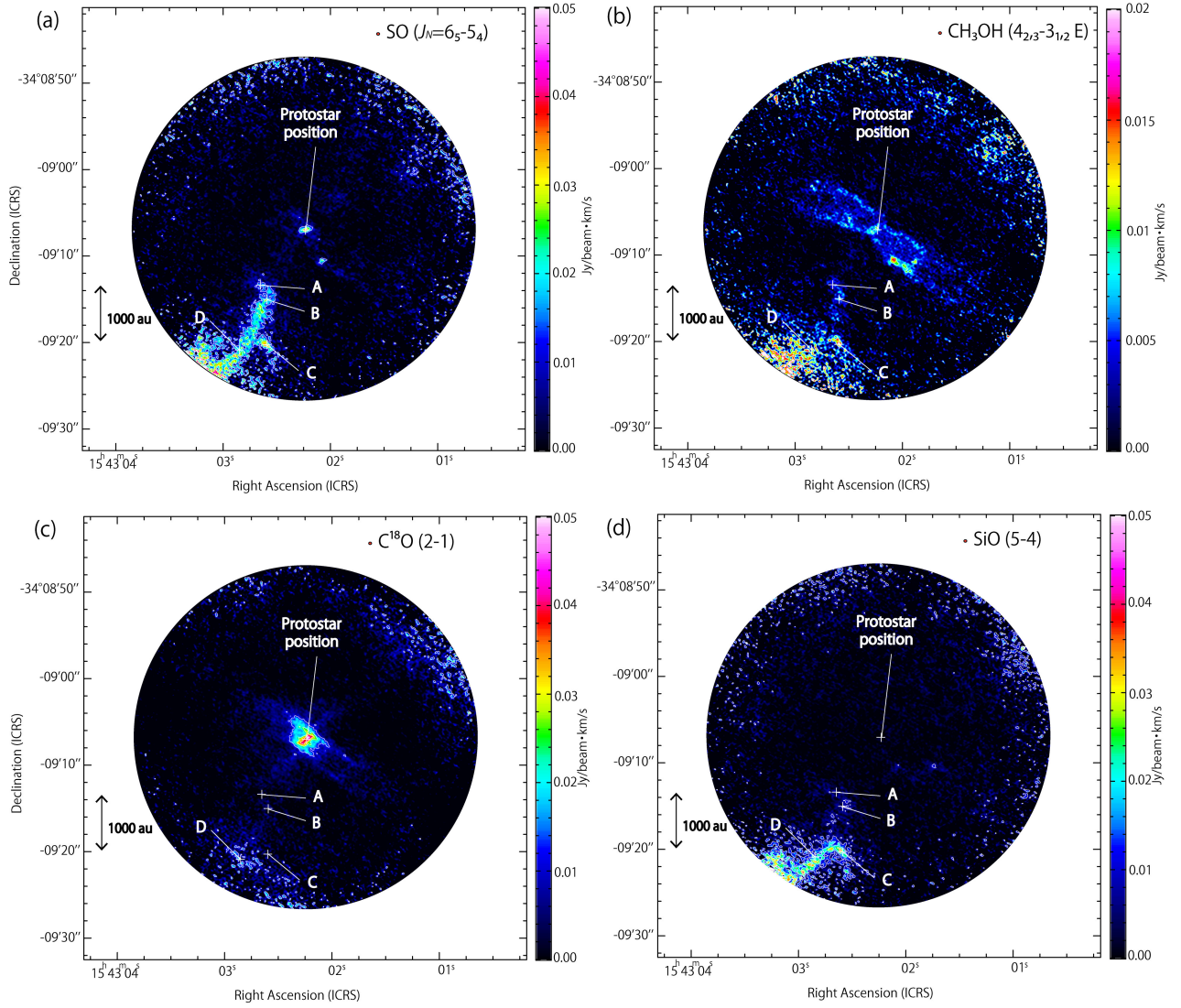
Figure 4.2: (a,b,c,d) Moment 0 maps of the SO, CH_3OH, $C^{18}O$ and SiO line emission. Contour levels are every σ from 3σ, where σ is 4 mJy beam^{-1}km s^{-1}, 3 mJy beam^{-1}km s^{-1}, 4 mJy beam^{-1}km s^{-1}, and 3 mJy beam^{-1}km s^{-1}, respectively. See Figure 4.1 caption for additional details.
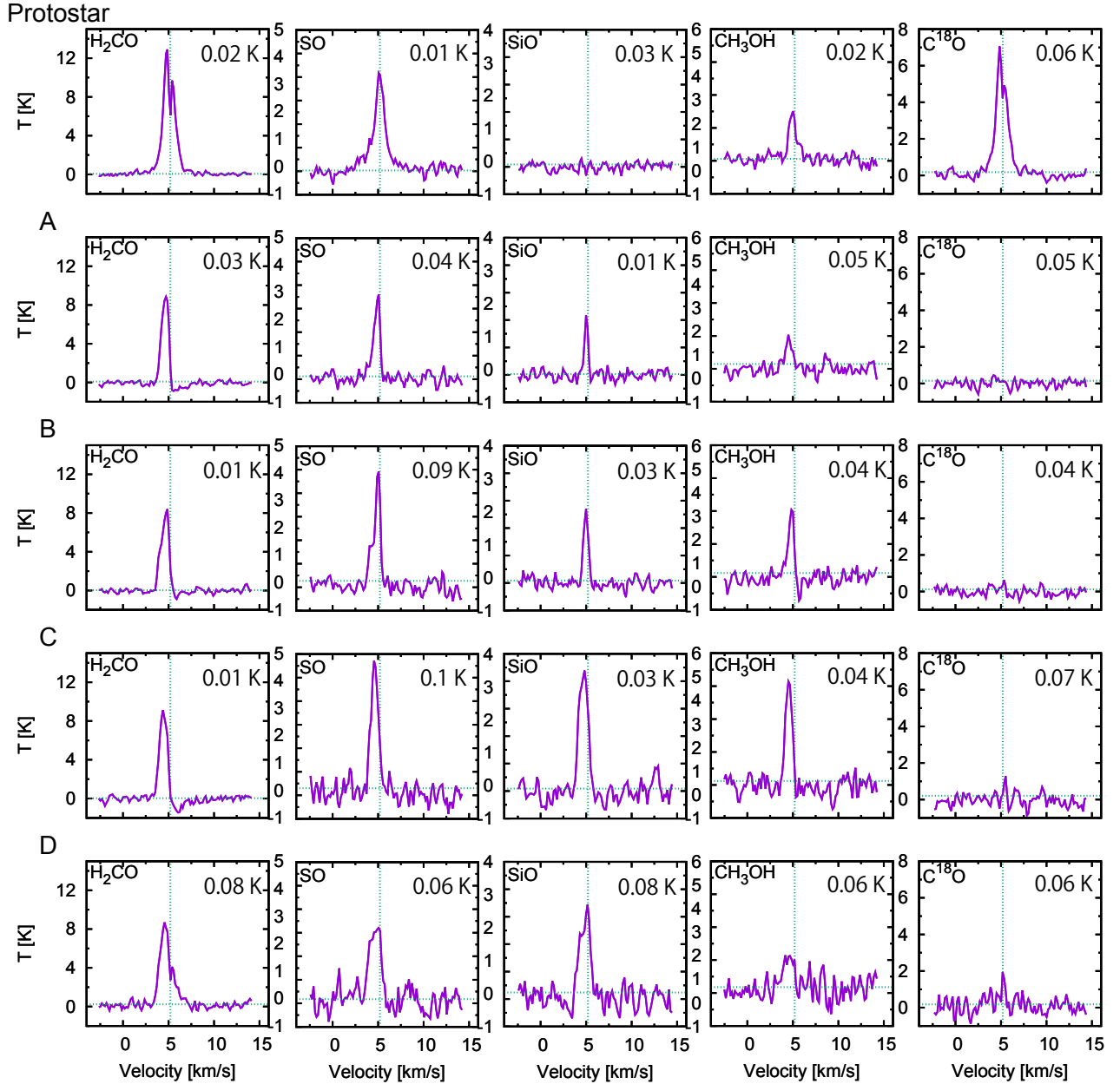
Figure 4.3: Molecular line profiles observed toward the four positions (A-D; see Figures 4.1 and 4.2) in the arc-like structure and at the protostellar position. These spectra are extracted from the apertures of 1."0. The horizontal green dotted lines represent each 3 σ. The top-right values indicate σ for each line profile. The vertical green dotted lines represent the systemic velocity of the protostellar core, 5.2 km s^{-1} (Yen et al., 2017)
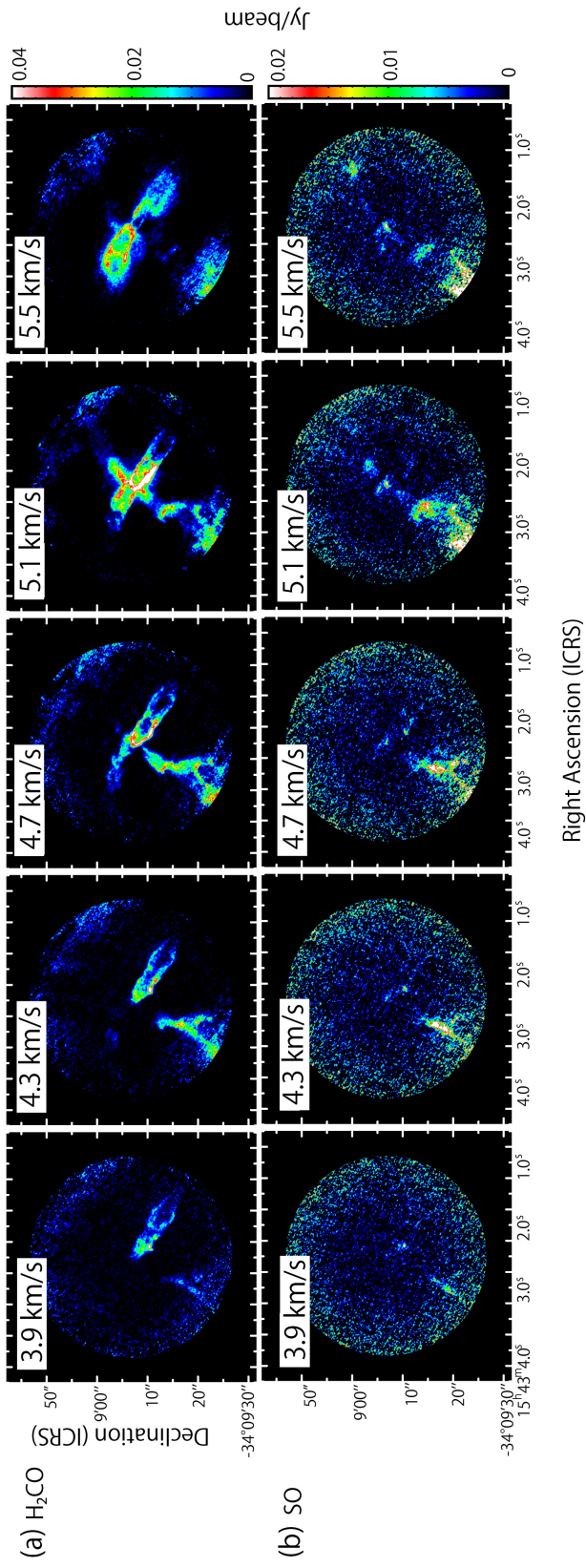
Figure 4.4: Velocity channel maps of SO, H_2CO, SiO, CH_3OH, and $C^{18}O$. Each panel represents the intensity averaged over a velocity range of 0.4 km s^{-1} centered at the quoted velocity. For instance, the 3.9 km s^{-1} panel shows the average between 3.7 km s^{-1} and 4.1 km s^{-1}. The systemic velocity of the protostellar core is 5.2 km s^{-1}.
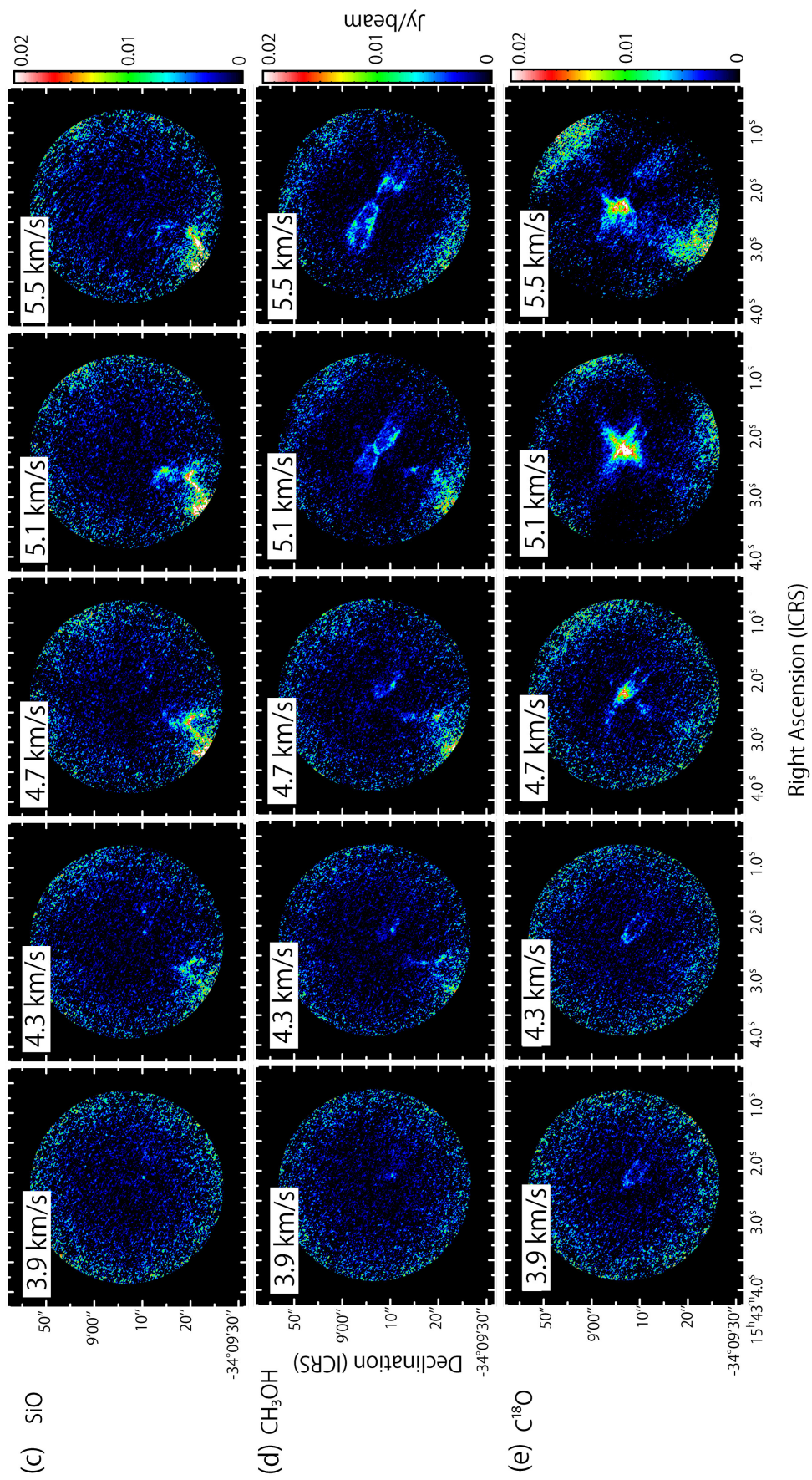
Figure 4.4: Continued.

4.4.2 Shocks in the Arc-Like Structure

The SO, SiO, and CH_3OH line emission are known to be enhanced in the gas phase by shocks and are often detected in active outflow-shocked regions (e.g., Bachiller, & Pérez Gutiérrez, 1997), although SO and CH_3OH are also present in quiescent starless cores (e.g., Spezzano et al., 2017; Punanova et al., 2018). A typical example of such a shocked region in a low-mass star-forming region occurs in the outflow driven from the Class 0 protostar, IRAS 20386+6751, in L1157 (Mikami et al., 1992; Gueth et al., 1996; Bachiller, & Pérez Gutiérrez, 1997, : See Chapter 1). Outflows often produce shocked emission at locations where they interact with ambient gas. In these outflow-shocked regions, the chemical composition of the gas is drastically changed, mainly due to liberation of molecules from dust grains and subsequent gas-phase reactions. In L1157, the shocked region in the blue-shifted outflow lobe (L1157-B1) is traced by SO, SiO, CH_3OH, H_2CO, HCN, CN, and SO_2 line emission (Mikami et al., 1992; Gueth et al., 1996; Bachiller, & Pérez Gutiérrez, 1997; Podio et al., 2017; Codella et al., 2010, 2020; Feng et al., 2020). Enhancement of the same molecules has also been reported for other protostellar outflows: e.g., L1448-C (L1448-mm); Jiménez-Serra et al. (2005); Hirano et al. (2010), HH211; Hirano et al. (2006), NGCC1333-IRAS4A; Wakelam et al. (2005), BHR71; Gusdorf et al. (2015). Since SiO is a robust shock tracer, the observed arc-like structure to the southeast of IRAS 15398−3359 should also be a shocked region. We also detect enhancement in the abundance of other species, SO and CH_3OH (Figures 4.2(a) and (b)), which is consistent with the enhancement reported toward the shocked region, L1157-B1. Furthermore, the morphology resembles a bow shock, somewhat similar to those revealed by the simulations (Smith et al., 1997; Lee et al., 2001) and the observation (HH46/47; Arce et al., 2013).

The line width of the SiO emission in typical shocked regions is generally broad ($\sim$10 km s^{-1}; e.g., Mikami et al., 1992; Bachiller, & Pérez Gutiérrez, 1997). Here, however, the SiO emission has a narrow line width about 1 km s^{-1} toward the arc-like structure (Figure 4.3 and 4.4(c)). The lack of a broad line width may be evidence that the shock is relatively old and that the turbulent motions produced within the shock region have dissipated. Such a fossil shock has been suggested as the explanation for similar observations of the sources HH7-11 (SVS13-A) and NGC 2264 by Codella et al. (1999) and López-Sepulcre et al. (2016), respectively. This hypothesis will be further discussed in relation to the origin of the arc-like structure in Subsection 4.6.2. We note that narrow line width of SiO can also be interpreted in terms of magnetohydrodynamic C-shocks (Jiménez-Serra et al., 2004, 2005, 2008, 2009).

IRAS 15398−3359 is located at the edge of Lupus-1 molecular cloud, as can be seen in large-scale dust continuum and CO observations (Tothill et al., 2009; Gaczkowski et al., 2015; Mowat et al., 2017). A protostellar source has never been found through infrared observations (Rygl et al., 2013) toward the southeastern region of IRAS 15398−3359 (Chapman et al., 2007). Furthermore, sub-mm continuum emission is not detected at the location where the arc-like structure resides in our data sets, nor has ALMA previously uncovered continuum emission there (Jørgensen et al., 2013; Oya et al., 2014; Okoda et al., 2018). Combined with the pre-

viously mentioned lack of significant $C^{18}O$ emission, these null results suggest that there is no nearby enhancement of dense gas to the southeast of IRAS 15398−3359. Thus, the arc-like structure likely originates from the interaction of an outflow oriented along the northwest to southeast axis ejected from IRAS 15398−3359 and its natal ambient gas. If this is the case, a detectable counter lobe might be expected to the northwest of IRAS 15398−3359. A hint of this counter lobe can be seen in the SO emission, as described in the next subsection.

4.4.3 Linear Structure in the Northwest to Southeast Direction

Focusing on the vicinity of the protostar, within 5″, a linear structure is seen in the H_2CO emission, connecting the southeast arc-like structure to the protostar and continuing toward the northwest (Figure 4.1(a)). This structure is more clearly identified in the velocity maps at 4.7 km s^{-1} and 5.1 km s^{-1} (Figure 4.4(a)). Investigating this linear structure near the protostar, we find that the geometry is not simply an extension of the disk/envelope system related to the primary outflow (Figure 4.5). The linear structure is slightly inclined by about 10° from the disk/envelope axis (P.A. 130°) reported previously (Oya et al., 2014; Yen et al., 2017; Okoda et al., 2018), and their origin (α and β in Figure 4.5(a)) are offset by 1″−2″ (∼150−300 au) from the disk/envelope axis. This feature is also seen weakly in $C^{18}O$ emission over the same velocity range of 4.5 km s^{-1} to 5.7 km s^{-1} (Figure 4.5(b)).

The SO emission also shows evidence of an extension to the northwest in the velocity maps of 5.1 km s^{-1} and 5.5 km s^{-1} (Figure 4.4(b)). This emission is extended from the protostar along the same orientation as the linear structure (P.A. 140°) in the 5.1 km s^{-1} channel map (Figure 4.5). At 5.5 km s^{-1}, additional emission appears further toward the northwest and shows a slight offset from the above axis. In contrast to the emission from H_2CO, SO is more structured and less continuous in the vicinity of the protostar. Nevertheless, the observed SO emission is consistent with the geometry seen in the H_2CO emission. The morphology near the protostar in the H_2CO and $C^{18}O$ emission and the apparent symmetry in the SO emission strongly suggest that these features are part of an outflow structure, rather than a structure formed from gas accreting toward the protostar as seen in the source Per-emb-2 by Pineda et al. (2020).

The possible secondary outflow is verified by the velocity structure. Figure 4.6(a) presents the position-velocity (PV) diagram for the H_2CO emission along the northwest to southeast axis (P.A. 140°), centered at the protostellar position. The position axis is approximately along the linear feature seen in the H_2CO emission (Figure 4.1(a)). The velocity toward the northwest remains roughy constant and only slightly blue-shifted with respect to the systemic velocity. In contrast, toward the southeast there is a clear velocity gradient, with the emission becoming more blue-shifted with increasing distance from the protostar and toward the arc-like structure. Furthermore, as seen in the PV diagram, the velocity width increases up to about 1 km s^{-1} at the southeastern terminus (Position A; Figure 4.1(a)). This location is coincident with the northern tip of the arc-like structure. A similar velocity structure can be seen in the PV diagram for the $C^{18}O$ emission (Figure 4.6(b)).

The velocity gradient is calculated to be about 1.2 km s^{-1} over 1200 au by assuming that the systemic velocity is 5.2 km s^{-1}. This gradient is unexpectedly large if identified as an infalling motion to the protostar. A more natural explanation is that the velocity gradient is associated with outflow motion. A lack of a red-shifted component in the northwestern part is puzzling but may be due to less gas being affected by the outflow. Alternatively, this could be reproduced if accretion of material is not symmetric (Zhao et al., 2018). The slight shift of the origin points of the linear structure near the protostar (Figure 4.5) can also be understood if these origin points are part of this secondary outflow.

One may expect that the secondary outflow would be detected in the ^{12}CO lines, which are the most commonly observed outflow tracers. Indeed, a faint blue-shifted component near the arc-like structure on the southeastern part can marginally be seen in the interferometric ^{12}CO (J =2−1) observations by Bjerkeli et al. (2016a) and Yen et al. (2017). This would be a remnant of part of the arc-like structure. On the other hand, the linear structure and its extension to the northwest are not seen in the ^{12}CO emission. The velocity shift is so close to that of the ambient gas that they are likely to be resolved out. The absence of the red-shifted emission at the northwestern part is puzzling, as mentioned above.
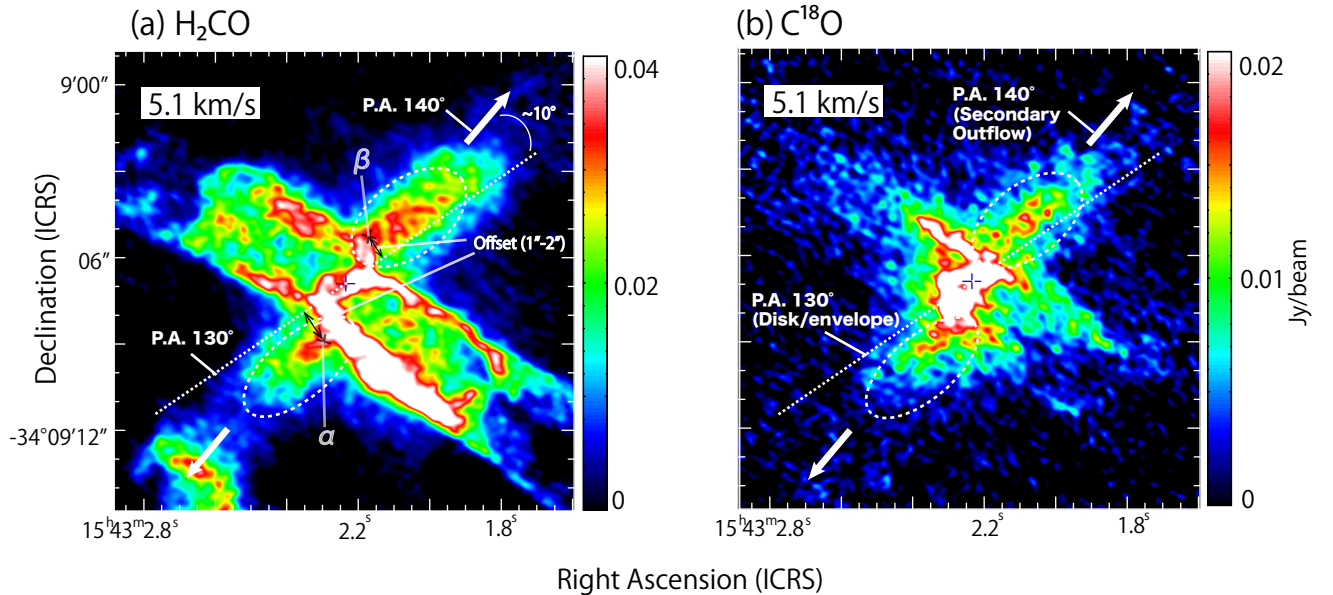
Figure 4.5: Blow-ups of the 5.1 km s^{-1} channel maps from Figures 4.4(b) and 4.4(e). The white dashed ovals indicate the linear structure. The arrows indicate the direction of the secondary outflow (P.A. 140°). The dotted lines represent the disk/envelope axis (P.A. 130°). α and β represent the origin points of the linear structure described in Subsection 4.4.3. They represent the intersection points between the linear structure and the primary outflow cavity. The cross marks indicate the continuum peak position.
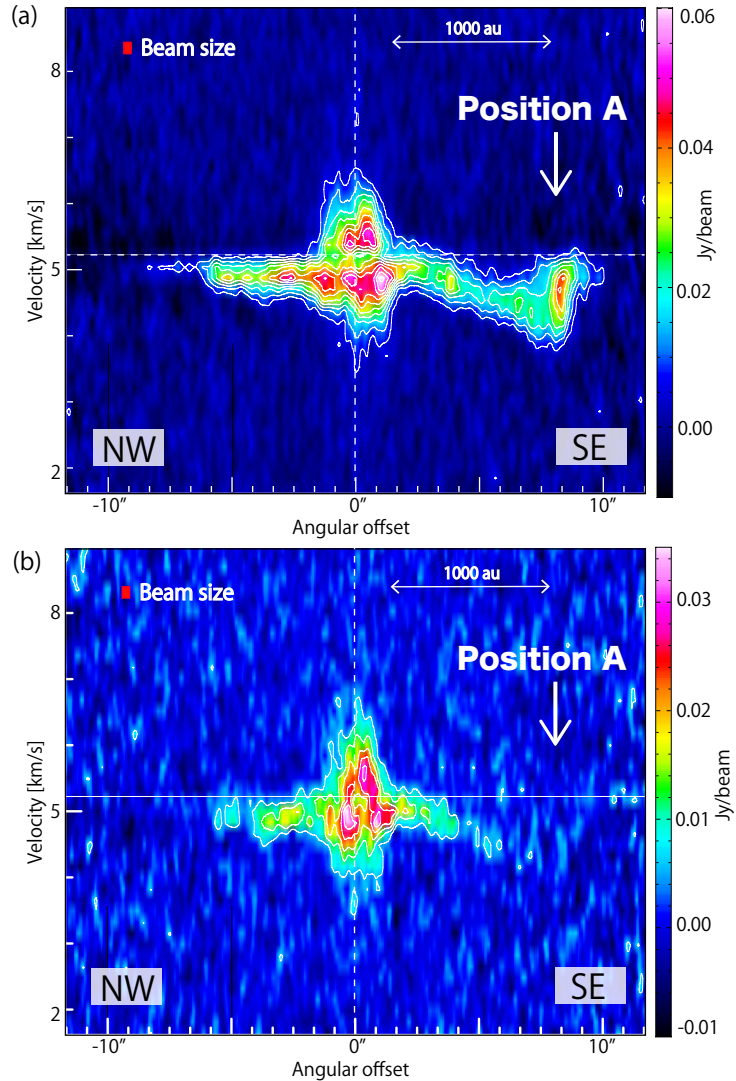
Figure 4.6: (a,b) PV diagrams for H_2CO and $C^{18}O$ along the northwest to the southeast axis (P.A. 140°; Figure 4.1(a)). The origin shows the continuum peak position. The horizontal dashed lines indicate the systemic velocity of the protostellar core (5.2 km s^{-1}). The cut width is 1.″0.

4.5 Analyses of the Secondary Outflow

4.5.1 Dynamical Timescale of the Outflow and Outflow Mass

We have identified a linear structure along the northwest to southeast axis (P.A. 140°) as well as an arc-like structure further to the southeast. A northwestern counterpart can marginally be seen in SO emission. This extended feature is most likely a secondary outflow, which has not been previously identified. Collimated features similar to the linear structure seen near the protostar are expected to form around young protostellar sources (e.g., Machida et al., 2008; Inutsuka, 2012; Velusamy et al., 2014; Busch et al., 2020).

We evaluate the dynamical timescale of the secondary outflow from the PV diagram of the H_2CO emission (Figure 4.6(a)). The plane-of-the-sky distance and the line-of-sight velocity shift from the systemic velocity are 1200 au and ~1.2 km s^{-1}, respectively. Thus, the timescale is estimated to be ~5000× cot(i) yr, where i is the inclination angle of the second outflow axis (i =0° for pole-on). On the basis of the morphology of the observed secondary outflow, the axis may be close to the plane of the sky (i =90°) and the dynamical timescale is regarded as an upper limit. The observed feature might also be a relic of a previous fast outflow, considering the relatively narrow observed line width (See Subsection 4.6.2). In this case, the observed velocities might be significantly lower than they were in the past, and the calculated dynamical timescale would be an overestimate. Note that the dynamical timescale of the primary outflow (P.A. 220 °) is reported to be 10^2–10^3 yr (Oya et al., 2014; Yıldız et al., 2015; Bjerkeli et al., 2016a). Hence, the secondary outflow would likely have formed before the primary outflow. The dynamical timescale of the secondary outflow is comparable to the time for depletion of SiO onto dust grains: 10^3–10^4 yr if the H_2 density is roughly 10^5–10^6 cm^{-3} (Equation 1.3) (e.g., Caselli et al., 1999). Thus, if SiO molecules were liberated from dust grains in the past by shocks related to a secondary outflow, they would be able to survive in the gas phase until the present day. We roughly estimate the total mass within the observed secondary structure seen in SO emission to be 10^{-5}–10^{-4} $M_{\odot}$, where we use the apparent size and an assumed H_2 density of 10^5–10^6 cm^{-3} based on the critical densities of the observed lines. Similarly, we estimate the mass of the primary outflow from the H_2CO emission to be 10^{-4}–10^{-3} $M_{\odot}$ by assuming the same H_2 density range.

4.5.2 Molecular Abundances around the Arc-like Structure

In order to compare the molecular abundances of the IRAS 15398−3359 with other outflow shock regions, we derive the lower limits to the abundance ratio for several molecules relative to C^{18}O at the four positions (A-D) and the abundance ratio at the protostar position (Figures 4.1 and 4.2). Positions A and D are the bending point from the linear structure toward the arc-like structure and the south of the arc-like structure, respectively, while positions B and C are the local peak positions of CH$_3$OH in Figure 4.2(b). We calculate the column densities of H_2CO, SO, SiO, and CH$_3$OH as well as the upper limit of C^{18}O by using the non-LTE radiative transfer code, RADEX (van der Tak et al., 2007), toward these positions, assuming that the gas temperature is 20−80 K and the H_2 density is 10^5–10^6 cm^{-3} (Table 4.3). Regarding the C^{18}O column density at the four positions, we use the upper limits to the intensity and the mean line width of other molecular lines (H_2CO, SO, SiO, and CH$_3$OH). Any extended component traced by the C^{18}O emission at the systemic velocity may be resolved out. In this case, the upper limits to the C^{18}O intensity might be underestimated. However, we here discuss the molecular abundances in the arc-like structure which is blue-shifted from the systemic velocity by 0.5 km s^{-1}. Such a compact structure should be observed even in the C^{18}O emission without the resolved-out problem. Moreover, the maximum recoverable size (12.″8) is larger than the arc-like structure (at most 10″). For these reasons, the resolved-out

effect should not affect the molecular abundances significantly. For the protostar position, the $C^{18}O$ column density is derived to be $(5.5–6.4)\times10^{15}$ cm^{-2}, where the gas temperature and the H_2 density are assumed to be 54 K (Okoda et al., 2020) and $10^5–10^7$ cm^{-3}, respectively. Then, the abundance ratios relative to $C^{18}O$ are evaluated from the column densities, where the same temperature is assumed for the molecular species and $C^{18}O$.

Only lower limits are obtained for the abundance ratios at all the four positions. Nevertheless, the abundances of SO, SiO, and CH_3OH are found to be significantly enhanced in the shocked region in comparison with the protostar position (Table 4.3). Moreover, the abundance ratios are as high as those reported for L1157-B1 (Table 4.4), further supporting the outflow shock. We note, however, that the physical conditions of L1157-B1 are likely different from those of IRAS 15398−3359. L1157-B1 shows a broad line width of SiO. Hence, we also compare the SiO abundance of the arc-like structure to that of the shocked region with the narrow SiO line in the Class I protostellar source, HH7-11 (SVS13-A) (Codella et al. (1999); t_{des} ~10^4 yr). We estimate the SiO abundance relative to H_2 by using the nominal $C^{18}O$ fractional abundance of 1.7×10^{-7} (Frerking et al., 1982). In Table 4.4, the abundance of the arc-like structure is much higher than that found for HH7-11 (SVS13-A). This result seems to be related to the shorter timescale of the secondary outflow than that of the HH7-11 (SVS13-A) outflow, ~10^5 yr (Lefloch et al., 1998). In HH7-11, most of SiO would have already been depleted on dust grains.

Table 4.3: Column Densities [10^{14} cm^{-2}]

Molecule	Protostar[a]	A [b]	B[b]	C [b]	D [b]
H_2CO	0.4−2	0.2−2	0.2−2	0.2−3	0.2−3
SO	0.4−1	0.2− 2	0.3−3	0.5−5	0.4−3
SiO	<0.03[c]	0.01−0.8	0.02−1	0.07−5	0.05−3
CH_3OH	0.7−6	1−6	2−9	3−20	2−10
$C^{18}O$	55−64	<1[c]	<0.8[c]	<2[c]	<2[c]

[a] The positions are shown in Figures 4.1 and 4.2. The temperature and the H_2 density are assumed to be 54 K (Okoda et al., 2020) and $10^5–10^7$ cm^{-3}, respectively. A range of the column density is shown for each molecule.

[b] The temperature and the H_2 density are assumed to be 20−80 K and $10^5–10^6$ cm^{-3}, respectively. A range of the column density is shown for each molecule at each position.

[c] The 3σ upper limits, where σ is shown in Figure 4.3.

4.6   Origin of the Secondary Outflow

4.6.1   Scenario 1: Two Outflows Driven by a Binary System

It is well known that some Class 0 protostellar sources contain a binary or multiple system (e.g., Tobin et al., 2016b, 2018). A possible explanation for the secondary outflow is that IRAS 15398−3359 is a binary system, launching outflows in two different directions with respect to the plane of the sky. Such binary/multiple systems

Table 4.4: Molecular Relative Abundance Ratios with Respect to $C^{18}O$

Molecule	Protostar[a]	A[a]	B[a]	C[a]	D[a]	L1157-B1[b]	HH7-11 (SVS13-A)
$[H_2CO]/[C^{18}O]$	0.005–0.03	> 0.2	> 0.2	> 0.1	> 0.1	0.5–1	–
$[SO]/[C^{18}O]$	0.007–0.02	> 0.2	> 0.4	> 0.3	> 0.2	0.5–0.8	–
$[SiO]/[C^{18}O]$	<0.001	> 0.01	> 0.03	> 0.04	> 0.02	0.1	–
$[CH_3OH]/[C^{18}O]$	0.01–0.1	> 1	> 2	> 2	> 1	0.8–4	–
$X(SiO)^c[10^{-9}]$		1.7	5.1	6.8	3.4	17	0.08–0.3[d]

[a] These values are derived by assuming the same temperature for the two molecular species for the ratio.

[b] The abundance ratios in the outflow-shocked region of L1157-B1. Values are extracted from Bachiller, & Pérez Gutiérrez (1997).

[c] X(SiO) indicates the SiO abundance relative to H_2 estimated by using the normal $C^{18}O$ abundance, 1.7×10^{-7} (Frerking et al., 1982).

[d] Lefloch et al. (1998); Codella et al. (1999).

launching more than one distinct outflow toward different directions have been previously observed within IRAS 16293-2422 Source A (van der Wiel et al., 2019; Maureira et al., 2020a), BHR71 (Zapata et al., 2018; Tobin et al., 2019), NGC1333 IRAS2A (Tobin et al., 2015b), and NGC2264 CMM3 (Watanabe et al., 2017b). In all these cases, however, the binaries are separated by more than 40–50 au. Most binary sources observed to have a circumbinary disk/envelope structure show only a single outflow or parallel outflows, e.g., BHB07-11 (Alves et al., 2017), L1448 IRS3B-a, b (Tobin et al., 2016a), and L1551NE (Reipurth et al., 2000; Lim et al., 2016). An exception is the VLA1623 case. Hara et al. (2020) report that this source is a close binary system with a separation of 34 au, and two molecular outflows are inclined by 70° from each other across the plane of the sky.

The high-resolution observation (∼30 au) of IRAS 15398−3359 with ALMA (Chapter 3) show a single peak in the dust continuum, indicating that this source is not a wide binary. In addition, they find a well defined Keplerian disk structure with a size of 40 au in the SO line. If IRAS 15398−3359 is a close binary system instead of being two independent systems that should be accidentally aligned in a line of sight of our observation, it poses a very difficult question on how to create such complex system from a molecular cloud core. In principle, a single molecular cloud core can have very complicated internal angular momentum distribution, but there is no theory to explain the formation of binary stars with an apparent separation much smaller than the above ALMA resolution (∼30 au) and with very different rotation axes. Indeed, MHD simulations by Matsumoto et al. (2017) reveal that a single outflow is launched in the case of complex angular momentum distribution in the core. Note also that it is very unlikely that two, almost orthogonal, outflows would be launched from the circumbinary disk. We thus conclude that binary hypothesis for the secondary outflow is unlikely, although we cannot completely rule out the possibility of a tight binary (<30 au) system or that of a binary system whose components are aligned close to the line of sight. More observations at higher resolution will be required to investigate the multiplicity of IRAS 15398−3359.

4.6.2 Scenario 2: Outflow Outburst and Reorientation

A second possible explanation for the observed secondary structure is a past reorientation of the outflow launched from a single protostar. By assuming that outflow reorientation likelihood is random, the observed orthogonality of the secondary and primary outflows suggest a low expectation for this specific geometry, especially if the secondary outflow lies nearly along the plane of the sky as in the case of the primary outflow. This difficulty can be mitigated if the secondary outflow is a relic and the fast-moving component expected along the outflow has already been dissipated. In this case, the observed outflow direction may be significantly inclined with respect to the plane of the sky and the observed velocity may be close to the true velocity of the present relic.

The dissipation timescale of the high-velocity component can be roughly calculated as (Codella et al., 1999):

$$t_{\text{dis}} = \frac{8}{3}\frac{\rho}{\rho_1}\frac{r}{v}, \tag{4.1}$$

where ρ/ρ_1 is the mass density ratio of the shocked gas over the ambient gas, r the size of the shocked region, and v the shock velocity. In the case of IRAS 15398−3359, we assume the shock velocity to be 10 km s^{-1} and employ the size of the shocked region of 300 au according to a typical width of the arc-like structure (Figure 4.1). In addition, the ρ/ρ_1 ratio is assumed to be 10. The turbulent dissipation timescale is estimated to be ~4000 yr based on the above assumptions. This timescale is comparable to the dynamical timescale of the secondary outflow (~5000× $\cot(i)$ yr). Thus, the absence of the high-velocity component seems reasonable.

It is further worth pointing out two specific features of IRAS 15398−3359 in relation to the reorientation hypothesis. First, the protostellar mass is as low as 0.007 $M_\odot$ on the basis of the disk Keplerian motion (Chapter 3). This mass is lower than the expected mass of the first hydrostatic core proposed by star formation theories (0.01−0.05 $M_\odot$; Larson, 1969; Masunaga et al., 1998; Saigo & Tomisaka, 2006; Inutsuka, 2012). Thus, IRAS 15398−3359 appears to be in the earliest stages of protostellar evolution, a notion reinforced by the significantly larger reported envelope mass, 0.5−1.2 $M_\odot$ (Kristensen et al., 2012; Jørgensen et al., 2013). Second, past episodic accretion events have been suggested for this source by Jørgensen et al. (2013) and Bjerkeli et al. (2016b). Jørgensen et al. (2013) find a ring structure of H^{13}CO$^+$ at a scale of 150−200 au around the protostar. The lack of H^{13}CO$^+$ interior to the ring is inconsistent with the present heating rate from the central protostar; however, a previous burst of enhanced luminosity due to an accretion burst would have removed that H^{13}CO$^+$ through chemical reaction with sublimated H$_2$O from dust grains. The authors predict that the accretion burst occurred 10^2−10^3 yr ago, consistent with the dynamical timescale of the primary outflow (Oya et al., 2014; Bjerkeli et al., 2016a). Bjerkeli et al. (2016b) report that the HDO (1$_{0,1}$−0$_{0,0}$) emission is localized on the cavity wall in the vicinity of the protostar, interpreting that this is also due to a past accretion burst. The timescale for the outflow reorientation would be similar to the interval of episodic accretion in the case that the angular momentum of the gas in a molecular core is non-uniform (See below).

By assuming that the secondary structure reflects a previous change in the outflow direction for IRAS 15398−3359, can the observed velocity and orientation of the feature be reconciled? Relatively high-velocity shocks (> 5−20 km s^{-1}) are required to liberate SiO from dust grains (e.g., Caselli et al., 1997; Jiménez-Serra et al., 2008). Thus, the low, ~1 km s^{-1} velocity shift of the SiO arc-like structure needs to be considered carefully.

As discussed above, the possibility that the secondary outflow velocity is underestimated due to the structure lying very close to the plane of the sky is small. Alternatively, a more likely hypothesis is that the observed secondary outflow represents a relic structure which is no longer powered by current mass ejection from the protostar and inner disk. Thus, the fast component of the secondary outflow should have dissipated through interaction with ambient gas leaving only the observed motions close to the systemic velocity. This is also the reason why we can see the linear structure from the vicinity of the protostar. Previous observations of low-velocity features in SiO have also suggested this kind of hypothesis (Lefloch et al., 1998; Codella et al., 1999; López-Sepulcre et al., 2016). The relatively narrow line widths observed for the shock tracer lines described in Subsection 4.4.2 are consistent with this picture.

We must also reconcile the orientation of the secondary outflow, which is almost perpendicular to the angular momentum axis of the currently accreting gas. If the angular momentum of the episodically accreting gas varies with time, the direction of the outflow axis may change drastically, even as much as observed in this source. According to Misugi et al. (2019), the angular momentum of the gas in a molecular core is related to the degree of centroid velocity fluctuations within the parental filamentary molecular cloud, resulting in the angular momentum versus cloud mass relation determined by the Kolmogorov power spectrum of weak (i.e. subsonic or transonic) turbulence. In this analysis, the total angular momentum of a star-forming core is a vector sum of the various angular momenta of turbulent fluid elements whose directions are almost randomly oriented. The summation over angular momentum vectors inevitably includes cancellation of opposite components of angular momentum vectors. In addition, the temporal variation of the angular momentum of the accreting gas has also been studied by Takaishi et al. (2020). They investigate the evolution of the angle between the protostellar spin and the rotation axes of the protoplanetary disks in turbulent molecular cloud cores.

The identification of such an origin for the core rotation has important implications, because the actual collapse process of the core is not homologous but rather undergoes a 'run-away' process where a central dense region collapses first and the outer regions accrete onto the central region later. Thus, episodic accretion events with very different angular momenta are expected to occur during this run-away collapse process. Applying this model to the early evolution of the IRAS 15398−3359 protostellar core, and recognizing that the mass of the central protostar is extremely low, there should only have been a very few discrete episodic accretion events and random angular momentum reorientations. Moreover, the central velocity of the disk structure observed with the SO line is 5.5 km s^{-1}, which is shifted 0.3 km s^{-1} from the systemic velocity of the protostellar core at 5.2 km s^{-1} (Yen et al., 2017), as shown in Chapter 3. This result may also naturally

caused by the continual accretion of fluid elements that have various momenta as well as various angular momenta. The secondary outflow feature provides plausible observational evidence for this picture. It is interesting to note that a change in the angular momentum axis of the accreting gas has also recently been suggested observationally for some other young protostellar sources (Sakai et al., 2019; Zhang et al., 2019; Gaudel et al., 2020).

If the rotation axis is misaligned with the global magnetic field direction, the MHD simulations show that the directions of the jet/outflow and disk randomly change over the time (Matsumoto & Tomisaka, 2004; Hirano et al., 2020; Machida et al., 2020). Since the misalignment can naturally be caused by the above picture, this mechanism would also contribute to the outflow reorientation of this source. Note that the global direction of the magnetic field around IRAS 15398−3359 is almost along the primary outflow direction (Redaelli et al., 2019).

4.7 Third Outflow Associated with IRAS 15398−3359

The above picture of the outflow reorientation is further strengthened by the discovery of the third outflow structure in this source. We found it, when we analyzed the ALMA archival data for IRAS 15398−3359 to study the environment around the protostar at a larger scale (~10^4 au). The ^{12}CO and HCO$^+$ line emission data observed with ALMA Cycle 4 operation are available: 2019.1.01063.S (PI: Sai, Jinshi) and ALMA Cycle 6 operation: 2017.1.01399.S (PI: Rygi, Kazi), respectively. The parameters of the molecular lines are listed in Table 4.5. These data are observed in the ACA standalone mosaic mode, which delineate an extended molecular distribution at a coarse spatial resolution. The details of these observations are summarized in Table 4.6.

Table 4.5: List of Detected Lines with the ALMA Archival Data[a]

Molecule	Frequency (GHz)	$S\mu^2(D^2)$	$E_u k^{-1}$(K)	Beam size	σ(mJy beam^{-1})
^{12}CO ($J = 2-1$)	230.5380000	0.0242	17	7.″82×4.″11 (P.A. 86°)	200
HCO$^+$ ($J = 1-0$)	89.1885247	15.211	4	17.″18×10.″90 (P.A. -89°)	100

[a] Line parameters are taken from CDMS (Endres et al., 2016). The beam size for each line is obtained from the observations.

Figures 4.7(a) and (b) show the moment 0 maps of the ^{12}CO and HCO$^+$ line emission around IRAS 15398−3359 at a 10^3−10^4 au scale. The grey circle shown in Figure 4.7(a) represents the field of view for the FAUST observation (e.g., Figures 4.1 and 4.2). Thus, these two lines are observed with a much larger field of view. For the ^{12}CO line, the velocity ranges are from 1.7 km s^{-1} to 3.5 km s^{-1}and from 7.2 km s^{-1} to 8.1 km s^{-1} for the blueshifted and redshifted components, respectively. On the other hand, those for the HCO$^+$ line are 3.5 km s^{-1} to 5.0 km s^{-1}and from 5.7 km s^{-1} to 7.2 km s^{-1} for the blueshifted and redshifted components, respectively. These distributions are extended to the north-south direction which are different from the two outflows described in the earlier sections. Figure 4.8 shows

Table 4.6: Observation Parameters for the ALMA archival data

Parameter	2019.1.01063.S	2017.1.01399.S
PI	Jinshi Sai	Kazi Rygi
Array	7 m Mosaic	7 m Mosaic
Observation date	2019 Dec 19	2018 Jul 15
Time on Source (minute)	152	171
Number of antennas	20	22
Primary beam width (″)	144.5	172.8
Proj. baseline range (m)	8.9-48.9	8.9-48.9
Bandpass calibrator	J1337-1257	J1427-4206, J1517-2422
Phase calibrator	J1534-3526	J1517-2422, J1626-2951
Flux calibrator	J1337-1257	J1427-4206, J1517-2422
Pointing calibrator	J1454-3747, J1337-1257	J1427-4206, J1517-2422
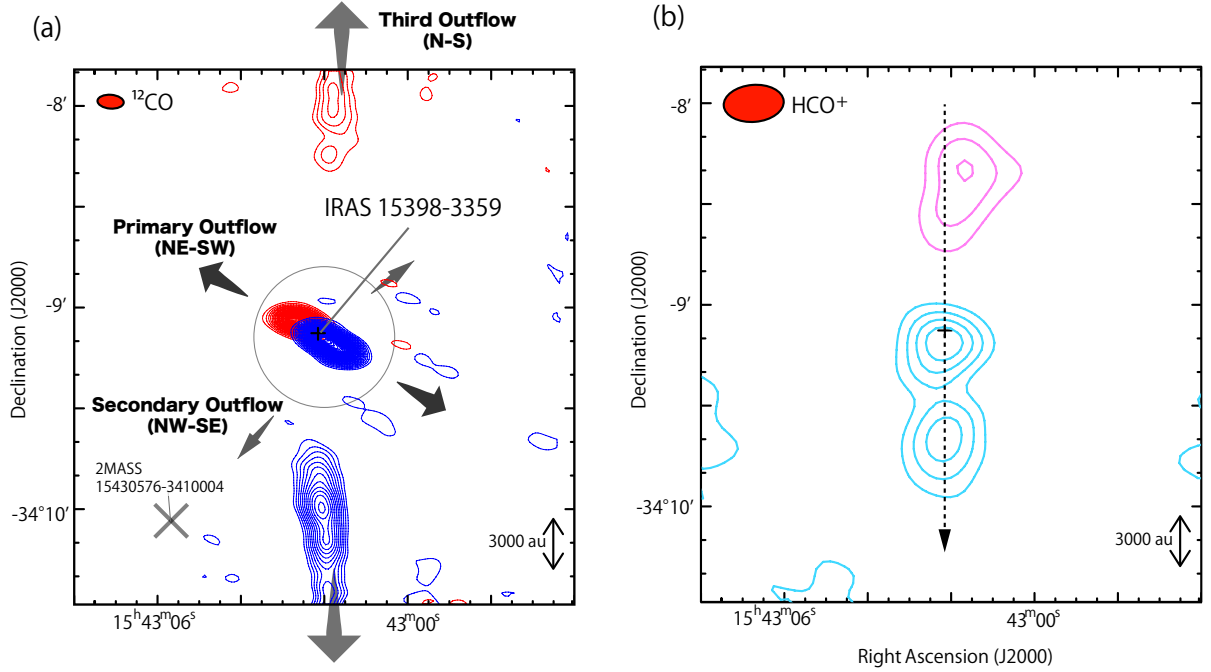
Figure 4.7: (a) Moment 0 map of the ^{12}CO emission. The red and blue contours represent the velocity ranges from 7.2 to 8.2 km s^{-1} and from 1.7 to 3.5 km s^{-1}, respectively. The grey circle shows the field of view of the FAUST observation in Figures 4.1 and 4.2. The arrows indicate each direction of the three outflows. (b) Moment 0 map of the HCO$^+$ emission. The pink and light-blue contours represent the velocity ranges from 5.7 to 7.2 km s^{-1} and 3.5 to 5.0 km s^{-1}, respectively. The red ellipses in the upper-left corner are the beam size of the molecular line. Contour levels for both images are every 3σ from 3σ, where σ is listed in Table 4.5.

the position-velocity diagram along the north to south line passing through the protostar position. In Figure 4.8, the color scale and the white contours show the velocity structures of the ^{12}CO and HCO$^+$ lines. In other words, the ^{12}CO and HCO$^+$
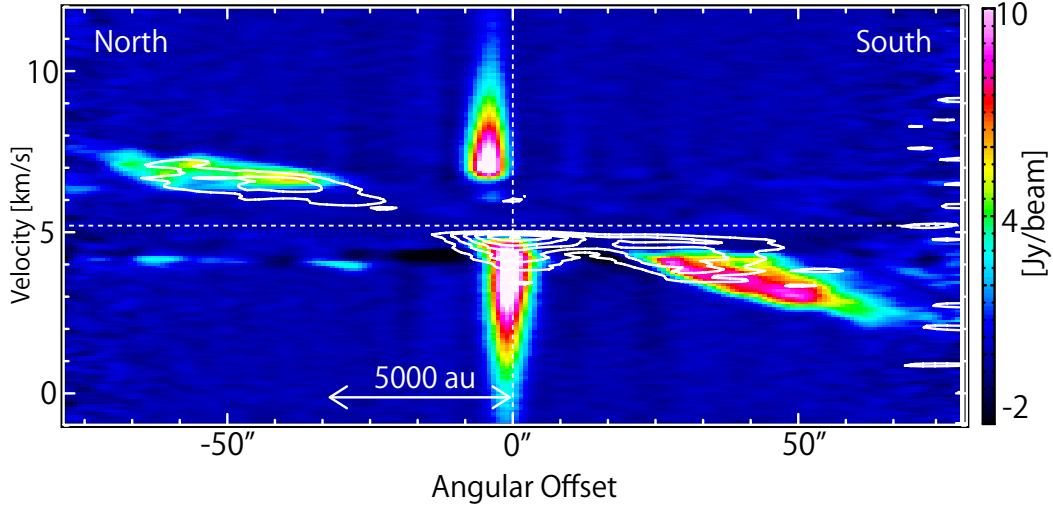
Figure 4.8: PV diagram along the north to south line as shown in Figure 4.7(b). Color scales and white contours show the velocity structure of the ^{12}CO and HCO$^+$ emission, respectively. The origin of the position corresponds to the continuum peak position, and the emission here represents part of the primary outflow structure. Both line emission show broad increasing velocity with increasing distance from the protostar, which can be interpreted as an outflow motion.

lines trace the outside and inside of the outflow. These features clearly indicate the outflow motion, where the velocity increases with the increasing distance from the protostar. When we employ the plane-of-the-sky distance and the line-of-sight velocity of 50″ (7800 au) and 2 km s^{-1}, respectively, the dynamical timescale is estimated to be ~18,000× $\cot(i')$ yr (i' =0° for pole-on), where i' is the inclination angle of the third outflow axis. The collimated structure of the outflow implies its nearly side-on configuration. In this case, the timescale would be much shorter than 18,000 yr. This discovery of the third outflow means that the outflow direction of IRAS 15398−3359 has been changed at least twice. Thus, the outflow reorientation scenario is much more likely than the binary (multiple) scenario.

4.8 Future Directions

Unfortunately, the above interesting feature is not yet well theoretically studied because most of the numerical MHD simulations for the formation of protostars and disks have been performed with the simplest initial condition for the rotation, i.e., rigid body rotation throughout the core (e.g., Machida & Basu, 2019; Inutsuka, 2012; Tsukamoto, 2016; Wurster & Li, 2018). Turbulent motion, however, could be important for angular momentum variation within the core as well as the thermal pressure of the gas.

We here propose the reorientation scenario as one possibility to account for this observation. As an independent study, Vazzano et al. (2021) report the similar structure to the secondary outflow in the southeast direction in the ^{12}CO (J =2−1) and SO (J_N =6$_5$−5$_4$) line emission. Their interpretation is that the outflow would

be launched from a 2MASS 15430576-3410004 located ~69″ in the southeast of IRAS 15398−3359 (Figure 4.7(a)). However, the 2MASS source is not detected in the longer wavelength than 5 μm and is not cataloged as a YSO in the Spitzer c2d project (Chapman et al., 2007). Considering the detection of the third outflow, we think that their interpretation is not the case. Nevertheless, it is important to explore the environment of IRAS 15398−3359 more widely. Furthermore, we need additional observations to investigate other possibilities carefully, particularly, the existence of the close binary system (<30 au). For testing the close binary hypothesis, centimeter-wave observations at a high angular resolution (<30 au) are essential to resolve the components without obscuration from the optically thick dust continuum. It is also interesting to observe the velocity field of the parent core at a high angular resolution in order to investigate the distribution of the angular momentum as previously done at a larger scale for the other sources (e.g., Caselli et al., 2002b).

4.9 Summary

We have uncovered an interesting feature along the direction almost perpendicular to the primary outflow in IRAS 15398−3359 with the ALMA observations. This is most likely the relic of a secondary outflow ejected from the single protostar at the center of this system. Furthermore, we have found the third outflow along the north to the south, which strengthens our reorientation scenario. Our results present an important implication on the earliest stage of star formation. The main results are listed below.

1. We have identified an arc-like structure in SO, SiO, and CH$_3$OH line emission. Since these molecular species are known to be shock tracers, the arc-like structure is most likely a shock region produced by a relic outflow. The molecular abundances of H$_2$CO, SO, SiO, and CH$_3$OH in the arc-like structure are clearly enhanced in comparison with those at the protostar position, and they are consistent with those reported for shocked regions in the source L1157-B1.

2. The H$_2$CO, SO and C^{18}O line emission produce a linear feature around the protostar. The SO emission also reveals an additional structure to the northwest. In the velocity structure of the H$_2$CO and C^{18}O emission, the velocity increases with increasing distance from the protostar toward the southeast. Such morphological and kinematic features are consistent with those expected from an outflow.

3. We roughly estimate the dynamical timescale of the secondary outflow to be ~5000× $\cot(i)$ yr (i =0° for pole-on). The timescale is similar to that of depletion of SiO onto dust grains, which is 10^3−10^4 yr.

4. As described in Chapter 3, the Keplerian disk structure around IRAS 15398−3359 is seen in the SO line emission at a resolution of 30 au, and the dust continuum maps show only a single peak. Given this geometry, the launch of two

almost orthogonal outflows from the circumbinary disk (<30 au) is very unlikely, although we cannot completely exclude a tight binary hypothesis. Higher resolution observations are needed to examine the possibility further.

5. We thus hypothesize that the secondary outflow is a relic of a past reorientation of the outflow launched from a single protostar. The narrow line width of the SiO emission implies that the arc-like structure has dissipated the turbulent motions associated with the earlier shocks. The change in the direction of the outflow axis may be related to non-uniform internal angular momentum distribution in the molecular core, advected onto the central region via episodic accretion. Such events may occur during the earliest stages of protostar formation like IRAS 15398−3359.

6. We have recently recognized the third outflow along the north to the south in the ^{12}CO and HCO$^+$ emission with the ALMA archival data. This further strengthens the reorientation scenario.

Chapter 5
Accretion Shock Heating around the Protostar: B335

In this chapter, we investigate the temperature distribution of the disk/envelope system of the low-mass protostellar source, B335. The temperature is an important parameter related to the physical process and the associated chemical evolution. For this purpose, we observe the four species, HCOOH, NH_2CHO, CH_2DOH, and CH_3OH, with ALMA at a high angular resolution of ~ 3 au. While all of them are detected within a few 10 au, the distributions of the HCOOH and NH_2CHO lines are more compact around the continuum peak than those of the CH_2DOH and CH_3OH lines. We discuss the heating mechanism of the surrounding gas around the protostar, based on the derived temperature distribution. The result provides us with a clue to understanding the chemical structure in protostellar sources (See Chapter 9).

5.1 Introduction

Complex Organic Molecules (COMs), which consist of more than six atoms with one carbon atom at least, are important species to understand the molecular evolution in the Universe. They have extensively been found in various environments of star formation: quiescent dense clouds, prestellar cores (e.g., Bacmann et al., 2012; Cernicharo et al., 2012; Ceccarelli et al., 2017; Soma et al., 2018; Scibelli & Shirley, 2020), disk/envelope systems of protostellar cores (e.g., Cazaux et al., 2003; Bottinelli et al., 2004b; Kuan et al., 2004; Pineda et al., 2012; Jørgensen et al., 2016; Oya et al., 2016; Lee et al., 2019; Imai et al., 2019; Bianchi et al., 2020), and outflow shock regions around protostars (e.g., Arce et al., 2008; Sugimura et al., 2011; Codella et al., 2020; De Simone et al., 2020). Many observations of organic molecules toward various sources reveal a chemical differentiation between nitrogen-bearing and oxygen-bearing species (e.g., Wyrowski et al., 1999; Bottinelli et al., 2004b; Kuan et al., 2004; Beuther et al., 2005; Fontani et al., 2007; Calcutt et al., 2018; Oya et al., 2018; Csengeri et al., 2019), where the nitrogen-bearing ones generally tend to have a compact distribution in contrast to a rather extended distribution of oxygen-bearing ones in star-forming regions. An exception is HCOOH. While this molecule is an oxygen-bearing molecule, it shows a similar trend to the nitrogen-bearing COMs in low-mass and high-mass protostellar sources (e.g., Oya

et al., 2017; Csengeri et al., 2019). The observational results indicate increasing complexity of chemical structures in interstellar clouds and star-forming regions. Although the chemical processes in star-forming regions have been investigated in experimental (e.g., Ioppolo et al., 2011) and theoretical works (e.g., Charnley et al., 1992; Caselli et al., 1993; Garrod et al., 2008; Vasyunin et al., 2017), our understanding is far from complete. To step forward, characterizing the temperature structure around the protostar needs to be clarified in detail, because it is tightly related to the chemical structure (e.g., Jørgensen et al., 2018; Taquet et al., 2019; van Gelder et al., 2020; Ambrose et al., 2021). Hence, we here investigate the temperature distribution around the low-mass protostellar source, B335, rich in COMs. Since this source is in an isolated condition without any influence of nearby star-formation activities, it has been used as an excellent testbed for star-formation studies.

B335 is a Bok globule (Keene et al., 1980) harboring the Class 0 protostellar source, IRAS 19347+0727. The distance to B335 is a bit controversial: it is reported to be 90-164.5 pc (Olofsson & Olofsson, 2009; Watson, 2020). For the consistency with some previous works (e.g., Bjerkeli et al., 2019; Imai et al., 2016, 2019), we here employ the conventional distance of 100 pc. The bolometric temperature (T_{bol}) and the bolometric luminosity (L_{bol}) are 37 K (Andre et al., 2000) and 0.72 $L_\odot$ (Evans et al., 2015), respectively. A bipolar outflow extending along the east to west direction has been detected with single-dish and interferometric observations (Hirano et al., 1988, 1992; Bjerkeli et al., 2019). It is almost parallel to the plane of the sky, where the inclination angle is reported to be between $3°$ and $10°$ (Hirano et al., 1988; Stutz et al., 2008).

Some observational works for the disk/envelope system of this source have been done with ALMA. Evans et al. (2015) and Yen et al. (2015b) indicate that the infall motion dominates at 100 au scale around the protostar without a clear rotation motion at a spatial resolution of 0."3 (~30 au). Yen et al. (2015b) estimate the upper limit of the protostellar mass to be 0.05 $M_\odot$ on the assumption of a Keplerian disk with the radius of 10 au, based on their observation of the $C^{18}O$ and SO emission. Later, higher angular resolution observations have revealed a rotation structure at ~10 au scale (Imai et al., 2019). The CH_3OH and $HCOOH$ lines are detected in the vicinity of the protostar, which reveal the velocity gradient along the envelope direction. They apply the infalling-rotating envelope (IRE) model to these velocity structures, and derive the protostellar mass and the radius of the centrifugal barrier to be 0.02−0.06 $M_\odot$ and <5 au, respectively. Thus, this source also has a very low-mass protostar such as IRAS 15398−3359 described in Chapters 3 and 4, and its disk radius is relatively small even among low-mass protostars. Bjerkeli et al. (2019) independently report the velocity gradient in the CH_3OH and SO_2 lines, and find that it is consistent with a Keplerian rotation with the protostellar mass of 0.05 $M_\odot$. They also estimate the dust mass from the dust continuum emission within 7 au to be 3×10^{-4} $M_\odot$, which is comparable to the mass 7.5×10^{-4} $M_\odot$ derived with the radius of 25 au by Evans et al. (2015).

As well as the above physical structures, B335 has interesting features from the chemical point of view. The CO, CN, HCO^+, HCN, HNC, N_2H^+, H_2CO, CS, CCH, and c-C_3H_2 lines were detected at a few 100−1000 au scale in this source with ALMA

(Evans et al., 2015; Imai et al., 2016). Association of CCH and c-C_3H_2 around the protostar on a few 100 au scale indicate Warm Carbon Chain Chemistry (WCCC) nature of this source (Sakai et al., 2008; Sakai & Yamamoto, 2013) (See Chapter 1). For the inner region at a few 10 au scale, various COM lines, such as CH_3CHO, $HCOOCH_3$, and NH_2CHO, were observed with ALMA by Imai et al. (2016). Hence, B335 is recognized as the WCCC source containing a hot corino: namely a hybrid source (Oya et al., 2017). This feature is different from IRAS 15398−3359 where COMs have not been detected at a resolution of ∼30 au.

In our observations, the HCOOH, NH_2CHO, CH_2DOH, and CH_3OH lines are imaged within a few 10 au scale at a higher angular resolution (∼3 au), which is almost the highest resolution achievable with ALMA. The result will contribute to our understanding of the physical and chemical structures in the disk/envelope system of this source. In this chapter, the physical aspect of the results is mainly presented. Characterization of the chemical structure is left for Chapters 8 and 9.

5.2 Observation

Four blocks of the ALMA observations toward B335 were carried out with the Band 6 receiver in the Cycle 6 operation on 2019 June 10, 12, 13, and 23. The observational parameters are summarized in Table 5.1. We combined these visibility data in the uv plane. Spectral lines of HCOOH, NH_2CHO, CH_2DOH, and CH_3OH listed in Table 5.2 were observed in the frequency range from 244−249 GHz and 261−263 GHz. In all the observations, 52 antennas were used, where the baseline length ranged from 83 to 16196 m. The total on-source time was 180.2 minutes. The primary beam (half-power beam) width was 23."7. The backend correlator for HCOOH ($11_{3,8}$−$10_{3,7}$), NH_2CHO ($13_{0,13}$−$12_{1,12}$), CH_2DOH ($4_{2,2}$−$4_{2,3}$, e_0, $10_{2,8}$−$10_{1,9}$, o_1 , and $5_{2,4}$−$5_{1,5}$, o_1), and CH_3OH ($21_{3,18}$−$21_{2,19}$, A, $17_{3,14}$−$17_{2,15}$, A, $12_{6,7}$−$13_{5,8}$, E, and $2_{1,1}$−$1_{0,1}$, A) was set to a resolution of 564 kHz and a bandwidth of 234.38 MHz, and that for HCOOH ($11_{9,2}$−$10_{9,1}$, $11_{9,3}$−$10_{9,2}$, $11_{6,6}$−$10_{6,5}$, $11_{6,5}$−$10_{6,4}$, $11_{5,7}$−$10_{5,6}$, $11_{5,6}$−$10_{5,5}$, and $12_{0,12}$−$11_{0,11}$), NH_2CHO ($12_{0,12}$−$11_{0,11}$, v_t =1 and $12_{0,12}$−$11_{0,11}$) and CH_2DOH ($3_{2,1}$−$3_{1,2}$, e_0), and CH_3OH ($4_{2,2}$−$5_{1,5}$, A and $18_{3,15}$−$18_{2,16}$, A) was set to a resolution of 488.281 kHz and a bandwidth of 234.38 MHz. The field center was taken to be (α_{2000}, δ_{2000})= ($19^h37^m00^s$.898, +07°34′09."528) for all the observation blocks. The bandpass calibrator, the flux calibrator, and the pointing calibrator were J1924-2914. The phase calibrator was J1938+0448.

The data were reduced by Common Astronomy Software Applications package (CASA) 5.8.0 (McMullin et al., 2007) as well as a modified version of the ALMA calibration pipeline. Phase self-calibration was performed by using the continuum data, and then the solutions were applied to the spectral line data. After the self-calibration procedures, the data images were prepared by using the CLEAN algorithm, where the Briggs' weighting with a robustness parameter of 0.5 was employed. The largest angular size is 0."3 for all these observations. The original synthesized beam sizes are summarized in Table 5.2.

Table 5.1: Observation Parameters for B335[a]

Execution block	1[b]	2[c]	3[d]	4[e]
Observation date(s)	2019 June 10	2019 June 12	2019 June 13	2019 June 23
Time on Source (minute)	45.05	44.93	45.12	45.10
Number of antennas	49	44	47	48
Primary beam width ($''$)	23.7			
Total bandwidth (GHz)	0.234			
Continuum bandwidth (GHz)	0.234			
Proj. baseline range (m)	83–16196			
Bandpass calibrator	J1924-2914			
Phase calibrator	J1938+0448			
Flux calibrator	J1924-2914			
Pointing calibrator	J1924-2914			
Resolution($''\times''$(P.A.$^\circ$))	0.031×0.026 (-7.853)			
σ (mJy beam^{-1}channel^{-1})	1.0			

[a] These observations are conducted with Band 6.

[b] uid://A002/Xdd7b18/X2f30

[c] uid://A002/Xdd7b18/Xa010

[d] uid://A002/Xdd7b18/X66c

[e] uid://A002/Xdd7b18/X73f4

Table 5.2: Observed Molecular Lines in B335[a]

Molecule	Transition	Frequency (GHz)	$S\mu^2$ (D^2)	$E_u k^{-1}$ (K)	Beam size	σ (mJy beam^{-1}· km s^{-1})
HCOOH	$(11_{9,2}-10_{9,1})$	247.4211284	7.3468	328	0."030×0." 023 (P.A. -32°)	4
	$(11_{9,3}-10_{9,2})$					
	$(11_{6,6}-10_{6,5})$	247.4462429	15.614	186	0."030×0." 023 (P.A. -32°)	3
	$(11_{6,5}-10_{6,4})$					
	$(11_{5,7}-10_{5,6})$	247.5139713	17.633	151	0."030×0." 023 (P.A. -32°)	3
	$(11_{5,6}-10_{5,5})$	247.5141176				
	$(11_{3,8}-10_{3,7})$	248.2744893	20.573	100	0."030×0." 023 (P.A. -31°)	2
	$(12_{0,12}-11_{0,11})$	262.1034810	24.157	83	0."029×0."022 (P.A. -29°)	3
NH$_2$CHO	$(13_{0,13}-12_{1,12})$	244.8542130	6.6085	91	0."030×0." 023 (P.A. -32°)	2
	$(12_{0,12}-11_{0,11}, v_t=1)$	247.3273220	156.34	494	0."030×0." 023 (P.A. -32°)	2
	$(12_{0,12}-11_{0,11})$	247.3907190	156.32	78	0."030×0." 023 (P.A. -32°)	2
CH$_2$DOH	$(4_{2,2}-4_{2,3}, A)$	244.8411349	2.540	38	0."030×0." 023 (P.A. -32°)	2
	$(10_{2,8}-10_{1,9}, o_1)$	244.9888456	3.439	153	0."030×0." 023 (P.A. -32°)	2
	$(3_{2,1}-3_{1,2}, e_1)$	247.6257463	2.360	29	0."030×0." 023 (P.A. -32°)	2
	$(5_{2,4}-5_{1,5}, o_1)$	261.6873662	4.006	48	0."029×0."022 (P.A. -29°)	3
CH$_3$OH	$(21_{3,18}-21_{2,19}, A)$	245.2230190	82.489	586	0."030×0." 023 (P.A. -32°)	3
	$(4_{2,2}-5_{1,5}, A)$	247.2285870	4.3444	61	0."030×0." 023 (P.A. -32°)	3
	$(18_{3,15}-18_{2,16}, A)$	247.6109180	69.431	447	0."030×0." 023 (P.A. -32°)	3
	$(17_{3,14}-17_{2,15}, A)$	248.2824240	65.259	405	0."030×0." 023 (P.A. -31°)	3
	$(12_{6,7}-13_{5,8}, E)$	261.7044090	8.5234	360	0."029×0."022 (P.A. -29°)	3
	$(2_{1,1}-1_{0,1}, A)$	261.8056750	5.336	28	0."029×0."022 (P.A. -29°)	3

[a] Line parameters are taken from CDMS (Endres et al., 2016) and JPL (Pickett et al., 1998). The rms noise (σ) and the beam size are based on the observation data.

5.3 Distributions and Velocity Structures

Figure 5.1 shows the dust continuum emission at 1.2 mm. Its peak position and peak intensity are derived from a 2D Gaussian fit to the image : $(\alpha_{2000}, \delta_{2000}) = (19^h37^m00^s.90\pm0.00001, +7°34'09.''49\pm0.00021)$ and 6.142 ± 0.047 mJy beam^{-1}, respectively. These values are consistent with the previous report (4.8 mJy beam^{-1} at 230 GHz with the 0.''03 beam; Bjerkeli et al., 2019), considering the slight difference of the observing frequency. It is an almost round shape and faintly extended in the northwest.
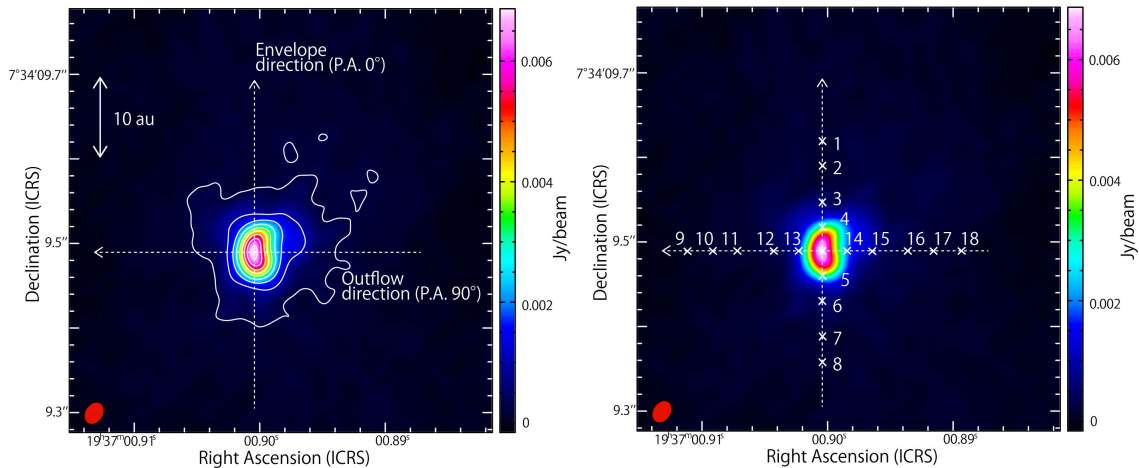
Figure 5.1: Dust continuum emission at 1.2 mm. Contour levels are every 10σ from 3σ, where σ is 0.08 mJy beam^{-1}. The horizontal and vertical dashed arrows show the outflow and envelope directions, respectively. The cross marks shown in the right panel correspond to the positions for the derivation of the rotation temperature and column density. The numbers indicate the positions presented in Tables 5.3 and 5.4.

Figures 5.2 (a), (b), (c) and (d) show the moment 0 maps of HCOOH $(12_{0,12}-11_{0,11})$, NH_2CHO $(12_{0,12}-11_{0,11})$, CH_2DOH $(4_{2,2}-4_{2,3}, e_0)$, and CH_3OH $(4_{2,2}-5_{1,5}, A)$, respectively. The distributions of the HCOOH and NH_2CHO lines are more compact around the continuum peak than those of the CH_2DOH and CH_3OH lines. All of them conspicuously show an intensity depression at the continuum peak position, which suggests that these lines are optically thick.

An overall distribution of the four line emission and the continuum emission has a round shape, which looks different from the flattened structure expected for the disk/envelope system at a glance. This seems to originate from the small protostellar mass. The vertical scale of the disk/envelope system, which is defined by the scale height H, can be evaluated by assuming hydrostatic equilibrium as:

$$H = \sqrt{\frac{2}{GM}}c_s r^{\frac{3}{2}} \tag{5.1}$$

where G is gravitational constant, M the protostellar mass (0.05 $M_\odot$), r the distance

from the protostar, and c_s the sound speed defined as:

$$c_S = \left(\frac{k_B T}{\mu m_H} \right)^{\frac{1}{2}}.$$

(5.2)

Here, k_B is Boltzmann constant, T the temperature (200 K), and μ the mean molecular weight (2.3) in units of the mass of the hydrogen atom, m_H. At the radius of 10 au, H is derived to be about 6 au. This is indeed comparable to the observed distribution considering the inclination of the disk of 3°-10° (Hirano et al., 1988; Stutz et al., 2008).

It should be noted that the intensity peaks of HCOOH and NH$_2$CHO are offset from the protostar position to the west by ∼4 au. On the other hand, the peak position of CH$_3$OH is offset to the northwest, and that of CH$_2$DOH is to the north. The continuum emission also shows a little extension to the west. The intensity peaks except for CH$_2$DOH are located near the peak in the red lobe of the outflow near the protostar traced by the SiO emission reported in Bjerkeli et al. (2019) (Figure 5.3). Hence, part of the HCOOH, NH$_2$CHO, and CH$_3$OH emission seems to be affected by the shock caused by an outflow impact.

Some differences other than the size of the distribution among the four molecules can also be recognized in their position-velocity (PV) diagrams, as shown in Figure 5.4. We assume the outflow direction to be along the east to the west (P.A. 90°), as defined by Imai et al. (2019). The envelope direction is thus taken to be perpendicular to it (P.A. 0°), as shown in Figure 5.1. Figures 5.4(a) and (b) show the PV diagrams of CH$_3$OH ($4_{2,2}$−$5_{1,5}$, A) along the envelope direction and the outflow direction, respectively. The CH$_3$OH line seems to trace the infalling-rotating envelope on 20 au scale because the diamond shape is seen in the PV diagram along the envelope direction (Figure 5.4(a)) (Oya et al., 2014). For the outflow direction (Figure 5.4(b)), the velocity increases as increasing distance from the ±6 au positions to the outside, indicating that the emission also traces part of the outflow structure. In contrast, the PV diagrams of NH$_2$CHO and HCOOH reveal the inner region up to 10 au. While these velocity structures could also be an infalling-rotating motion, the rotation motion is likely more dominant. For these two species, the velocity shifts of ∼ 5 km s^{-1} from the systematic velocity (8.34 km s^{-1}; Yen et al., 2015b) can be seen in the vicinity of the protostar.

Thus, we find the differences and the similarities in the line distributions and the velocity structures among the four lines. Interestingly, HCOOH, the oxygen-bearing species, shows a similar trend to the nitrogen-bearing molecule, NH$_2$CHO. This trend is also suggested in other low-mass and high-mass sources (e.g., Oya et al., 2017; Csengeri et al., 2019). This may be an important clue to unravel chemical pathways responsible for these molecules (See also Chapter 9). In the next section, we study the temperature distribution around the protostar by using the detected lines listed in Table 5.2.
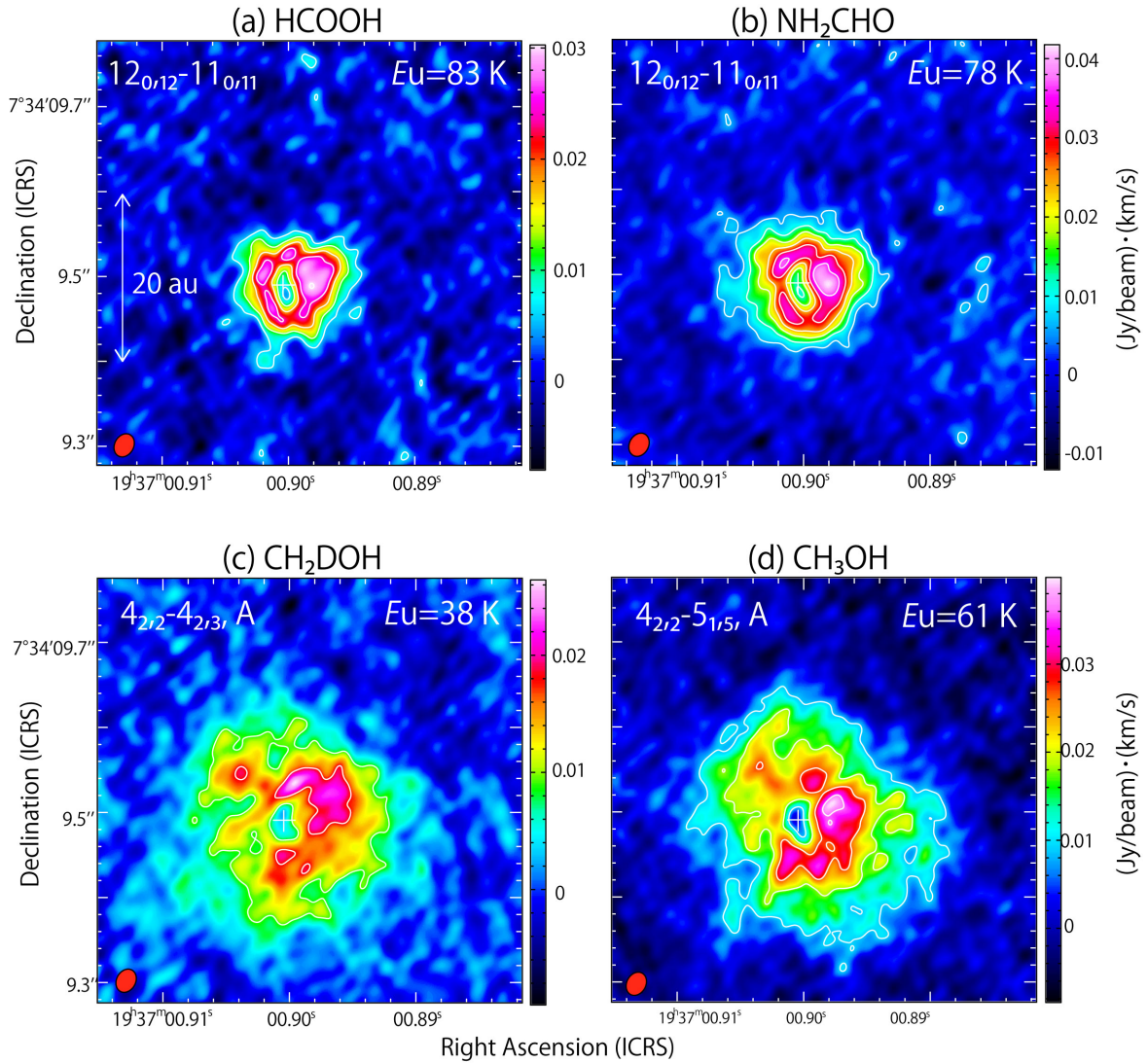
Figure 5.2: Moment 0 maps of the HCOOH, NH$_2$CHO, CH$_2$DOH, and CH$_3$OH lines. Contour levels are every σ from 3σ, where σ is 2 mJy beam^{-1}km s^{-1}, 2 mJy beam^{-1}km s^{-1}, 3 mJy beam^{-1}km s^{-1}, and 3 mJy beam^{-1}km s^{-1}, respectively, for the above lines. The number in the upper-right corner of each panel represents the upper-state energy of the molecular line. Red circle in the lower-left corner of each panel shows the beam size. The cross marks show the continuum peak position.
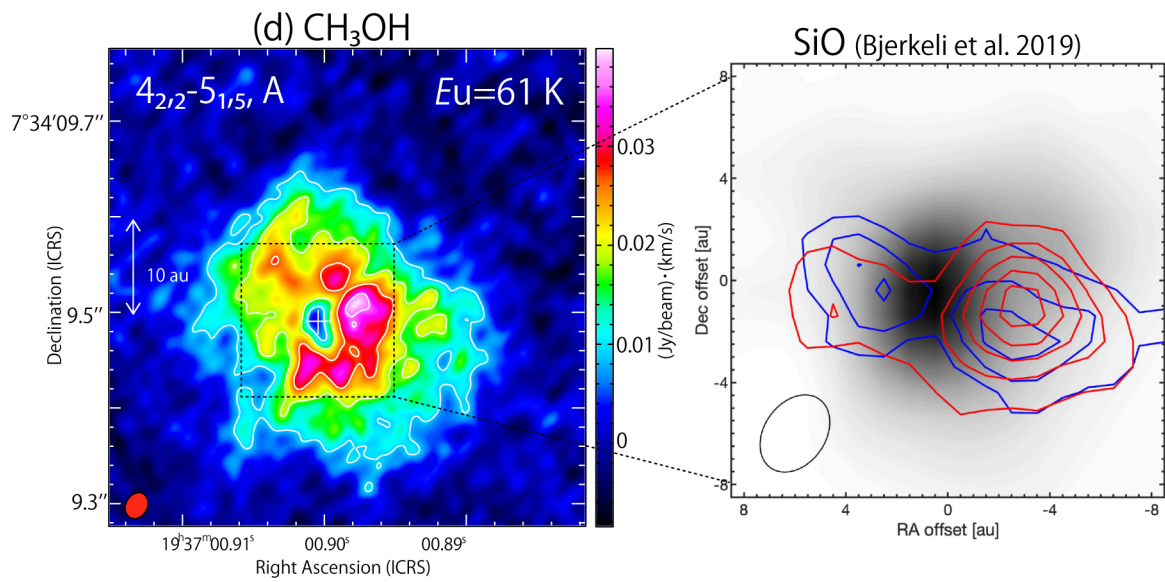
Figure 5.3: The left panel represents the moment 0 map of the CH_3OH line, which is the same as Figure 5.2(d). The right panel is the moment 0 map of the SiO ($J =5-4$) line reported by Bjerkeli et al. (2019). The red and blue contours show the redshifted and blueshifted outflow lobes, respectively. The intensity peak of CH_3OH almost corresponds to that of SiO, where the shock is caused by the outflow interaction.
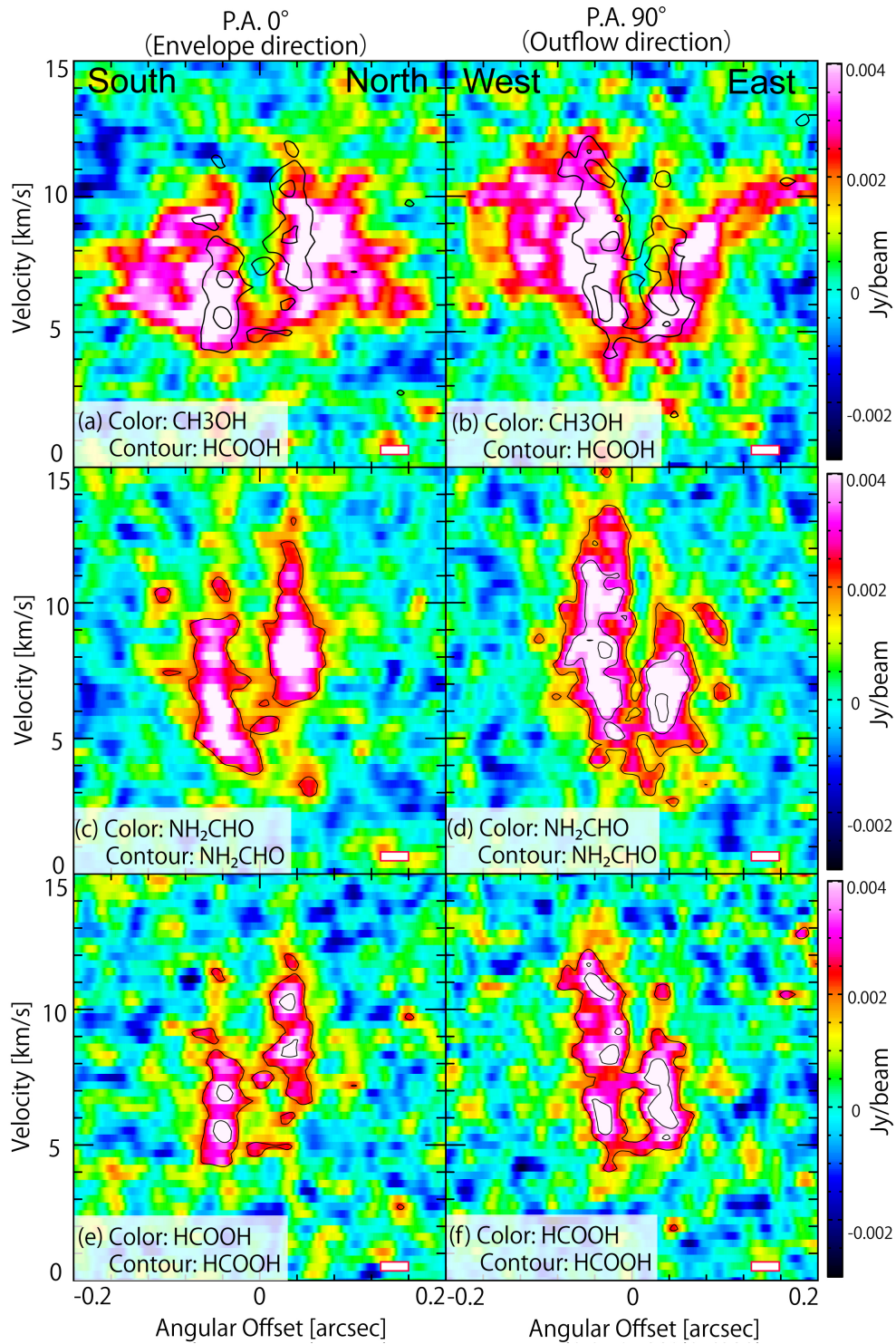
Figure 5.4: Color scales show the position-velocity (PV) diagram of the CH_3OH (a,b), NH_2CHO (c,d), and HCOOH (e,f) lines. Contours overlaid on the PV diagram for CH_3OH represent the corresponding PV diagram of HCOOH for comparison. For NH_2CHO and HCOOH, the contours show their own PV diagrams. Contour levels are every 3 σ, where σ are 0.6 mJy beam^{-1} and 0.7 mJy beam^{-1} for NH_2CHO and HCOOH, respectively.

5.4   Rotation Temperature and Column Density

Variations of the rotation temperatures and the column densities along the envelope direction and the outflow direction are derived under the assumption of LTE (local thermodynamic equilibrium) by using the observed intensities and the velocity widths of the HCOOH, NH_2CHO, CH_2DOH, and CH_3OH lines (Table 5.2). Since the dust emission is bright particularly toward the protostar position, we need to consider the optical depth of the dust. For simplicity, we assume the equilibrium condition that gas and dust are well mixed and thermalized with each other and the gas temperature is equal to the dust temperature. In this case, the observed intensity (T_{obs}) is represented as follows based on radiative transfer:

$$T_{obs} = \frac{c^2}{2\nu^2 k_B} \left[B_\nu(T) + \exp\left\{-(\tau_{line} + \tau_{dust})\right\} \left\{B_\nu(T_{cb}) - B_\nu(T)\right\} - I_{dust} \right], \qquad (5.3)$$

where $B_\nu(T)$ and $B_\nu(T_{cb})$ are the Plank function with the source temperature at T and the cosmic microwave background temperature T_{cb}, respectively, τ_{line} the optical depth of the molecular line, and τ_{dust} the dust optical depth. τ_{line} can be written as:

$$\tau_{line} = \frac{8\pi^3 S \mu^2}{3h \Delta\nu U(T)} \left\{\exp\left(\frac{h\nu}{k_B T}\right) - 1\right\} \exp\left(-\frac{E_u}{k_B T}\right) N, \qquad (5.4)$$

where S is the line strength, μ the dipole moment responsible for the transition, h the Plank constant, $U(T)$ the partition function of the molecule at the source temperature T, ν the frequency, E_u the upper-state energy, N the column density (e.g., Yamamoto, 2017). On the other hand, the intensity of the dust continuum emission (I_{dust}) is:

$$I_{dust} = B_\nu(T) + \exp\left(-\tau_{dust}\right) [B_\nu(T_{cb}) - B_\nu(T)]. \qquad (5.5)$$

Here, we ignore the frequency dependence of the dust emissivity because the dust intensity is measured near the line frequency. Then, if the source temperature (T) is derived from the multi-line analysis, we obtain τ_{dust} at the continuum peak as below.

$$\tau_{dust} = -\ln\left\{\frac{I_{dust} - B_\nu(T)}{B_\nu(T_{cb}) - B_\nu(T)}\right\}. \qquad (5.6)$$

Here, if we assume that $B_\nu(T) \gg B_\nu(T_{cb})$,

$$\tau_{dust} \sim -\ln\left\{\frac{B_\nu(T) - I_{dust}}{B_\nu(T)}\right\}. \qquad (5.7)$$

Figure 5.5(b) shows the plot of the derived rotational temperatures along the envelope direction, where the colors represent the molecules: orange, green, yellow, and blue circles denote the rotation temperatures for HCOOH, NH_2CHO, CH_2DOH, and CH_3OH, respectively. The error bar is shown for each value, and the purple line represents the intensity profiles of the 1.2 mm continuum, whose brightness temperature is 141 K at its peak position. The intensity profiles of the molecular lines

along the envelope direction are shown in Figure 5.5(c), where those of HCOOH and NH$_2$CHO are more compact than the other two. Hence, we derive the rotation temperatures within the radius of 6 au (0."06) for all molecules, and even outside its radius for CH$_3$OH and CH$_2$DOH. The distribution of CH$_3$OH is more extended than those of any other molecules (Figure 5.2), and hence, we also calculate the temperatures for the positions of 16 au to the east and the west. The positions for deriving the temperature are shown in Figure 5.1, and the results are summarized in Tables 5.3 and 5.4. The errors are the fitting errors in the multi-line analysis.

5.4.1   An Implication of the Accretion Shock

First, we discuss a heating mechanism around the protostar, based on the derived rotation temperature. For all of these molecules, the rotation temperature is the highest at the continuum peak position, which is almost 193−215 K, and decreases as increasing the distance from the protostar. Such a high temperature toward the continuum peak is often seen in hot corino sources (e.g., Watanabe et al., 2017b; Oya & Yamamoto, 2020). The temperatures are 154−195 K at the positions of ±3 au (±0."03) for the four molecules. However, at the positions of ±6 au (±0."06), the temperatures are remarkably different among the molecules. While CH$_3$OH and CH$_2$DOH show the high temperature of 150-165 K in the south and north side, the temperatures of HCOOH and NH$_2$CHO are 75 and 112 K, respectively, significantly lower than them. These errors are listed in Table 5.3. Namely, the temperatures of HCOOH and NH$_2$CHO decrease more steeply as an increasing distance from the protostar than CH$_3$OH and CH$_2$DOH (Figure 5.5(a)). CH$_3$OH and CH$_2$DOH having an extended distribution show the high temperature even in the outer parts (Figure 5.5). The different temperature distributions suggest that the outer region is heated by some mechanisms other than the protostellar radiation.

On the other hand, the derived temperatures and the intensity profiles along the outflow direction are shown in Figure 5.6. The temperatures of NH$_2$CHO are as high as that of CH$_3$OH at the positions of ±3 au (±0."03). The particularly high temperature is derived for CH$_3$OH to be about 193±3 and 176±3 K on the western side (−3 and 6 au; −0."03 and −0."06, respectively), where the dust continuum shows a shoulder and the shock would be caused by the outflow impact as described in Section 5.3. In the eastern side, the temperature of CH$_3$OH is still as high as 134±4 K at 6 au. Comparing to these results for CH$_3$OH, the temperature of NH$_2$CHO is significantly lower at the position, which are 74±29 and 132±3 K in the east and west sides, respectively. Thus, the temperatures are different at ±6 au (±0."06) positions along the outflow direction as well as the envelope direction. Note that the intensities of the CH$_2$DOH lines are not strong enough in the outer region along the outflow direction. Hence, the derived temperatures have relatively large errors at the outer positions of ±10 au (±0."10) (Table 5.4).

Accretion shock can be a possible explanation for the difference of the rotation temperature at the positions of ±6 au. A similar idea is reported for the other source, IRAS 16293−2422 Source A, by Oya & Yamamoto (2020). They derived the rotation temperature of H$_2$CS along the disk/envelope system of IRAS 16293-2422 Source A. The flatten temperature profile within the radius of 50 au and the local

Table 5.3: Rotation Temperature and Column Density along the Envelope Direction[a]

		Temperature [K]							
Position	Offset (″)	HCOOH		NH$_2$CHO		CH$_2$DOH		CH$_3$OH	
Continuum peak	0	212	(0.4)	215	(8)	193	(11)	211	(3)
1	0.13	-	-	-	-	44	(4)	102	(0.2)
2	0.1	-	-	-	-	74	(3)	110	(5)
3	0.06	75	(7)	112	(15)	150	(21)	156	(7)
4	0.03	177	(8)	195	(5)	161	(3)	194	(9)
5	-0.03	155	(9)	159	(8)	154	(6)	176	(5)
6	-0.06	75	(2)	112	(5)	165	(27)	160	(5)
7	-0.1	-	-	-	-	127	(13)	136	(9)
8	-0.13	-	-	-	-	65	(5)	110	(13)

		Column density [10^{18} cm^{-2}]							
Position	Offset (″)	HCOOH		NH$_2$CHO		CH$_2$DOH		CH$_3$OH	
Continuum peak	0	2.2	(0.6)	0.18	(0.05)	2.5	(1.4)	8.5	(2)
1	0.13	-	-	-	-	1.2	(0.9)	1.6	(0.01)
2	0.1	-	-	-	-	0.67	(0.15)	4.6	(1)
3	0.06	0.17	(0.09)	0.17	(0.07)	0.89	(0.07)	7.9	(2.5)
4	0.03	3.4	(2.1)	0.31	(0.03)	2.5	(0.1)	17	(9)
5	-0.03	5.1	(9.5)	0.37	(0.09)	2.2	(0.3)	16	(7)
6	-0.06	4.1	(0.9)	0.17	(0.02)	1.1	(0.09)	8.6	(1.9)
7	-0.1	-	-	-	-	0.83	(0.15)	4.8	(1.6)
8	-0.13	-	-	-	-	0.49	(0.35)	2.4	(1.8)

[a] The derived rotation temperatures and the column densities derived from multiline analysis. The quoted error is the fitting error. The envelope direction and the position numbers are shown in Figure 5.1.

Table 5.4: Rotation Temperature and Column Density along the Outflow Direction[a]

		Temperature [K]							
Position	Offset (″)	HCOOH		NH$_2$CHO		CH$_2$DOH		CH$_3$OH	
Continuum peak	0	212	(0.4)	215	(8)	193	(11)	211	(3)
9	0.16	-	-	-	-	-	-	118	(10)
10	0.13	-	-	-	-	-	-	119	(5)
11	0.1	-	-	-	-	-	-	87	(5)
12	0.06	-	-	74	(29)	124	(17)	134	(4)
13	0.03	139	(10)	166	(1.5)	137	(10)	159	(9)
14	-0.03	166	(7.4)	173	(6)	143	(8)	193	(3)
15	-0.06	114	(6)	132	(3)	110	(5)	176	(3)
16	-0.1	-	-	-	-	94	(6)	128	(5)
17	-0.13	-	-	-	-	109	(12)	104	(3)
18	-0.16	-	-	-	-	-	-	115	(14)

		Column density [10^{18} cm^{-2}]							
Position	Offset (″)	HCOOH		NH$_2$CHO		CH$_2$DOH		CH$_3$OH	
Continuum peak	0	2.2	(0.6)	0.18	(0.05)	2.5	(1.4)	8.5	(2)
9	0.16	-	-	-	-	-	-	0.32	(0.04)
10	0.13	-	-	-	-	-	-	0.42	(0.03)
11	0.1	-	-	-	-	-	-	5.8	(2.1)
12	0.06	-	-	0.035	(0.05)	0.5	(0.04)	7.6	(2.1)
13	0.03	3.1	(2.2)	0.14	(0.004)	0.83	(0.07)	9.1	(4.7)
14	-0.03	1.2	(1.8)	0.34	(0.04)	1.8	(0.3)	11	(1.1)
15	-0.06	3.5	(2.4)	0.22	(0.16)	1.3	(0.2)	10	(1.3)
16	-0.1	-	-	-	-	0.47	(0.03)	4.5	(0.8)
17	-0.13	-	-	-	-	0.21	(0.02)	3.6	(0.6)
18	-0.16	-	-	-	-	-	-	0.5	(0.09)

[a] The derived rotation temperatures and the column densities derived from multiline analysis. The quoted error is the fitting error. The envelope direction and the position numbers are shown in Figure 5.1.

steep rise around 50 au cannot be explained by only the radiation heating by the central protostar (A1), and hence, they suggest the accretion shock as another heating mechanism. Oya & Yamamoto (2020) also propose that if the inside and outside

of the disk/envelope system are heated by the protostar radiation and the accreting gas, respectively, the temperature profile as a function of the distance from the protostar would show a local minimum between the inner and outer regions (Figure 5.5(a)), which will result in the ring-like structure of an enhanced temperature region surrounding the disk structure. This is also indicated by the model study reported in Fateeva et al. (2011). In our observation, the ring-like structure is not observed because the disk/envelope system is almost edge-on. However, the derived temperatures depend on the molecules at ±6 au, where the compact distributed HCOOH and NH_2CHO lines show the relatively lower temperatures, suggesting the temperature decrease around the boundary between the inner and outer regions. This picture is further supported by the fact that the CH_3OH temperatures in the outside of 10 au are higher than 100 K despite a weak dust emission.

Thus, our results suggest the accretion shock heating occurs at the radius of 6 au or larger. It should be noted that the HCOOH and NH_2CHO lines cannot be seen in the outer region despite the high temperature. They do not seem to appear in the gas phase through simple evaporation from dust grains. We discuss this point in detail in Chapter 9.
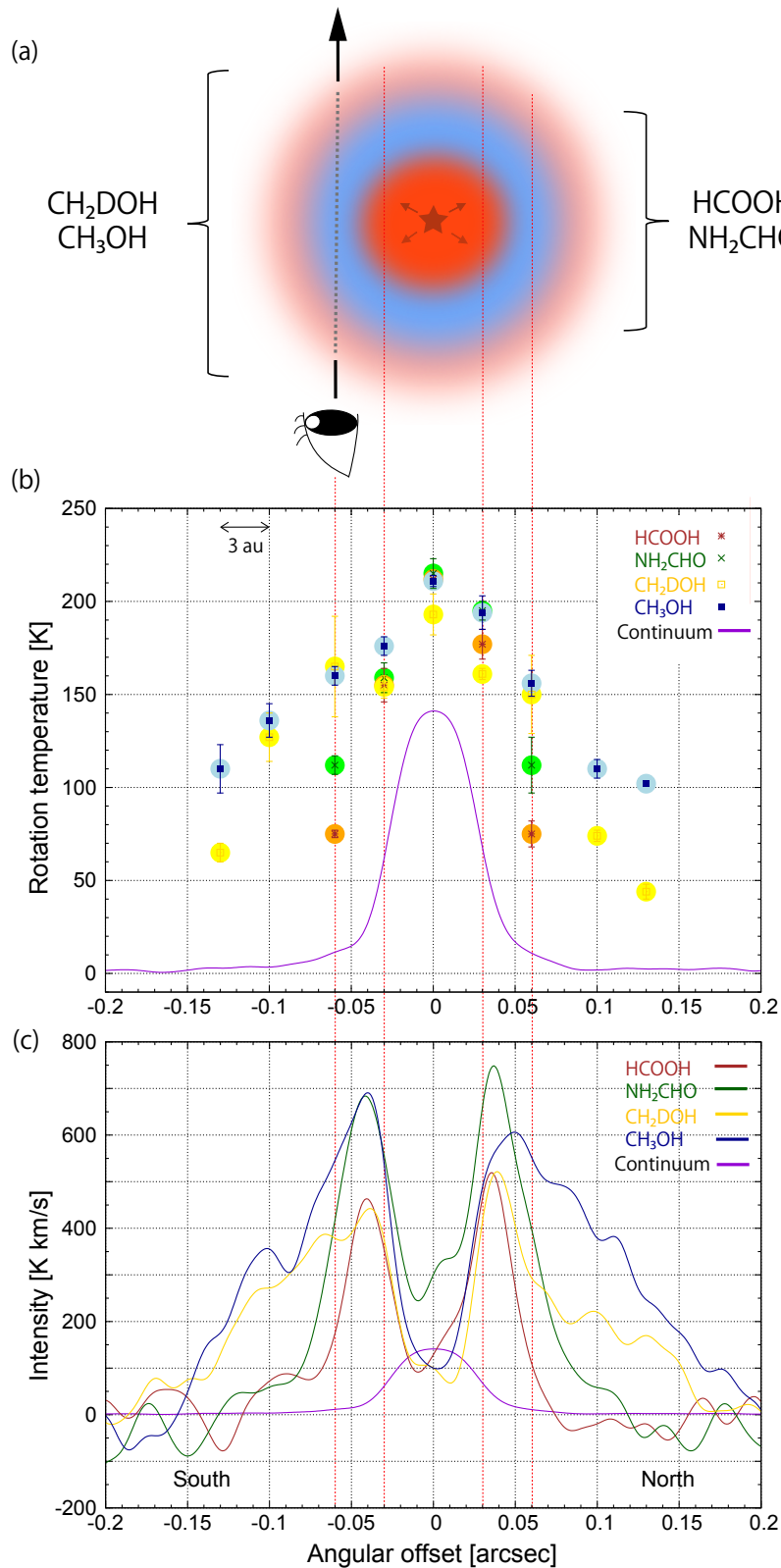
Figure 5.5: (a) Schematic illustration of the disk/envelope system. Accretion shock by an infalling gas raises the temperature of the outer part. (b) Rotation temperature distribution along the envelope direction. The quoted errors are the fitting error of the multi-line analysis. (c) Intensity profiles of the molecular lines presented in Figure 5.1 along the envelope direction.
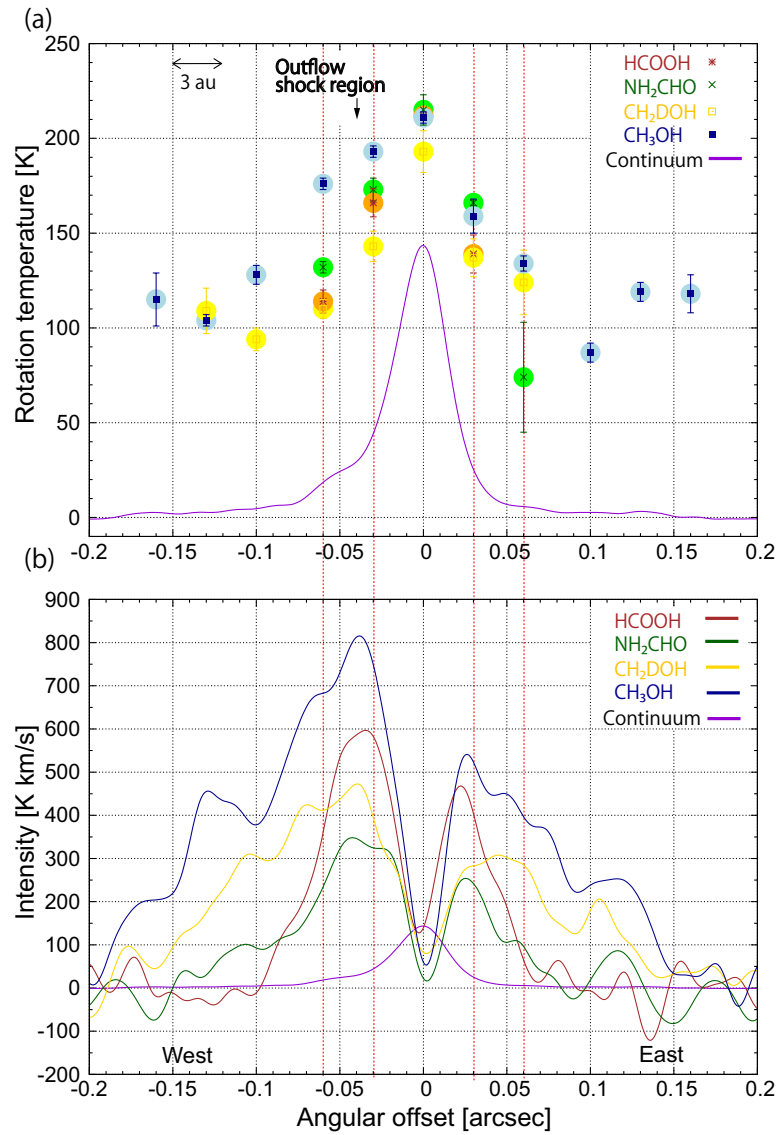
Figure 5.6: (a) Rotation temperature distribution along the outflow direction. The quoted errors are the fitting error of the multi-line analysis. (b) Intensity profiles of the molecular lines presented in Figure 5.1 along the outflow direction.

5.4.2 Abundances of the Molecules

The column densities along the envelope and outflow directions are plotted in Figure 5.7 and 5.8, respectively. These values are listed in Tables 5.3 and 5.4. The errors are the fitting errors in the multi-line analysis. In Figure 5.7 (envelope direction), the column densities of CH_3OH, CH_2DOH, and NH_2CHO are high at ± 3 au and decrease outside it. In contrast, the column density of HCOOH is not changed largely within 6 au, although that at -3au has a large error. For the outflow direction, the molecules tend to be enhanced at the positions of -3 and -6 au, which correspond to the outflow shocked region on the west side (Figure 5.8). Particularly NH_2CHO is the most abundant at -3 au. For both directions, CH_3OH is the most abundant, whose column density is as high as $\sim 1.5 \times 10^{19}$ cm^{-2}. The abundance of CH_3OH at the continuum peak is slightly higher than that reported by Bjerkeli et al. (2019) (6.8×10^{18}). They assume optically thin condition for CH_3OH as well as the LTE, and hence, this would be the reason for the slight difference.
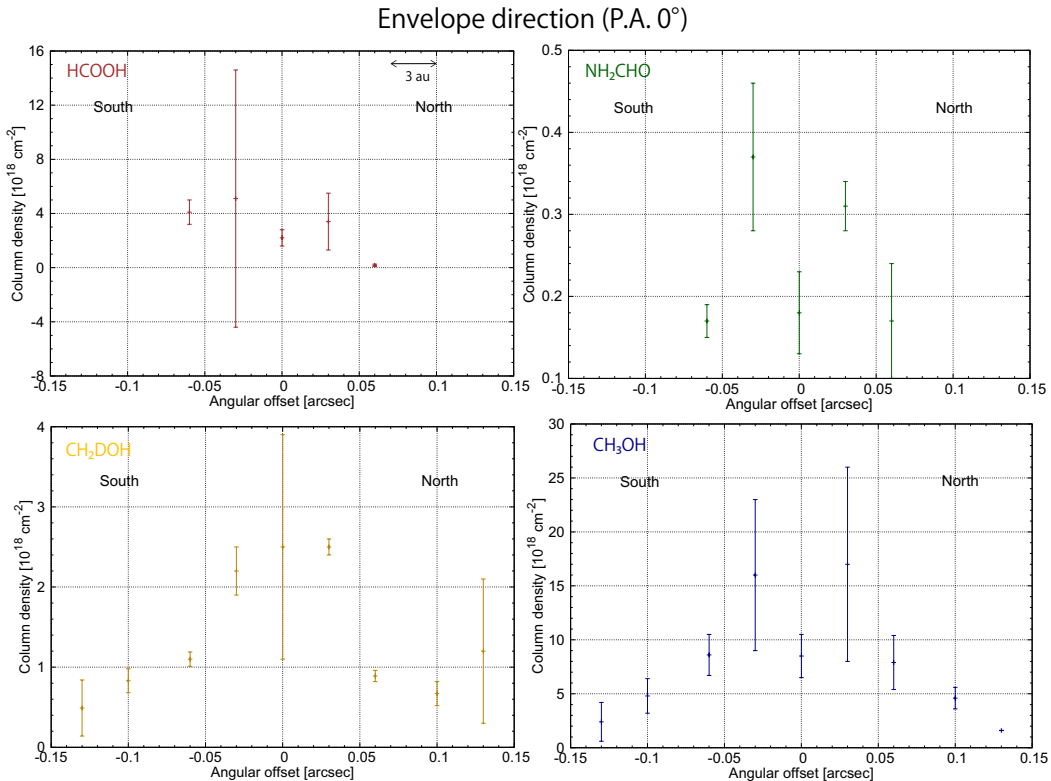
Figure 5.7: Column densities of HCOOH (a), NH_2CHO(b), CH_2DOH(c), and CH_3OH(d) along the envelope direction.

We here compare the observed column densities with those of the other protostellar sources (Table 5.5). Jacobsen et al. (2019) report the column densities of NH_2CHO and CH_2DOH at a few 10 au scale around the low-mass Class 0 protostellar source, L483, under the assumption of the LTE at the temperature of 100 K to be 1.0×10^{16} cm^{-2} and 4.0×10^{17} cm^{-2}, respectively. On the other hand, van Gelder et al. (2020) estimate the column densities of HCOOH, CH_3OH, and CH_2DOH for the low-mass protostars, B1-c and S68N, at a few 100 au scale to be $\sim 10^{14}$, $\sim 10^{18}$, and $\sim 10^{16}$–10^{17} cm^{-2}, respectively, where the LTE condition at the temperature
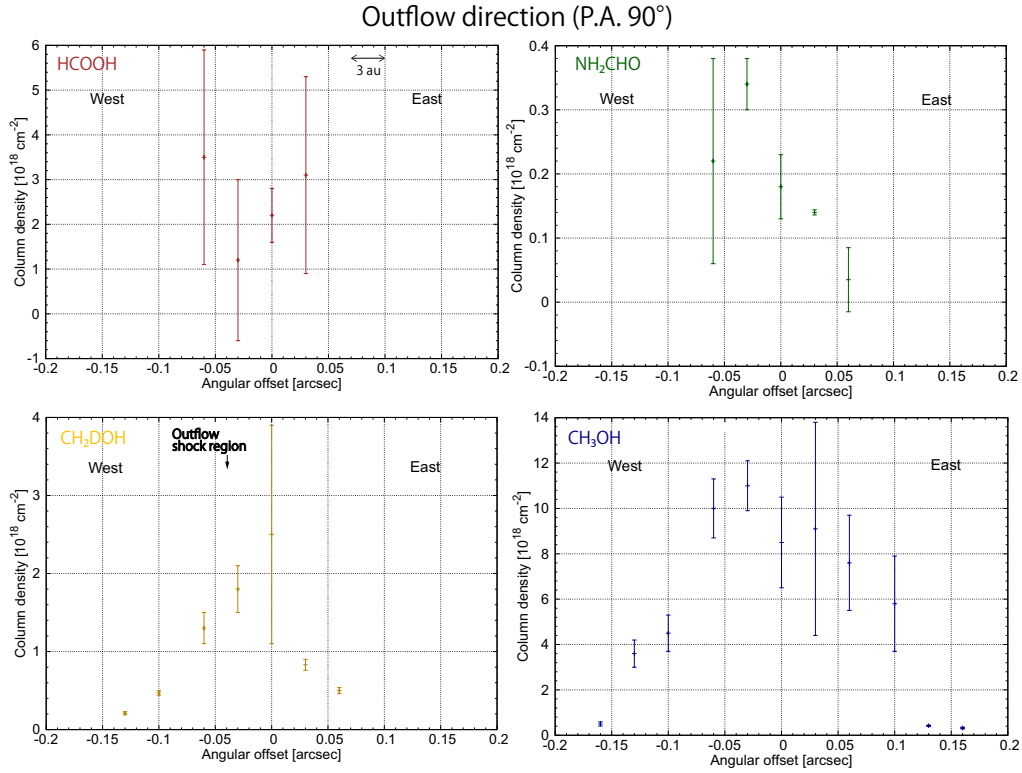
Figure 5.8: Column densities of HCOOH (a), NH$_2$CHO(b), CH$_2$DOH(c), and CH$_3$OH(d) along the outflow direction.
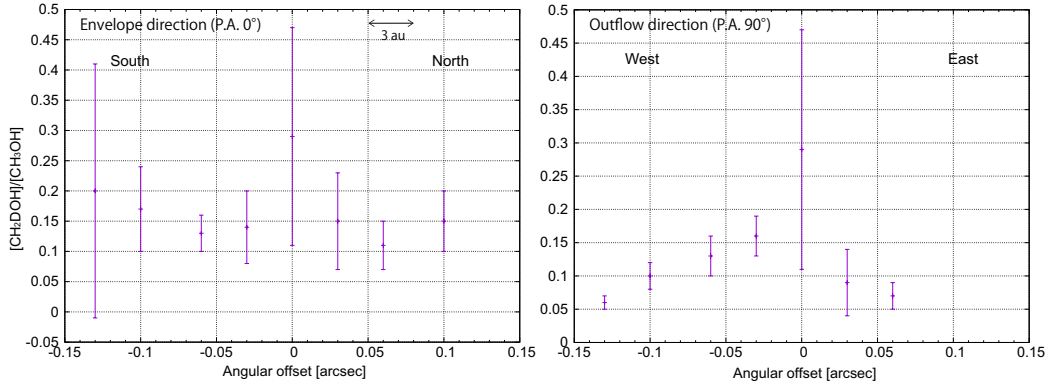
Figure 5.9: The ratios of the column densities of of CH$_2$DOH relative to that of CH$_3$OH along the envelope direction (a) and the outflow direction (b).

of 200 K is assumed. For the Class 0 protostar, IRAS 16293-2422 Source B, the ALMA spectral line survey was conducted at a 100 au scale (Jørgensen et al., 2018). The column densities of CH$_2$DOH and HCOOH are 7.1×10^{17} cm^{-2} and 5.6×10^{16} cm^{-2}, respectively. For fair comparison, we calculate the fractional abundances of HCOOH, NH$_2$CHO, and CH$_2$DOH relative to CH$_3$OH toward the protostar (Table 5.5). The fractional abundances of the above three species relative to CH$_3$OH for these sources are generally much lower than those for B335. We find that they are rich in B335. However, we need to recognize that the spatial resolutions are different. The lower abundances of HCOOH, NH$_2$CHO, and CH$_2$DOH for the other sources would originate from their beam dilution effect, if the distributions of the

three species are more compact than that of CH_3OH. In this case, the abundances of HCOOH, NH_2CHO, and CH_2DOH are underestimated. The fractional abundance of NH_2CHO in B335 is comparable to that in the high-mass protostellar source, G328.2551-0.5321 at a resolution of ~ 500 au (Csengeri et al., 2019), while HCOOH is more abundant in B335. These may imply the diversity of the chemical composition in hot corinos and hot cores.

Table 5.5: Column Densities and Fractional Abundances Relative to CH_3OH toward Protostar Positions

Source	Column density (10^{18} cm^{-2})					
	B335[a]	L483[b]	B1-c[c]	S68N[c]	IRAS 16293 B[d]	G328.2551-0.5321[e]
CH_3OH	8.5	17	1.9	1.4	10	4.1
	(2)	(3.4)	(0.6)	(0.6)	(2)	-
HCOOH	2.2	-	7.00×10^{-4}	9.10×10^{-4}	5.60×10^{-2}	1.37×10^{-2}
	(0.6)	-	(2.0×10^{-4})	(2.1×10^{-4})	(1.12×10^{-2})	(-)
NH_2CHO	0.18	0.01	-	-	-	0.042
	(0.05)	(0.002)	-	-	-	(-)
CH_2DOH	2.5	0.4	0.16	0.060	0.71	-
	(1)	(0.08)	(0.01)	(0.007)	(0.1)	-
Source	Fractional abundances relative to CH_3OH					
	B335[a]	L483[b]	B1-c[c]	S68N[c]	IRAS 16293 B[d]	G328.2551-0.5321[e]
[HCOOH]/[CH_3OH]	0.26	-	3.7×10^{-4}	6.5×10^{-4}	5.6×10^{-3}	3.3×10^{-3}
	(0.09)	-	(2.0×10^{-4})	(3.0×10^{-4})	(2.0×10^{-3})	-
[NH_2CHO]/[CH_3OH]	0.02	5.9×10^{-4}	-	-	-	0.01
	(0.01)	(2×10^{-4})	-	-	-	(-)
[CH_2DOH]/[CH_3OH]	0.29	0.024	0.084	0.043	0.071	-
	(0.2)	(0.007)	(0.03)	(0.02)	(0.02)	-
Resolution	$\sim$3 au	$\sim$50 au	$\sim$100-200 au		$\sim$60 au	$\sim$500 au

[a] Work in this chapter. [b] Jacobsen et al. (2019). [c] B1-c in the Perseus Barnard 1 cloud and Serpens S68N (van Gelder et al., 2020). [d] IRAS 16293-2422 Souce B (Jørgensen et al., 2018). [e] These values are derived for the protostellar envelope (Csengeri et al., 2019). The number in the parenthesis shows the uncertainty.

Furthermore, we derive the ratios of the column density of CH_2DOH to that of CH_3OH in B335. Figure 5.9 shows the ratios along the envelope direction and the outflow direction. For the envelope direction, it seems that the ratios do not vary significantly among the positions and are almost 0.15. For the outflow direction, it seems to be enhanced slightly at the outflow shocked region (-3 and -6 au). This result suggests that the ratio might be affected by the outflow shock.

CH_3OH and CH_2DOH are formed on ice mantle of dust grains in the cold prestellar phase, and are liberated into the gas phase in the hot region ($T > 100$ K) after onset of star formation. The constant ratio means that further chemical processes changing the deuterium fractionation to be lower do not work even at the high temperature of 100-200 K for this source. As a result, the ratio is conserved. Since the timescale for the gas phase reaction is 10^4–10^5 yr, the constant ratio would be related to the youth of the B335 protostar ($t_{\mathrm{dyn}} \sim 10^4$ yr; Yıldız et al., 2015). In this context, a slight enhancement of the ratio at the outflow shocked region is puzzling.

The observed CH_2DOH/CH_3OH ratio seems higher than those reported for other low-mass protostars measured on larger scales, where the ratio is almost below 0.1 (Taquet et al., 2019; van Gelder et al., 2020). The ratio is also lower at a 100 au

scale. In IRAS 16293–2422 Source B, it is reported to be 0.07 in Jørgensen et al. (2018). However, such comparison is not fair because these spatial resolutions are different among observations. The systematic observation is needed to compare between sources. Nevertheless, we note that CHD_2OH and CH_3OD are detected in our observations (See Chapter 8), and hence, the deuterated fractionation must be high in B335.

5.5 Summary

1. We have detected the HCOOH, NH_2CHO, CH_2DOH, and CH_3OH line emission in the low-mass Class 0 protostellar source B335 with ALMA at a high angular resolution of ~3 au. Although all of them show a round distribution around the continuum peak position, the HCOOH and NH_2CHO distributions are more compact.

2. We derive the rotation temperatures under the assumption of LTE condition by using the molecular lines. For the envelope direction, the temperatures at the radius of 6 au of CH_3OH and CH_2DOH (150-165 K) are found to be higher than those of HCOOH and NH_2CHO (75 and 112 K, respectively). We propose the accretion shock as the mechanism heating the outer envelope, based on the temperature distribution.

3. The compact distributions of HCOOH and NH_2CHO raise an important question on their formation mechanism. These molecules are not observed in the outer region where the temperature is higher than the evaporation temperature of ice mantle (>100 K). This result implies that they are not simply supplied by ice mantle evaporation in the central part (See also Chapter 9).

4. The fractional abundances of HCOOH, NH_2CHO, CH_2DOH relative to CH_3OH are higher than those in other low-mass protostars. HCOOH is particularly abundant, which is even higher than in the high-mass protostellar source, G328.2551-0.5321. The deuterated fractionation also seems to be higher in B335. The ratio of the column densities of CH_3OH and CH_2DOH is almost constant around the protostar, and does not depend on the rotation temperature. This may be related to the youth of the B335 protostar.

Part II

Chemical Structure

Chapter 6
Principal Component Analysis (PCA)

Molecular-line distributions reflect the chemical structures and the physical condition, and hence, they are different from molecule to molecule and even from transition to transition as seen in our observational results in Part I as well as the previous reports (e.g., Sakai et al., 2014a; Oya et al., 2016, 2017, 2019; Lee et al., 2017; Jacobsen et al., 2019). It is thus suggested that the molecular-line distributions can be used as a useful tool to study physical and chemical evolutionary processes of disk formation in protostellar sources. Recently, sensitive observations with a broad instantaneous bandwidth become popular in various radio telescopes including ALMA, so that many molecular lines can be observed at a single observation. This situation enables us to obtain rich information on chemical composition as well as physical structures. On the other hand, it takes huge efforts to characterize the distributions of all the observed lines in a one-by-one way (e.g., Jørgensen et al., 2016; Imai et al., 2016; Watanabe et al., 2017a). For this reason, physical and chemical structures are often explored by using only a few arbitrarily selected lines, where interpretations could be biased by the selection. To make a full use of the observed lines without any preconception, introduction of sophisticated-analysis process is essential. Hence, we introduce Principal Component Analysis (PCA) for observed molecular-line data. The fundamental basis of PCA and the method to evaluate the noise effect are described in this chapter.

6.1 Principal Component Analysis (PCA) Using a Correlation Matrix

Suppose that x_j is the observed molecular-line data, and we look for the functions $\mathbf{z}_i$ called as the principal component (PC) formed by a linear combination of the data x_j, where the i th function is uncorrelated with all the others.

   As a simple example, PCA for the two molecular-line distributions (Moment 0 maps) is shown here. Figure 6.1 shows the moment 0 maps of the CCH (N =4−3, J =7/2−5/2, F =4-3 and 3−2) and H_2CO ($5_{2,4}$−$4_{2,3}$) lines near the protostar, IRAS 15398−3359, whose observations are described in Chapter 3. Now, x_1 and x_2 are the vector for the distributions of the CCH (N =4−3, J =7/2−5/2, F =4-3 and 3−2)

and H_2CO ($5_{2,4}$–$4_{2,3}$) lines, respectively. Note that we need to make the beam size uniform before performing PCA, and we here select 0.5″. We set it with a gaussian kernel by using *imsmooth*, which is the task of the Common Astronomy Software Applications package (CASA) (McMullin et al., 2007).
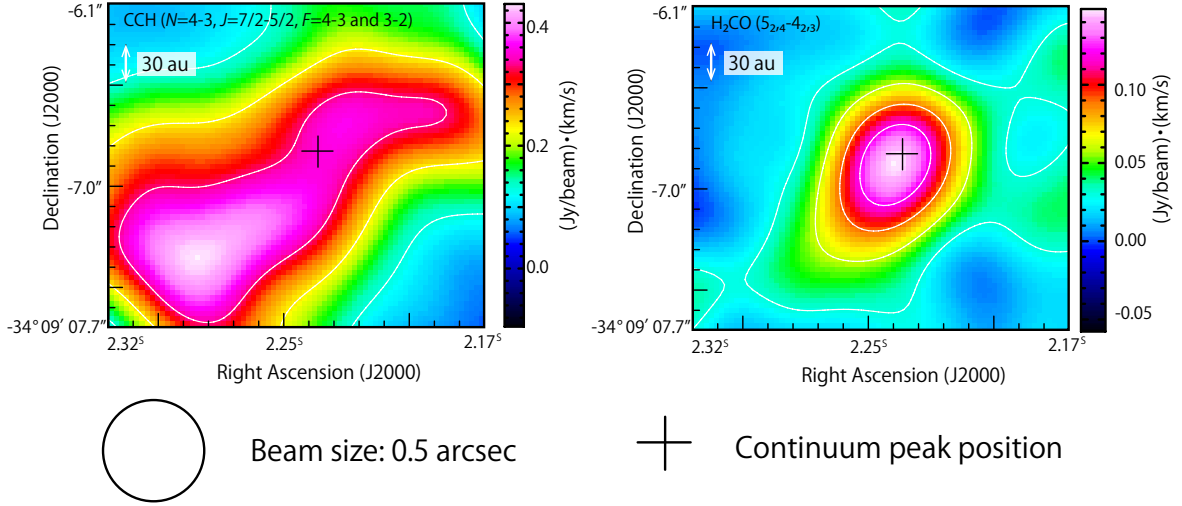
Figure 6.1: Moment 0 maps of the CCH (N =4–3, J =7/2–5/2, F =4-3 and 3–2) and H_2CO ($5_{2,4}$–$4_{2,3}$) lines near the protostar at the left and right, respectively. The beam sizes are set to be 0.5″, which is shown in the lower-left circle. The plus marks represent the continuum peak position.

We conduct PCA in this thesis by using a correlation matrix among the observed molecular-line intensities:

$$r_{jj'} = \frac{\sum\limits_{p,q} (x_j(p,q) - \bar{x}_j)(x_{j'}(p,q) - \bar{x}_{j'})}{s_j s_{j'}}, \tag{6.1}$$

where p and q are the coordinates of the image, $\bar{x}_j$ the average of $x_j(p,q)$, and s_j the variance of $x_j(p,q)$. PC_i (the functions $\mathbf{z}_i$) are obtained by diagonalizing the correlation matrix. In the calculation of the correlation coefficients between two intensity distributions, the data above three times the rms noise level ($3\sigma_j$) for the both distributions are used as a threshold. In Figure 6.2, the data surrounded by the yellow box are used to evaluate the correlation of the two molecular lines, where the dashed lines represent three times the rms noise levels of the observational data.

Use of the correlation matrix means that the average of the original data is shifted to zero, and the distribution is normalized by the variance because the intensity depend on each molecular line. Hence, the distributions for PCs, $\mathbf{y}$ is written as:

$$\mathbf{y} = \mathbf{A}\mathbf{x}^*, \tag{6.2}$$

where $\mathbf{A}$ is the transformation matrix for the diagonalization of the correlation matrix and $\mathbf{x}^*$ the normalized distribution. This normalization can take off the effect of the weight for each molecular line. The jth vector of $\mathbf{x}^*$ is related to the original

distribution as:

$$x_j^* = (x_j - \overline{x_j})/s_j^{1/2}. \tag{6.3}$$

The second term of Equation (2), $\overline{x_j}/s_j^{1/2}$, just provides the offset on the distribution, and does not affect the distribution of PCs. Hence, we omit this term in the presentation of PCs. This allows us to display PCs compatible with the images of the original distribution. Here, the eigenvalues λ_i of i th PC are also derived, which represent the variance for the corresponding PCs. It is worth nothing that the intensity of PCi is dimensionless.

In the case of the above two molecular-line distribution, the correlation matrix $\mathbf{C}$ is derived as:

$$\mathbf{C} = \begin{pmatrix} 1.00 & 0.12 \\ 0.12 & 1.00 \end{pmatrix}. \tag{6.4}$$

The eigenvector $\mathbf{z}_1$ is determined as having the largest variance (PC1), and $\mathbf{z}_2$ is to be the orthogonal axis without the correlation for PC1, showing the second largest variance. $\mathbf{z}_i$ are derived as:

$$\mathbf{z_1} = \begin{pmatrix} 0.71 \\ -0.71 \end{pmatrix} \tag{6.5}$$

$$\mathbf{z_2} = \begin{pmatrix} -0.71 \\ 0.71 \end{pmatrix}. \tag{6.6}$$

Orthogonality of PCs is guaranteed because the correlation matrix is a symmetric matrix. The distributions of PC$_i$ (y_i) are shown in Figure 6.3. They have the opposite intensity distribution to each other, and represent the extended distribution showing the double peak and the compact distribution around the continuum peak. These features resemble the distributions of CCH and H_2CO because the two distributions are almost uncorrelated. Thus, the main features can be extracted from the observed data set. In the case of the multidimensional data set, PCA can be used as a data reduction tool through essentially the same process as this example.

A contribution ratio (p) of each principal component can be calculated by dividing the eigenvalue λ_i by the dimension of the matrix. It represents how much PCi contributes to all the original distributions:

$$p_i = \frac{\lambda_i}{\sum\limits_{n=1}^{N} \lambda_i} = \frac{\lambda_i}{N}. \tag{6.7}$$

Here, N is the number of the data. If $p_i << \frac{1}{N}$ would almost represent noise. The values for the example are shown in Table 6.1. To perform the above procedure, we write the code by using python libraries, *numpy*, *matplotlib*, *pandas*, and *astropy*.

Table 6.1: . PCA for the CCH and H_2CO Lines

PC ($\mathbf{z}_i$)	λ_i (eigenvalue)	p_i (contribution ratio) (%)
PC1	1.483	74.1
PC2	0.517	25.9
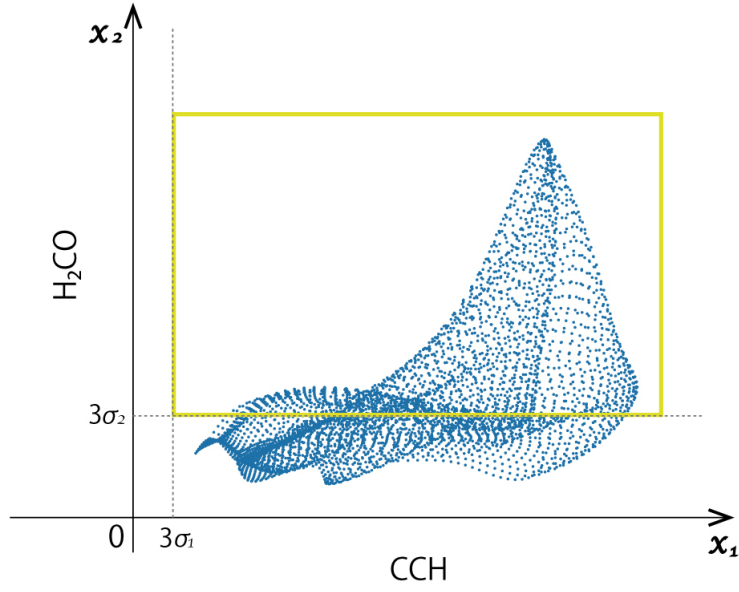
Figure 6.2: Correlations between the distributions of CCH and H_2CO. The dashed lines show three times each rms noise level. The data surrounded by the yellow box are used for PCA.
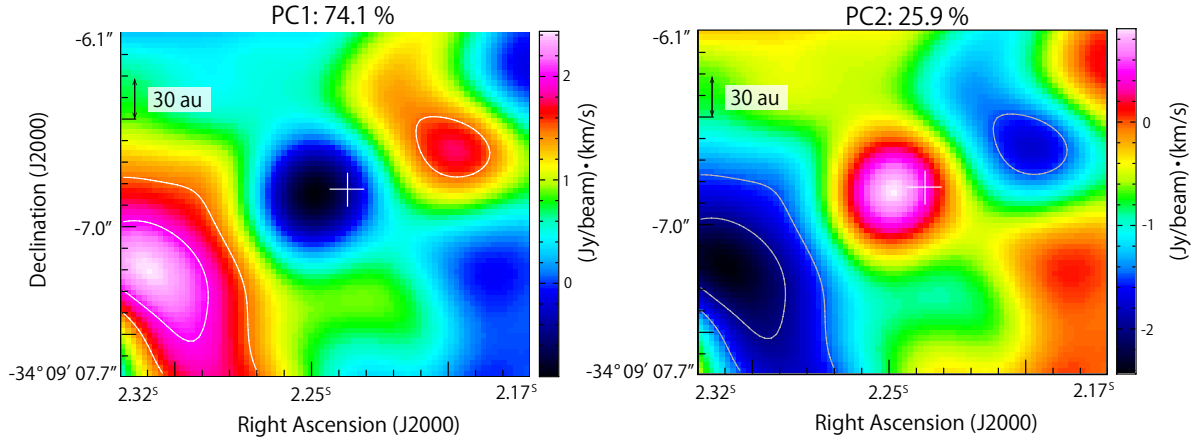
Figure 6.3: Distributions of PC1 and PC2 at the left and right, respectively. The plus marks represent the continuum peak position. Note that the color scale is different between the two panels.

6.2 Correlation Coefficients of the Principal Components to the Molecular Distributions

We calculate the correlation coefficients between the principal components and the molecular distributions. They help us to understand which molecular line distributions the principal component contributes to. The correlation coefficient can be calculated as (Jolliffe, 1986):

$$Cor(x_j^*, y_i) = \sqrt{\lambda_i} z_{ji}, \tag{6.8}$$

where λ_i is the eigenvalue for the PC_i, y_i the distribution for the i th principal component, and z_{ji} the i th eigenvector component for the j th emission.

6.3   Standard Deviation of the PCA Components

We consider the effect of the noise in PCA. We conduct it for cube data (PCA-3D), moment 0 maps (PCA-2D), and spectral line profiles (PCA-1D). The standard deviation for the principal component value of each molecular line (Gratier et al., 2017; Spezzano et al., 2017; Okoda et al., 2020) for each PCA are obtained as follows. As for PCA-3D and PCA-2D, we generate the Gaussian random noise for each image pixel and each velocity channel of the molecular-line data. The noise distribution is convolved by the beam size of the molecular lines, where the noise level corresponds to 1σ noise level of each image. As for PCA-1D, the Gaussian random noise is prepared for each channel of the molecular-line data. We add these artificial noises to the original data for each molecular line and conduct PCA. This procedure is repeated 1000 times, and we finally calculate the standard deviations of the PC values. We also calculate the standard deviations for the correlation coefficients between the molecular lines and the principal components by using each eigenvalue and each eigenvector value as :

$$\delta Cor(x_j^*, y_i) = Cor(x_j^*, y_i)\sqrt{\left(\frac{\delta\lambda_i}{2\lambda_i}\right)^2 + \left(\frac{\delta z_{ji}}{z_{ji}}\right)^2}, \qquad (6.9)$$

where $Cor(x_j^*, y_i)$ is described above). $\delta\lambda_i$ and δz_{ji} are the standard deviations of λ_i and z_{ji}, respectively.

Chapter 7
PCA for the Moment 0 Maps:
IRAS 15398−3359[*]

We first perform the principal component analysis for 15 molecular-line distributions and one continuum image (PCA-2D) on the two different scales, the outflow and the disk/envelope structure, of the low-mass Class 0 protostar IRAS 15398−3359. A PCA successfully classifies the molecular-line distributions into a few groups. An effect of the excitation condition is revealed by the PCA for the H_2CO (K_a =0,1,2, and 3) lines in the disk/envelope scale. Thus, we find that PCA is effective to extract the characteristic feature of the molecular line distributions around the protostar in an unbiased way. As well, our analyses for two scales indicate that the results of the PCA depend on the field range which we select. In the PCA for the whole structure (outflow) scale, a few blobs in the outflow structure are identified, and the gas temperature there is studied by the multi-line analysis of with the H_2CO lines. The result suggests that the blobs are found by shocks due to the local impact of the outflow on clumps of the ambient gas.

7.1 Introduction

A principal component analysis (PCA) is a powerful method to characterize the distributions comprehensively (Jolliffe, 1986). This method has sometimes been used for radio astronomical observations of molecular lines. It was conducted for large-scale observation data of external galaxies and galactic molecular clouds (e.g., Ungerechts et al., 1997; Meier & Turner, 2005; Watanabe et al., 2016). Spezzano et al. (2017) used this method to investigate the chemical structure of the L1544 starless core and successfully highlighted four characteristic distributions, as described in Chapter 1. Thus, it is now important to apply this method to various sources including protostellar sources.

We conduct a PCA for the two scales of a very low-mass Class 0 protostar IRAS 15398−3359 to explore similarities and differences of molecular-line distributions in an unbiased way. In this protostellar source, various molecular lines are detected with ALMA in its Cycle 2 and Cycle 3 observations (Table 7.1) and are used for the PCA. As for the continuum data, we use only the Cycle 3 data in this analysis. The signal-to-noise ratio for the Cycle 2 continuum data is lower than that of the Cycle

---

[*]The content of this chapter is published as: Okoda et al. 2020, ApJ, 900, 40

3 continuum data, and hence, this is excluded. Thus, we use 16 dimension dataset which consists of 15 molecular line data and the Cycle 3 continuum data for the whole structure. For the disk/envelope structure, we exclude c-C_3H_2 ($9_{1,8}-8_{2,7}$ and $9_{2,8}-8_{1,7}$) because there are not enough data above the threshold level defined in Section 6.1 for this line.

7.2　Observation

The ALMA observations were carried out toward IRAS 15398−3359 in the Cycle 2 and Cycle 3 operations. The details of the Cycle 2 observation are described in Section 3.2. Hence, major points for the Cycle 3 observation are summarized below.

The Cycle 3 observation was conducted on 2016 March 31. Spectral lines of H_2CO, c-C_3H_2, CCH, CH_3OH, and DCN listed in Table 7.1 were observed in the frequency range from 349 to 365 GHz with the Band 7 receiver. Forty-two antennas were used in the observations, where the baseline length ranged from 14.70 to 452.72 m. The field center was (α_{2000}, δ_{2000})= ($15^h43^m02^s.242$, $-34°09'06.''70$), which was the same as that of the Cycle 2 observation. The total on-source time was 19.30 minutes. The primary beam (half-power beam) width was 17.''08. The backend correlator for molecular line observations except for the DCN observation was set to a resolution of 122 kHz and a bandwidth of 59 MHz, and that for the DCN observation was set to a resolution of 977 kHz and a bandwidth of 938 MHz. It should be noted that the velocity of all spectral windows is blue-shifted by 2.5 km s^{-1} due to the fault in the observation setting. Hence, we do not discuss the velocity structures and only focus on the distribution of the molecules. The original synthesized beam size of the continuum image is 0.''48×0.''45 (P.A. 83°), while those of the lines are summarized in Table 7.1.

Images were prepared by using the CLEAN algorithm, where the Briggs' weighting with a robustness parameter of 0.5 was employed. The continuum image was obtained by averaging line-free channels, and the line images were obtained after subtracting the continuum component directly from the visibilities. Self-calibration was not applied in this study, because the continuum emission is not bright enough. Since these largest angular sizes are 2.''5 for both of these observations, the intensities of the structures extended more than that size could be resolved-out.

Table 7.1: Parameters of Observed Lines [a]

Band [b]	Molecule	Transition	Frequency (GHz)	$S\mu^2$ (D^2)	$E_u k^{-1}$ (K)	Original beam size	σ (mJy beam^{-1})
6	CCH	$N=3-2$, $J=7/2-5/2$, $F=4-3$	262.0042600^c	2.3	25	$0.''22 \times 0.''16$ (P.A. 60°)	4
		$N=3-2$, $J=7/2-5/2$, $F=3-2$	262.0064820^c	1.7	25		4
6	SO	$J_N=7_6-6_5$	261.8437210	16.4	47	$0.''22 \times 0.''16$ (P.A. 55°)	4
6	CS	$5-4$	244.9355565	19.2	35	$0.''24 \times 0.''17$ (P.A. 60°)	4
7	H$_2$CO	$5_{0,5}-4_{0,4}$	362.7360480	27.2	52	$0.''48 \times 0.''46$ (P.A. 72°)	9
		$5_{1,5}-4_{1,4}$	351.7686450	78.3	62	$0.''50 \times 0.''47$ (P.A. 78°)	10
		$5_{2,4}-4_{2,3}$	363.9458940	22.8	100	$0.''48 \times 0.''45$ (P.A. 77°)	10
		$5_{3,2}-4_{3,1}$	364.2888840	52.2	158	$0.''48 \times 0.''45$ (P.A. 78°)	9
		$5_{3,3}-4_{3,2}$	364.2751410	52.2	158	$0.''48 \times 0.''45$ (P.A. 78°)	8
7	c-C$_3$H$_2$	$9_{1,8}-8_{2,7}$	351.9659690^c	238	93	$0.''50 \times 0.''47$ (P.A. 79°)	8
		$9_{2,8}-8_{1,7}$	351.9659690^c	79.3	93		
		$10_{0,10}-9_{1,9}$	351.7815780^c	101	96	$0.''50 \times 0.''47$ (P.A. 78°)	8
		$10_{1,10}-9_{0,9}$	351.7815780^c	303	96		
7	CCH	$N=4-3$, $J=9/2-7/2$, $F=5-4$	349.3377056^c	2.90	42	$0.''50 \times 0.''47$ (P.A. 78°)	9
		$N=4-3$, $J=9/2-7/2$, $F=4-3$	349.3389882^c	2.32	42		
		$N=4-3$, $J=7/2-5/2$, $F=4-3$	349.3992756^c	2.27	42	$0.''50 \times 0.''47$ (P.A. 78°)	9
		$N=4-3$, $J=7/2-5/2$, $F=3-2$	349.4006712^c	1.69	42		
		$N=4-3$, $J=7/2-5/2$, $F=3-3$	349.4146425	0.099	42	$0.''50 \times 0.''47$ (P.A. 78°)	8
7	CH$_3$OH	$4_{0,4}-3_{1,3}$ E	350.6876620	6.22	36	$0.''50 \times 0.''47$ (P.A. 45°)	8
7	DCN	$5-4$	362.0457535	134	52	$0.''48 \times 0.''46$ (P.A. 71°)	5

[a] Line parameters are taken from CDMS (Endres et al., 2016). The rms and the beam size are based on the observation data.
[b] ALMA receiver band. Band 6 observation was carried out in Cycle 2, while the Band 7 in Cycle 3.
[c] Blended

7.3 Data for PCA

In order to compare the molecular distributions at the same spatial resolution, the beam size was set to be 0.″5×0.″5 by using the task of the Common Astronomy Software Applications package (CASA) (See Section 6.1). The pixel sizes were set to be (2048, 2048) for the whole observed area in the CLEAN procedure.

Now, we have 16 images including the continuum emission. It should be noted that there are a few pairs of lines unresolved in the observation. The velocity width of the line is typically 1.0–1.5 km s^{-1}, as shown in Figure 7.1, which corresponds to 0.9–1.3 MHz and 1.2–1.8 MHz for the Band 6 and Band 7 observations, respectively. Hence, the hyperfine splitting of CCH (F =5−4 and 4−3 of the N =4−3, J =9/2−7/2 transition) and that of CCH (F =4−3 and 3−2 of the N =4−3, J =7/2−5/2 transition) are not resolved. Similarly, the $9_{1,8}−8_{2,7}$ and $9_{2,8}−8_{1,7}$ lines of c-C$_3$H$_2$ are degenerated, and the $10_{0,10}−9_{1,9}$ and $10_{1,10}−9_{0,9}$ lines of this species are, too. These unresolved pairs were treated as a single line. For the CCH (N =3−2, J =7/2−5/2, F =4−3 and 3−2) lines, a single image was prepared in order to increase the signal-to-noise ratio.

7.4 Molecular Distributions

Figure 7.2 shows the continuum map and the moment 0 maps of the observed molecular lines, while Figure 7.3 depicts their blow-ups for the 1.″9×1.″6 area around the protostar. Figures 7.2(a) and 7.3(a) show the 0.8 mm continuum distribution (Cycle 3), whose peak intensity is 23.95±0.48mJy beam^{-1}. The coordinates of the peak are derived from a 2D Gaussian fit to the image: (α_{2000}, δ_{2000})= (15$^{\rm h}$43$^{\rm m}$02$^{\rm s}$.2359±0.0004, −34°09′06.″8348±0.0045), which are consistent with the previous reports (e.g., Oya et al., 2014; Okoda et al., 2018). The continuum emission has a single peak with a circular distribution.

As shown in Figure 7.2, the distribution is different from molecular line to molecular line. The outflow structure along the northeast-southwest axis reported previously (Oya et al., 2014; Bjerkeli et al., 2016a; Okoda et al., 2018) can be seen particularly in the CCH, CS, and H$_2$CO (K_a =0 and 1) lines. The outflow seems to have the double-ring structures in the CS emission (Figure 7.2(b)). This may be caused by the episodic accretion (Bjerkeli et al., 2016a). The c-C$_3$H$_2$ emission does not have a component clearly associated with the protostar. It traces a part of the outflow cavity wall of the southwestern side. DCN seems to be distributed in the outflow cavity wall to some extent and also has a compact distribution around the protostar. The SO, CH$_3$OH, and H$_2$CO (K_a =2 and 3) emission reveal blobs in the outflow as well as the compact distribution around the protostar.

In the blow-up version of the moment 0 maps (Figure 7.3), the component associated with the protostar can be found in most of the observed lines except for the c-C$_3$H$_2$ lines. The disk/envelope structure perpendicular to the outflow direction is seen more clearly. The CCH emission traces the envelope extending from northwest to southeast (Chapter 3; Okoda et al., 2018). Note that the distribution of the CCH (N =4−3, J =7/2−5/2, F =3−3) line looks slightly different from those
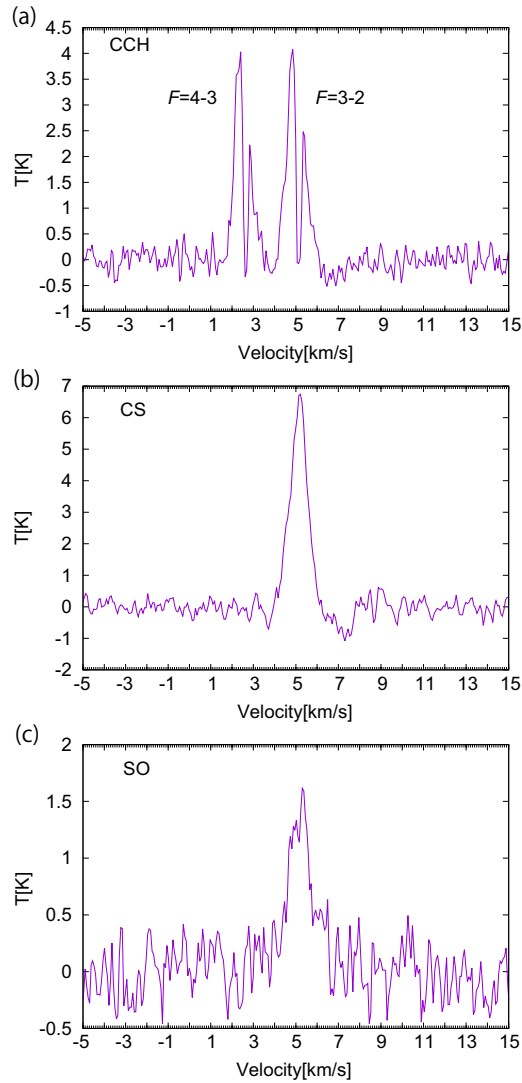
Figure 7.1: Examples of the spectra of the CCH (N =3−2, J =7/2−5/2, F =4−3 and 3−2), CS, and SO lines observed toward the continuum peak position. A systemic velocity is 5.2 km s^{-1}. In the CCH spectrum, two hyperfine components (F =4−3 and 3−2) are seen, where an intensity dip near the center of each component is due to self-absorption by a foreground gas. In the imaging, these two lines are stacked to improve the signal-to-noise ratio (See Section 7.3).

of the other CCH lines. This is probably due to the low signal-to-noise ratio of the line. The CS emission seems to be distributed over the envelope around the protostar. However, the CS emission in the southeastern side of the envelope is brighter than that in the northwestern side, as shown in Figure 7.3(b). For the CS emission, there is an asymmetry in the distribution around the protostar, which is also seen for the H$_2$CO (K_a =0) emission. As above, the distributions of the observed molecular emissions look different from one another. However, their classification by eye may suffer from our preconception, and hence, we employ the PCA to characterize the distributions.
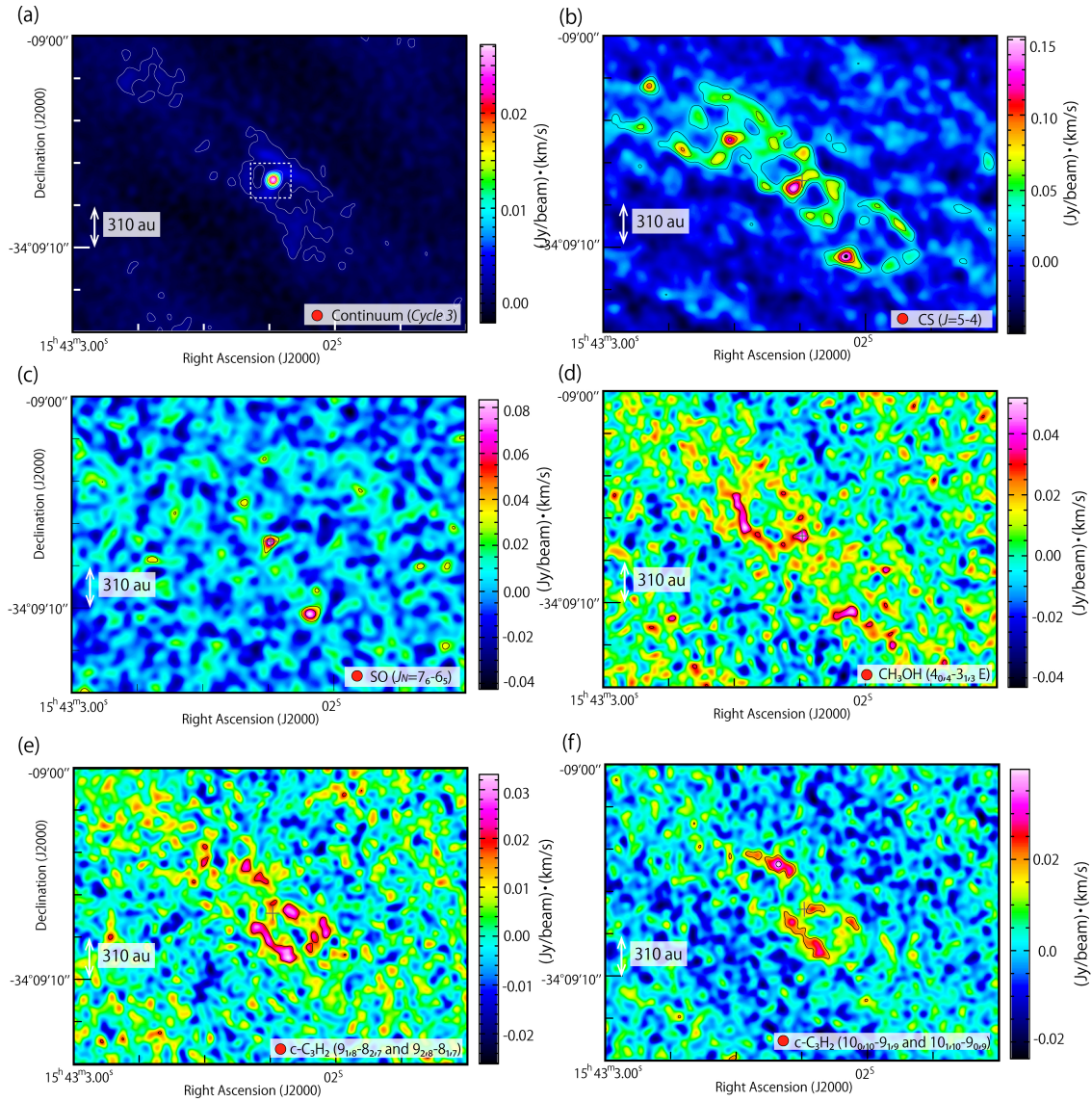
Figure 7.2: (a) The 0.8 mm continuum image and (b-p) the moment 0 maps of 15 molecular lines. The area enclosed by a white dashed line shows the blow-up area for Figure 7.3. The red circle in the bottom right corner of each map shows the beam size, which is unified to be 0."5×0."5. The cross marks show the continuum peak position. Contour levels are every σ, every 2σ, every 3σ, every 5σ, and every 10σ from 3σ for (l, p), (n), (b-f, h-k, m), (g) and (a, o) respectively. 3σ is listed in Table 7.2.

(g)

(h)

(i)

(j)

(k)

(l)
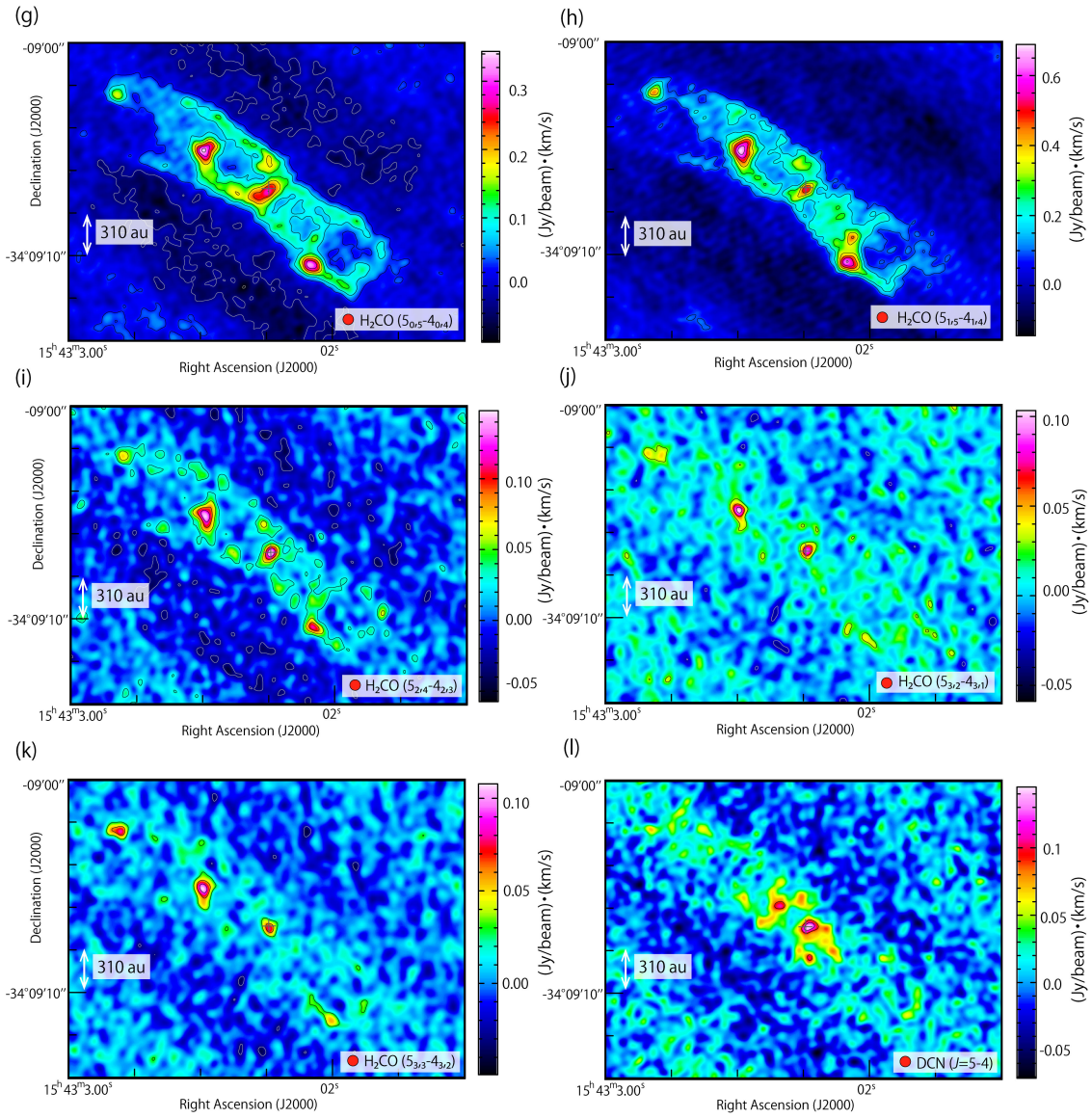
Figure 7.2: . Continued.
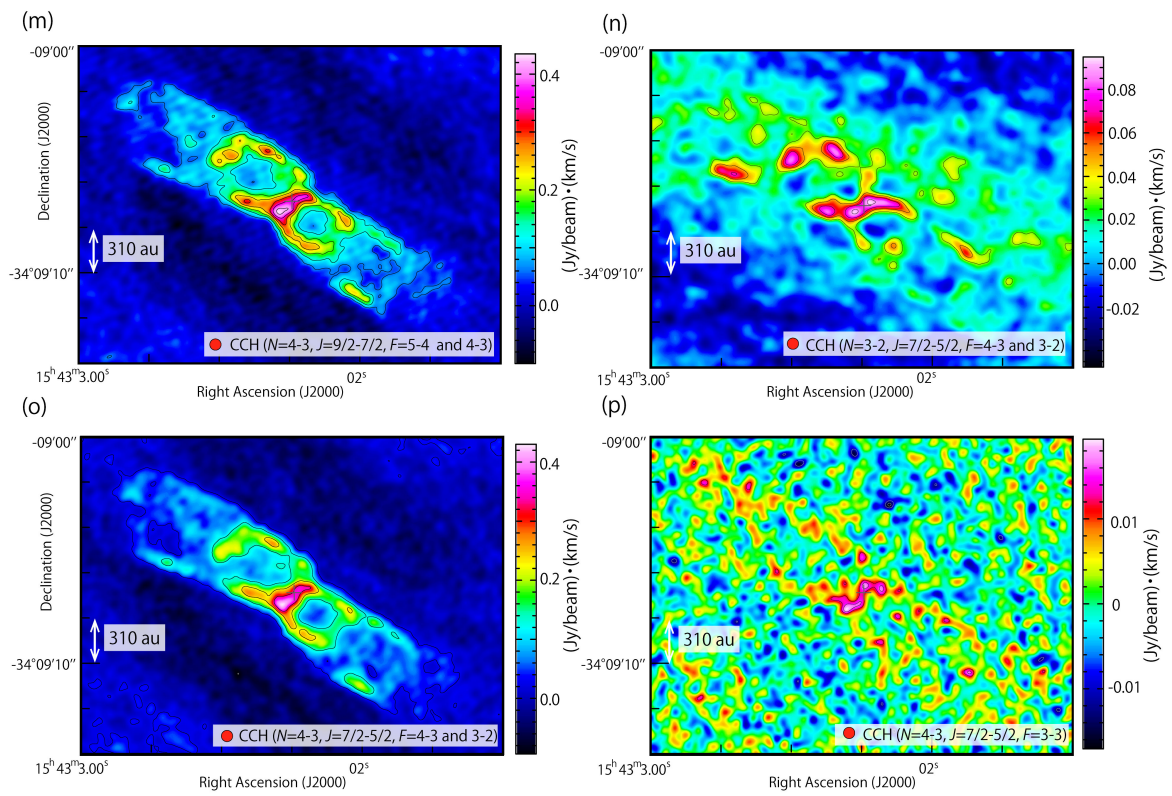
Figure 7.2: . Continued.
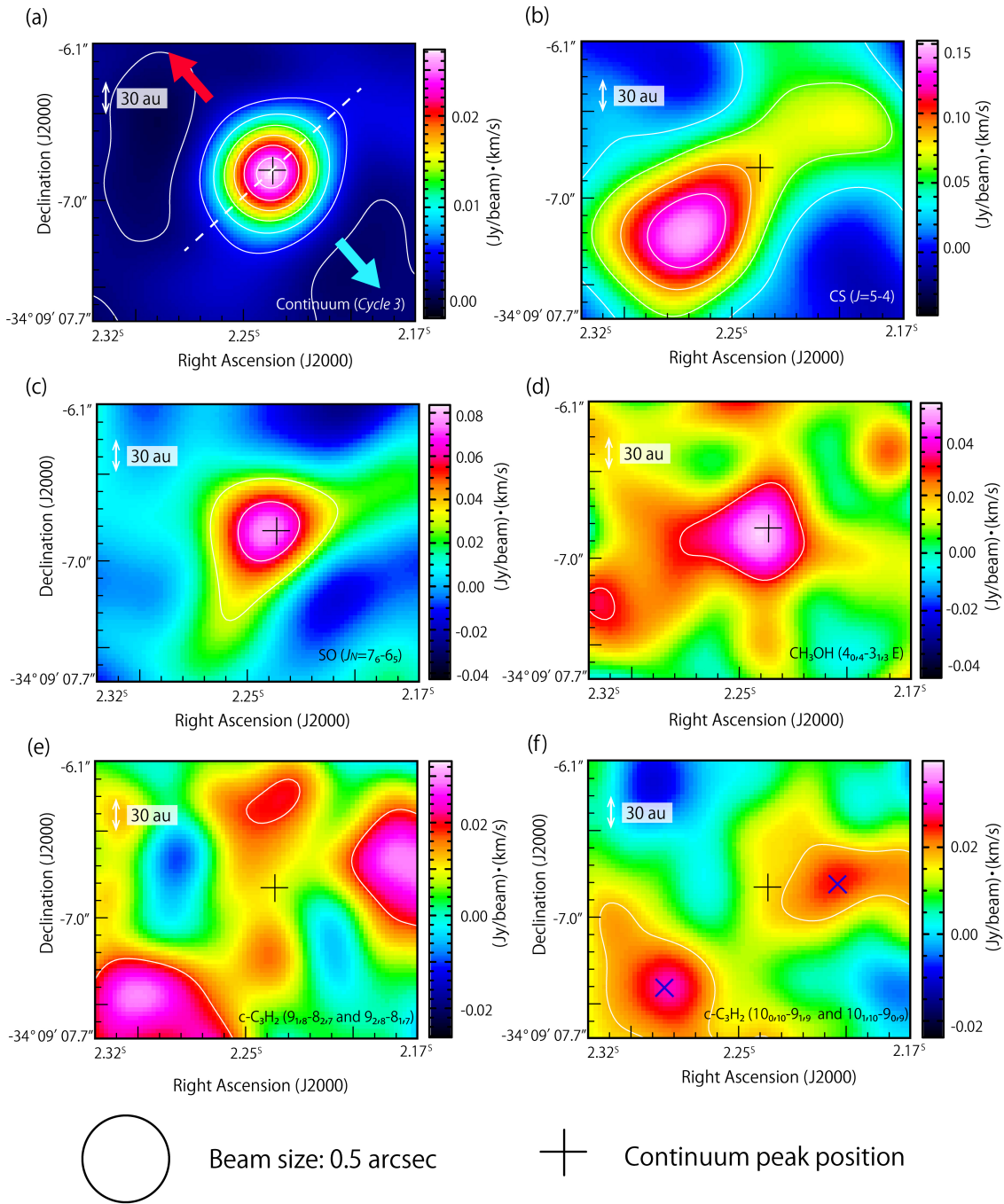
Figure 7.3: The blow-ups of Figure 7.2 around the protostar. The outflow (P.A. 220°) and envelope direction (P.A. 130°) are shown by the arrows and the dashed line, respectively, in panel (a). The blue cross marks in panel (f) represent the peak positions for the calculation of the column density ratios relative to H_2CO in Section 7.7. The circle at the bottom shows the beam size. The black cross marks indicate the continuum peak position. Contour levels are the same as those in Figure 7.2.

(g) H$_2$CO ($5_{0,5}$-$4_{0,4}$)

(h) H$_2$CO ($5_{1,5}$-$4_{1,4}$)

(i) H$_2$CO ($5_{2,4}$-$4_{2,3}$)

(j) H$_2$CO ($5_{3,2}$-$4_{3,1}$)

(k) H$_2$CO ($5_{3,3}$-$4_{3,2}$)

(l) DCN (J=5-4)

Beam size: 0.5 arcsec   Continuum peak position

Figure 7.3: . Continued.

(m) CCH (N=4-3, J=9/2-7/2, F=5-4 and 4-3)

(n) CCH (N=3-2, J=7/2-5/2, F=4-3 and 3-2)

(o) CCH (N=4-3, J=7/2-5/2, F=4-3 and 3-2)

(p) CCH (N=4-3, J=7/2-5/2, F=3-3)

Beam size: 0.5 arcsec   Continuum peak position

Figure 7.3: . Continued.

7.5 PCA of the Whole Structure

First, we conduct the PCA for the whole structure (Figure 7.2). The correlation matrix is calculated for the 16 distributions (15 lines and one continuum) observed for the whole structure (Table 7.2) and is diagonalized to find the principal components (See Section 6.1). Here, the i th principal component is denoted as PCi (i=1-16), where the number i is assigned in a decreasing order of the eigenvalue (λ_i). The eigenvalues and the eigenvectors are listed in Table 7.3. As mentioned Section 6.1, we can almost reproduce the molecular-line and continuum distributions by using only a few principal components. According to Table 7.3, PC1 and PC2 have the two largest contribution ratios, 42.1 % and 20.3 %, respectively. The sum of the contribution ratios of the two 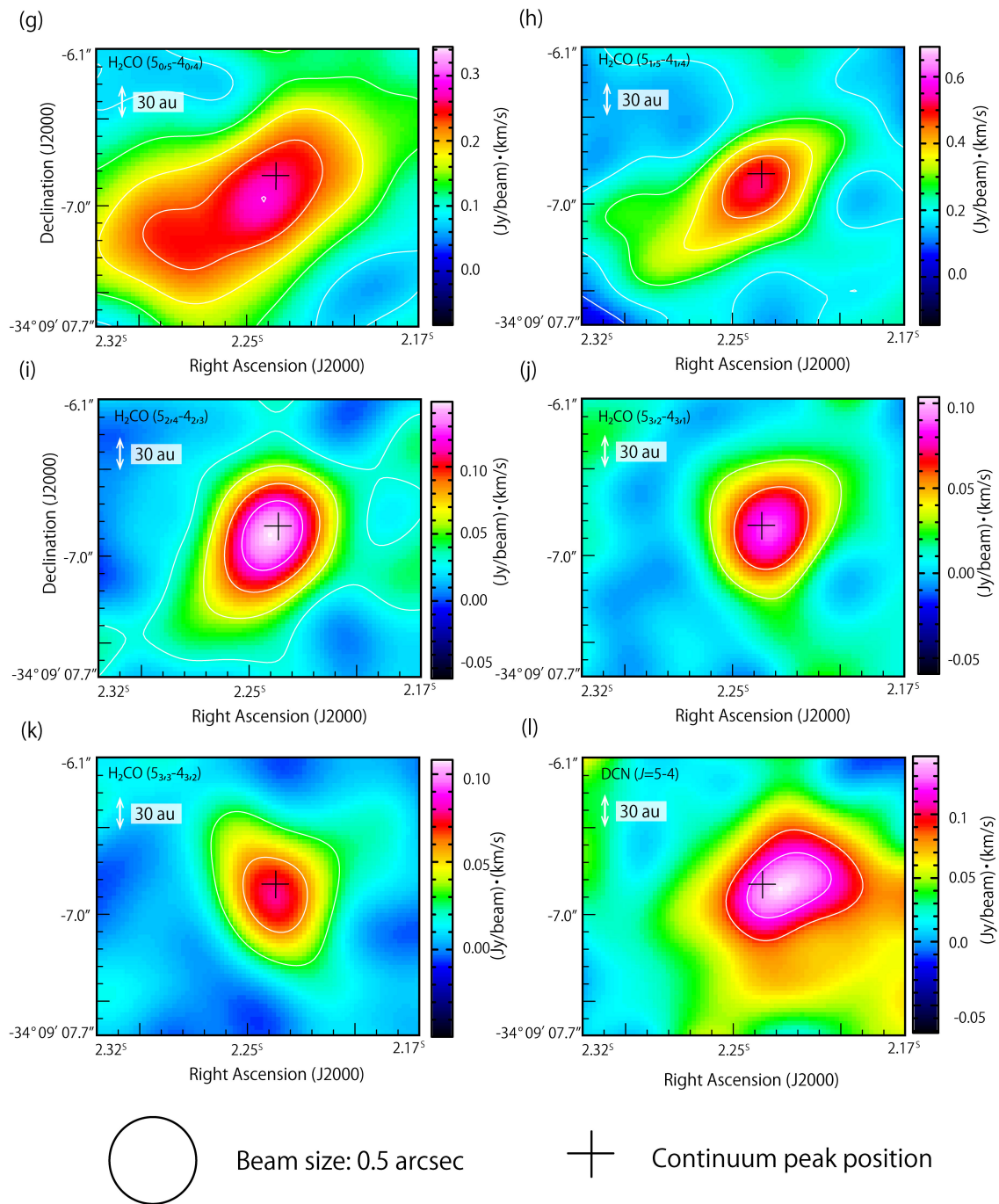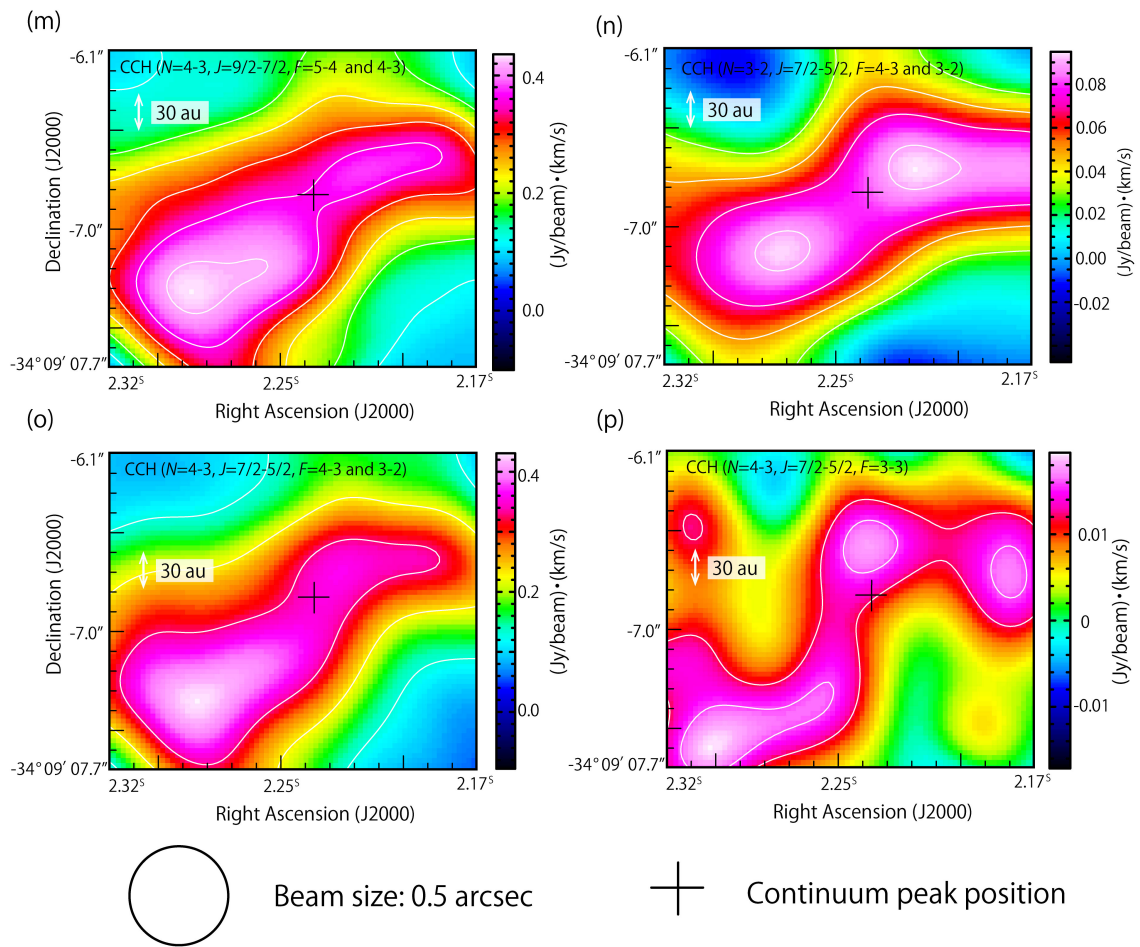components is 62.4 %, which indicates that these two components can be regarded as the main components. The contribution ratios of PC3 and PC4 are 8.7 % and 8.2 %, respectively, which are significantly smaller than that of PC2. Nevertheless, PC3 and PC4 show some trends in the distributions. We here discuss the first four components, although the observed images can approximately be reproduced by the linear combinations of the first two component images, which means the reduction of the original dimension of the images (16) to 2.

Figures 7.4(a), (b), (c), and (d) show the maps of PC$_i$ (i =1-4). PC1 represents an overall shape of the outflow, two blobs in the outflow, and a component concentrated around the protostellar position. PC2 mainly represents the disk/envelope structure. The foot of the outflow can also be seen partly. PC3 represents the two blobs in the outflow as PC1, where the southwestern one is brighter in PC3 than the northeastern one in contrast to PC1. As well, PC3 has a negative component near the protostar position. Meaning of PC4 is not as clear as PC3. The contributions of the principal components for each molecular-line distribution and the correlations between PC$_i$ (i =1−4) and the molecular-line distributions are investigated as follows.

Contributions of the first two principal components for each molecular-line distribution are represented on the PC1-PC2 plane (Figure 7.4(e)). Correlations between PC$_i$ (i =1−4) and the observed distributions are also presented in Figure 7.5. We calculate them by using the method described in Section 6.2. Grey dashed ellipses in Figure 7.4(e), (f), and (g) and grey bars in Figure 7.5 represent the estimated errors due to noise, whose details are described in Section 6.3. As shown in Figure 7.4(e), the majority of the line emissions and the continuum emission show the positive values of PC1. The distributions of these lines are well correlated to PC1. For these lines, the negative and positive values on the PC2 axis can classify them into two groups, one with compact distributions around the protostar (Group 1) and the other showing rather extended structures (Group 2), respectively (Figure 7.4(e)). The CCH and CS lines as well as the H$_2$CO (K_a =0) line belong to Group 2, which well trace the extended feature of the outflow. Indeed, these lines are often employed as a tracer of the outflow cavity wall on a 1000 au scale (e.g., Codella et al., 2014; Oya et al., 2015, 2019; Zhang et al., 2018). On the other hand, the c-C$_3$H$_2$ ($10_{0,10}-9_{1,9}$ and $10_{1,10}-9_{0,9}$), c-C$_3$H$_2$ ($9_{1,8}-8_{2,7}$ and $9_{2,8}-8_{1,7}$) and CCH (N =4−3, J =7/2−5/2, F =3−3) lines are located at the peculiar area on the PC1-PC2 plot: they

have negative PC1 and positive PC2. This result suggests that these three molecular lines have a clumpy feature in the outflow.

In contrast to the PC1 and PC2 cases, the interpretations of PC3 and PC4 are not very clear. PC3 shows blobs in the outflow and the negative distribution near the protostar. The SO line showing a southwestern blob naturally takes the large PC3 value on the PC1-PC3 plane (Figure 7.4(f)) and has the positive correlation with PC3 (Figure 7.5). The large positive contribution of c-C_3H_2 ($9_{1,8}-8_{2,7}$ and $9_{2,8}-8_{1,7}$) and the negative contribution of DCN seem to reflect the negative component near the protostar of PC3. According to the correlations between PC4 and the molecular distributions (Figure 7.5), PC4 mainly represents the peculiar distribution of c-C_3H_2 ($10_{0,10}-9_{1,9}$ and $10_{1,10}-9_{0,9}$). As shown in the PC1-PC4 plane (Figure 7.4(g)), c-C_3H_2 ($10_{0,10}-9_{1,9}$ and $10_{1,10}-9_{0,9}$) has a large negative value along PC4 axis.

The molecular emission distributed in the blobs are represented by the positive PC1 and positive PC3 values. These blobs are most likely a shocked region caused by a local impact of the outflow on an ambient gas, as described below. The molecular lines showing the positive PC1 and the positive PC3 (H_2CO, CS, CCH (N =3−2), SO, and CH_3OH) trace both or one of the two blobs (Figure 7.4(f)). We finally identify four blobs (A-D in Figure 7.6) in the outflow structure by using the H_2CO (K_a =1) line (Table 7.4). They are also seen in the other H_2CO lines, although blobs B and C can hardly be seen in the highest excitation lines of H_2CO (K_a =3). Blob D is bright in the CS and SO emission, although blob A is seen in the CS and CCH (N =3−2) lines. The CH_3OH emission has an extended distribution from the protostar to blob A.

The gas kinematic temperature for each blob is evaluated from the detected H_2CO lines under the non-LTE (local thermodynamic equilibrium) method assuming the large velocity gradient (LVG) approximation (Goldreich & Kwan, 1974). The data used in the analysis are shown in Table 7.5. The derived gas kinematic temperature ranges from 43 K to 63 K (Table 7.6). Such high temperatures as well as absence of associated continuum emission indicate that the four blobs should be the shocked regions caused by the outflow impact. It seems that a local shock is occurring on the cavity wall by the interaction with ambient gas. This situation is also pointed out for blob A by Oya et al. (2014). Such a shocked region can be seen in L1157 B1, where strong emissions of various molecules including H_2CO, CS, SO, and CH_3OH are detected (e.g., Bachiller, & Pérez Gutiérrez, 1997; Benedettini et al., 2007; Codella et al., 2010, ; See also Chapters 1 and 4). These molecules are thought to be liberated from dust grains and/or produced through the gas-phase shock chemistry. Detailed comparison with the L1157 B1 result for exploring shock chemistry would require observations of more molecular lines.

Table 7.2: Correlation Matrix for the Whole Structure

Molecular spices Transition[a]	c-C$_3$H$_2$ (10−9)	c-C$_3$H$_2$ (9−8)	CCH (3−2)	CCH (4−3 a)	CCH (4−3 b)	CCH (4−3 c)	CH$_3$OH	CS	DCN	H$_2$CO K_a=0	H$_2$CO K_a=1	H$_2$CO K_a=2	H$_2$CO K_a=3$_u$	H$_2$CO K_a=3$_l$	SO	Continuum (Cycle3)
c-C$_3$H$_2$ (10−9)	1	0.0701	0.2025	0.1514	0.0125	0.0806	-0.5217	0.0407	-0.0718	0.0229	-0.0012	-0.1951	-0.3934	-0.5902	-0.5435	-0.1789
c-C$_3$H$_2$ (9−8)	0.0701	1	0.3635	0.4171	0.3925	0.3666	-0.7422	0.0419	-0.5622	0.268	0.1289	0.0137	-0.6535	-0.4883	-0.7263	-0.1822
CCH (3−2)	0.2025	0.3635	1	-0.0859	0.6308	0.5969	0.3057	0.5005	0.4118	0.5671	0.3846	0.4195	0.3982	0.2723	0.4117	0.479
CCH (4−3 a)	0.1514	0.4171	-0.0859	1	0.3216	0.2884	-0.2207	0.1013	-0.1804	0.135	-0.058	0.0228	0.0936	-0.1387	-0.2487	-0.0685
CCH (4−3 b)	0.0125	0.3925	0.6308	0.3216	1	0.9726	0.1568	0.3827	0.548	0.6669	0.3183	0.335	0.5353	0.2789	0.0086	0.5312
CCH (4−3 c)	0.0806	0.3666	0.5969	0.2884	0.9726	1	0.0176	0.3561	0.5355	0.6511	0.3314	0.326	0.5103	0.2236	-0.0362	0.5254
CH$_3$OH	-0.5217	-0.7422	0.3057	-0.2207	0.1568	0.0176	1	0.3185	0.1145	0.3633	0.3024	0.2747	0.3566	0.2606	0.5191	0.6838
CS	0.0407	0.0419	0.5005	0.1013	0.3827	0.3561	0.3185	1	0.2621	0.5845	0.5144	0.4508	0.2112	0.1348	0.0559	0.3402
DCN	-0.0718	-0.5622	0.4118	-0.1804	0.548	0.5355	0.1145	0.2621	1	0.5817	0.6523	0.4827	0.6319	0.2087	0.018	0.6525
H$_2$CO(K_a=0)	0.0229	0.268	0.5671	0.135	0.6669	0.6511	0.3633	0.5845	0.5817	1	0.794	0.7737	0.6021	0.541	0.5379	0.6023
H$_2$CO(K_a=1)	-0.0012	0.1289	0.3846	-0.058	0.3183	0.3314	0.3024	0.5144	0.6523	0.794	1	0.777	0.5855	0.6165	0.6532	0.4361
H$_2$CO(K_a=2)	-0.1951	0.0137	0.4195	0.0228	0.335	0.326	0.2747	0.4508	0.4827	0.7737	0.777	1	0.6729	0.6473	0.4643	0.843
H$_2$CO(K_a=3$_u$)	-0.3934	-0.6535	0.3982	0.0936	0.5353	0.5103	0.3566	0.2112	0.6319	0.6021	0.5855	0.6729	1	0.6974	0.4244	0.8205
H$_2$CO(K_a=3$_l$)	-0.5902	-0.4883	0.2723	-0.1387	0.2789	0.2236	0.2606	0.1348	0.2087	0.541	0.6165	0.6473	0.6974	1	0.355	0.6219
SO	-0.5435	-0.7263	0.4117	-0.2487	0.0086	-0.0362	0.5191	0.0559	0.018	0.5379	0.6532	0.4643	0.4244	0.355	1	0.3517
Continuum	-0.1789	-0.1822	0.479	-0.0685	0.5312	0.5254	0.6838	0.3402	0.6525	0.6023	0.4361	0.843	0.8205	0.6219	0.3517	1
3σ	18	18	30	12	30	60	30	30	90	30	90	30	30	30	30	1.2

[a] c-C$_3$H$_2$ (10−9), (9−8), CCH (3−2), (4−3 a), (4−3 b), (4−3 c), H$_2$CO (K_a=0), (K_a=1), (K_a=2), (K_a=3$_u$), and (K_a=3$_l$) denote c-C$_3$H$_2$ (10$_{0,10}$−9$_{1,9}$ and 10$_{1,10}$−9$_{0,9}$), c-C$_3$H$_2$ (9$_{1,8}$−8$_{2,7}$ and 9$_{2,8}$−8$_{1,7}$), CCH (N =3−2, J =7/2−5/2, F =4−3 and 3−2), (N =4−3, J =7/2−5/2, F =3−3), (N =4−3, J =7/2−5/2, F =4−3 and 3−2), (N =4−3, J =9/2−7/2, F =5−4 and 4−3), H$_2$CO (5$_{0,5}$−4$_{0,4}$), (5$_{1,5}$−4$_{1,4}$), (5$_{2,4}$−4$_{2,3}$), (5$_{3,2}$−4$_{2,3}$), (5$_{3,3}$−4$_{3,1}$), and (5$_{3,3}$−4$_{3,2}$), respectively. The units of σ (root mean square) are 'mJy beam^{-1}km s^{-1}' and 'mJy beam^{-1}' for the molecular lines and the continuum data, respectively.

Table 7.3: Eigenvectors of the Principal Components and their Eigenvalues in the Analysis of the Whole Structure

Principal Component	PC1	PC2	PC3	PC4	PC5	PC6	PC7	PC8	PC9	PC10	PC11	PC12	PC13	PC14	PC15	PC16
c-C$_3$H$_2$ (10–9)	-0.098	0.298	-0.131	-0.559	0.215	0.234	0.188	0.46	-0.165	0.31	-0.025	0.077	0.018	0.102	0.018	0.288
c-C$_3$H$_2$ (9–8)	-0.077	0.514	0.385	0.213	-0.014	-0.269	-0.188	0.024	0.234	-0.043	0.125	0.062	0.178	-0.093	-0.111	0.546
CCH (3–2)	0.249	0.203	0.136	-0.267	-0.316	-0.318	0.178	0.263	-0.296	-0.404	0.363	-0.188	-0.041	-0.161	0.099	-0.224
CCH (4–3 a)	-0.006	0.288	-0.02	0.436	0.001	0.666	0.293	0.074	0.038	-0.154	0.287	-0.138	-0.242	-0.069	-0.04	-0.022
CCH (4–3 b)	0.257	0.328	-0.221	0.15	-0.242	-0.128	0.121	-0.145	-0.024	0.177	0.012	-0.052	0.141	0.762	-0.021	-0.089
CCH (4–3 c)	0.244	0.345	-0.249	0.112	-0.151	-0.155	0.139	-0.122	-0.034	0.16	-0.345	0.433	-0.367	-0.376	0.236	-0.024
CH$_3$OH	0.201	-0.299	0.033	-0.086	-0.58	0.227	-0.127	0.047	0.228	0.337	0.302	0.044	0.057	-0.073	0.345	0.264
CS	0.203	0.147	0.224	-0.277	-0.192	0.423	-0.405	-0.362	-0.385	-0.217	-0.235	0.073	-0.02	0.05	-0.178	0.093
DCN	0.268	0.013	-0.461	-0.279	0.253	-0.076	-0.054	-0.359	0.286	-0.206	0.22	-0.311	-0.232	-0.054	-0.033	0.331
H$_2$CO(K_a =0)	0.339	0.155	0.224	-0.041	0.078	0.063	0.122	-0.079	0.138	0.391	-0.28	-0.568	0.262	-0.302	-0.051	-0.208
H$_2$CO(K_a =1)	0.304	0.014	0.318	-0.155	0.386	0.041	0.091	-0.244	0.117	0.178	0.455	0.476	0.053	0.026	-0.048	-0.279
H$_2$CO(K_a =2)	0.32	-0.007	0.216	0.061	0.297	0.079	-0.252	0.328	0.217	-0.27	-0.248	-0.036	-0.141	0.264	0.556	-0.029
H$_2$CO(K_a =3$_u$)	0.328	-0.124	-0.3	0.191	0.123	0.103	0.154	0.077	-0.182	-0.261	-0.051	0.208	0.689	-0.168	0.05	0.206
H$_2$CO(K_a =3$_l$)	0.264	-0.196	0.047	0.336	0.237	-0.162	-0.167	0.096	-0.591	0.331	0.182	-0.158	-0.268	0.005	-0.04	0.258
SO	0.211	-0.325	0.348	-0.053	-0.096	-0.049	0.601	-0.017	0.09	-0.141	-0.268	0.061	-0.214	0.159	-0.246	0.344
Continuum	0.334	-0.046	-0.172	0.042	-0.108	0.015	-0.309	0.476	0.274	0.003	-0.035	0.136	-0.11	-0.04	-0.625	-0.149
Eigenvalues	6.731	3.243	1.397	1.310	1.108	8.830	7.450	5.940	4.710	2.960	1.660	8.100	1.300	4.000	-8.900	-9.540
Contribution ratio (%)	42.1	20.3	8.7	8.2	6.9	5.5	4.7	3.7	2.9	1.9	1.0	0.5	0.1	0.0	-0.6	-6.0

c-C$_3$H$_2$ (10–9), (9–8), CCH (3–2), (4–3 a), (4–3 b), (4–3 c), H$_2$CO (K_a=0), (K_a=1), (K_a=2), (K_a=3$_u$), and (K_a=3$_l$) denote c-C$_3$H$_2$ (10$_{0,10}$–9$_{1,9}$ and 10$_{1,10}$–9$_{0,9}$), c-C$_3$H$_2$ (9$_{1,8}$–8$_{2,7}$ and 9$_{2,8}$–8$_{1,7}$), CCH (3–2), c-C$_3$H$_2$ (9$_{1,8}$–8$_{2,7}$ and 9$_{2,8}$–8$_{1,7}$), CCH (N =3–2, J =7/2–5/2, F =4–3 and 3–2), (N =4–3, J =7/2–5/2, F =3–3), (N =4–3, J =7/2–5/2, F =4–3 and 3–2), (N =4–3, J =9/2–7/2, F =5–4 and 4–3), H$_2$CO (5$_{0,5}$–4$_{0,4}$, (5$_{1,5}$–4$_{1,4}$), (5$_{2,4}$–4$_{2,3}$), (5$_{3,2}$–4$_{3,1}$), and (5$_{3,3}$–4$_{3,2}$), respectively.
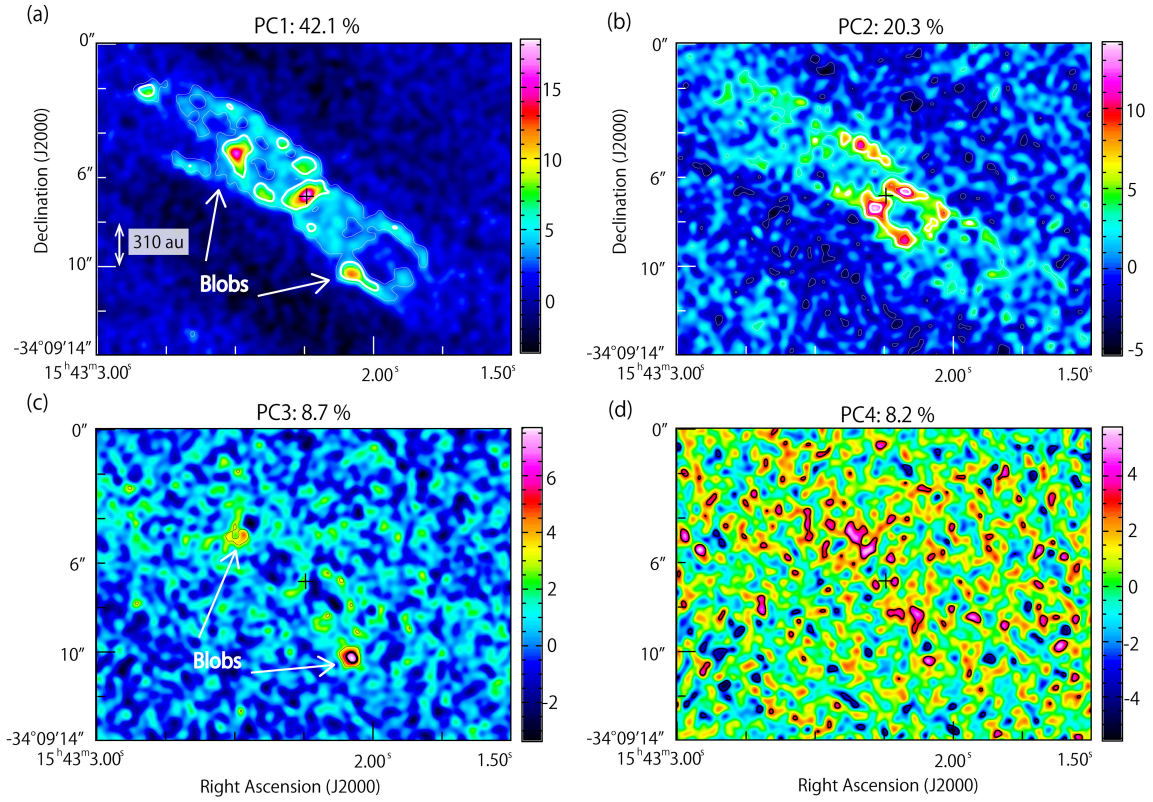
Figure 7.4: (a, b, c, d) The principal components, PC1 (a), PC2 (b), PC3 (c), and PC4 (d) for the whole-scale structure (Figure 7.2). The cross marks show the continuum peak position. The contour level interval is 3.0 starting from 3.0. (e, f, g) The plot of the principal components for each distribution on the PC1-PC2 (e), PC1-PC3 (f), and PC1-PC4 (g) planes. The grey dashed ellipses represent the uncertainties (See Section 6.3). The red dashed circles show the groups of the compact distribution (Group 1) and the extended distribution (Group 2). Blobs in (a) is consistent with the blobs A and D in Figure 7.6. c-C$_3$H$_2$ (10−9), (9−8), CCH (N =3−2), (N =4−3 a), (N =4−3 b), (N =4−3 c), H$_2$CO (K_a=0), (K_a=1), (K_a=2), (K_a=3$_u$), and (K_a=3$_l$) denote c-C$_3$H$_2$ (10$_{0,10}$−9$_{1,9}$ and 10$_{1,10}$−9$_{0,9}$), c-C$_3$H$_2$ (9$_{1,8}$−8$_{2,7}$ and 9$_{2,8}$−8$_{1,7}$), CCH (N =3−2, J =7/2−5/2, F =4−3 and 3−2), (N =4−3, J =7/2−5/2, F =3−3), (N =4−3, J =7/2−5/2, F =4−3 and 3−2), (N =4−3, J =9/2−7/2, F =5−4 and 4−3), H$_2$CO (5$_{0,5}$−4$_{0,4}$), (5$_{1,5}$−4$_{1,4}$), (5$_{2,4}$−4$_{2,3}$), (5$_{3,2}$−4$_{3,1}$), and (5$_{3,3}$−4$_{3,2}$), respectively.

121
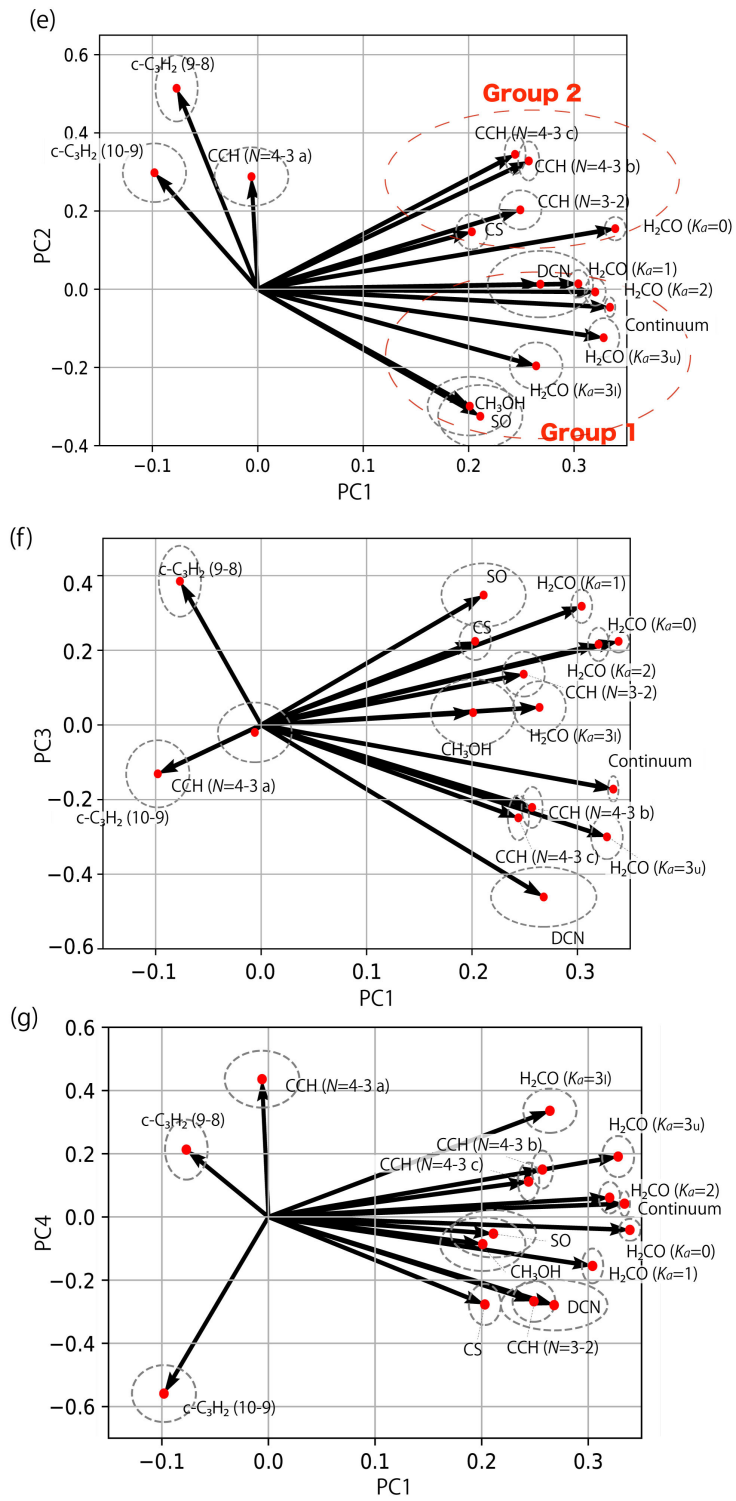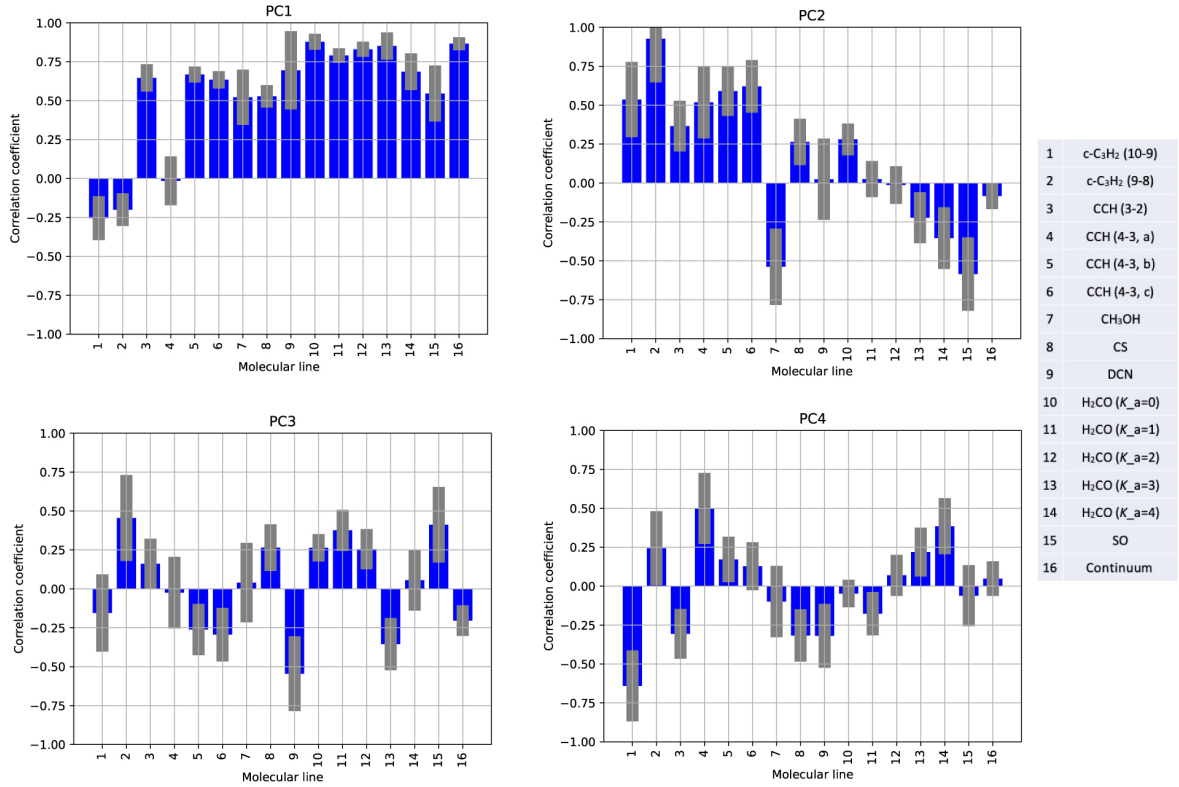
Figure 7.4: . Continued.

Figure 7.5: Correlation coefficients between the first four principal components and the molecular distributions of the whole-structure scale. The uncertainties are shown in grey (See Section 6.3). c-C_3H_2 (10−9), (9−8), CCH (3−2), (4−3 a), (4−3 b), (4−3 c), H_2CO ($K_a=0$), ($K_a=1$), ($K_a=2$), ($K_a=3_u$), and ($K_a=3_l$) denote c-C_3H_2 ($10_{0,10}-9_{1,9}$ and $10_{1,10}-9_{0,9}$), c-C_3H_2 ($9_{1,8}-8_{2,7}$ and $9_{2,8}-8_{1,7}$), CCH (N =3−2, J =7/2−5/2, F =4−3 and 3−2), (N =4−3, J =7/2−5/2, F =3−3), (N =4−3, J =7/2−5/2, F =4−3 and 3−2), (N =4−3, J =9/2−7/2, F =5−4 and 4−3), H_2CO ($5_{0,5}-4_{0,4}$), ($5_{1,5}-4_{1,4}$), ($5_{2,4}-4_{2,3}$), ($5_{3,2}-4_{3,1}$), and ($5_{3,3}-4_{3,2}$), respectively.

Table 7.4: Positions of the H_2CO Blobs

Position	R.A. (J2000)	Decl. (J2000)
A	$15^h43^m02^s.47$	$-34°09'04.''94$
B	$15^h43^m02^s.25$	$-34°09'05.''55$
C	$15^h43^m02^s.07$	$-34°09'09.''23$
D	$15^h43^m02^s.08$	$-34°09'10.''63$
Center	$15^h43^m02^s.24$	$-34°09'06.''83$

Table 7.5: Line Parameters of H_2CO at the H_2CO Blobs and the Protostar Position[a]

Position	Transition	T_{peak} (K)	V_{LSR} (km s^{-1})	FWHM (km s^{-1})
A	$K_a=0$	6.5 (0.15)	7.1 (0.01)	0.9 (0.04)
	$K_a=1$	10 (0.22)	7.1 (0.02)	1.1 (0.06)
	$K_a=2$	2.0 (0.08)	7.1 (0.03)	0.9 (0.04)
	$K_a=3_u$	1.3 (0.09)	7.1 (0.05)	0.9 (0.07)
	$K_a=3_l$	1.5 (0.07)	7.0 (0.03)	0.9 (0.04)
B	$K_a=0$	3.4 (0.21)	5.7 (0.08)	1.4 (0.06)
	$K_a=1$	5.6 (0.44)	6.0 (0.30)	1.5 (0.06)
	$K_a=2$	0.6 (0.08)	5.7 (0.21)	1.5 (0.14)
	$K_a=3_u$	0.6 (0.08)	5.3 (0.07)	1.1 (0.14)
	$K_a=3_l$	0.3 (0.05)	5.9 (0.13)	1.1 (0.22)
C	$K_a=0$	1.7 (0.15)	3.5 (0.24)	1.9 (0.14)
	$K_a=1$	4.5 (0.33)	3.5 (0.24)	2.1 (0.11)
	$K_a=2$	0.6 (0.04)	3.2 (0.16)	1.6 (0.14)
	$K_a=3_u$	0.3 (0.09)	3.1 (0.11)	0.9 (0.31)
	$K_a=3_l$	0.4 (0.05)	3.4 (0.12)	1.4 (0.20)
D	$K_a=0$	4.5 (0.22)	4.6 (0.04)	1.1 (0.04)
	$K_a=1$	7.6 (0.39)	4.5 (0.04)	1.2 (0.05)
	$K_a=2$	1.1 (0.05)	4.6 (0.04)	1.0 (0.05)
	$K_a=3_u$	0.5 (0.05)	4.5 (0.10)	1.3 (0.16)
	$K_a=3_l$	0.6 (0.06)	4.6 (0.06)	0.9 (0.10)
Center	$K_a=0$	6.0 (0.13)	5.5 (0.01)	0.9 (0.02)
	$K_a=1$	8.0 (0.46)	5.6 (0.04)	1.1 (0.07)
	$K_a=2$	1.9 (0.08)	5.5 (0.03)	0.9 (0.04)
	$K_a=3_u$	0.8 (0.06)	5.2 (0.09)	1.6 (0.16)
	$K_a=3_l$	0.7 (0.06)	5.5 (0.08)	1.4 (0.14)

[a] Measured for a circular area in Figure 7.6 with a diameter of 1″. 'Center' denotes the protostar position. The line parameters are obtained by using gaussian-fitting. The numbers in parentheses represent the Gaussian-fitting errors. $K_a=0$, $K_a=1$, $K_a=2$, $K_a=3_u$, and $K_a=3_l$ denote H_2CO ($5_{0,5}-4_{0,4}$), ($5_{1,5}-4_{1,4}$), ($5_{2,4}-4_{2,3}$), ($5_{3,2}-4_{3,1}$), and ($5_{3,3}-4_{3,2}$), respectively.

Table 7.6: Gas Kinematic Temperatures and Column Densities of the Blobs[a]

Blob	Column density (10^{14} cm^{-2})	T_{gas} (K)	ortho/para
Center	0.87± 0.06	54 ± 2	1.7± 0.13
A	0.83± 0.03	63 ± 2	2.0 ± 0.09
B	0.67±0.07	43±3	2.3± 0.26
C	0.48 ±0.05	54± 4	3.3± 0.39
D	0.78±0.06	45± 2	2.3±0.2

[a] The H$_2$ density is assumed to be 10^6 cm^{-3}. The derived values are not much different even if the H$_2$ densitiy is 10^5 cm^{-3} or 10^7 cm^{-3}. The errors are derived from the least-squares analysis on the intensities of five H$_2$CO lines. 'Center' denotes the protostar position.
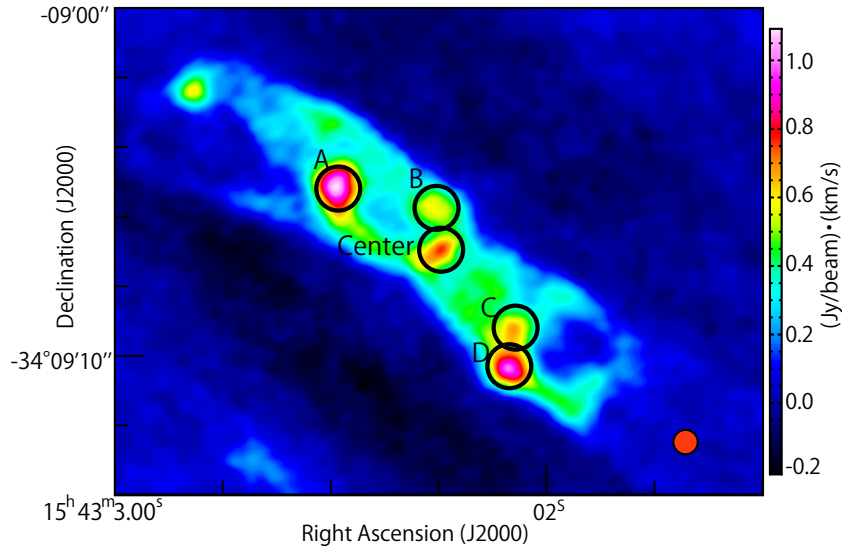

Figure 7.6: . Blobs in the outflow indicated on the moment 0 map of H$_2$CO (K_a =1). The positions of the blobs are listed in Table 7.4. The red circle on the bottom right shows the beam size of 0.″5×0.″5.

7.6 PCA of the Disk/Envelope Structure

The PCA for the observed distributions in the narrower range (Figure 7.3) is helpful to investigate the chemical structure around the protostar in more detail. We use 14 molecular line data except for c-C$_3$H$_2$ ($9_{1,8}$–$8_{2,7}$ and $9_{2,8}$–$8_{1,7}$) in addition to the Cycle 3 continuum data as explained in Section 7.3. Table 7.7 shows the correlation matrix and Table 7.8 the eigenvalues and eigenvectors obtained by diagonalizing it. On the disk/envelope scale, PC1 and PC2 stand for 76.7 % of the contribution ratio. The molecular distributions can mostly be reproduced by only the first two components, so that we mainly discuss PC1 and PC2. The contribution ratio of PC3 is 8.5 %, which is similar to that of PC4 (7.8 %).

In Figure 7.7(a), PC1 shows the distribution centered near the protostellar position with extension along the northwest-southeast direction. This component apparently represents the disk/envelope structure. All the molecular lines except for CCH (N =4−3, J =7/2−5/2, F =3−3) and c-C$_3$H$_2$ ($10_{0,10}$–$9_{1,9}$ and $10_{1,10}$–$9_{0,9}$) have

the positive PC1 component, as shown in the PC1-PC2 plane (Figures 7.7(e)). Here, grey dashed ellipses represent the estimated errors (Section 6.3). The exception for CCH (N =4−3, J =7/2−5/2, F =3−3) and c-C_3H_2 ($10_{0,10}-9_{1,9}$ and $10_{1,10}-9_{0,9}$) means that they are not mainly distributed in the disk/envelope system, as noted in Sections 7.4 and 7.5. PC2 has negative values at almost all the positions with two large negative peaks at the both sides of the protostellar position (Figure 7.7(b)). Its 'red part' in the northeastern and southwestern extension is close to zero. SO shows the large positive value for the PC2 axis, as shown in Figure 7.7(e). This result means that its distribution is very compact toward the protostar: the southeastern and northwestern extension of PC1 is almost compensated by the positive PC2. It is consistent with our previous finding of the compact SO distribution (Chapter 3: Okoda et al., 2018). Similarly, the lines showing positive PC1 and positive PC2 have a compact distribution around the protostar (Group A). On the other hand, the lines showing positive PC1 and negative PC2 have a rather extended distribution (Group B). Thus, PC2 can be an indicator of how much the distribution is concentrated around the protostar.

As in the case of the whole structure scale, PC3 and PC4 also represent the peculiar distributions of some molecular lines on the disk/envelope scale. PC3 has the positive and negative distributions around the protostar position in Figure 7.7(c). According to the correlations between PC3 and the molecular distributions (Figure 7.8), PC3 represents a characteristic feature of DCN and H_2CO (K_a =3_u): these molecular lines have a large PC3 value (Figure 7.7 (f)). PC4 solely looks like the distribution of CCH (N =3−2, J =7/2−5/2, F =4−3 and 3−2) (Figures 7.7 (d) and 7.3(p)). This trend can also be seen in Figure 7.8.

For the two large negative peaks of PC2, the southeastern side of the protostar has a stronger peak than the northwestern side (Figure 7.7(b)). This feature contributes to an asymmetric distribution in the disk/envelope system. The CS and H_2CO (K_a =0) distributions are clearly brighter in the southeastern side, and hence, the PC2 values take a negative value. The chemical composition seems azimuthally non-uniform even in the protostellar envelope, as revealed in the other sources (TMC-1A and L483: Sakai et al., 2016; Oya et al., 2017).

Next, we focus on the behavior of the H_2CO lines with different upper state energies along the PC2 axis in Figure 7.7(e). For para H_2CO, the K_a =2 line shows the positive contribution of PC2, while the K_a =0 line shows the negative contribution. Likewise, ortho H_2CO reveals a similar trend: the K_a =3 lines take the larger positive value of PC2, while the K_a =1 line takes the negative PC2. This trend represents that the emissions of the higher excitation lines (i.e., higher K_a lines) tend to be more concentrated around the protostar. This is reasonable because the gas temperature and the gas density are expected to be higher as approaching to the protostar. The gas kinematic temperature is calculated to be 54 K (Table 7.6) by using the non-LTE calculation which is applied to the analysis of the blobs (Section 7.5). The gas is significantly heated near the protostar.

Table 7.7: Correlation Matrix for the Disk/Envelope

Molecular spices Transition[a]	c-C_3H_2 (10–9)	CCH (3–2)	CCH (4–3 a)	CCH (4–3 b)	CCH (4–3 c)	CH_3OH	CS	DCN	H_2CO K_a=0	H_2CO K_a=1	H_2CO K_a=2	H_2CO $K_a=3_u$	H_2CO $K_a=3_l$	SO	Continuum (Cycle3)
c-C_3H_2 (10–9)	1	0.0113	0.1657	0.5656	0.5949	-0.429	0.4517	-0.1288	0.2988	0.1921	-0.3543	-0.6046	-0.5911	-0.6924	-0.198
CCH (3–2)	0.0113	1	-0.2787	0.6607	0.7061	0.2147	0.5318	0.4118	0.6789	0.6262	0.4443	0.3952	0.3602	0.1209	0.4145
CCH (4–3 a)	0.1657	-0.2787	1	0.1107	0.0151	-0.2921	-0.1203	-0.1804	-0.2132	-0.2431	-0.063	0.0539	-0.2268	-0.2487	-0.2696
CCH (4–3 b)	0.5656	0.6607	0.1107	1	0.9888	0.3357	0.8041	0.3622	0.9099	0.6555	0.4827	0.5609	0.5075	0.0518	0.4411
CCH (4–3 c)	0.5949	0.7061	0.0151	0.9888	1	0.1952	0.8226	0.4028	0.9089	0.6669	0.466	0.4068	0.427	-0.0568	0.4256
CH_3OH	-0.429	0.2147	-0.2921	0.3357	0.1952	1	0.0393	0.1145	0.6638	0.7567	0.7953	0.4929	0.7601	0.8797	0.7287
CS	0.4517	0.5318	-0.1203	0.8041	0.8226	0.0393	1	0.0297	0.7369	0.6131	0.2341	0.174	0.2541	-0.0589	0.1175
DCN	-0.1288	0.4118	-0.1804	0.3622	0.4028	0.1145	0.0297	1	0.472	0.5036	0.3842	0.6319	0.2087	0.018	0.5621
$H_2CO(K_a$=0)	0.2988	0.6789	-0.2132	0.9099	0.9089	0.6638	0.7369	0.472	1	0.8341	0.7556	0.7234	0.6727	0.5264	0.7105
$H_2CO(K_a$=1)	0.1921	0.6262	-0.2431	0.6555	0.6669	0.7567	0.6131	0.5036	0.8341	1	0.8873	0.7993	0.7796	0.6823	0.8143
$H_2CO(K_a$=2)	-0.3543	0.4443	-0.063	0.4827	0.466	0.7953	0.2341	0.3842	0.7556	0.8873	1	0.7817	0.8834	0.8691	0.9289
$H_2CO(K_a=3_u$)	-0.6046	0.3952	0.0539	0.5609	0.4068	0.4929	0.174	0.6319	0.7234	0.7993	0.7817	1	0.7436	0.5551	0.8988
$H_2CO(K_a=3_l$)	-0.5911	0.3602	-0.2268	0.5075	0.427	0.7601	0.2541	0.2087	0.6727	0.7796	0.8834	0.7436	1	0.8139	0.8934
SO	-0.6924	0.1209	-0.2487	0.0518	-0.0568	0.8797	-0.0589	0.018	0.5264	0.6823	0.8691	0.5551	0.8139	1	0.8104
Continuum	-0.198	0.4145	-0.2696	0.4411	0.4256	0.7287	0.1175	0.5621	0.7105	0.8143	0.9289	0.8988	0.8934	0.8104	1

[a] c-C_3H_2 (10–9), CCH (3–2), CCH (4–3 a), (4–3 b), (4–3 c), H_2CO (K_a=0), (K_a=1), (K_a=2), ($K_a=3_u$), and ($K_a=3_l$) denote c-C_3H_2 ($10_{0,10}-9_{1,9}$ and $10_{1,10}-9_{0,9}$), c-C_3H_2 ($9_{1,8}-8_{2,7}$ and $9_{2,8}-8_{1,7}$), CCH (N =3–2, J =7/2–5/2, F =4–3 and 3–2), (N =4–3, J =7/2–5/2, F =3–3), (N =4–3, J =7/2–5/2, F =4–3 and 3–2), (N =4–3, J =9/2–7/2, F =5–4 and 4–3), H_2CO ($5_{0,5}-4_{0,4}$), ($5_{1,5}-4_{1,4}$), ($5_{2,4}-4_{2,3}$), ($5_{3,2}-4_{3,1}$), and ($5_{3,3}-4_{3,2}$), respectively.

Table 7.8: Eigenvectors of the Principal Components and their Eigenvalues in the Analysis of the Disk/Envelope

Principal Component	PC1	PC2	PC3	PC4	PC5	PC6	PC7	PC8	PC9	PC10	PC11	PC12	PC13	PC14	PC15
c-C$_3$H$_2$ (10–9)	-0.045	-0.496	-0.18	0.067	0.548	-0.084	-0.077	0.186	0.083	-0.133	0.058	0.012	-0.101	0.144	-0.555
CCH (3–2)	0.227	-0.189	0.101	-0.331	-0.459	-0.693	-0.088	0.092	0.101	-0.166	0.078	-0.043	0.083	0.1	-0.153
CCH (4–3 a)	-0.078	-0.084	0.264	0.832	-0.079	-0.26	-0.128	-0.079	-0.061	0.048	0.148	-0.201	0.219	0.109	0.029
CCH (4–3 b)	0.263	-0.341	0.013	0.182	-0.057	0.037	0.38	-0.071	0.014	-0.252	0.398	0.484	-0.17	-0.3	0.23
CCH (4–3 c)	0.248	-0.379	0.024	0.049	-0.036	-0.016	0.229	0.192	-0.158	0.273	-0.438	-0.415	-0.058	-0.481	0.059
CH$_3$OH	0.263	0.231	-0.313	0.04	0.207	-0.231	0.338	-0.52	-0.269	-0.163	-0.196	0.007	0.351	-0.009	-0.191
CS	0.177	-0.366	-0.259	-0.027	-0.35	0.431	-0.377	-0.182	-0.044	0.163	0.072	0.113	0.463	-0.006	-0.147
DCN	0.178	-0.036	0.664	-0.3	0.283	0.063	-0.01	-0.234	-0.259	0.295	0.331	-0.054	0.1	-0.031	-0.143
H$_2$CO(K_a =0)	0.335	-0.174	-0.09	-0.004	0.083	0.039	0.189	-0.276	0.481	0.292	0.005	-0.213	-0.156	0.517	0.275
H$_2$CO(K_a =1)	0.341	-0.048	-0.085	-0.025	0.213	-0.014	-0.551	-0.083	-0.34	-0.384	-0.005	-0.196	-0.248	0.04	0.392
H$_2$CO(K_a =2)	0.325	0.152	-0.019	0.165	0.059	-0.205	-0.214	0.171	-0.15	0.478	-0.274	0.593	-0.176	0.107	-0.053
H$_2$CO(K_a =3$_u$)	0.297	0.131	0.408	0.152	-0.163	0.291	-0.068	-0.155	0.311	-0.381	-0.374	0.04	-0.193	-0.041	-0.378
H$_2$CO(K_a =3$_l$)	0.308	0.191	-0.112	0.091	-0.244	0.25	0.288	0.398	-0.397	-0.037	0.269	-0.219	-0.136	0.358	-0.242
SO	0.241	0.36	-0.273	0.082	0.047	-0.085	-0.211	-0.039	0.331	0.204	0.42	-0.222	-0.156	-0.474	-0.222
Continuum	0.32	0.153	0.109	-0.016	0.299	0.049	0.018	0.504	0.282	-0.162	-0.012	0.04	0.598	-0.018	0.222
Eigenvalues	7.918	3.581	1.281	1.166	0.708	0.376	0.289	0.247	0.121	0.109	-0.023	-0.033	-0.062	-0.13	-0.548
Contribution ratio (%)	52.8	23.9	8.5	7.8	4.7	2.5	1.9	1.6	0.8	0.7	-0.2	-0.2	-0.4	-0.9	-3.7

c-C$_3$H$_2$ (10–9), CCH (3–2), CCH (4–3 a), (4–3 b), (4–3 c), H$_2$CO (K_a=0), (K_a=1), (K_a=2), and (K_a=3$_l$) denote c-C$_3$H$_2$ (10$_{0,10}$–9$_{1,9}$ and 10$_{1,10}$–9$_{0,9}$), c-C$_3$H$_2$ (9$_{1,8}$–8$_{2,7}$ and 9$_{2,8}$–8$_{1,7}$), CCH (N =3–2, J =7/2–5/2, F =4–3 and 3–2), (N =4–3, J =7/2–5/2, F =3–3), (N =4–3, J =7/2–5/2, F =4–3 and 3–2), (N =4–3, J =9/2–7/2, F =5–4 and 4–3), H$_2$CO (5$_{0,5}$–4$_{0,4}$), (5$_{1,5}$–4$_{1,4}$), (5$_{2,4}$–4$_{2,3}$), (5$_{3,2}$–4$_{3,1}$), and (5$_{3,3}$–4$_{3,2}$), respectively.
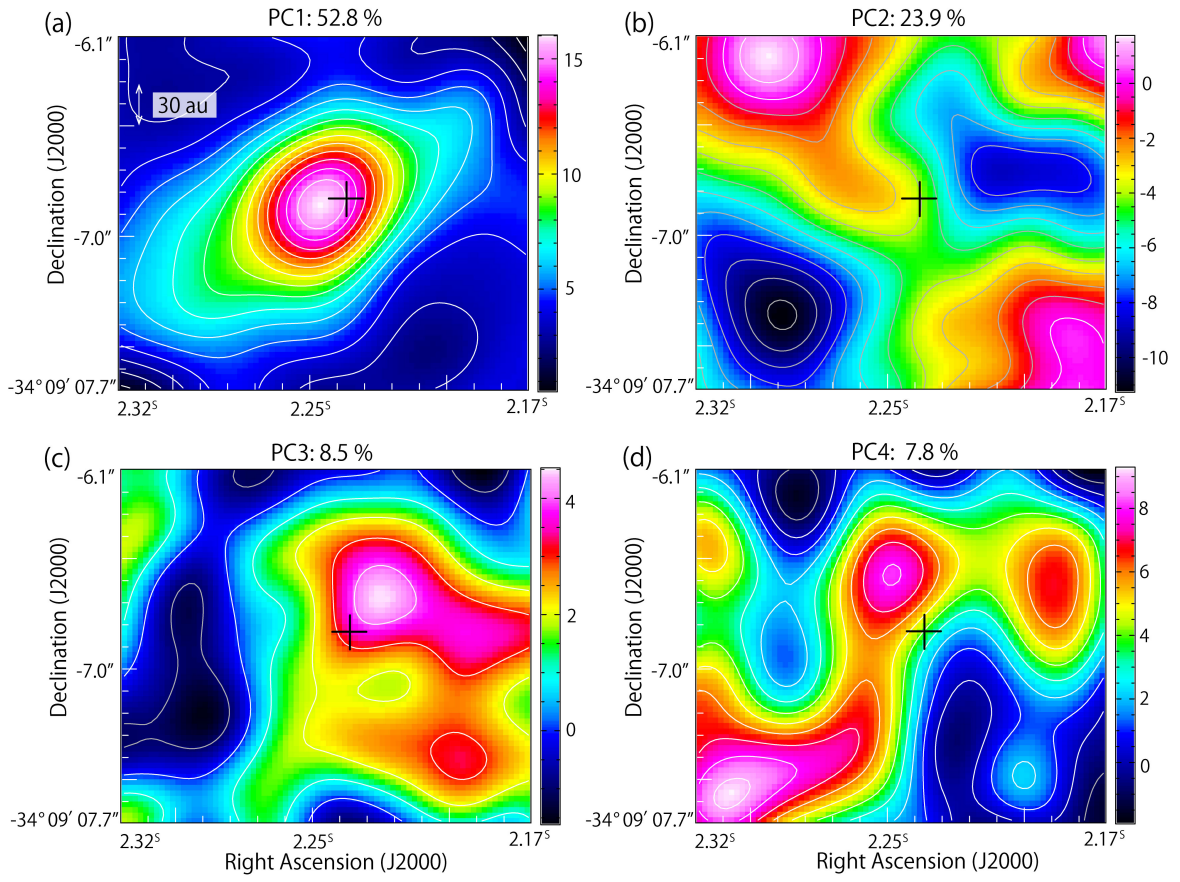
128

Figure 7.7: (a, b, c, d) The principal components, PC1 (a), PC2 (b), PC3 (c), and PC4 (d) for the disk/envelope structure (Figure 7.3). The cross marks show the continuum peak position. The contour level interval is 1.0 starting from 0.0. (e, f, g) The plot of the principal components for each distribution on the PC1-PC2 (e), PC1-PC3 (f), and PC1-PC4 (g) planes. The red dashed circles show the groups of the compact distribution (Group A) and the extended distribution (Group B). The grey dashed ellipses represent the uncertainties (See Section 6.3). c-C_3H_2 (10−9), CCH (N =3−2), (N =4−3 a), (N =4−3 b), (N =4−3 c), H_2CO (K_a=0), (K_a=1), (K_a=2), (K_a=3$_u$), and (K_a=3$_l$) denote c-C_3H_2 ($10_{0,10}$−$9_{1,9}$ and $10_{1,10}$−$9_{0,9}$), c-C_3H_2 ($9_{1,8}$−$8_{2,7}$ and $9_{2,8}$−$8_{1,7}$), CCH (N =3−2, J =7/2−5/2, F =4−3 and 3−2), (N =4−3, J =7/2−5/2, F =3−3), (N =4−3, J =7/2−5/2, F =4−3 and 3−2), (N =4−3, J =9/2−7/2, F =5−4 and 4−3), H_2CO ($5_{0,5}$−$4_{0,4}$), ($5_{1,5}$−$4_{1,4}$), ($5_{2,4}$−$4_{2,3}$), ($5_{3,2}$−$4_{3,1}$), and ($5_{3,3}$−$4_{3,2}$), respectively.
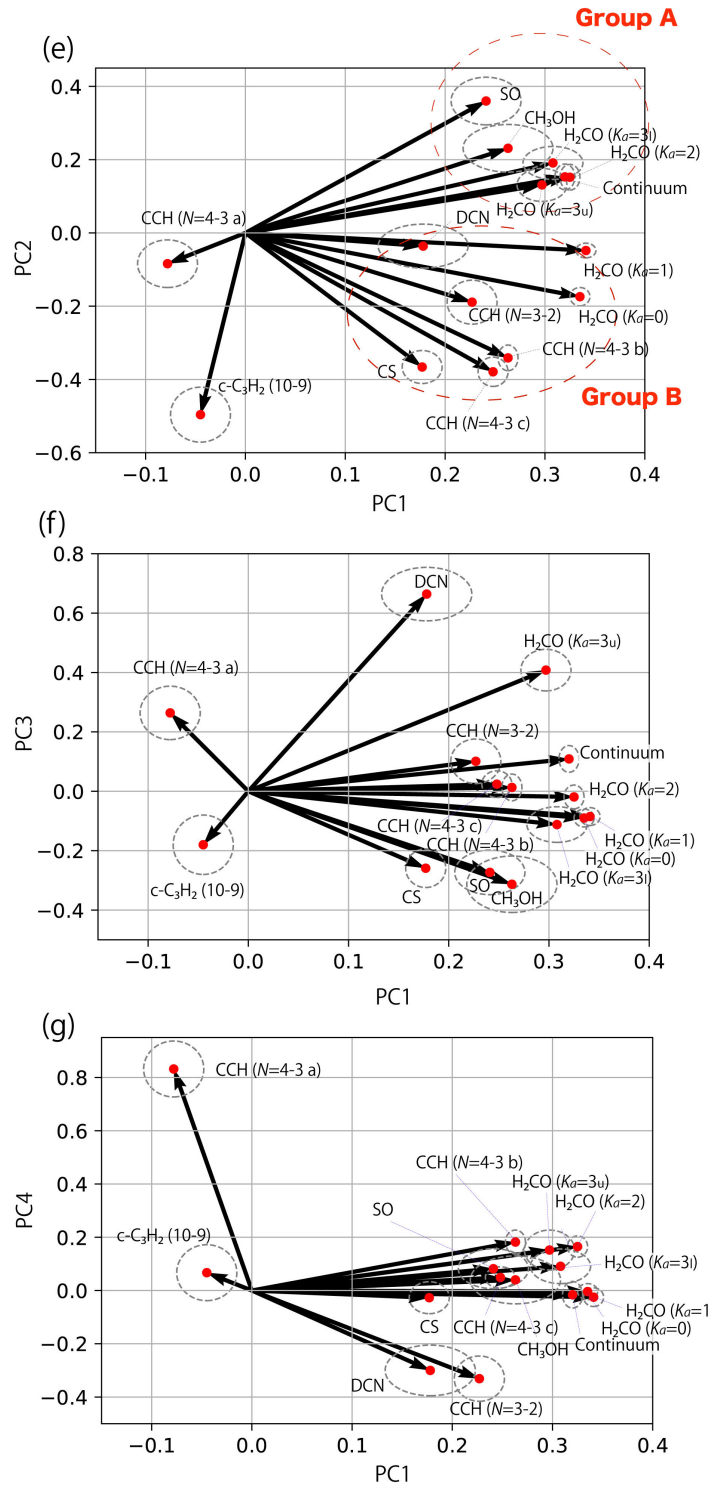
Figure 7.7: . Continued.
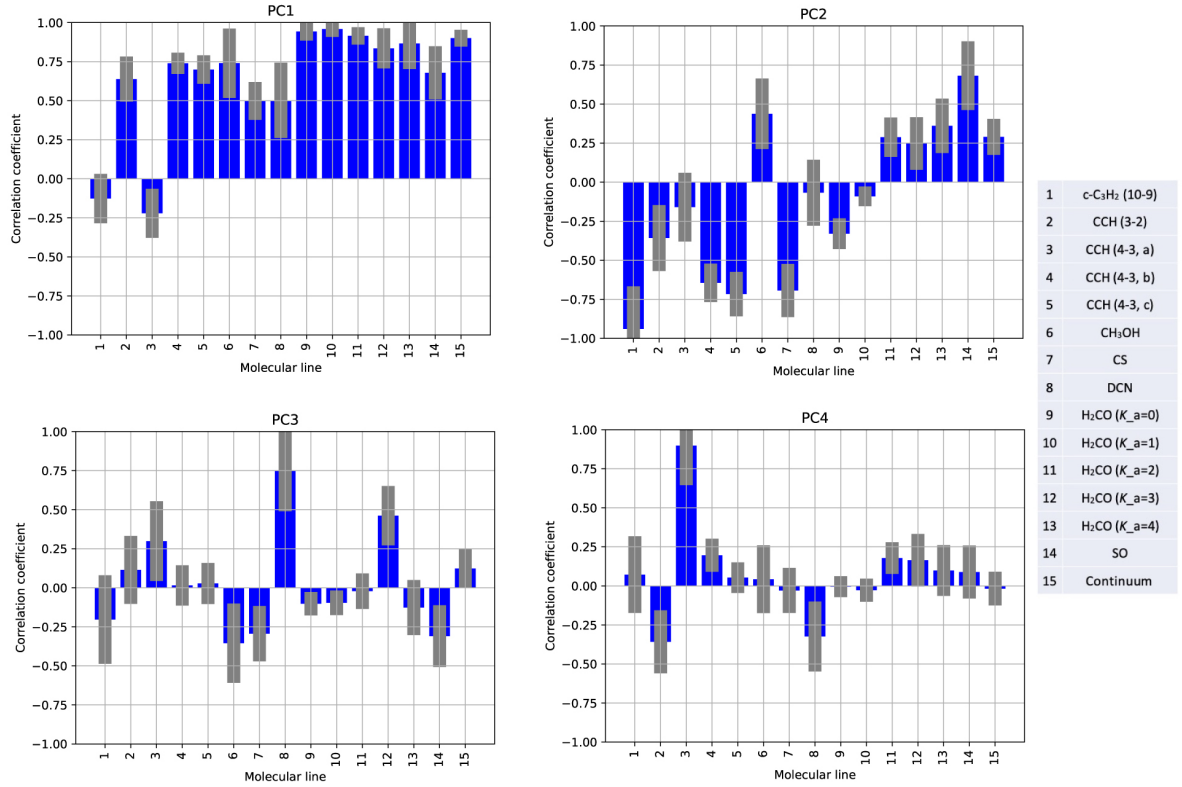
Disk/envelope scale

Figure 7.8: Correlation coefficients between the first four principal components and the molecular distributions of the disk/envelope scale. The uncertainties are shown in grey (See Section 6.3). c-C_3H_2 (10−9), CCH (3−2), (4−3 a), (4−3 b), (4−3 c), H_2CO (K_a=0), (K_a=1), (K_a=2), (K_a=3_u), and (K_a=3_l) denote c-C_3H_2 ($10_{0,10}$−$9_{1,9}$ and $10_{1,10}$−$9_{0,9}$), c-C_3H_2 ($9_{1,8}$−$8_{2,7}$ and $9_{2,8}$−$8_{1,7}$), CCH (N =3−2, J =7/2−5/2, F =4−3 and 3−2), (N =4−3, J =7/2−5/2, F =3−3), (N =4−3, J =7/2−5/2, F =4−3 and 3−2), (N =4−3, J =9/2−7/2, F =5−4 and 4−3), H_2CO ($5_{0,5}$−$4_{0,4}$), ($5_{1,5}$−$4_{1,4}$), ($5_{2,4}$−$4_{2,3}$), ($5_{3,2}$−$4_{3,1}$), and ($5_{3,3}$−$4_{3,2}$), respectively.

7.7 Comparison with the Other Protostellar Sources

As mentioned in Chapter 1, IRAS 15398−3359 is regarded as a WCCC source which is rich in carbon-chain molecules on a few 1000 au scale. Molecular distributions observed in the disk/envelope region (~100 au scale) of this source are therefore compared with those of the other WCCC sources. In the prototypical WCCC source L1527, Sakai et al. (2014a,b) reported the chemical structure around the protostar with ALMA. According to their result, CCH, CS, and c-C_3H_2 mainly trace the infalling-rotating envelope gas outward of its centrifugal barrier, while SO mainly exists near the centrifugal barrier and partly inward of it. H_2CO resides over the disk/envelope region, and CH_3OH seems to exist around the centrifugal barrier and in the disk region. For TMC-1A, which is the WCCC source in the Class I stage, the distributions of CS, SO, and SO_2 were observed with ALMA by Sakai et al. (2016). In this source, CS also traces the infalling-rotating envelope gas, while SO seems to trace the centrifugal barrier.

These characteristic features are indeed found in IRAS 15398−3359. In the PCA for the disk/envelope structure, PC2 shows that CCH and CS can be classified to one group (Group B in Figure 7.7(e)) showing the existence in the infalling-rotating envelope, while SO and CH_3OH can be classified to another group (Group A in Figure 7.7(e)) revealing more compact distributions. On the other hand, the H_2CO lines take different PC2 component values depending on their upper-state energy. This feature of H_2CO is consistent with that found in L1527, where H_2CO resides over the disk/envelope region.

An exception is c-C_3H_2. While this species clearly traces the infalling-rotating envelope in L1527, it shows a rather different distribution in IRAS 15398−3359. In order to compare the c-C_3H_2 abundances between L1527 and IRAS 15398−3359, we derive the column density ratios of c-C_3H_2 relative to H_2CO at the intensity peak positions of the c-C_3H_2 ($10_{0,10}−9_{1,9}$ and $10_{1,10}−9_{0,9}$) line (Figure 7.3(f)) by using the non-LTE radiation transfer code RADEX (van der Tak et al., 2007). Here, the northwestern and southeastern peak positions are ($15^h43^m02^s.20$, −34°09′06.″80) and ($15^h43^m02^s.28$, −34°09′07.″40), respectively (Figure 7.3(f)). The assumptions for the calculation are as follows: the ortho para ratio of H_2CO is 3 (statistical value), the H_2 density 10^6 cm^{-3}, and the gas kinematic temperature from 20 K to 40 K. We employ only the H_2CO ($K_a = 0$) line to estimate the column density of H_2CO, because the other lines (K_a =1, 2, and 3) are weak at the intensity peaks of the c-C_3H_2 ($10_{0,10}−9_{1,9}$ and $10_{1,10}−9_{0,9}$) line. On the above assumptions, the column densities of ortho c-C_3H_2 and ortho H_2CO for the northwestern side are (0.14−0.85)×10^{14} cm^{-2} and (0.72−2.5)×10^{14} cm^{-2}, respectively, while those for the southeastern side are (0.12−0.75)×10^{14} cm^{-2} and (0.92−3.5)×10^{14} cm^{-2}, respectively. A large column density range is due to the assumed temperature range. The c-C_3H_2/H_2CO ratio is calculated from the column densities derived at the same assumed temperature. In this case, the temperature dependence is mitigated. The ratios for the northwestern and southeastern sides are from 0.2 to 0.3 and from 0.1 to 0.2, respectively. These values are comparable to that found toward L1527 (0.17−0.36; Sakai et al.,

2014b). Hence, the abundance of c-C$_3$H$_2$ is not very different between this source and L1527. The peculiar distribution of c-C$_3$H$_2$ might be due to the overwhelming contribution of the outflow in this source, which is not significant in L1527.

It is interesting to note that the above characteristic distributions of molecules can also be seen in the hybrid sources, L483 and B335, where the envelope and its inner most part show WCCC and hot corino chemistry, respectively (Imai et al., 2016; Oya et al., 2017). Hot corino chemistry is characterized by rich existence of saturated complex organic molecules such as HCOOCH$_3$ and (CH$_3$)$_2$O (e.g., Bottinelli et al., 2004a,b; Sakai & Yamamoto, 2013). In these sources, the CCH distribution is extended over the envelope with deficiency toward the protostar. CS traces the infalling-rotating envelope and the inward component, while SO mainly traces the region within the centrifugal barrier. Although the central concentration of CS looks different from the case of the WCCC sources including IRAS 15398−3359, the overall feature is similar. At present, the origin of the different feature of CS between the WCCC sources and the hybrid sources is puzzling. This may originate from an insufficient spatial resolution. In addition, chemical behavior of sulfur-bearing species in the protostellar core has not been investigated well by the chemical model yet (e.g., Aikawa et al., 2008, 2012). This will be an important target for future astrochemical study.

7.8 Summary

We have imaged IRAS 15398−3359 in 15 molecular lines and the dust continuum emission and have conducted the PCA for characterization of their distributions. The PCA has been performed on the two different scales, the whole structure scale and the disk/envelope scale.

1. On the whole structure scale, we apply the PCA to 16 dataset consisting of 15 molecular line data and the Cycle 3 continuum data. PC2 can classify the samples having the positive PC1 into two groups, one with compact distributions around the protostar (Group 1) and the other showing rather extended structures (Group 2) (Figure 7.4). The molecular lines in the latter group well trace the outflow structure. The local peaks in the map of PC1 represent the blobs in the outflow, which are probably shocked regions caused by the impact of the outflow on an ambient gas.

2. On the disk/envelope scale, we use 15 dataset except for c-C$_3$H$_2$ ($9_{1,8}-8_{2,7}$ and $9_{2,8}-8_{1,7}$) for the PCA. The combination of PC1 and PC2 shows how much the distribution is concentrated toward the protostar. More compact distributions of the H$_2$CO lines with higher upper-state energies are revealed by PC2 (Figure 7.7). The characteristic molecular distributions revealed by the PCA are consistent with those in the other WCCC sources, L1527 and TMC-1A.

3. PCA helps us to characterize the molecular line distributions without preconception. It should also be noted that the result of the PCA depends on the field range which we select. Hence, it is important to determine a suitable range of interest for the PCA depending on a scientific purpose. Expanding the dataset will further

improve the analysis of this source. More systematic observations of various molecular lines toward this source as well as application of the PCA to various sources are awaited.

Chapter 8
PCA for the Cube Data of
the COM sources: L483 and B335[*]

As demonstrated in Chapter 7, the PCA can extract the characteristic features of the molecular line distributions successfully. While the PCA has been applied for the moment 0 maps which have the 2 dimensions, the molecular-line data has another dimension, the velocity. If we analyze the distributions and the velocity structures simultaneously, the complex molecular line distributions around protostars would fully be characterized. We here examine the application of PCA for image cube data (PCA-3D) observed toward the low-mass Class 0 protostellar sources, L483 and B335, at a 10−100 au scale. The purpose is to find characteristic molecular distributions in a disk-forming region of these sources in an unbiased way. The result will be an important base for investigating the chemical evolution to planetary systems. As far as we know, there is no previous report on the PCA for the cube data of any protostellar sources.

8.1 Introduction

We select L483 as the first target for the application of PCA for image cube data around a protostar at a 100 au scale, because various Complex Organic Molecules (COMs) are detected in the vicinity of the protostar (Oya et al., 2017; Agúndez et al., 2019; Jacobsen et al., 2019). L483 is a dark cloud in the Aquila Rift harboring the Class 0 protostellar source IRAS 18148−0440 (Fuller et al., 1995; Chapman et al., 2013), whose bolometric luminosity is 10−14 $L_\odot$ (Ladd et al., 1991; Shirley et al., 2000; Tafalla et al., 2000). The distance to L483 is still controversial. The distance to Aquila has been revised to be 436±9 pc by a recent survey (Ortiz-León et al., 2018). However, the Gaia-DR2 catalog within 1° of L483 shows that its location is closer, as supported by Jacobsen et al. (2019). Therefore, the conventional distance to L483 of 200 pc (Dame & Thaddeus, 1985) is adopted in this paper.

Previous single-dish observations suggested that L483 is a possible candidate for Warm Carbon-Chain Chemistry (WCCC) source because of the relatively high abundance of C_4H (Sakai et al., 2009; Hirota et al., 2009, 2010; Sakai & Yamamoto, 2013). It is also known as an interesting source for astrochemistry, where some peculiar molecules such as HCCO, HCS, HSC, and CNCN have been detected for

---

[*]Part of the content of this chapter is published as: Okoda et al. (2021), ApJ, 923, 168

the first time (e.g., Agúndez et al., 2015a,b, 2018, 2019). On the other hand, Oya et al. (2017) detected the compact emission of COMs in the vicinity of the protostar on a 100 au scale based on the ALMA observation, which reveals characteristic of hot corinos. Hence, L483 shows a hybrid chemical character of WCCC and hot corino chemistry at different scales. Jacobsen et al. (2019) also reported the detection of various COM lines in this source at a higher angular resolution (0."1−0."3; 20 au−60 au).

Many works have also been done for physical structures of L483. Particularly, structures of the outflow extending along the east to west axis and the disk/envelope system have extensively been studied since 1990s. (e.g., Fuller et al., 1995; Park et al., 2000; Tafalla et al., 2000; Jørgensen, 2004; Takakuwa et al., 2007; Oya et al., 2017, 2018; Jacobsen et al., 2019). Park et al. (2000) evaluated the outflow position angle to be 95° based on the HCO^+ (J =1−0) observation. Chapman et al. (2013) later suggested the position angle of a magnetic pseudodisk to be 36° based on the 4.5 μm Spitzer image, as well as the outflow position angle of 105° based on the shocked H_2 emission reported by Fuller et al. (1995). The kinematics of the disk/envelope system on a few 100 au scale or smaller has been studied by using molecular lines observed with ALMA. Oya et al. (2017) analyzed the velocity structure of the CS (J =5−4) emission by the infalling-rotating model and roughly evaluated the protostellar mass and the radius of the centrifugal barrier to be 0.1−0.2 $M_\odot$ and 30−200 au, respectively. They also suggested that the CS (J =5−4) emission partly traces the Keplerian disk within the centrifugal barrier. Meanwhile, Jacobsen et al. (2019) favoured an infall motion around the protostar on the basis of kinematics of the CS (J =7−6) and $H^{13}CN$ (J =4−3) emission observed at a higher resolution (∼40 au), which means the absence of a Keplerian disk down to at least 15 au in radius. The outflow inclination angle was evaluated to be between 75° and 90° (0° for a pole-on configuration) with the ALMA observations of the CS and CCH line emission by Oya et al. (2018), which confirms the nearly edge-on configuration of the disk/envelope system. Thus, high angular resolution observations with ALMA have allowed us to investigate the disk/envelope system in detail as well as the outflow structure.

The disk/envelope system of L483 harbors various COMs, as mentioned above. Although their distributions are concentrated around the protostar, the spectra toward the protostar position as well as the position-velocity diagram along the disk/envelope midplane show significant differences (Oya et al., 2017, 2018; Jacobsen et al., 2019). This implies the differentiation of the COM distributions. As well, B335, described in Chapter 5, is also known as a hybrid chemistry source containing a hot corino, which is rich in COMs. It is of fundamental importance to elucidate the characteristics of the distributions of COMs in terms of the physical structure for exploring their production chemistry through comparisons between L483 and B335 as well as among various sources. As the first step, we apply PCA to the observed cube data of L483 and B335. The molecular line features found in this chapter are discussed in Chapter 9.

8.2 Observations

8.2.1 L483

Two ALMA observations toward L483 were carried out in the Cycle 4 operation on 2017 July 8. The observational parameters are summarized in Table 8.1. Spectral lines of SO (J_N =6_5−5_4), CH_3OH ($10_{3,7}$−$11_{2,9}$, E; $4_{2,3}$−$3_{1,2}$, E; and $18_{3,16}$−$17_{4,13}$, A), CH_3CN, H_2CO ($3_{0,3}$−$2_{0,2}$ and $3_{2,2}$−$2_{2,1}$), HNCO ($10_{0,10}$−$9_{0,9}$), H_2CS, HC_3N, and $C^{18}O$ listed in Table 8.2 were observed in the frequency range from 218−237 GHz. For this observation, 40 antennas were used, where the baseline length ranged from 16 to 2647 m. The total on-source time was 14.48 minutes. The primary beam (half-power beam) width was 24."6. Spectral lines of CH_3OH ($4_{2,2}$−$5_{1,5}$, A and $5_{1,4}$−$4_{1,3}$, A), SO (J_N =7_6−6_5), SO_2, CS, HNCO ($12_{0,12}$−$11_{0,11}$), C_2H_5CN, NH_2CHO, C_2H_5OH, and SiO also listed in Table 8.2 were observed in the frequency range from 243−264 GHz. The baseline length ranged from 16 to 2647 m. The total on-source time was 16.52 minutes, and the primary beam (half-power beam) width was 23."8. Note that, in Table 8.2, the molecular lines are listed in a decreasing order of the first principal component derived later in the PCA-3D for L483 for easy comparison with the PCA results.

Both observations were conducted with the Band 6 receiver. The backend correlator for molecular line observations except for NH_2CHO ($12_{0,12}$−$11_{0,11}$) was set to a resolution of 122 kHz and a bandwidth of 59 MHz, and that for the NH_2CHO ($12_{0,12}$−$11_{0,11}$) observation was set to a resolution of 282 kHz and a bandwidth of 234 MHz. The field centers were taken to be (α_{2000}, δ_{2000})= ($18^h17^m29^s.947$, −04°39′39."55). The bandpass calibrator and the pointing calibrator were J1751+0939. The flux calibrator and the phase calibrator were J1733-1304 and J1743-0350, respectively.

Table 8.1: Observation Parameters for L483[a]

Execution block	1[a]	2[c]
Observation date(s)	2017 July 8	
Time on Source (minute)	14.48	16.52
Number of antennas	40	42
Primary beam width (″)	23.8	
Continuum bandwidth (GHz)	0.234	
Proj. baseline range (m)	16-2647	
Bandpass calibrator	J1751+0939	
Phase calibrator	J1743-0350	
Flux calibrator	J1733-1304	
Pointing calibrator	J1751+0939	

[a] These observations are conducted with Band 6.
[b] uid://A002/Xc1d834/X143e
[c] uid://A002/Xc1d834/X15b0

The data were reduced by Common Astronomy Software Applications package (CASA) 5.4.1 (McMullin et al., 2007) using a modified version of the ALMA calibration pipeline. Phase self-calibration was performed using the continuum data, and

then the solutions were applied to the spectral line data. After the self-calibration procedures, the data images were prepared by using the CLEAN algorithm, where the Briggs' weighting with a robustness parameter of 0.5 was employed. The largest angular size is 2."0 for both of these observations. The original synthesized beam sizes are summarized in Table 8.2.

8.2.2 B335

The details for the observations of B335 are described in Section 5.2. Spectral lines that we use for PCA are listed in Table 8.3. The backend correlator for CH_2DOH ($4_{2,2}-4_{2,3}$, e_0, $10_{2,8}-10_{1,9}$, o_1, and $5_{2,4}-5_{1,5}$, e_0), CH_3OH ($21_{3,18}-21_{2,19}$, A, $17_{3,14}-17_{2,15}$, A, $12_{6,7}-13_{5,8}$, E, and $2_{1,1}-1_{0,1}$, A), CS (5–4), SO (J_N =7_6-6_5), HNCO ($12_{1,12}-11_{1,11}$), CHD_2OH (6–5, K =1+, o_1), CHD_2OH (6–5, K =1+, e_0), CH_3OD (5_1-4_0, E), and CH_3OCHO ($21_{7,14}-20_{7,13}$, A, $21_{7,14}-20_{7,13}$, E, $20_{11,10}-19_{11,9}$, E) was set to a resolution of 564 kHz and a bandwidth of 234.38 MHz, and that for HCOOH ($11_{6,6}-10_{6,5}$, $11_{6,5}-10_{6,4}$, $11_{5,7}-10_{5,6}$, $11_{5,6}-10_{5,5}$, and $12_{0,12}-11_{0,11}$), NH_2CHO ($12_{0,12}-11_{0,11}$), CH_2DOH ($3_{2,1}-3_{1,2}$), CH_3OH ($4_{2,2}-5_{1,5}$, A and $18_{3,15}-18_{2,16}$, A), CH_3CHO ($14_{1,14}-13_{1,13}$, A), HNCO ($12_{0,12}-11_{0,11}$), H_2CO ($10_{1,9}-10_{1,10}$), SO_2 ($10_{3,7}-10_{2,8}$), HC_3N (27–26), CH_3CHO ($14_{0,14}-13_{0,13}$, E, v_t =1), C_2H_5OH ($13_{2,12}-12_{1,11}$), CH_3COCH_3 ($14_{11,3}-13_{10,4}$), and CH_2OHCHO ($7_{7,1}-6_{6,0}$ and $7_{7,0}-6_{6,1}$) was set to a resolution of 488.281 kHz and a bandwidth of 234.38 MHz. These original synthesized beam sizes are summarized in Table 8.3. Note that, in Table 8.3, the molecular lines are listed in a decreasing order of the first principal component derived later in the PCA-3D for B335 for easy comparison with the PCA results.

Table 8.2: Parameters of Observed Lines for L483[a]

Number	Molecule	Transition	Frequency (GHz)	$S\mu^2$ (D^2)	$E_u k^{-1}$ (K)	Original beam size	σ (Cube) (mJy beam^{-1})	σ (Moment 0) (mJy beam^{-1}km s^{-1})	σ (Spectral) (K)
1	CH_3OH	$5_{1,4}$–$4_{1,3}$, A	243.915788	15.5	50	0."228×0."146 (P.A. -59°)	4	14	0.5
2	CH_3OH	$4_{2,2}$–$5_{1,5}$, A	247.228587	4.34	61	0."227×0."144 (P.A. -59°)	4	14	0.5
3	SO	J_N=6_5–5_4	219.949442	14	35	0."244×0."141 (P.A. -65°)	4	15	0.7
4	CH_3OH	$4_{2,3}$–$3_{1,2}$, E	218.440063	13.9	46	0."244×0."142 (P.A. -65°)	4	13	0.7
5	SO	J_N=7_6–6_5	261.843721	16.4	48	0."241×0."157 (P.A. -53°)	4	15	0.5
6	CH_3OH	$10_{3,7}$–$11_{2,9}$, E	232.945797	12.1	190	0."232×0."133 (P.A. -64°)	4	14	0.6
7	H_2CO	$3_{2,1}$–$2_{2,0}$	218.760066	9.06	68	0."245×0."142 (P.A. -65°)	4	12	0.7
8	H_2CO	$3_{2,2}$–$2_{2,1}$	218.475632	9.06	68	0."245×0."142 (P.A. -65°)	4	14	0.7
9	SO_2	$14_{0,14}$–$13_{1,13}$	244.2542183	28	94	0."229×0."145 (P.A. -59°)	4	13	0.5
10	CH_3CN	$12_{2,0}$–$11_{2,0}$	220.7302611	359	97	0."242×0."138 (P.A. -65°)	4	12	0.7
11	H_2CO	$3_{0,3}$–$2_{0,2}$	218.222192	16.3	21	0."245×0."142 (P.A. -65°)	4	12	0.7
12	CS	5–4	244.9355565	19.2	35	0."229×0."146 (P.A. -58°)	4	16	0.5
13	CH_3OH	$18_{3,16}$–$17_{4,13}$, A	232.783446	21.8	447	0."230×0."132 (P.A. -64°)	4	14	0.6
14	HNCO	$10_{0,10}$–$9_{0,9}$	219.798274	25	58	0."245×0."142 (P.A. -65°)	4	12	0.7
15	HNCO	$12_{0,12}$–$11_{0,11}$	263.748625	30	82	0."239×0."157 (P.A. -53°)	4	11	0.7
16	H_2CS	$7_{1,7}$–$6_{1,6}$	236.7270204	56	59	0."229×0."132 (P.A. -63°)	4	12	0.6
17	C_2H_5CN	$11_{4,8}$–$10_{3,7}$	260.5411331	6.96	46	0."243×0."158 (P.A. -53°)	4	11	0.5
18	C_2H_5OH	$12_{1,11}$–$11_{2,9}$	244.5874939	3.93	129	0."229×0."146 (P.A. -58°)	4	13	0.5
19	NH_2CHO	$12_{1,11}$–$11_{1,10}$	261.3274496	156	85	0."241×0."158 (P.A. -53°)	4	12	0.5
20	HC_3N	26–25	236.5127888	362	153	0."229×0."132 (P.A. -63°)	4	12	0.5
21	NH_2CHO	$12_{0,12}$–$11_{0,11}$	247.390719	156	78	0."227×0."143 (P.A. -58°)	4	13	0.5
22	$C^{18}O$	2–1	219.5603541	0.024	16	0."245×0."142 (P.A. -65°)	4	12	0.7
23	SiO	6–5	260.518009	57.6	44	0."243×0."158 (P.A. -53°)	4	14	0.5

[a] Line parameters are taken from CDMS (Endres et al., 2016) and JPL (Pickett et al., 1998). The root-mean-square noise (σ) and the beam size are based on the observation data. The molecular lines are ordered by PC1 of PCA-3D for L483 in Table 8.5 for consistency in the numbering of molecular lines in this chapter.

Table 8.3: Parameters of Observed Lines for B335[a]

Number	Molecule	Transition	Frequency (GHz)	$S\mu^2$ (D^2)	$E_u k^{-1}$ (K)	Original beam size	σ (Cube) (mJy beam^{-1})	σ (Moment 0) (mJy beam^{-1}km s^{-1})
1	CH$_3$OH	$18_{3,15}$–$18_{2,16}$,A	247.610918	69.431	447	0."030×0."023 (P.A. -32°)	0.6	3
2	CH$_3$OH	$21_{3,18}$–$21_{2,19}$,A	245.223019	82.489	586	0."030×0."023 (P.A. -32°)	0.6	3
3	CH$_3$OH	$12_{6,7}$–$13_{5,8}$,E	261.704409	8.5234	360	0."029×0."022 (P.A. -29°)	0.6	3
4	CH$_3$CHO	$14_{1,14}$–$13_{1,13}$, A	260.5440195	175.9719	96	0."030×0."023 (P.A. -32°)	0.7	3
5	CH$_3$OH	$17_{3,14}$–$17_{2,15}$, A	248.282424	65.259	405	0."030×0."023 (P.A. -32°)	0.7	3
6	CH$_3$OH	$4_{2,2}$–$5_{1,5}$, A	247.228587	4.344	61	0."030×0."023 (P.A. -32°)	0.6	3
7	CH$_2$DOH	$4_{2,2}$–$4_{2,3}$, e0	244.8411349	2.54	38	0."030×0."023 (P.A. -32°)	0.6	3
8	CH$_2$DOH	$5_{2,4}$–$5_{1,5}$, e0	261.6873662	4.006	48	0."029×0."022 (P.A. -29°)	0.6	3
9	CH$_2$DOH	$3_{2,1}$–$3_{1,2}$, e0	247.6257463	2.36	29	0."030×0."023 (P.A. -32°)	0.6	3
10	CH$_3$OH	$2_{1,1}$–$1_{0,1}$, A	261.805675	5.336	28	0."029×0."022 (P.A. -29°)	0.6	3
11	HNCO	$12_{0,12}$–$11_{0,11}$	263.748625	29.956	82	0."028×0."022 (P.A. -31°)	0.8	3
12	CS	5–4	244.9355565	19.2	35	0."030×0."023 (P.A. -32°)	0.5	3
13	NH$_2$CHO	$12_{0,12}$–$11_{0,11}$	247.390719	156.32	78	0."030×0."023 (P.A. -32°)	0.6	3
14	SO	J_N =7_6–6_5	261.843721	16.4	48	0."029×0."022 (P.A. -29°)	0.6	3
15	CH$_2$DOH	$10_{2,8}$–$10_{1,9}$, o1	244.9888456	3.439	153	0."030×0."023 (P.A. -32°)	0.6	3
16	H$_2$CO	$10_{1,9}$–$10_{1,10}$	264.27014	3.1665	210	0."028×0."022 (P.A. -31°)	1	5
17	CHD$_2$OH	6–5, K =1+, o1	246.143259	-	-	0."030×0."023 (P.A. -32°)	0.6	3
18	HNCO	$12_{1,12}$–$11_{1,11}$	262.7687626	29.413	125	0."029×0."022 (P.A. -31°)	0.7	3
19	HCOOH	$11_{5,7}$–$10_{5,6}$ and $11_{5,6}$–$10_{5,5}$	247.5139713	17.633	151	0."030×0."023 (P.A. -32°)	0.6	3
20	SO$_2$	$10_{3,7}$–$10_{2,8}$	245.5634219	14.513	73	0."030×0."023 (P.A. -32°)	0.6	3
21	HCOOH	$12_{0,12}$–$11_{0,11}$	262.103481	24.157	83	0."029×0."022 (P.A. -29°)	0.6	3
22	CHD$_2$OH	6–5, K =1+, e0	246.252986	-	-	0."030×0."023 (P.A. -32°)	0.5	3
23	CH$_3$CHO	$14_{0,14}$–$13_{0,13}$, E, v_t =1	263.8319277	175.5781	300	0."028×0."022 (P.A. -31°)	0.8	3
24	HCOOH	$11_{6,6}$–$10_{6,5}$ and $11_{6,5}$–$10_{6,4}$	247.4462429	15.614	186	0."030×0."023 (P.A. -32°)	0.6	3
25	CH$_3$OD	5_1–4_0, E	245.142988	-	-	0."030×0."023 (P.A. -32°)	0.6	3
26	HC$_3$N	27–26	245.6063199	375.98	165	0."030×0."023 (P.A. -32°)	0.6	3
27	CH$_3$OCHO	$21_{7,14}$–$20_{7,13}$, A	261.74658	99.483	170	0."029×0."022 (P.A. -29°)	0.5	3
28	C$_2$H$_5$OH	$13_{2,12}$–$12_{1,11}$	262.1542443	12.186	81	0."029×0."022 (P.A. -29°)	0.7	3
29	CH$_3$OCHO	$21_{7,14}$–$20_{7,13}$, E	261.715518	97.5789	170	0."029×0."022 (P.A. -29°)	0.6	3
30	CH$_3$COCH$_3$	$14_{11,3}$–$13_{10,4}$	264.2428888	126.0112	90	0."028×0."022 (P.A. -31°)	0.9	3
31	CH$_2$OHCHO	$7_{7,1}$–$6_{6,0}$ and $7_{7,0}$–$6_{6,1}$	245.5362413	35.102	45	0."030×0."023 (P.A. -32°)	0.6	3
32	CH$_3$OCHO	$20_{11,10}$–$19_{11,9}$, E	246.308272	74.4142	204	0."030×0."023 (P.A. -32°)	0.6	3

[a] Line parameters are taken from CDMS (Endres et al., 2016) and JPL (Pickett et al., 1998) except for CH$_3$OD and CHD$_2$OH.
[b] The parameter for CH$_3$OD and CHD$_2$OH are taken from (Duan et al., 2003) and (Mukhopadhyay, 2016), respectively. The root-mean-square noise (σ) and the beam size are based on the observation data. The molecular lines are ordered by PC1 of PCA-3D for B335 in Table 8.8 for consistency in the numbering of molecular lines in this chapter.

8.3 Data for PCA

For L483 and B335, we employ 23 and 32 molecular lines listed in Tables 8.2 and 8.3, respectively. Since these two sources are fairly rich in molecular lines, spectral lines are often blended with other lines. For PCA, we only use the lines without apparent contamination from other lines. Here, line contamination is checked by using the spectral line databases: CDMS (Endres et al., 2016) and JPL (Pickett et al., 1998). The data used for the PCA are briefly summarized in Table 8.4.

8.3.1 L483

We focus on the distributions in the $2.''0 \times 2.''0$ area around the protostar, which covers the disk/envelope system, and the kinematics in the velocity range from -2.9 km s^{-1} to 14.25 km s^{-1} (V_{sys} ~5.5 km s^{-1}; Hirota et al., 2009). The latter is based on the spectral line features observed toward the protostar position (Oya et al., 2017). The spatial area and the velocity range correspond to 80×80 pixels and 50 velocity channels, respectively. To compare the molecular-line data at the same spatial and velocity resolution, the beam size is set to be $0.''3 \times 0.''3$ with a Gaussian kernel (See Section 6.1), and the velocity resolution is to be 0.35 km s^{-1}. This source is the first target that we conduct PCA for the cube data (PCA-3D), and hence, we also perform PCA for the moment 0 maps (PCA-2D) and that for the spectral line profiles (PCA-1D) for reference. The moment 0 maps and the spectral line profiles toward the continuum peak are prepared by using the $0.''3 \times 0.''3$ resolution cube, as shown in Figures 8.1 and 8.2, respectively. Distributions of most molecular lines are concentrated around the protostar. Notable exceptions are the $C^{18}O$ and SiO lines. These peak positions are apparently shifted from the protostar toward the northeastern direction. Therefore, they can be regarded as an outlier in its following analysis.

8.3.2 B335

This source harbors its disk/envelope system at a tiny scale (See Chapter 5), and hence, we focus on the distributions in the $0.''5 \times 0.''5$ area around the protostar. We conduct PCA only for the cube data (PCA-3D) for this source. The velocity range used for the data is from -0.2 km s^{-1} to 14.5 km s^{-1} (V_{sys} ~8.34 km s^{-1}; Yen et al., 2015b). For a fair comparison among the lines, we set the uniform beam size to be $0.''034 \times 0.''034$. These correspond to the spatial area and the velocity range of 100×100 pixels and 22 velocity channels, respectively. Figure 8.3 shows the moment 0 maps of the molecular lines integrated over the velocity axis.
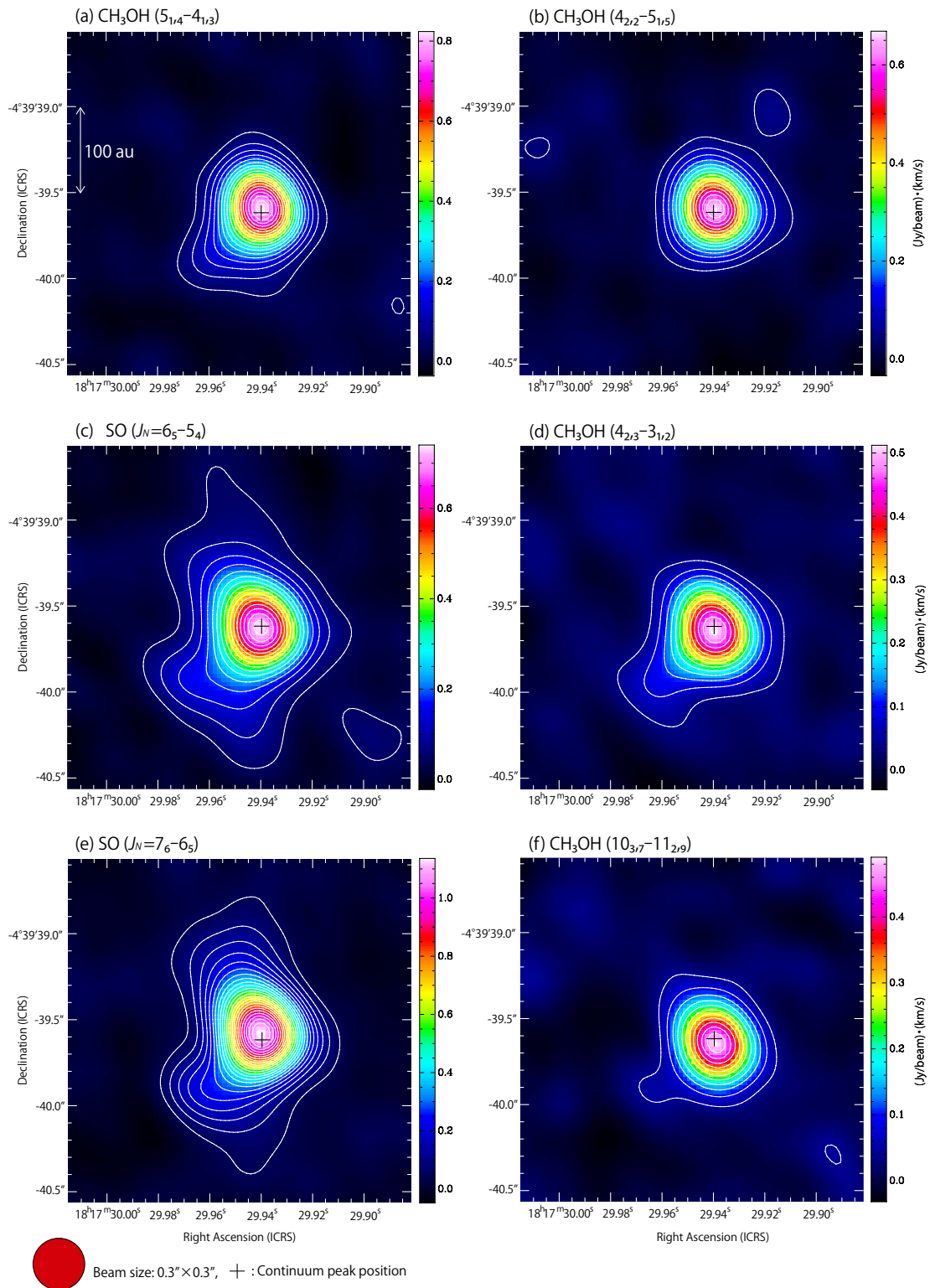
Figure 8.1: (a-w) Moment 0 maps of the 23 molecular lines in L483. The cross marks show the continuum peak position: $(\alpha_{2000}, \delta_{2000})=(18^h17^m29^s.940, -04°39'39.''60)$. The order of (a)-(w) is the same as that in Table 8.2 (1-23). The integrated velocity range is from -2.9 km s^{-1} to 14.25 km s^{-1}. Contour levels are every 3σ from 3σ, where σ is listed in Table 8.2.
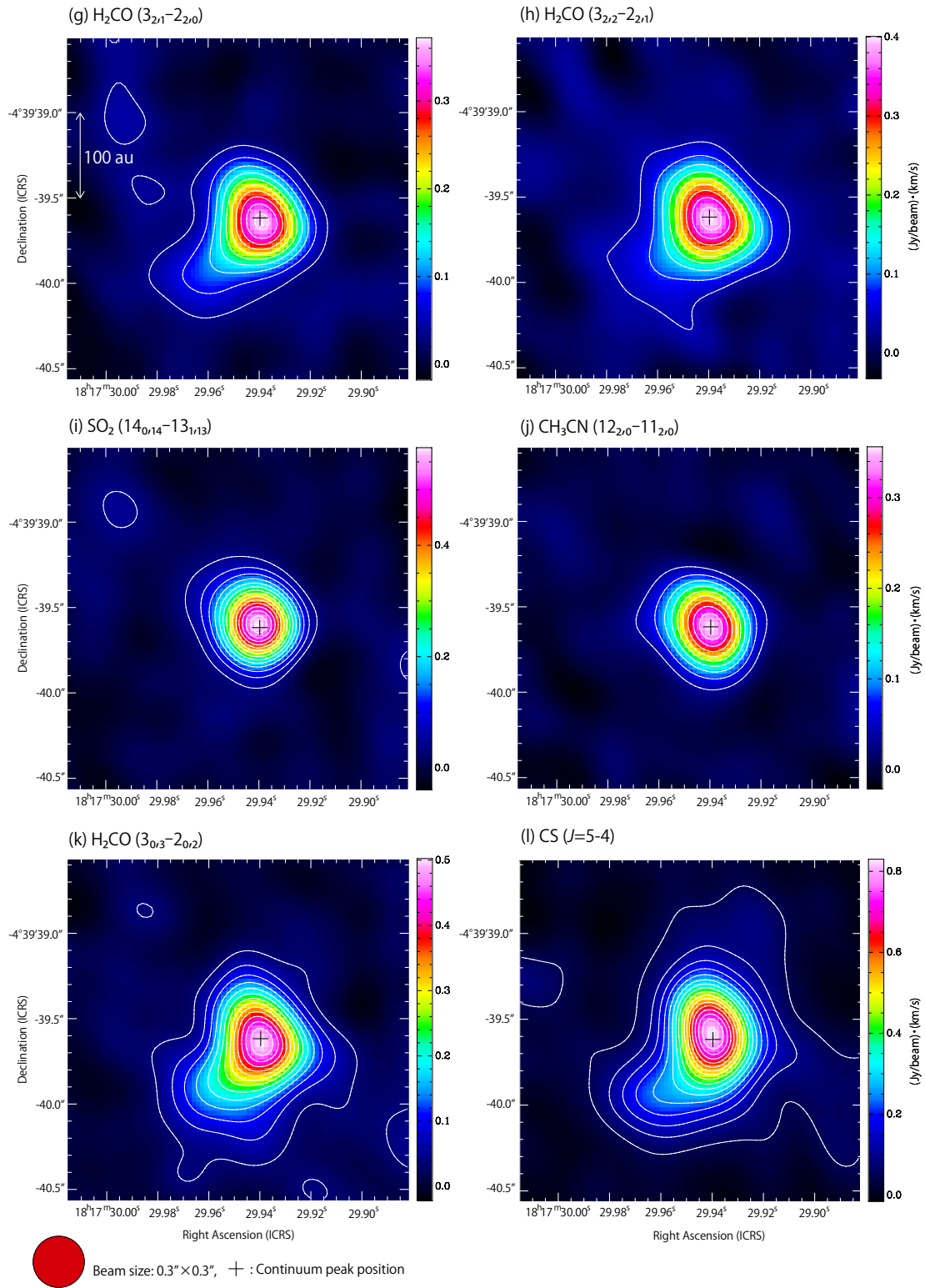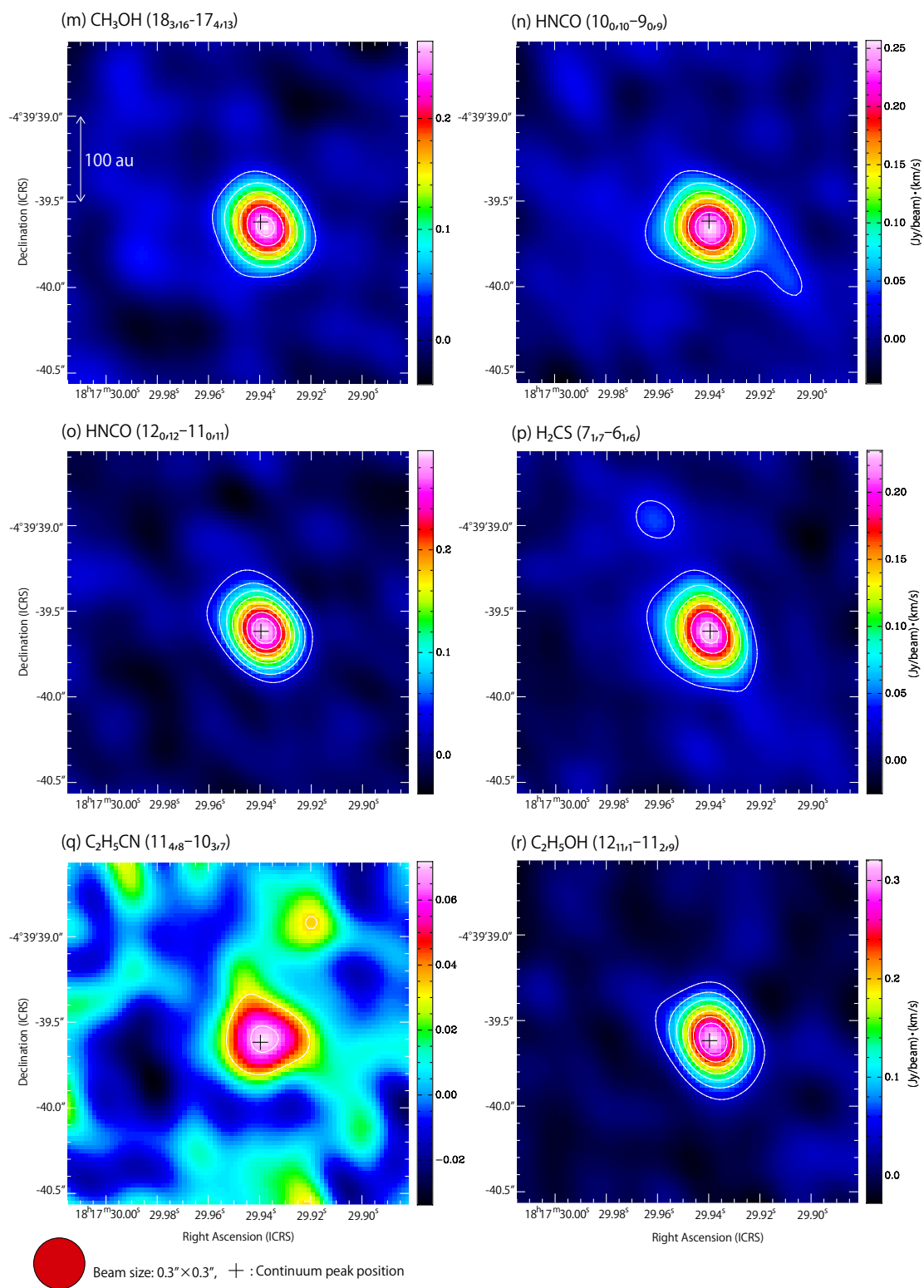
(g) H$_2$CO ($3_{2,1}$–$2_{2,0}$)

(h) H$_2$CO ($3_{2,2}$–$2_{2,1}$)

(i) SO$_2$ ($14_{0,14}$–$13_{1,13}$)

(j) CH$_3$CN ($12_{2,0}$–$11_{2,0}$)

(k) H$_2$CO ($3_{0,3}$–$2_{0,2}$)

(l) CS (J=5-4)

100 au

Beam size: 0.3″×0.3″, $+$: Continuum peak position

Figure 8.1: (Continued.)

(m) CH$_3$OH (18$_{3,16}$–17$_{4,13}$)

(n) HNCO (10$_{0,10}$–9$_{0,9}$)

(o) HNCO (12$_{0,12}$–11$_{0,11}$)

(p) H$_2$CS (7$_{1,7}$–6$_{1,6}$)

(q) C$_2$H$_5$CN (11$_{4,8}$–10$_{3,7}$)

(r) C$_2$H$_5$OH (12$_{11,1}$–11$_{2,9}$)

Beam size: 0.3″×0.3″,   + : Continuum peak position

Figure 8.1: (Continued.)

(s) NH$_2$CHO (12$_{1,11}$–11$_{1,10}$)

(t) HC$_3$N (J=26-25)

(u) NH$_2$CHO (12$_{0,12}$–11$_{0,11}$)

(v) C^{18}O (J=2–1)

(w) SiO (6–5)

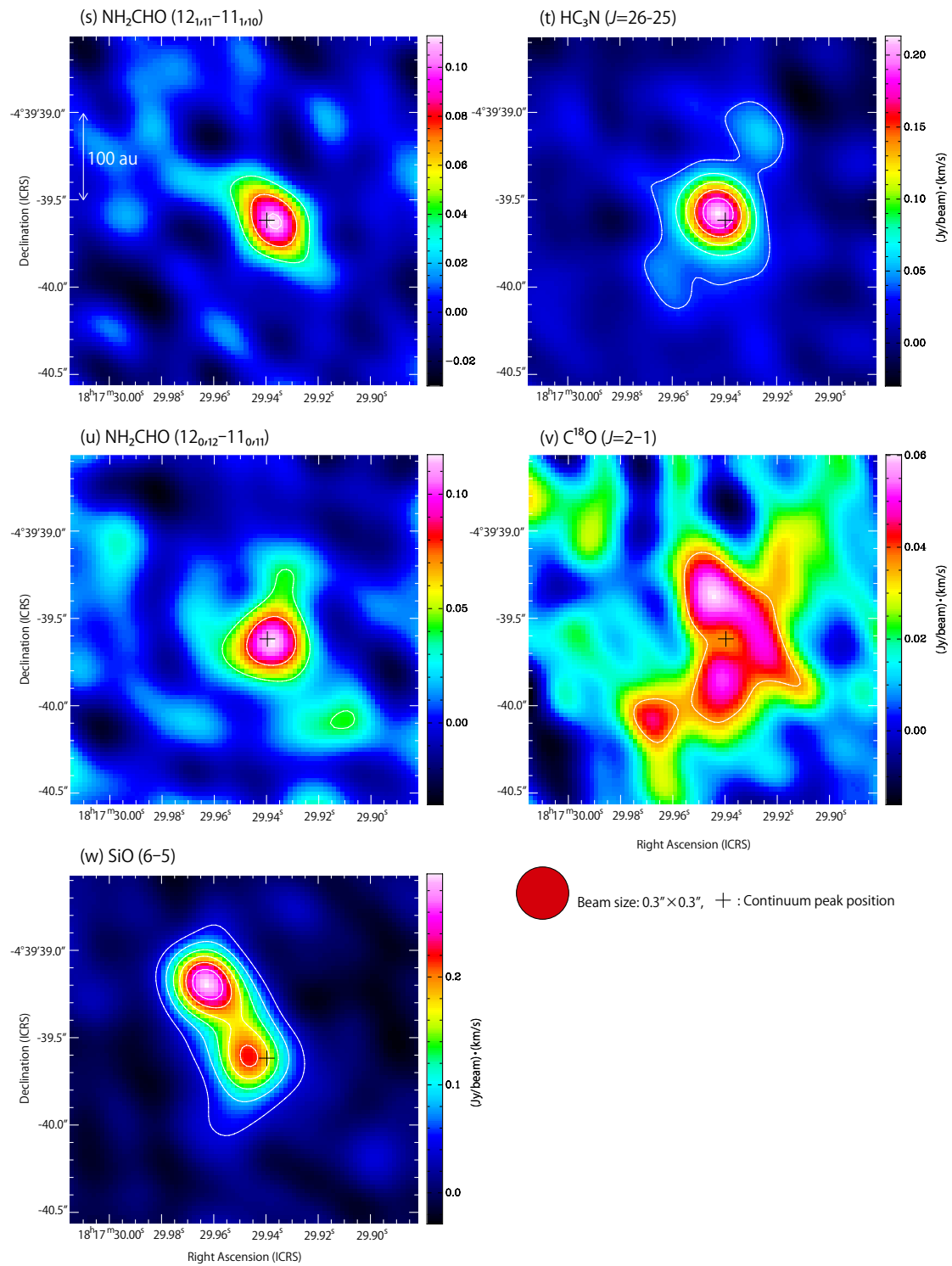Beam size: 0.3″×0.3″, + : Continuum peak position
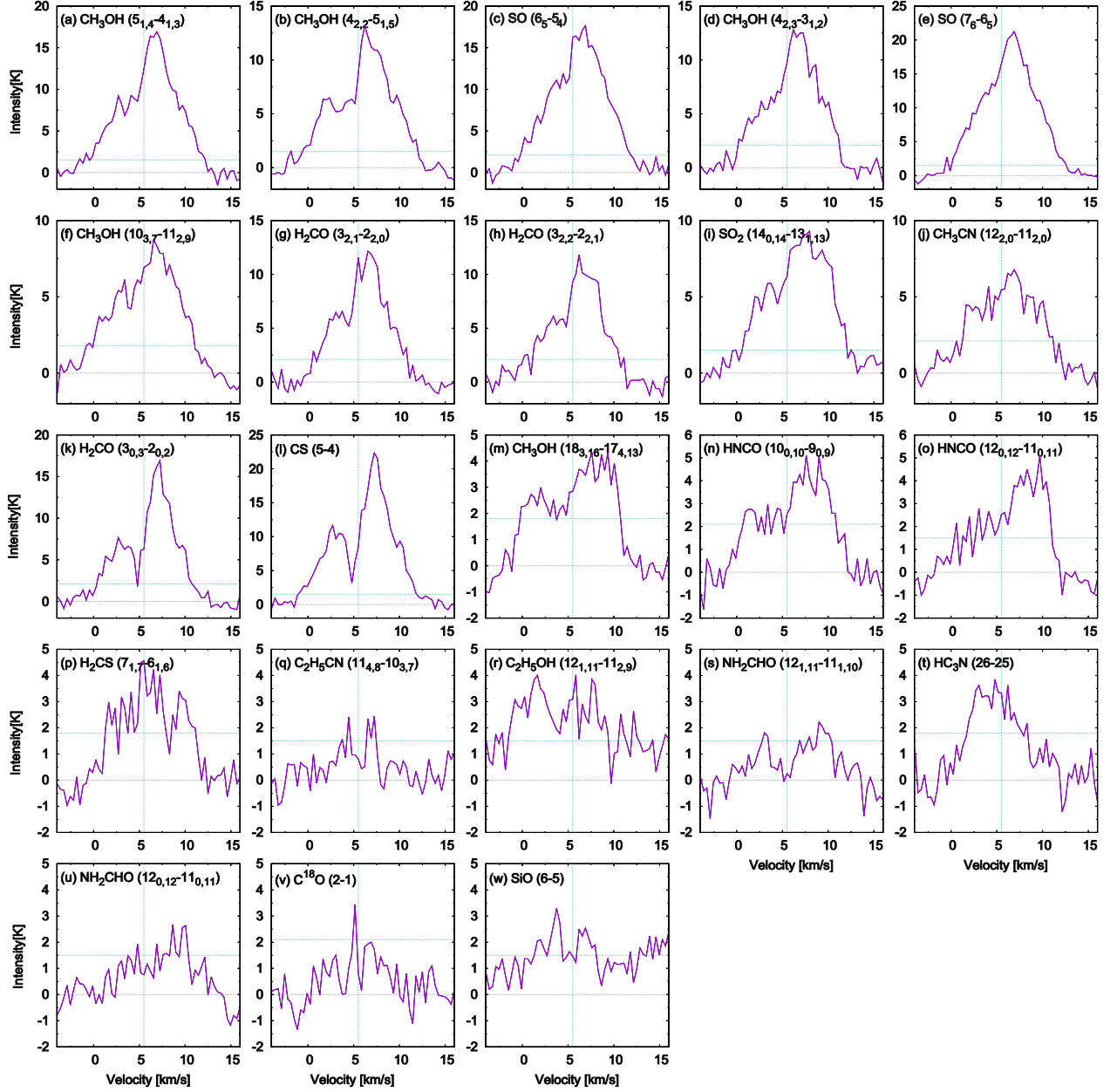
Figure 8.1: (Continued.)

145

Figure 8.2: (a-w) Molecular line profiles observed toward the continuum peak of L483. The spectra are prepared for a circular region with a diameter of 0.″5 centered at the continuum peak. The order of (a)-(w) is the same as that in Table 8.2 (1-23). The horizontal green dotted line in each panel represents 3σ for each spectrum, where σ is listed in Table 8.2. The horizontal black dotted line in each panel represents the zero-level intensity. The vertical green dotted lines represent the systemic velocity of 5.5 km s^{-1} (Hirota et al., 2009).
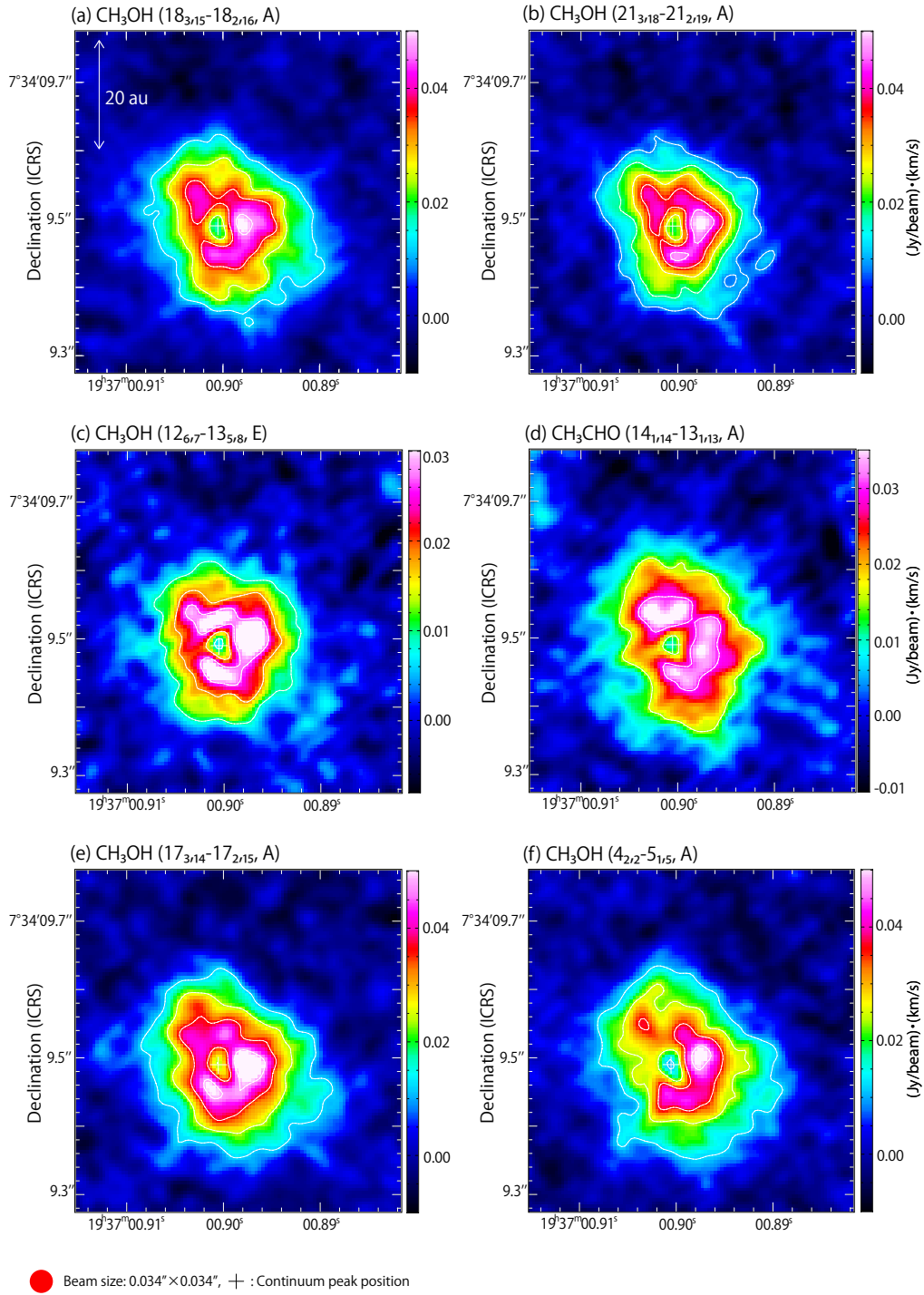
Figure 8.3: Moment 0 maps of the 32 molecular lines in B335. A uniform spatial resolution of 0."034×0."034 is applied for these images. Hence, the images of HCOOH ($12_{0,12}-11_{0,11}$), NH_2CHO ($12_{0,12}-11_{0,11}$), CH_2DOH ($4_{2,2}-4_{2,3}$, e_0), and CH_3OH ($4_{2,2}-5_{1,5}$, A) are slightly different from these presented in Chapter 5. The cross marks show the continuum peak position: (α_{2000}, δ_{2000}) = ($19^h37^m00^s.90\pm0.00001$, $+7°34'09."49\pm0.00021$). The order of (a)-(af) is the same as that in Table 8.3 (1-32). The integrated velocity range is from -0.2 km s^{-1} to 14.5 km s^{-1}. Contour levels are every 3σ from 3σ, where σ is listed in Table 8.3.

Figure 8.3: (Continued.)
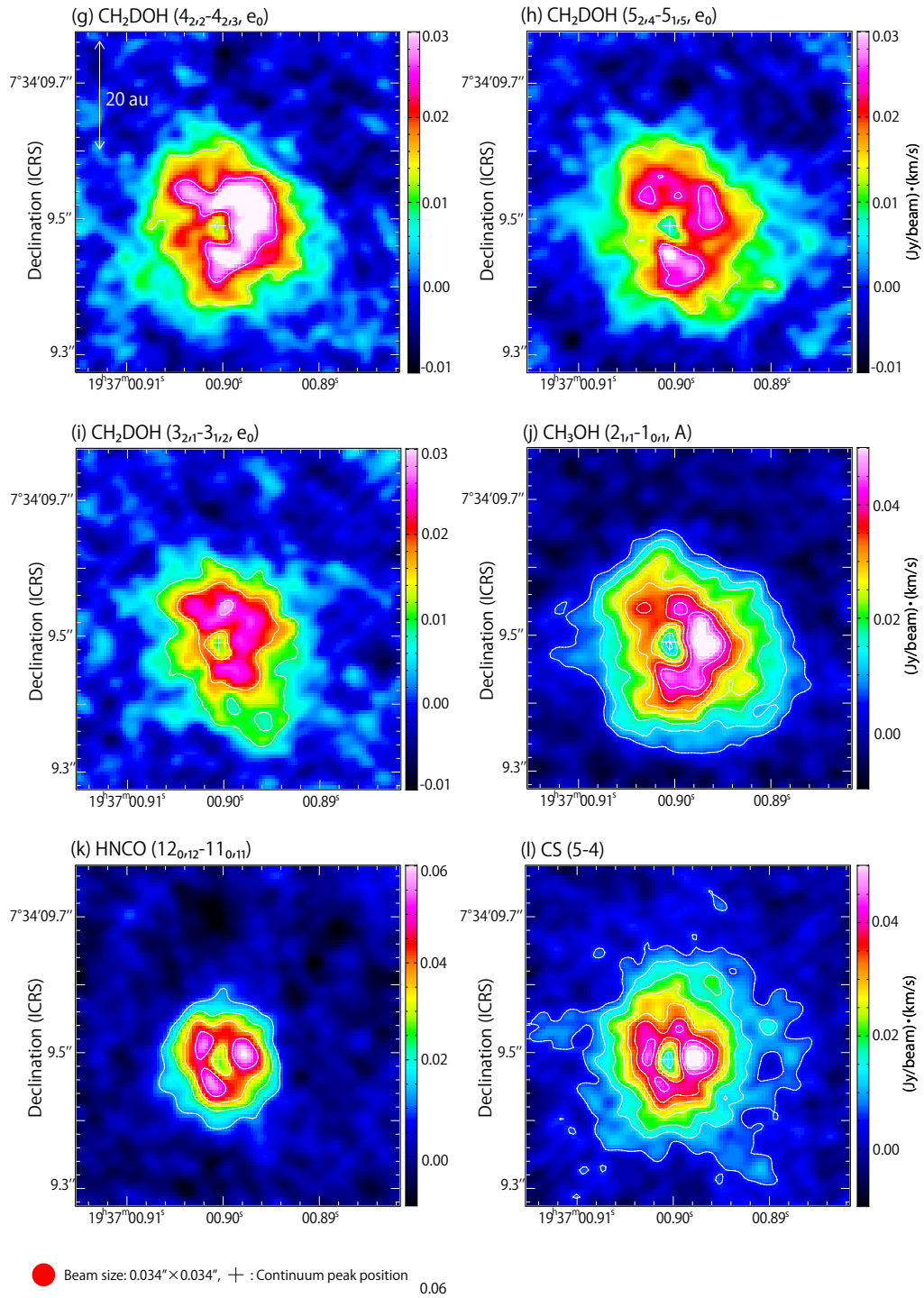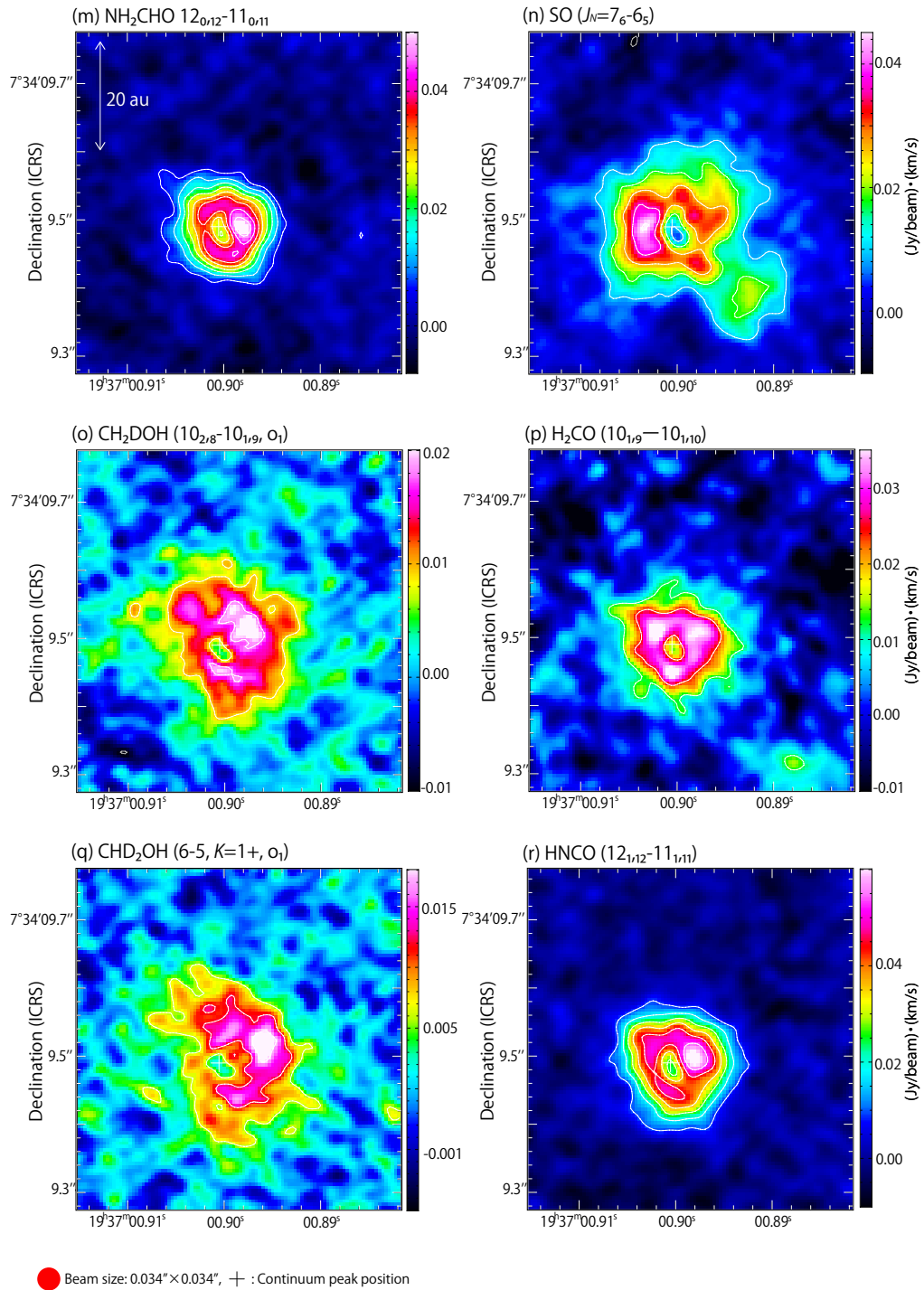
(m) NH$_2$CHO $12_{0,12}$-$11_{0,11}$

(n) SO (J_N=7_6-6_5)

(o) CH$_2$DOH ($10_{2,8}$-$10_{1,9}$, o_1)

(p) H$_2$CO ($10_{1,9}$—$10_{1,10}$)

(q) CHD$_2$OH (6-5, K=1+, o_1)

(r) HNCO ($12_{1,12}$-$11_{1,11}$)

Beam size: 0.034″×0.034″, + : Continuum peak position

Figure 8.3: (Continued.)

149

(s) HCOOH ($11_{5,7}$-$10_{5,6}$ and $11_{5,6}$-$10_{5,5}$)

(t) SO$_2$ ($10_{3,7}$-$10_{2,8}$)

(u) HCOOH ($12_{0,12}$-$11_{0,11}$)

(v) CHD$_2$OH (6-5, K=1+, e$_0$)

(w) CH$_3$CHO ($14_{0,14}$-$13_{0,13}$, E, v_t=1)

(x) HCOOH ($11_{6,6}$-$10_{6,5}$ and $11_{6,5}$-$10_{6,4}$)

Beam size: 0.034″×0.034″, $+$: Continuum peak position

Figure 8.3: (Continued.)

150

(y) CH$_3$OD (5$_1$-4$_0$, E)

(z) HC$_3$N (27-26)

(aa) CH$_3$OCHO (21$_{7,14}$-20$_{7,13}$, A)

(ab) C$_2$H$_5$OH (13$_{2,12}$-12$_{1,11}$)

(ac) CH$_3$OCHO (21$_{7,14}$-20$_{7,13}$, E)

(ad) CH$_3$COCH$_3$ (14$_{11,3}$-13$_{10,4}$)

⬤ Beam size: 0.034″×0.034″, ✛ : Continuum peak position

Figure 8.3: (Continued.)

(ae) CH$_2$OHCHO ($7_{7,1}$-$6_{6,0}$ and $7_{7,0}$-$6_{6,1}$)

(af) CH$_3$OCHO ($20_{11,10}$-$19_{11,9}$, E)

Beam size: 0.034″×0.034″, + : Continuum peak position

Figure 8.3: (Continued.)

Table 8.4: . Data for the PCA in L483 and B335

	L483	B335
Number of lines	23	32
Beam size	0.″3×0.″3	0.″034×0.″034
Area	2.″0×2.″0	0.″5×0.″5
	80 (pix.) × 80 (pix.)	100 (pix.) × 100 (pix.)
	400 (au) × 400 (au)	50 (au) × 50 (au)
Velocity	-2.9 km s^{-1} to 14.25 km s^{-1}	-0.2 km s^{-1} to 14.5 km s^{-1}
	50 channel	22 channel

8.4 PCA for the Cube Data (PCA-3D): L483

We conduct PCA-3D of the 23 molecular lines along the procedure described in Chapter 6. The eigenvalues and eigenvectors of the first 7 PCs are given in Table 8.5. As shown in Table 8.5, PC1 has the largest contribution ratio, 45.0 %. The contribution ratios of PC2 and PC3 are 11.4 % and 6.7 %, respectively, and hence, the sum of the three contribution ratios is 63.1 %. Figure 8.4 shows a scree plot of the contribution ratios for the principal components. In Figure 8.4(a), the contributions of PCi ($i \geq 3$) are relatively smaller than the first two components. Nevertheless, PC3 shows a characteristic distribution, as described later. Hence, we consider the three components here.

8.4.1 Characteristic Features of the Principal Components

Figures 8.5(d), (e), and (f) show the velocity channel maps of the three principal components. As shown in Figure 8.5(d), PC1 represents a distribution around the protostar. This is clearly seen in the moment 0 map of PC1 (Figure 8.5(a)). In particular, this component (PC1) slightly extends toward the north and south directions at the blueshifted and redshifted velocities, respectively (Figure 8.5(d)). These structures represent a rotation motion of the disk/envelope system, as reported previously (Oya et al., 2017; Jacobsen et al., 2019). Figure 8.6 shows the spectral line profiles of the principal components, which are prepared for a circular region with a diameter of 0.''5 centered at the continuum peak position. The spectral line profile of PC1 shows a broad line width with an intensity dip around the systemic velocity, 5.5 km s^{-1} (Figure 8.6(a)). Moreover, the peak intensity of the redshifted component is stronger than that of the blueshifted one. A similar trend of the spectrum is reported for a few molecular lines such as CS ($J =5-4$ and $7-6$), SO ($J_N =7_6-6_5$), HCN ($J =4-3$), and HCO$^+$ ($J =4-3$) (Oya et al., 2017; Jacobsen et al., 2019).

PC2 represents a compact distribution around the protostar, as seen in the moment 0 map of PC2 (Figure 8.5(b)). It is more compact than that of PC1. Although the channel maps of PC2 (Figure 8.5(e)) are noisy because of a relatively low contribution, the following features are seen: its distribution mostly shows faint or even negative intensities around the systemic velocity (5.5 km s^{-1}), whereas the emission toward the protostar is seen in the maps of 9.35 km s^{-1} and 11.1 km s^{-1} (Figure 8.5(e)). This is also shown up in the spectral line profile of PC2 (Figure 8.6(b)). The two intensity peaks are visible around 0 km s^{-1} and 10 km s^{-1}, where the redshifted one is much stronger than the blueshifted one. These peaks are offset by $\sim \pm 5$ km s^{-1} from the systemic velocity. The blueshifted one is lower than 3σ level of PC2, so that it cannot be seen clearly in the channel maps. Thus, PC2 reproduces the distribution concentrated around the protostar, which reveals the high-velocity components.

Figures 8.5(c) and 8.5(f) show the moment 0 map and the velocity channel maps of PC3, respectively. The moment 0 map shows the positive distribution extending to northeast from the protostar and the negative crescent-like distribution surrounding the protostar on its southern side. In Figure 8.5(f), the former is marginally

seen in the 0.6 km s^{-1} panel, whereas the latter is recognized in the 5.85 and 7.6 km s^{-1} panels. Figure 8.6(c) shows the spectrum of PC3 for the 0."5 area around the protostar. It has intensity peaks at -1 km s^{-1} and 4 km s^{-1}, both of which are seen in the -1.15 km s^{-1} and 4.1 km s^{-1} panels of Figure 8.5(f). A broad dip around 8 km s^{-1} in the PC3 spectrum is also consistent with the channel maps. In short, PC3 represents rather extended positive and negative distributions in the northeastern and southern parts, respectively.

8.4.2   Characteristics of the Molecular Lines Extracted by the PCA

In order to investigate the molecular-line distributions, we calculate the correlation coefficients between the principal components and the cube data for each molecular line, by using the method described in Section 6.2. A large correlation coefficient means that the corresponding principal component well represents the distribution and the velocity structure of the corresponding molecular line. Figure 8.7(a) shows the correlation coefficients for PC1, where the uncertainties due to the observation noise are evaluated by the method described in Section 6.3. The 16 molecular lines have the correlation coefficients larger than 0.5, and hence, these molecular-line data can mostly be reproduced by using PC1: these lines indeed have the characteristic distribution and spectral profile of PC1 described above (Figures 8.1 and 8.2). On the other hand, $C^{18}O$ and SiO have a small negative correlation coefficient of PC1 (Figure 8.7(a)).

The molecular lines less correlated with PC1 (lines 17−23) tend to have relatively large correlation coefficients of PC2, PC3, or both of them (Figures 8.7(b) and (c)). Figure 8.7(b) shows that the two NH_2CHO ($12_{11,1}-11_{11,0}$ and $12_{0,12}-11_{0,11}$) lines have the largest positive correlation with PC2. The HNCO ($10_{0,10}-9_{0,9}$ and $12_{0,12}-11_{0,11}$) lines and the high excitation line of CH_3OH ($18_{3,16}-17_{4,13}$, A) have a similar trend to NH_2CHO. These characteristic features are discussed later (Chapter 9). On the other hand, $C^{18}O$ has a negative correlation coefficient with PC2 as large as -0.6. It has the largest negative correlation coefficient (-0.75) with PC3, and hence, PC3 largely contributes to the distribution of $C^{18}O$. In fact, the negative "crescent" part in the moment 0 map of PC3 (Figure 8.5(c)) resembles the $C^{18}O$ distribution (Figure 8.1(v)). C_2H_5CN and SiO are positively correlated with PC3, which can reproduce an intensity dip around the systemic velocity and faint high-velocity components in each line profile (Figures 8.2(q) and (w)). Furthermore, both SiO and PC3 indeed show the component elongated from the continuum peak to the northeastern direction (Figure 8.1(w) and Figure 8.5(c)).

In PCA-3D, we extract the characteristic features of the molecular line distributions in an unbiased way. By using the contribution of PCi for each molecular distribution, we can classify them and discuss their formation processes. Such analyses for PCA-3D are described in Chapter 9.

8.4.3 Velocity Structure of PC1

Since most molecular lines are correlated with PC1, we prepare the moment 1 map of PC1 (Figure 8.8(a)) in order to study the 'standard' velocity structure of our data set. The velocity gradient can clearly be seen along the disk/envelope direction (P.A. 15°), as reported previously (Oya et al., 2017). The position velocity (PV) diagrams of PC1 along the disk/envelope direction and the direction perpendicular to it are shown in Figures 8.8(b) and (c), respectively. The PV diagram along the disk/envelope direction shows a clear velocity gradient (Figure 8.8(b)). On the other hand, an apparent gradient cannot be seen in the PV diagram along the line perpendicular to the disk/envelope system (Figure 8.8(c)). Hence, the velocity structure of PC1 is likely a rotation motion around the protostar.

This result is consistent with the previous reports. Oya et al. (2017) interpreted the velocity structure of CS (J =5−4) as a combination of the infalling rotating motion and the Keplerian motion around the protostar. They also reported that the velocity gradient of SO (J_N =7$_6$−6$_5$) originates from the rotation motion in the inner part of the disk/envelope system. Although these molecular distributions are different from each other on a scale larger than 2″, as reported by Oya et al. (2017), they are essentially similar to each other on a smaller scale considered in this study: it is revealed by high correlations of CS (J =5−4) and SO (J_N =7$_6$−6$_5$) with PC1. The kinematic structure of CS (J =7−6) line was also investigated by Jacobsen et al. (2019), whose moment 1 map shows the velocity gradient along the north to south axis. They further reported the rotation motion by using the lines of complex organic molecules (COMs). Thus, PCA-3D successfully extracts not only the most common distribution but the associated velocity structure. Although the lines showing the high correlation with PC1 (lines 1-16) come from the disk/envelope system around the protostar, it is difficult to distinguish between the infalling rotating motion and the Keplerian motion from this result.

It should be noted that PC2 and PC3 have negative intensities in their channel maps (Figures 8.5(e) and (f)). For these cases, moment 1 maps are not very useful. We need to directly inspect the principal component data (velocity channel maps) to discuss their velocity structures.

Table 8.5: Eigenvectors of the Principal Components and their Eigenvalues for PCA-3D for L483

Number	Molecule	PC1	PC2	PC3	PC4	PC5	PC6	PC7
1	CH_3OH ($5_{1,4}$–$4_{1,3}$, A)	0.286	-0.072	0.015	0.062	-0.017	-0.027	-0.133
2	CH_3OH ($4_{2,2}$–$5_{1,5}$, A)	0.278	0.003	-0.019	0.021	-0.055	-0.075	-0.113
3	SO (6_5–5_4)	0.277	-0.143	-0.037	-0.002	-0.034	0.187	0.115
4	CH_3OH ($4_{2,3}$–$3_{1,2}$, E)	0.276	-0.041	0.084	-0.099	0.043	-0.002	-0.13
5	SO (7_6–6_5)	0.27	-0.142	-0.138	0.051	-0.073	0.181	0.122
6	CH_3OH ($10_{3,7}$–$11_{2,9}$, E)	0.27	-0.037	0.054	0.019	0.023	-0.016	0.104
7	H_2CO ($3_{2,1}$–$2_{2,0}$)	0.256	-0.197	0.056	-0.137	0.027	-0.009	-0.077
8	H_2CO ($3_{2,2}$–$2_{2,1}$)	0.255	-0.208	0.123	-0.129	0.106	-0.195	-0.069
9	SO_2 ($14_{0,14}$–$13_{1,13}$)	0.255	0.112	-0.124	0.176	-0.081	0.046	-0.098
10	CH_3CN ($12_{2,0}$–$11_{2,0}$)	0.247	0.031	0.098	0.168	-0.081	-0.032	-0.13
11	H_2CO ($3_{2,1}$–$2_{2,0}$)	0.239	-0.124	0.008	-0.144	0.218	-0.01	-0.067
12	CS (5–4)	0.236	-0.065	-0.124	-0.057	0.267	-0.039	-0.141
13	CH_3OH ($18_{3,16}$–$17_{4,13}$, A)	0.2	0.32	-0.072	-0.047	0.193	0.075	0.07
14	HNCO ($10_{0,10}$–$9_{0,9}$)	0.185	0.26	0.033	0.176	0.239	-0.077	0.318
15	HNCO ($12_{0,12}$–$11_{0,11}$)	0.171	0.312	-0.186	0.014	0.107	-0.001	-0.038
16	H_2CS ($7_{1,7}$–$6_{1,6}$)	0.165	0.073	-0.142	0.241	-0.443	0.323	0.299
17	C_2H_5CN ($11_{4,8}$–$10_{3,7}$)	0.123	0.052	0.443	-0.315	-0.27	-0.421	0.539
18	C_2H_5OH ($12_{1,11}$–$11_{2,9}$)	0.092	0.125	-0.112	-0.531	-0.156	-0.013	-0.094
19	NH_2CHO ($12_{1,11}$–$11_{1,10}$)	0.078	0.351	-0.01	0.391	0.1	-0.284	0.163
20	HC_3N (26–25)	0.07	-0.274	0.241	0.409	-0.41	-0.223	-0.287
21	NH_2CHO ($12_{0,12}$–$11_{0,11}$)	0.021	0.454	-0.173	-0.126	-0.325	-0.37	-0.419
22	$C^{18}O$ (2–1)	-0.055	-0.373	-0.603	0.106	0.103	-0.556	0.211
23	SiO (6–5)	-0.062	0.044	0.434	0.213	0.388	-0.113	-0.163
	Eigenvalues	10.86	2.758	1.62	1.439	1.198	1.051	0.916
	Contribution ratio (%)	45.0	11.4	6.7	6.0	5.0	4.4	3.8

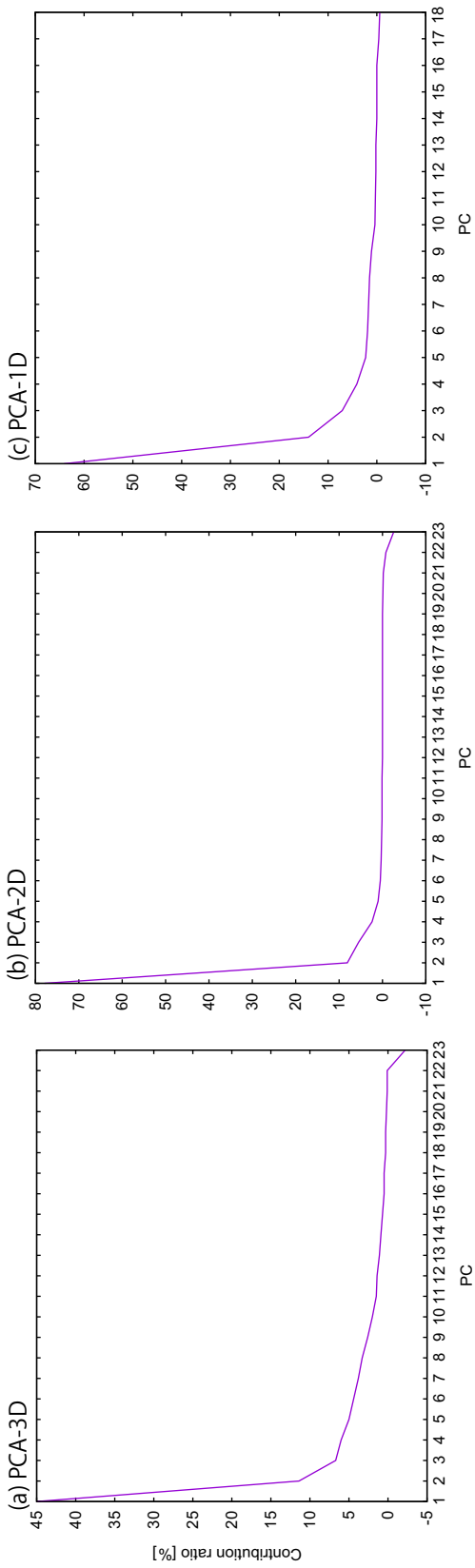These values are also called as 'loadings'.

Figure 8.4: Scree plots of the contribution ratios for the principal components for L483. (a) PCA for the cube data (Section 8.4; Table 8.5). (b) PCA for the moment 0 maps (Section 8.5; Table 8.6). (c) PCA for the spectral line profiles (Section 8.6; Table 8.7). Negative contribution ratios found in higher-order PCs are due to the observation noise.
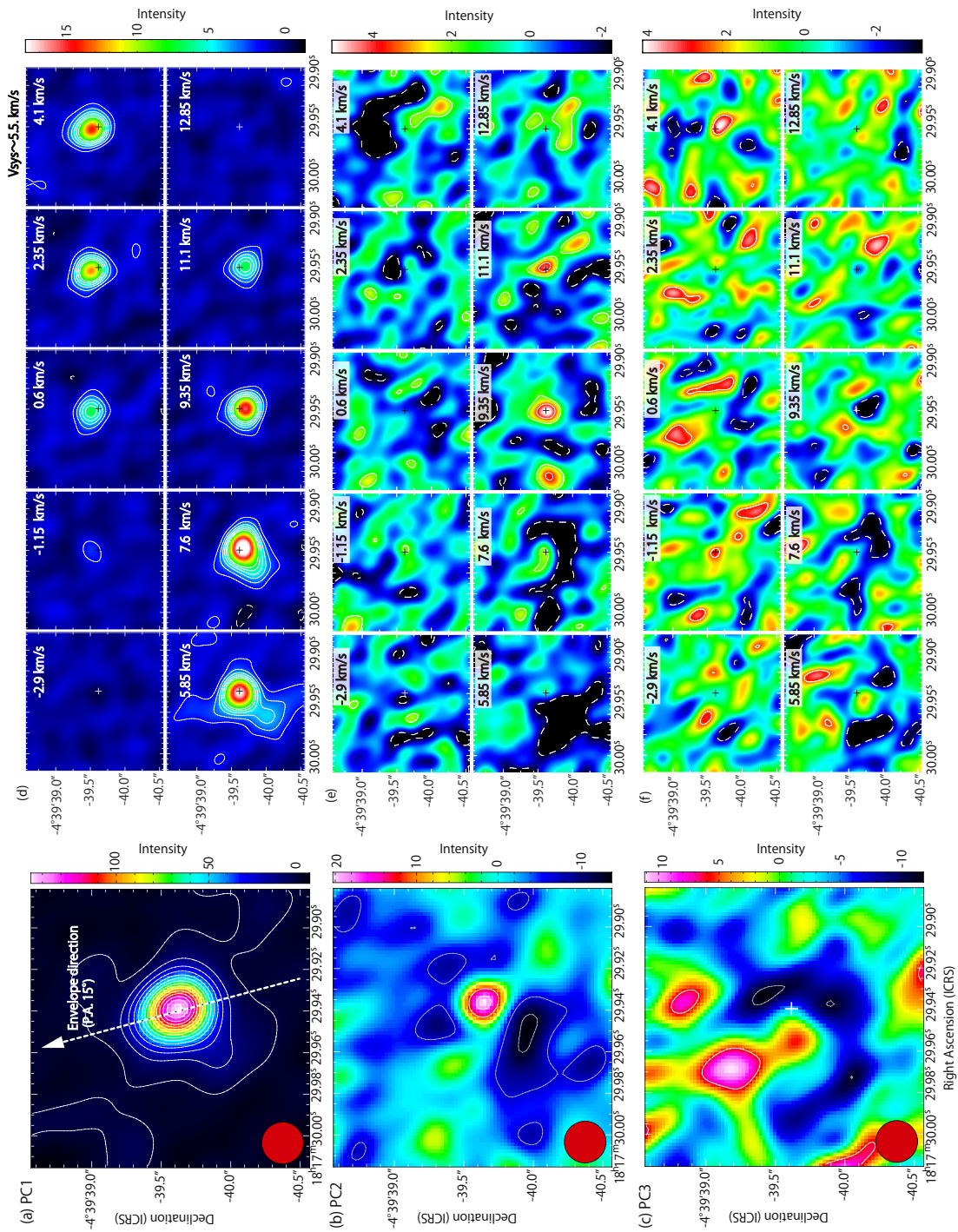
Figure 8.5: (a-c) Moment 0 maps of the first three principal components in PCA-3D for L483. Contour levels for PC1 (a) are every 10σ from 3σ, where σ is 1. Those for PC2 (b) and PC3 (c) are every 3σ from 3σ where σ is 2. The red circles in the lower-left corner of each panel show the beam size. (d-f) Channel maps of the first three principal components. Each panel represents the integrated intensity over a velocity range of 1.75 km s^{-1}, whose lower-end velocity is quoted on the upper right corner. The systemic velocity is 5.5 km s^{-1}. Contour levels for (d) PC1, (e) PC2 and (f) PC3 are every 3σ from 3σ, where σ is 0.4, 0.6 and 0.8, respectively. The cross marks show the continuum peak position.
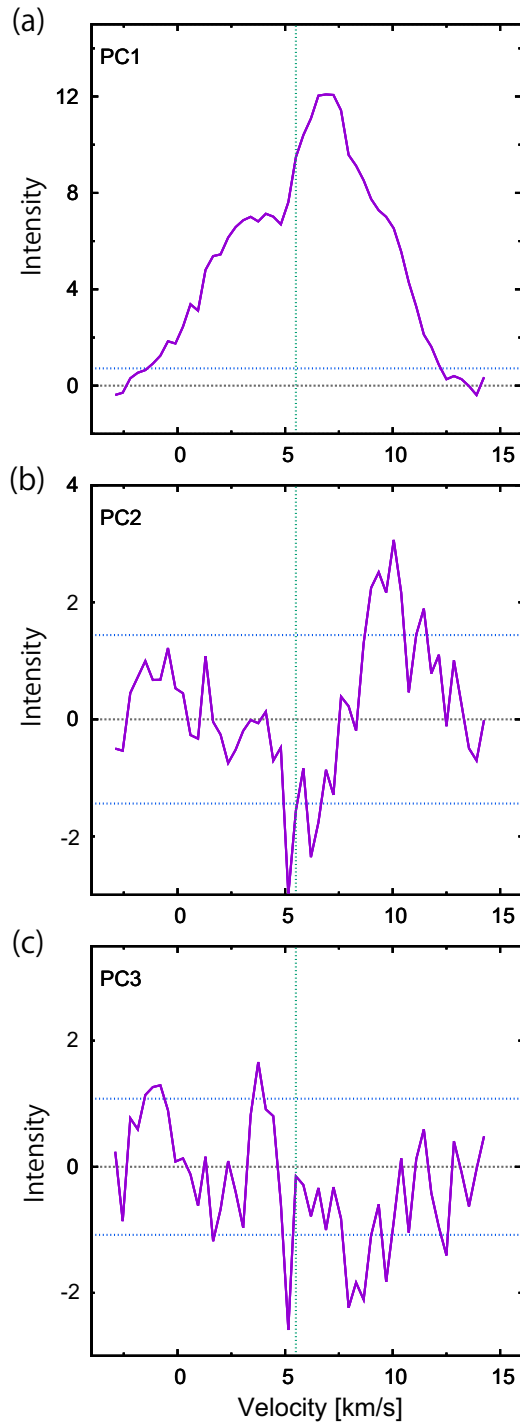
158

Figure 8.6: Spectral line profiles of the first three principal components in PCA-3D toward the continuum peak for L483. The spectra are prepared for a circular region with a diameter of 0.″5 centered at the continuum peak. The horizontal blue dotted lines represent each $\pm 3\sigma$, where σ of (a) PC1, (b) PC2, and (c) PC3 is 0.24, 0.36, and 0.48, respectively. The horizontal black dotted lines represent the zero-level intensity. The vertical green dotted lines represent the systemic velocity of 5.5 km s^{-1}.
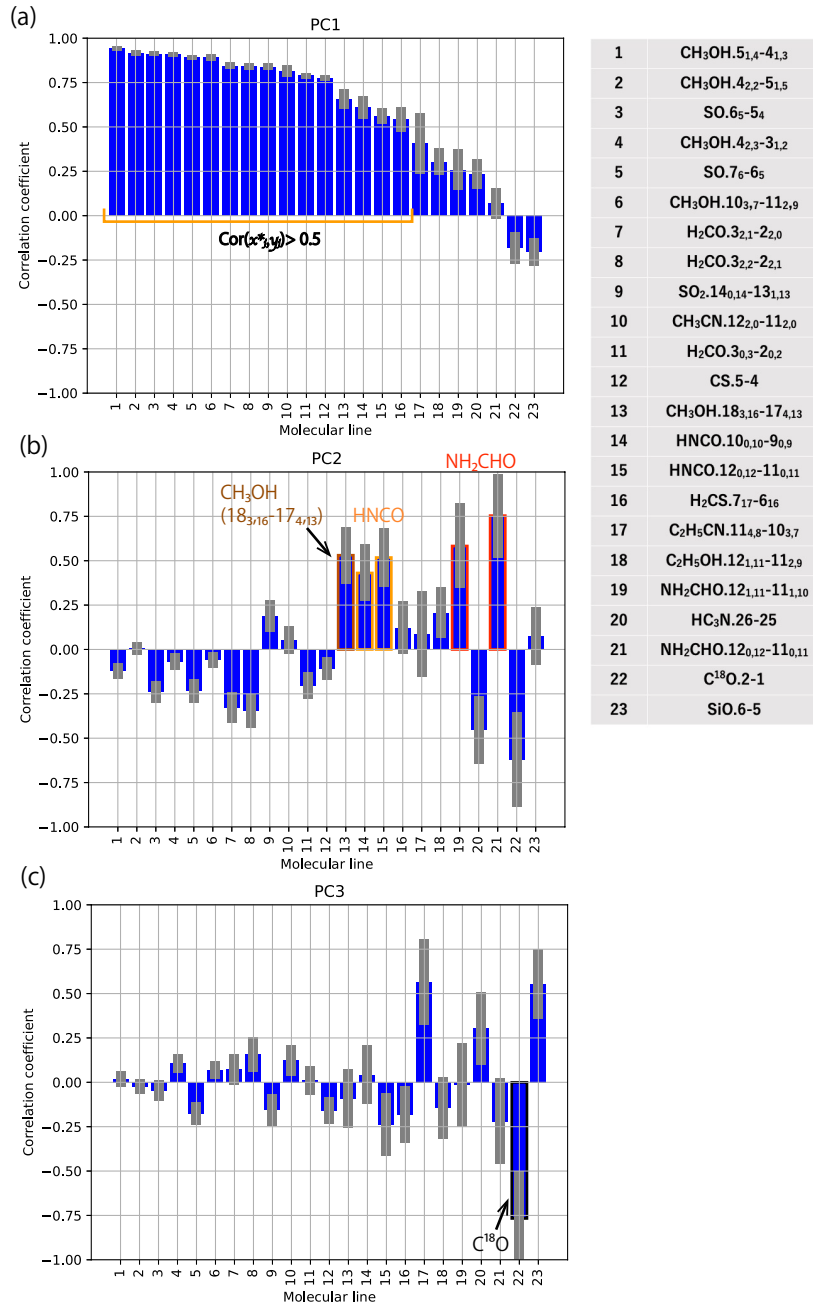
Figure 8.7: Correlation coefficients between the first three principal components in PCA-3D and the molecular cube data for L483. The numbers represent the molecular lines listed in the attached table. The uncertainties are shown in grey (See Section 6.3).
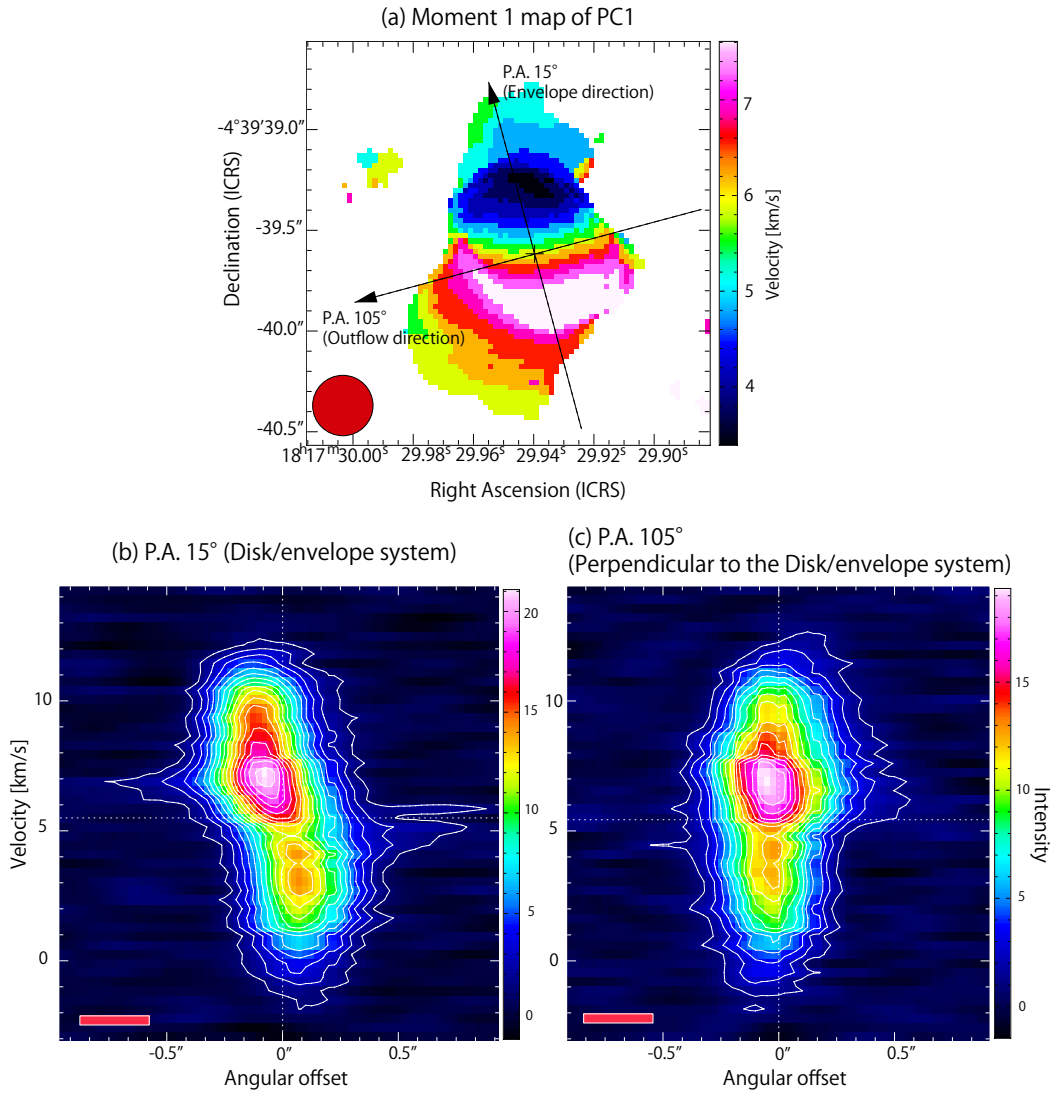
Figure 8.8: (a) Moment 1 map of PC1 in PCA-3D for L483. The red circle shows the beam size. The cross mark shows the continuum peak position. (b, c) PV diagrams of PC1 along the disk/envelope direction indicated in (a) and the direction perpendicular to it, respectively. Contour levels are every 3σ from 3σ, where σ is 0.4. The horizontal and vertical white dotted lines show the systemic velocity (5.5 km s^{-1}) and the continuum peak position, respectively. The red boxes represent the resolution.

161

8.5 PCA for the Moment 0 Maps (PCA-2D): L483

In this section, we apply the PCA for the 23 molecular-line images integrated over the velocity axis of the cube data used in Section 8.4 (moment 0 maps: Figure 8.1), and compare the results to those of PCA-3D. The result of PCA-2D is shown in Table 8.6. The contribution ratio of PC1 is 77.9 %, and hence, molecular-line distributions can mostly be represented by PC1. The contribution ratios of PC2 and PC3 are 8.1 % and 5.5 % (Table 8.6 and Figure 8.4(b)). We here discuss the first three components, the sum of whose ratios is 91.5 %.

Figures 8.9(a), (b), and (c) show the maps of PC1, PC2, and PC3 of PCA-2D, respectively. PC1 has a distribution concentrated around the continuum peak (Figure 8.9(a)), which looks similar to the moment 0 map of PC1 of PCA-3D (Figure 8.5(a)), while its contribution ratio is much larger than that in PCA-3D. PC2 has an extended distribution surrounding the continuum peak from the north to the southeast (Figure 8.9(b)). PC3 extends from the vicinity of the continuum peak to the northeastern direction (Figure 8.9(c)), most of which is concentrated in the northeastern part.

According to Figure 8.9(d), PC1 has the correlation coefficients larger than 0.5 for all molecular lines except for $C^{18}O$ and SiO. The large correlation coefficients for most molecular lines are consistent with their large contribution ratios of PC1. In Figures 8.9(e) and (f), the two molecular lines, $C^{18}O$ and SiO, are well correlated with PC2 and PC3, respectively, which means that these molecular lines have peculiar distributions among the 23 molecular lines. PC2 and PC3 (Figures 8.9(b) and (c)) look similar to the moment 0 maps of $C^{18}O$ and SiO, respectively (Figures 8.1(v) and (w)). This feature is also seen in the PC1-PC2, PC1-PC3, and PC2-PC3 biplots (Figures 8.10(a), (b), and (c), respectively), which display the contributions of the principal components for each molecular-line distribution. In these figures, all molecular lines except for the two species have a relatively small contribution of PC2 and PC3. $C^{18}O$ and SiO are located at the large positive parts of PC2 and PC3 on the PC2-PC3 biplot, respectively (Figure 8.10(c)). Thus, PC3 almost reproduces the distribution of SiO extending from the continuum peak to the northeastern direction (Figure 8.1(w)). Such a distribution of SiO was also reported by Oya et al. (2017). Since SiO is known as a shock tracer, the characteristic distribution may represent a shock related to the outflow: outflows launched from the protostar would likely hit a gas clump remaining around the protostar. On the other hand, HC_3N has a positive value of PC3 larger than the others, indicating that its distribution shows some similarity to that of SiO: its peak position is slightly shifted toward the northeast from the continuum peak. However, it seems too early to conclude that these two species are chemically related.

It should be noted that the peculiar distributions of $C^{18}O$ and SiO can also be identified by PCA-3D. On the contrary, the molecular lines having a rather broad component such as NH_2CHO are not identified in the PCA-2D.

Table 8.6: Eigenvectors of the Principal Components and their Eigenvalues for PCA-2D for L483

Number	Molecule	PC1	PC2	PC3	PC4	PC5	PC6	PC7
1	CH_3OH ($5_{1,4}-4_{1,3}$, A)	0.224	0.115	0.101	0.171	-0.159	-0.328	-0.383
2	CH_3OH ($4_{2,2}-5_{1,5}$, A)	0.222	0.031	0.031	0.103	-0.228	-0.252	-0.201
3	SO (6_5-5_4)	0.223	0.175	-0.075	0.214	0.013	0.269	0.325
4	CH_3OH ($4_{2,3}-3_{1,2}$, E)	0.224	0.068	0.051	0.092	0.197	-0.046	-0.179
5	SO (7_6-6_5)	0.212	0.231	-0.006	0.202	-0.29	0.212	0.289
6	CH_3OH ($10_{3,7}-11_{2,9}$, E)	0.223	-0.018	-0.023	0.002	0.226	0.032	0.01
7	H_2CO ($3_{2,1}-2_{2,0}$)	0.224	0.107	0.015	0.152	0.182	-0.138	-0.212
8	H_2CO ($3_{2,2}-2_{2,1}$)	0.224	0.116	-0.011	0.188	0.143	-0.06	-0.071
9	SO_2 ($14_{0,14}-13_{1,13}$)	0.219	0.023	0.085	-0.036	-0.287	0.269	0.092
10	CH_3CN ($12_{2,0}-11_{2,0}$)	0.225	-0.025	0.096	-0.061	-0.035	0.139	-0.14
11	H_2CO ($3_{2,1}-2_{2,0}$)	0.219	0.152	-0.068	0.176	0.192	-0.052	-0.016
12	CS ($5-4$)	0.218	0.23	-0.11	0.268	-0.088	-0.029	0.222
13	CH_3OH ($18_{3,16}-17_{4,13}$, A)	0.217	-0.132	-0.133	-0.127	0.267	-0.049	0.108
14	HNCO ($10_{0,10}-9_{0,9}$)	0.214	-0.079	0.014	-0.114	0.373	0.075	-0.093
15	HNCO ($12_{0,12}-11_{0,11}$)	0.224	-0.12	-0.102	-0.165	-0.123	0.057	0.165
16	H_2CS ($7_{1,7}-6_{1,6}$)	0.222	-0.12	0.112	-0.276	0.099	0.369	0.005
17	C_2H_5CN ($11_{4,8}-10_{3,7}$)	0.201	-0.185	-0.133	-0.309	-0.473	-0.32	0.068
18	C_2H_5OH ($12_{1,11}-11_{2,9}$)	0.223	-0.066	-0.114	-0.04	-0.082	-0.105	0.107
19	NH_2CHO ($12_{1,11}-11_{1,10}$)	0.199	-0.197	-0.269	-0.154	0.075	-0.341	0.185
20	HC_3N ($26-25$)	0.201	0.019	0.4	-0.211	-0.218	0.268	-0.383
21	NH_2CHO ($12_{0,12}-11_{0,11}$)	0.21	-0.21	-0.089	-0.244	0.147	0.075	0.003
22	$C^{18}O$ ($2-1$)	-0.03	0.766	0.067	-0.58	0.107	-0.187	0.117
23	SiO ($6-5$)	0.063	-0.182	0.794	0.07	0.12	-0.319	0.454
	Eigenvalues	19.37	2.011	1.377	0.602	0.239	0.135	0.087
	Contribution ratio (%)	77.9	8.1	5.5	2.4	1.0	0.5	0.3

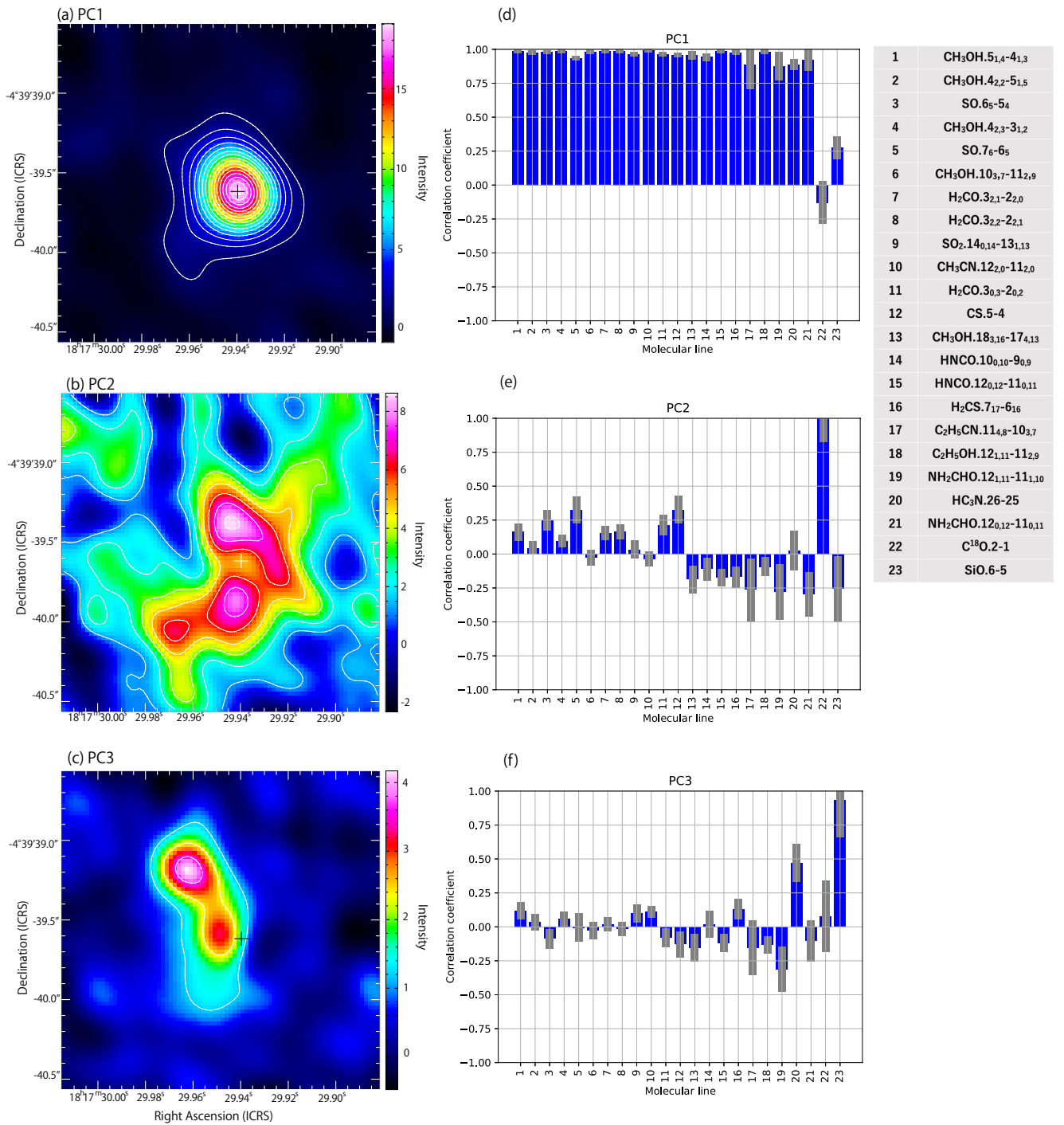These values are also called as 'loadings'.

Figure 8.9: (a-c) Moment 0 maps of the first three principal components in PCA-2D for L483. Contour levels for the first three components are every 3σ from 3σ, where σ is 0.4. (d-f) Correlation coefficients between the first three principal components in PCA-2D and the molecular-line distributions. The uncertainties are shown in grey (See Section 6.3). The numbers represent the molecular lines listed in the attached table.
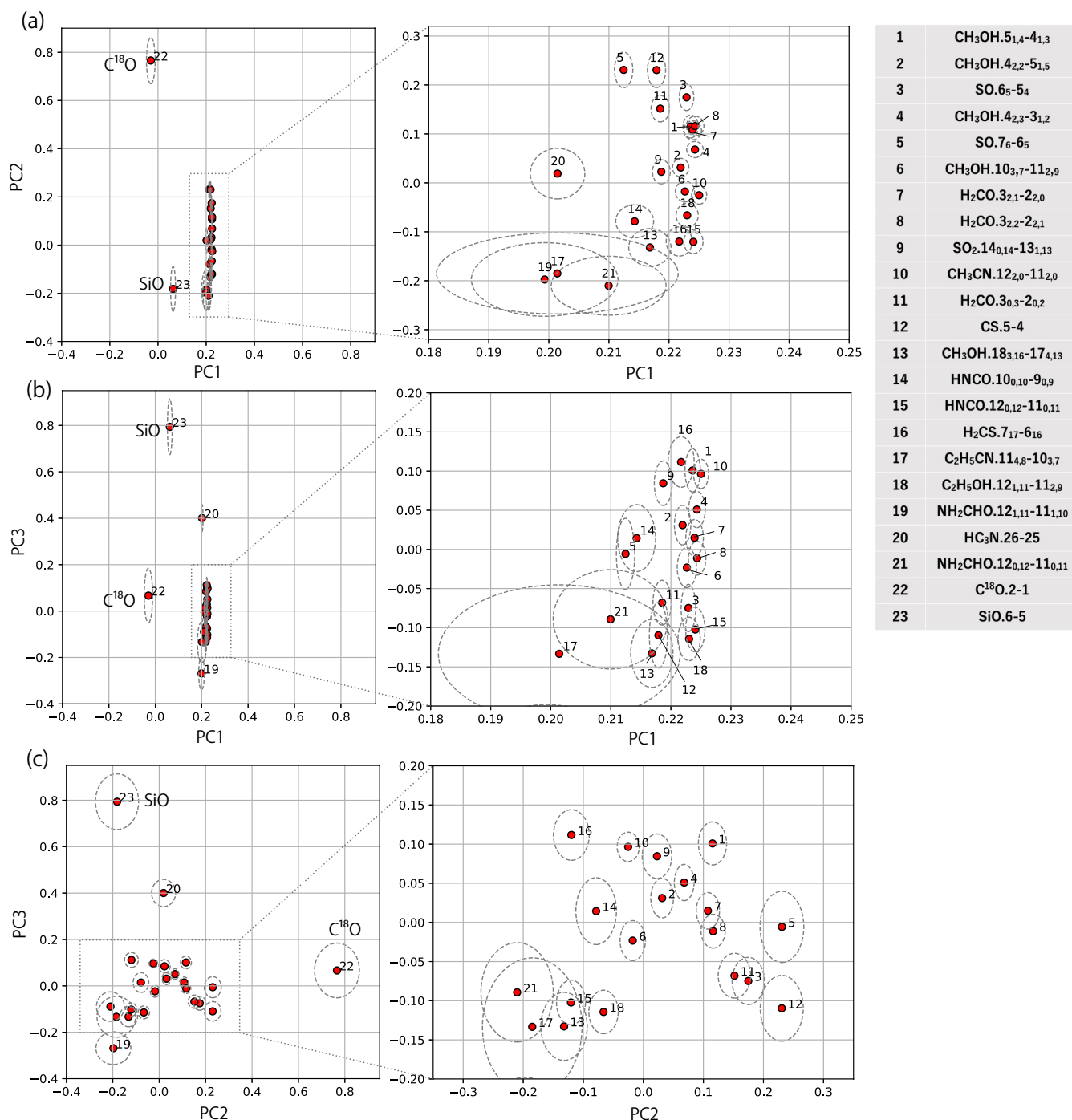
Figure 8.10: (a-c) Biplots of the contributions for the principal components in PCA-2D for each molecular-line distribution on the PC1-PC2, PC1-PC3, and PC2-PC3 planes for L483. The dashed ellipses represent the uncertainties (See Section 6.3). The numbers represent the molecular lines listed in the attached table.

8.6 PCA for the Spectral Line Profiles (PCA-1D): L483

In addition to the PCAs described above, we apply PCA for the spectral line profiles toward the continuum peak (Figure 8.2) in the same velocity range as the cube data. The spectra are prepared for a circular region with a diameter of 0."5 centered at the continuum peak to fairly consider the molecular lines extending around the protostar. The signal-to-noise ratios of the C_2H_5CN, $C^{18}O$, and SiO spectra are low toward the continuum peak (Figures 8.2(q), (v) and (w)). As well, the NH_2CHO ($12_{1,11}-11_{1,10}$ and $12_{0,12}-11_{0,11}$) lines are not bright enough for PCA-1D because of their compact distributions (Figures 8.1(s) and (u)). Hence, we here conduct PCA-1D for the 18 molecular lines except for these five lines. The result of PCA-1D is shown in Table 8.7. As seen in Table 8.7, PC1 has the largest contribution ratio, 64.1 %. The contribution ratios of PC2 and PC3 are 14.1 % and 7.1 %, respectively, while that of PC4 is 4.1 %. They are also seen in Figure 8.4(c). We here discuss the first three components, the sum of whose contributions is 85.3 %.

Figures 8.11(a), (b), and (c) show the PC1, PC2, and PC3 of PCA-1D, respectively. PC1 looks quite similar to the spectral line profile of PC1 obtained for PCA-3D. On the other hand, PC2 and PC3 of PCA-1D are different from those of PCA-3D. In PCA-1D, PC2 shows the intensity peak around the systemic velocity (5.5 km s^{-1}) with a blueshifted shoulder. PC3 has intensity dips around 3 km s^{-1} and 10 km s^{-1}. The lack of the data of C_2H_5CN, $C^{18}O$, SiO, and NH_2CHO ($12_{0,12}-11_{0,11}$ and $12_{1,11}-11_{1,10}$) in PCA-1D can be responsible for the differences of PC2 and PC3 between PCA-3D and PCA-1D.

As shown in Figure 8.11(d), most molecular lines show the large correlation coefficients of PC1. Molecular lines less correlated with PC1 tend to have a large correlation coefficients with PC2 or PC3 (Figures 8.11(e) and (f)). HC_3N(#18), HNCO ($12_{0,12}-11_{0,11}$;#15), CH_3OH ($18_{3,16}-17_{4,13}$, A; #13), HNCO ($10_{0,10}-9_{0,9}$;#14), and H_2CS (#16) are well correlated with PC2 (Figures 8.11(e)). The positive and negative PC2 values mean strong and weak blueshifted components, respectively, of these lines. On the other hand, C_2H_5OH has the correlation coefficients with PC3 as large as 1.0 (Figure 8.11(f)), and can almost be reproduced by PC3 with a little contribution of PC1. This means that only this molecular line has the peculiar spectral line profile, although it may be affected by the low signal-to-noise ratio. However, this feature should be confirmed by further observations of the other lines this molecule. The characteristics of the spectral line profiles are thus extracted to some extent by PC2 and PC3, which are seen more clearly in the PC1-PC2, PC1-PC3, and PC2-PC3 biplots, respectively (Figures 8.12). The results of PCA-1D are essentially consistent with the results of PCA-3D. It should be noted that the result would depend on the selected area for the spectral line profiles.

We have conducted the PCAs for the molecular-line data of L483. We can extract some characteristic features of the molecular lines even with PCA-2D and PCA-1D. However, PCA-2D does not consider the velocity information, and PCA-1D loses the information on their spatial distributions. For this reason, we need caution in characterization of the molecular line distributions based on PCA-2D and PCA-1D.

PCA-3D is thus desirable for full identification of the similarities and differences of the molecular-line distributions.

Table 8.7: Eigenvectors of the Principal Components and their Eigenvalues for PCA-1D for L483

| Number	Molecule	PC1	PC2	PC3	PC4	PC5	PC6	PC7
1	CH_3OH ($5_{1,4}$–$4_{1,3}$, A)	0.285	0.109	0.057	0.054	-0.107	0.03	-0.017
2	CH_3OH ($4_{2,2}$–$5_{1,5}$, A)	0.28	0.039	0.091	0.066	-0.011	-0.071	0.027
3	SO (6_5–5_4)	0.276	0.14	-0.013	0.053	-0.072	-0.146	-0.289
4	CH_3OH ($4_{2,3}$–$3_{1,2}$, E)	0.281	0.106	-0.006	0.057	0.005	-0.147	0.183
5	SO (7_6–6_5)	0.283	0.105	0.002	0.01	-0.079	-0.034	-0.252
6	CH_3OH ($10_{3,7}$–$11_{2,9}$, E)	0.27	0.093	-0.063	0.211	0.086	-0.165	-0.112
7	H_2CO ($3_{2,1}$–$2_{2,0}$)	0.263	0.208	0.032	-0.008	0.053	-0.044	0.122
8	H_2CO ($3_{2,2}$–$2_{2,1}$)	0.267	0.172	0.1	0.051	0.149	-0.255	-0.092
9	SO_2 ($14_{0,14}$–$13_{1,13}$)	0.254	-0.201	-0.088	-0.245	-0.184	0.014	-0.418
10	CH_3CN ($12_{2,0}$–$11_{2,0}$)	0.238	0.158	0.007	-0.068	0.066	0.726	0.307
11	H_2CO ($3_{2,1}$–$2_{2,0}$)	0.272	-0.008	-0.006	0.214	0.179	0.231	0.094
12	CS (5–4)	0.266	-0.148	0.02	0.133	0.186	0.074	0.002
13	CH_3OH ($18_{3,16}$–$17_{4,13}$, A)	0.191	-0.361	-0.18	-0.076	-0.211	-0.428	0.565
14	HNCO ($10_{0,10}$–$9_{0,9}$)	0.184	-0.33	-0.212	0.05	-0.658	0.273	-0.047
15	HNCO ($12_{0,12}$–$11_{0,11}$)	0.106	-0.502	-0.123	-0.328	0.453	0.091	-0.306
16	H_2CS ($7_{1,7}$–$6_{1,6}$)	0.146	0.272	-0.008	-0.824	0.002	-0.057	0.175
17	C_2H_5OH ($12_{1,11}$–$11_{2,9}$)	-0.009	-0.075	0.853	-0.111	-0.291	0.013	-0.087
18	HC_3N (26–25)	-0.152	0.453	-0.38	-0.06	-0.268	0.013	-0.225
	Eigenvalues	11.77	2.564	1.31	0.755	0.426	0.348	0.318
	Contribution ratio (%)	64.1	14.0	7.1	4.1	2.3	1.9	1.7

These values are also called as 'loadings'.
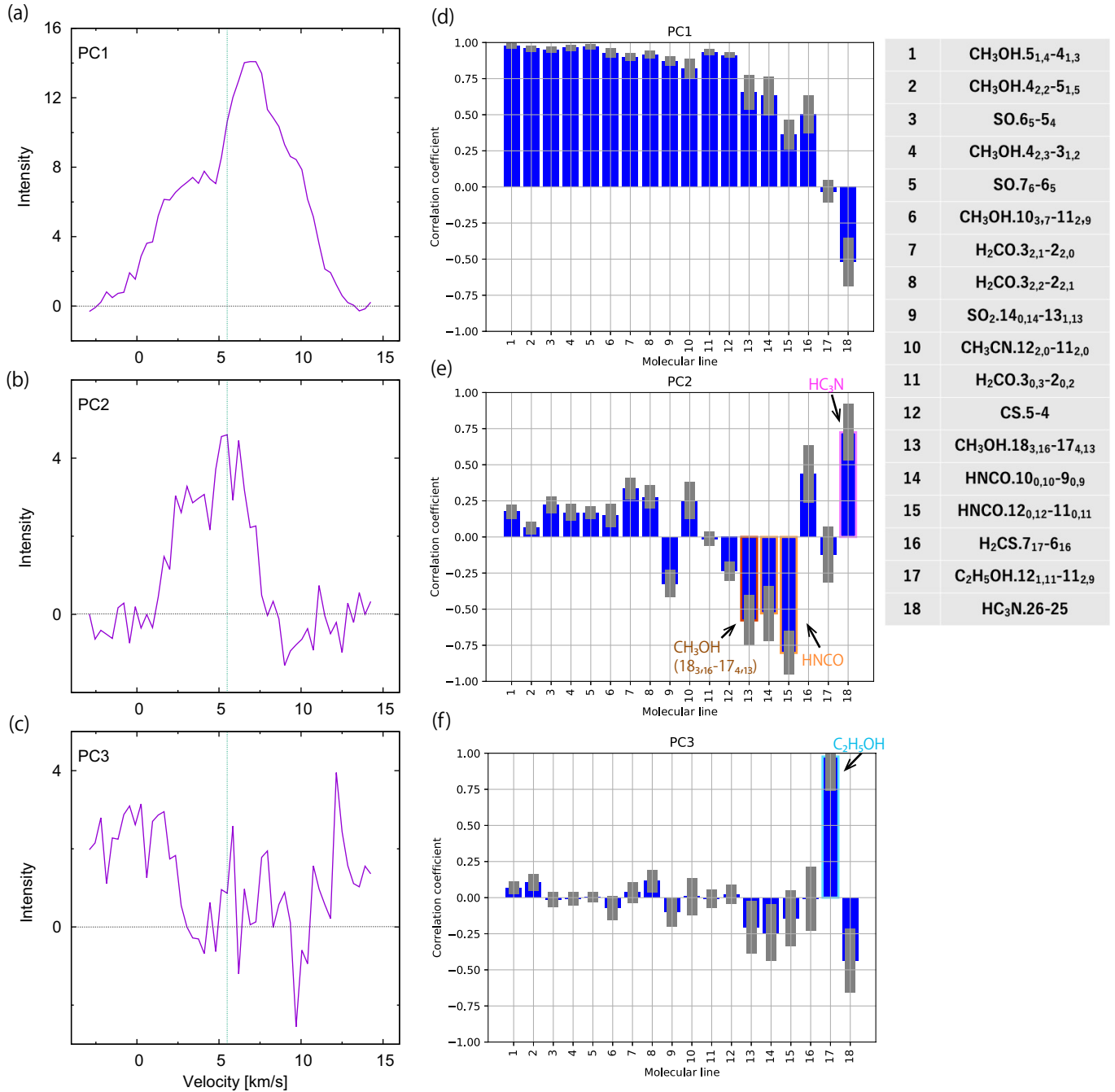
Figure 8.11: (a-c) Spectral line profiles of the first three principal components in PCA-1D toward the continuum peak position for L483. The spectra are prepared for a circular region with a diameter of 0.″5 centered at the continuum peak. The horizontal black dashed lines represent the zero-level intensity. The vertical green dashed lines represent the systemic velocity of 5.5 km s^{-1}. (d-f) Correlation coefficients between the first three principal components in PCA-1D and the molecular-line profiles. The uncertainties are shown in grey (See Section 6.3). The numbers represent the molecular lines listed in the attached table.
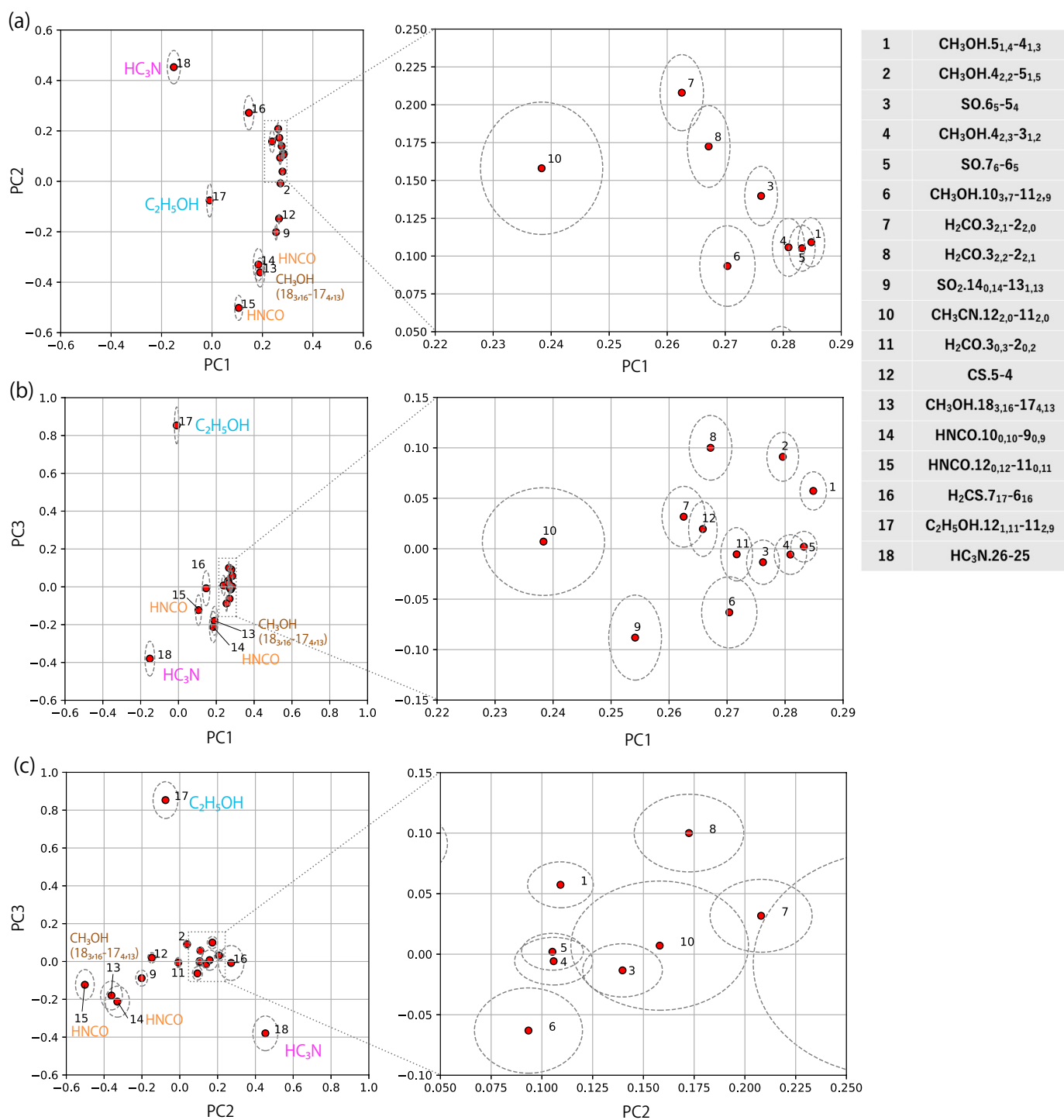
Figure 8.12: (a-c) Biplots of the contributions for the principal components in PCA-1D for each molecular-line distribution on the PC1-PC2, PC1-PC3, and PC2-PC3 planes for L483. The dashed ellipses represent the uncertainties (See Section 6.3). The numbers represent the molecular lines listed in the attached table.

8.7 PCA for the Cube Data (PCA-3D): B335

Now, we have found that PCA-3D is the most effective for the characterization of molecular-line data. Hence, we also perform it for the 32 molecular-line data in the Class 0 protostellar source, B335. The eigenvalues and eigenvectors of the first 7 PCs are given in Table 8.8. PC1 shows the largest contribution ratio, 31.7%. PC2 and PC3 have similar contribution ratios to each other, 13.0 % and 7.9 %, respectively, and PC4 has a lower ratio, 5.0 %. The sum of the four contribution ratios is 57.6 %. We discuss PCi ($i \geq 4$) based on the scree plot as shown in Figure 8.13.

Table 8.8: Eigenvectors of the Principal Components and their Eigenvalues for PCA-3D for B335

Number	Molecule	PC1	PC2	PC3	PC4	PC5	PC6	PC7
1	CH_3OH ($18_{3,15}-18_{2,16}$,A)	0.276	-0.007	-0.123	0.064	0.089	0.012	0.037
2	CH_3OH ($21_{3,18}-21_{2,19}$,A)	0.269	0.029	0.021	0.041	-0.083	0.006	0.03
3	CH_3OH ($12_{6,7}-13_{5,8}$,E)	0.261	-0.056	0.064	-0.102	0.003	-0.069	0.034
4	CH_3CHO ($14_{1,14}-13_{1,13}$, A)	0.24	-0.112	0.092	-0.091	-0.09	-0.041	-0.126
5	CH_3OH ($17_{3,14}-17_{2,15}$, A)	0.24	-0.008	-0.211	0.145	0.044	0.054	-0.124
6	CH_3OH ($4_{2,2}-5_{1,5}$, A)	0.235	0.008	-0.241	0.038	-0.031	0.117	0.004
7	CH_2DOH ($4_{2,2}-4_{2,3}$, e_0)	0.234	-0.176	0.048	0.02	-0.021	0.013	0.017
8	CH_2DOH ($5_{2,4}-5_{1,5}$, e_0)	0.23	-0.161	-0.043	0.005	0.09	-0.083	-0.096
9	CH_2DOH ($3_{2,1}-3_{1,2}$, e_0)	0.224	-0.17	0.037	-0.021	0.129	-0.091	-0.178
10	CH_3OH ($2_{1,1}-1_{0,1}$, A)	0.208	-0.027	-0.314	-0.014	-0.191	0.03	-0.184
11	$HNCO$ ($12_{0,12}-11_{0,11}$)	0.202	0.263	0.012	-0.077	-0.042	-0.063	0.135
12	CS ($5-4$)	0.192	-0.032	-0.27	0.02	0.003	-0.041	0.137
13	NH_2CHO ($12_{0,12}-11_{0,11}$)	0.188	0.322	0.136	-0.058	0.053	0.034	0.009
14	SO ($J_N =7_6-6_5$)	0.176	0.041	-0.247	0.136	-0.061	-0.229	0.186
15	CH_2DOH ($10_{2,8}-10_{1,9}$, o_1)	0.159	-0.184	0.214	-0.142	-0.116	0.156	0.067
16	H_2CO ($10_{1,9}-10_{1,10}$)	0.159	0.056	0.207	-0.138	0.067	0.111	0.006
17	CHD_2OH ($6-5$, $K =1+$, o_1)	0.159	-0.207	0.082	-0.089	0.118	0.258	0.042
18	$HNCO$ ($12_{1,12}-11_{1,11}$)	0.157	0.176	-0.168	0.038	-0.071	0.187	0.065
19	$HCOOH$ ($11_{5,7}-10_{5,6}$ and $11_{5,6}-10_{5,5}$)	0.156	0.279	0.117	0.008	0.128	0.242	-0.027
20	SO_2 ($10_{3,7}-10_{2,8}$)	0.155	0.211	0.077	0.144	-0.134	-0.38	0.126
21	$HCOOH$ ($12_{0,12}-11_{0,11}$)	0.145	0.282	0.23	-0.2	0.082	0.027	-0.029
22	CHD_2OH ($6-5$, $K =1+$, e_0)	0.134	-0.251	0.167	0.092	0.036	0.031	0.064
23	CH_3CHO ($14_{0,14}-13_{0,13}$, E, $v_t =1$)	0.122	-0.179	-0.132	-0.293	-0.139	-0.146	-0.366
24	$HCOOH$ ($11_{6,6}-10_{6,5}$ and $11_{6,5}-10_{6,4}$)	0.119	0.287	0.283	-0.132	0.105	0.012	-0.015
25	CH_3OD (5_1-4_0, E)	0.118	-0.278	0.165	0.278	0.019	0.042	0.129
26	HC_3N ($27-26$)	0.114	0.268	-0.07	0.278	-0.055	-0.071	0.142
27	CH_3OCHO ($21_{7,14}-20_{7,13}$, A)	0.114	-0.265	0.217	0.032	0.236	0.025	0.451
28	C_2H_5OH ($13_{2,12}-12_{1,11}$)	0.089	0.048	0.274	0.381	-0.245	-0.044	-0.319
29	CH_3OCHO ($21_{7,14}-20_{7,13}$, E)	0.048	-0.028	0.094	-0.537	-0.42	-0.123	0.043
30	CH_3COCH_3 ($14_{11,3}-13_{10,4}$)	0.034	0.008	0.17	0.136	0.395	-0.234	-0.52
31	CH_2OHCHO ($7_{7,1}-6_{6,0}$ and $7_{7,0}-6_{6,1}$)	0.016	0.093	-0.232	-0.095	0.215	0.557	-0.156
32	CH_3OCHO ($20_{11,10}-19_{11,9}$, E)	-0.019	-0.022	0.213	0.294	-0.545	0.384	-0.115
	Eigenvalues	10.27	4.212	2.549	1.618	1.482	1.242	1.165
	Contribution ratio (%)	31.7	13.0	7.9	5.0	4.6	3.8	3.6

These values are also called as 'loadings'.

8.7.1 Characteristic Features of the Principal Components

The channel maps and the moment 0 maps of the four PCs are shown in Figures 8.14. The moment 0 map of PC1 shows a round distribution around the protostar over ~20 au (Figure 8.14(a)). It slightly extends toward the southwest direction with an intensity depression at the continuum peak position. In its channel map, the extended distribution of PC1 is clearly seen in the panels from 5.4 km s^{-1} to 11 km s^{-1} (Figure 8.14(c)). The blueshifted and redshifted components can be seen mainly in the southeast and the northwest respectively, where the systemic velocity is 8.34 km s^{-1} (Yen et al., 2015b), which can be interpreted by rotating motion as pointed out by Imai et al. (2019) and Bjerkeli et al. (2019). In the 9.6 km s^{-1} and 11.0 km s^{-1} panels, we can see the intensity peak at the western side of the continuum peak. As described in Section 5.3, this corresponds to the shocked region caused by the outflow impact. Therefore, the velocity structure of PC1 would also reflect part of the outflow motion. Figure 8.15 shows the spectral line profiles of the PCs, which are prepared for a circular region with a diameter of 0.″1 centered at the continuum peak. The spectrum of PC1 reveals a single peak at the blueshifted velocity (Figure 8.15(a)).

As shown in Figure 8.14(b), the moment 0 map of PC2 shows a positive compact distribution in the vicinity of the protostar as well as the negative crescent distribution around it. Such a distribution is also seen clearly in the velocity channel map of PC2 (Figure 8.14(d)), where the positive compact distribution has the broader velocity width. The spectral line profile of PC2 has a positive double-peak feature (Figure 8.15(b)). PC2 seems to reproduce the high-velocity components of some molecular lines in combination with the broad velocity width of PC1.

The distributions of PC3 and PC4 have the low signal-to-noise ratio in comparison with those of PC1 and PC2. Nevertheless, some structures are seen in each velocity channel map. In Figure 8.14 (g), PC3 has a positive compact distribution with negative clumpy features from 6.8 km s^{-1} to 11.0 km s^{-1}. As shown in Figures 8.14(e), the intensity of the southern side is negatively brighter than that of the northern side. Meanwhile, PC4 shows a weak emission around the continuum peak (Figure 8.14(f)), where the positive emissions can be seen particularly at the panels of 6.8 km s^{-1} and 8.2 km s^{-1} (Figures 8.14 (h)). In the spectral line profiles, PC3 has a positive and negative peaks at the redshifted and blueshifted velocities, respectively (Figure 8.15(c)). On the other hand, the intensity of PC4 toward the continuum peak is lower than 3 σ, although it shows a positive intensity near the systemic velocity (Figure 8.15(d)). This is due to its extended and clumpy distribution.

8.7.2 Characteristics of the Molecular Lines Extracted by the PCA

As shown in Figure 8.16(a), 19 molecular lines have a correlation coefficient larger than 0.5 for PC1, where the high excitation CH$_3$OH lines and most of the CH$_2$DOH lines show the largest value. This suggests that most molecular lines have a roundly extended distribution around the protostar with an intensity depression at the continuum peak. The depression seems to originate from the optical depths of the line

emission and the continuum emission. Based on the velocity structure of PC1, these lines represent a rotating structure of the disk/envelope system (Figure 8.14(c)).

Figure 8.16(b) depicts the correlation between PC2 and each molecular line. While the CH_3OH and CH_2DOH lines showing the large correlation for PC1 are not well correlated with PC2, the nitrogen-bearing organic species, NH_2CHO, HNCO, and HC_3N, have a positive correlation for PC2. This indicates the difference between the distributions of the oxygen-bearing and nitrogen-bearing species. Furthermore, the HCOOH lines have a large positive correlation for PC2 and show a similar trend to the nitrogen-bearing molecular lines, despite being an oxygen-bearing species. A positive large correlation of PC2 means the compact distribution with the high-velocity component of these molecular lines. This classification of molecules based on PC2 is more discussed in Chapter 9. As well, the SO_2 line (#20) is also correlated with PC2 positively, indicating that its distribution is likely more compact than those of the oxygen-bearing organic species (Figure 8.3(t)). In contrast, the deuterated species of CH_3OH (CH_2DOH, CHD_2OH, and CH_3OD), CH_3OCHO (#27), and CH_3CHO (#4 and #23) lines are correlated with PC2 negatively. This indicates that PC2 extracts their crescent distribution without a compact distribution toward the protostar. In particular, it is remarkable in the moment 0 maps of CH_3OD (#25) showing the large correlation of PC2 (Figure 8.3(y)). The molecular lines with a negative correlation for PC2 tend to have a narrow line width.

While all the molecular lines have a correlation smaller than 0.5 for PC3, a few lines have a moderate correlation for PC3. The CS (#12) and CH_3OH ($2_{1,1}-1_{0,1}$) (#10) lines are relatively well correlated for PC3. PC3 can extract a more extended distribution than PC1 in the southwestern part, indicating the difference of the distribution depending on the excitation condition of each CH_3OH line. The HCOOH (#24) and C_2H_5OH (#28) lines have a positive correlation of PC3, and PC3 help to reproduce their compact distributions with high-velocity components. On the other hand, PC4 has a correlation with CH_3OCHO (#29) and C_2H_5OH (#28), in particular. The CH_3OCHO ($21_{7,14}-20_{7,13}$, E) line has the largest correlation of PC4, which is almost 0.75, and hence, PC4 mainly extracts the features of this line. In fact, these moment 0 map are similar to that of PC4, as shown in Figure 8.3 (ac) and 8.14(f).

Thus, we can understand the molecular-line distributions systematically by using PCA, and hence, the trend for the oxygen-bearing and nitrogen-bearing species can be extracted as well as PCA-3D in L483. Interestingly, the HCOOH lines in B335 show a similar trend to the nitrogen-bearing molecules. Studying these molecular distributions with the aid of PCA would be a clue to understanding of chemical evolution in protostellar sources. We will discuss these results in Chapter 9.

8.8 Summary

1. In order to fully characterize the distribution of molecular lines in the disk/envelope structure of the Class 0 protostellar sources L483 and B335, which are rich in complex organic molecules, we have conducted PCA-3D in the vicinity of the protostar. We have used the 23 and 32 molecular lines without apparent contamination from other lines with ALMA for L483 and B335, respectively.

PCA-3D successfully extracts the systematic chemical differentiation within the disk/envelope system of each source.

2. For reference, we have also performed PCA-2D and PCA-1D in L483. For these two PCAs, there is a limitation in extracting specific distribution features because of using part of the data, and hence, special caution should be paid in interpretation of their results. PCA-3D enables us the full characterization of the distribution and the kinematics of the various molecular lines simultaneously without any preconception.

3. In PCA-3D for L483, PC1 represents the average distribution of the molecular-line data, and the 16 molecular lines are well correlated with PC1. We find that these lines trace a rotation motion of the disk/envelope system based on the PV diagram of PC1. $C^{18}O$ and SiO are notable exceptions, which have a small negative correlation of PC1.

4. In PCA-3D for L483, some molecular lines less correlated with PC1 tend to have large correlation coefficients of PC2. They are the NH_2CHO ($12_{0,12}-11_{0,11}$ and $12_{11,1}-11_{11,0}$), HNCO ($10_{0,10}-9_{0,9}$ and $12_{0,12}-11_{0,11}$), and very high excitation CH_3OH ($18_{3,16}-17_{4,13}$, A) lines, which have a compact distribution with high-velocity components. Association of the very high excitation CH_3OH line with the compact region implies a hot and dense condition of the emitting region of NH_2CHO and HNCO.

5. PCA-3D for B335 also shows that NH_2CHO ($12_{0,12}-11_{0,11}$) and HNCO ($12_{0,12}-11_{0,11}$ and $12_{1,12}-11_{1,11}$) are concentrated toward the protostar. We find that the distributions of these molecular lines are more compact than that of the high excitation CH_3OH line in B335, based on the results of PCA-3D, in contrast to the L483 case. This difference feature seems to be visible thanks to the higher resolution of the B335 data.

6. The results of PCA-3D suggest a chemical differentiation of the nitrogen-bearing and oxygen-bearing molecular-line data in both L483 and B335. The oxygen-bearing molecules tend to have a distribution slightly more extended than the nitrogen-bearing molecules.

7. In PCA-3D for B335, the HCOOH lines are classified into the group of the nitrogen-bearing molecules, despite an oxygen-bearing species. This result suggests a possible chemical link between HCOOH and the nitrogen-bearing molecules.
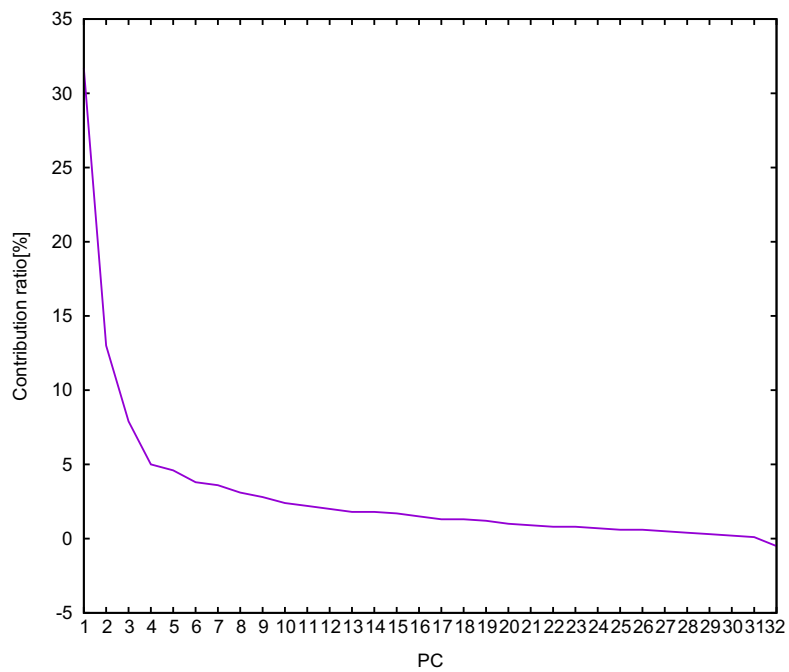
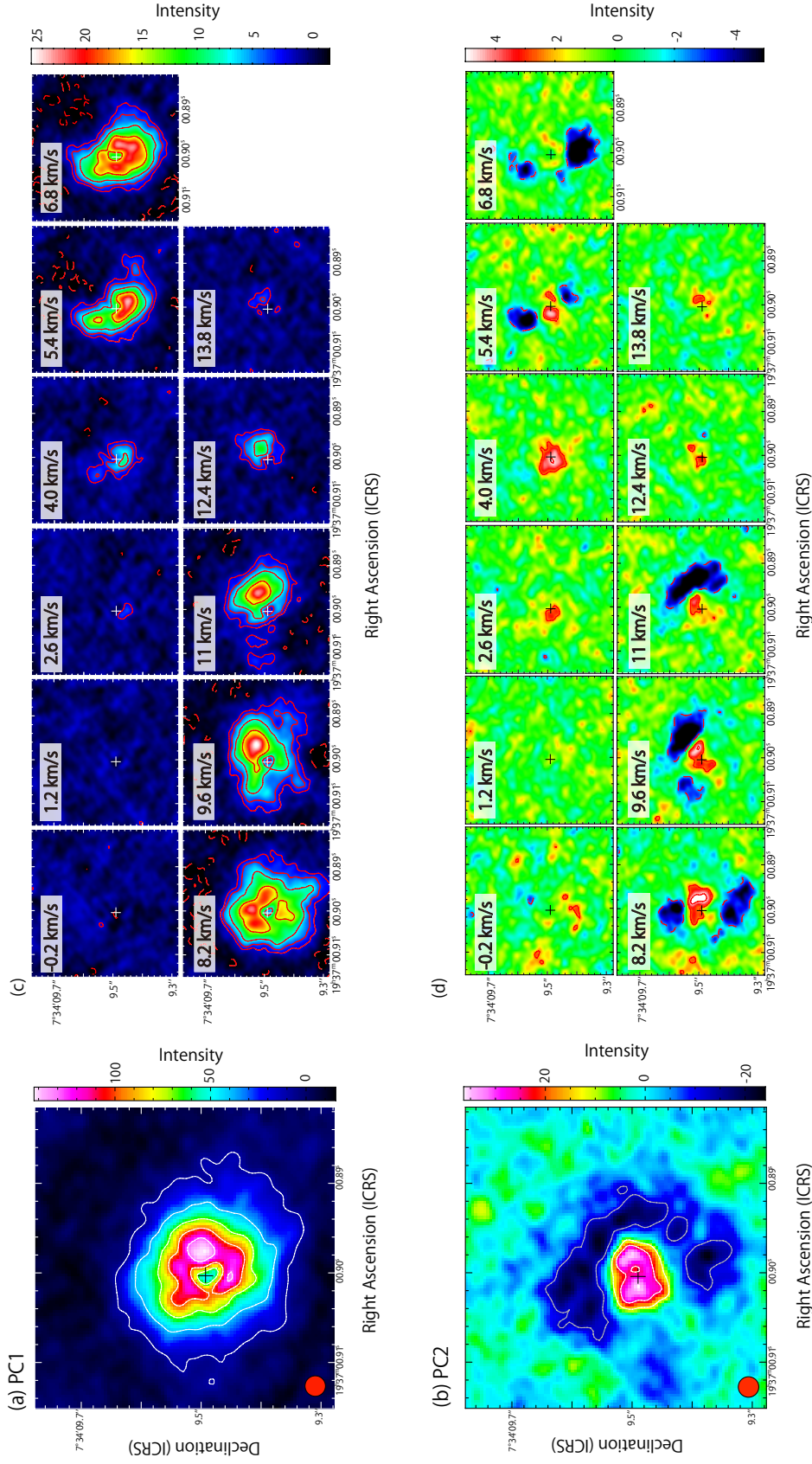Figure 8.13: Scree plots of the contribution ratios for the principal components for B335.

Figure 8.14: (a-d) Moment 0 maps of the first four principal components in PCA-3D for B335. Contour levels for PC1 (a) are every 10σ from 3σ, where σ is 3. Contour levels for PC2 (b), PC3 (e), and PC4 (f) are every 3σ from 3σ, where σ is 4, 5, and 5, respectively. The red circles show the beam size. (c, d, g, h) Channel maps of the first four principal components. Each panel represents the integrated intensity over a velocity range of 1.4 km s^{-1}, whose lower-end velocity is quoted on the upper-left corner. The systemic velocity is 8.34 km s^{-1}. Contour levels for PC1 (c), PC2 (d), PC3 (g), and PC4 (h) are every 3σ from 3σ, where σ is 0.6, 0.8, 0.9, and 1.0, respectively. The cross marks show the continuum peak position.
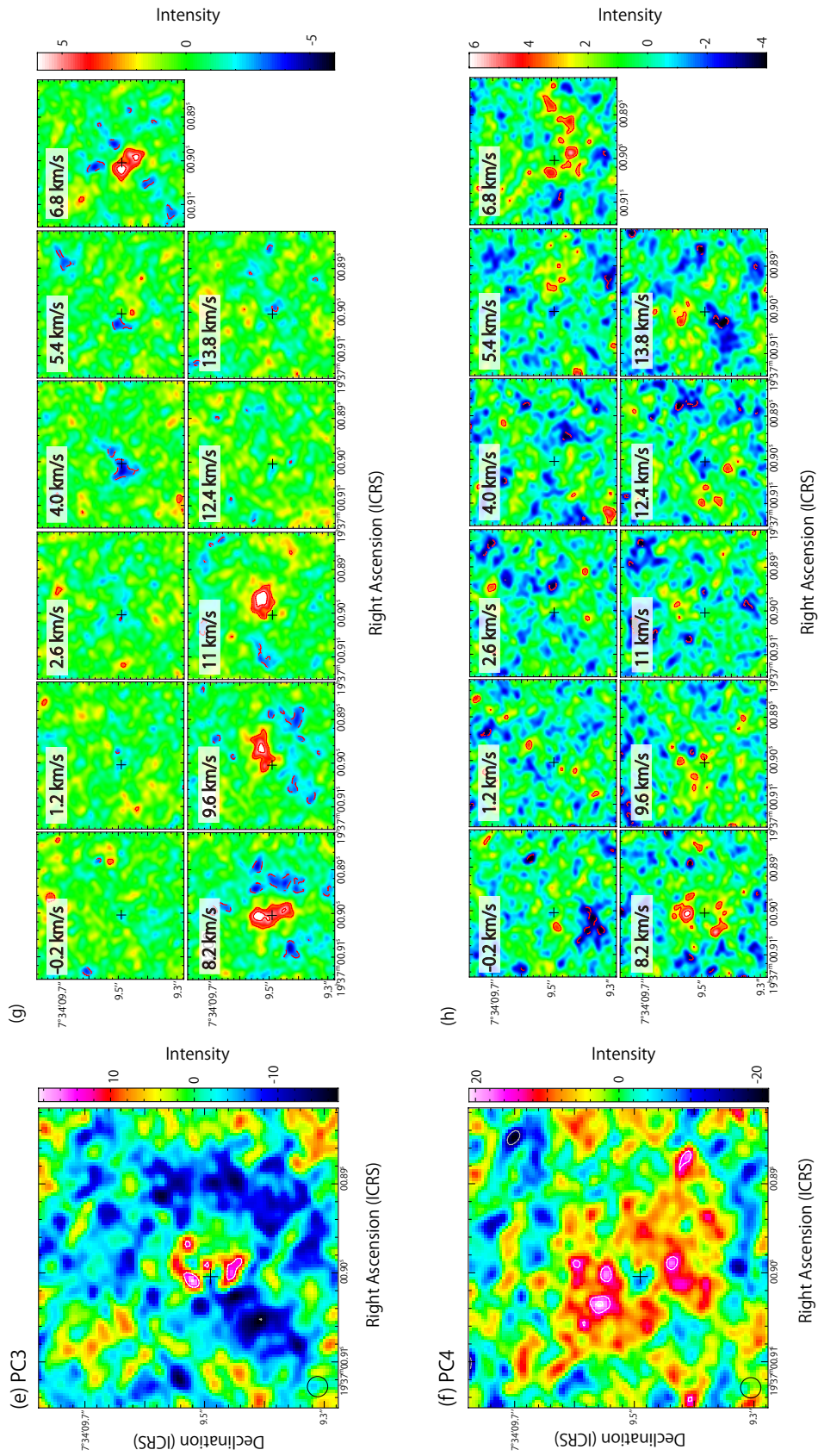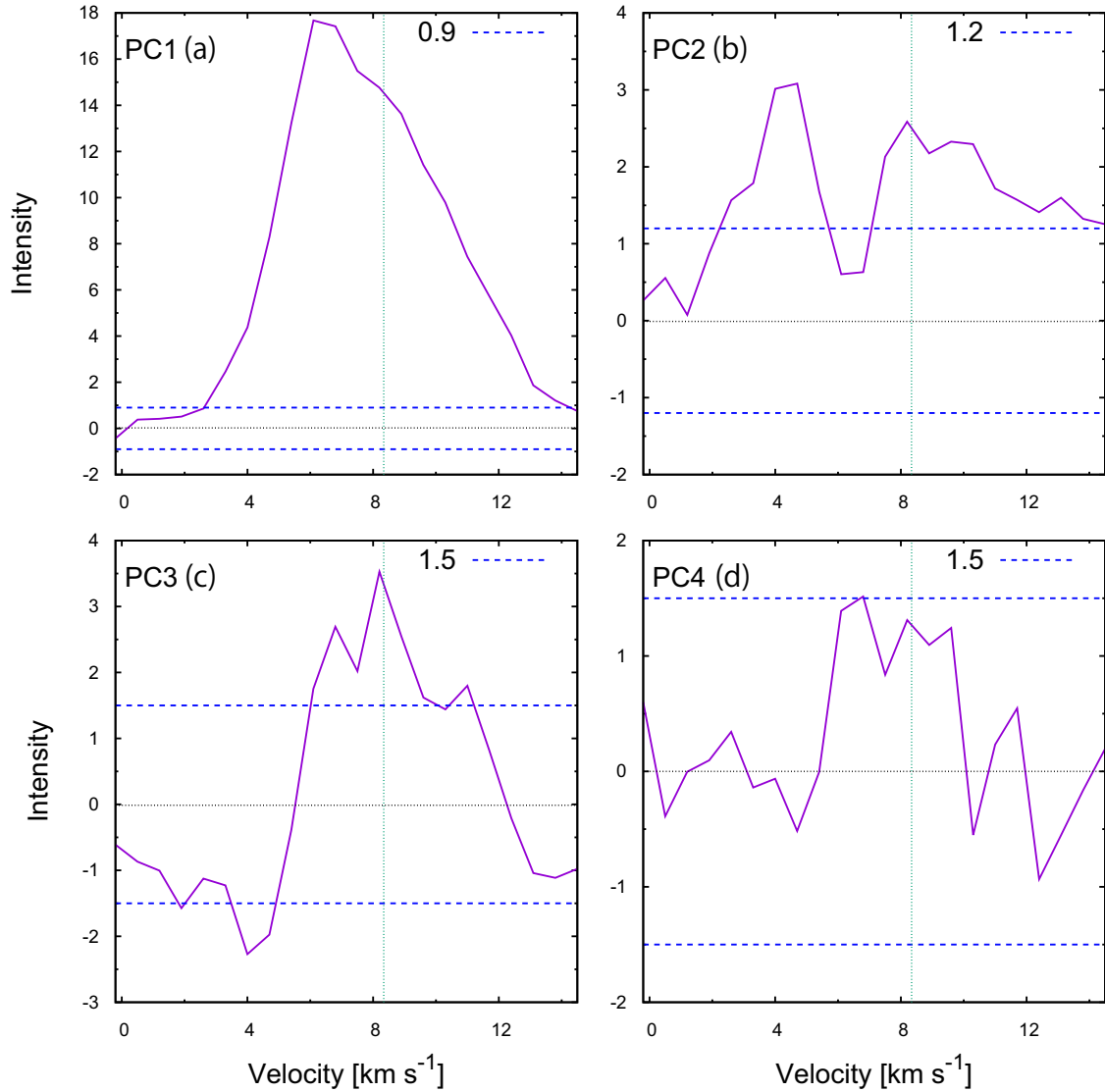
Figure 8.14: . continued.

Figure 8.15: Spectral line profiles of the first four principal components in PCA-3D for B335. The spectra are prepared for a circular region with a diameter of 0."1 centered at the continuum peak. The horizontal blue dashed lines represent each $\pm 3\sigma$, where σ for (a) PC1, (b) PC2, (c) PC3, and (d) PC4 is 0.3, 0.4, 0.5, and 0.5, respectively. The horizontal black dotted lines represent the zero-level intensity. The vertical green dotted lines represent the systemic velocity of 8.34 km s^{-1}.
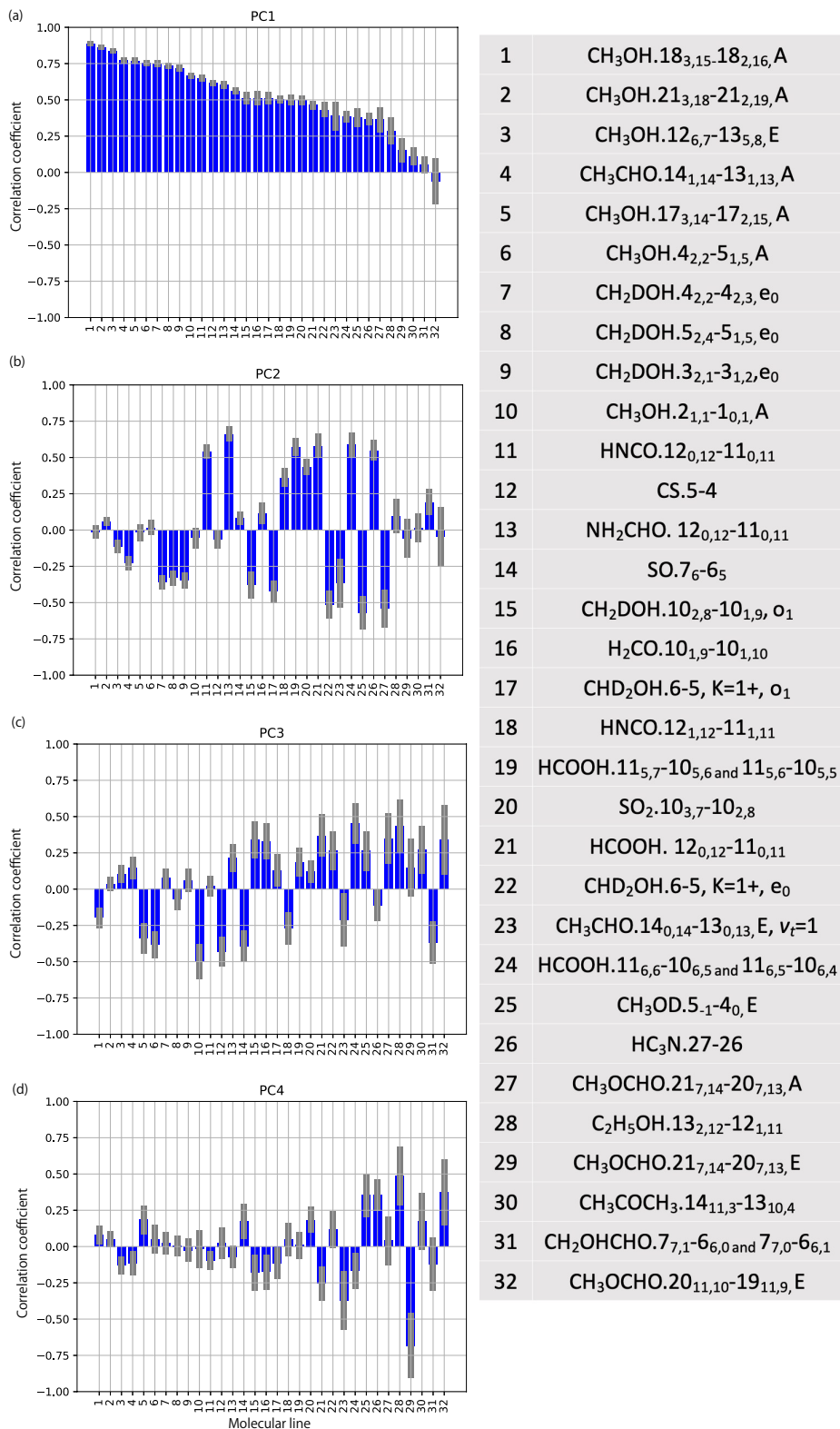
Figure 8.16: Correlation coefficients between the first four principal components in PCA-3D for B335 and the molecular lines. The uncertainties are shown in grey (See Section 6.3). The numbers represent the molecular lines listed in the attached table.

Chapter 9

Molecular Distribution in the Disk/Envelope System of the Hot Corino Chemistry Sources[*]

As described in Chapters 6-8, PCA is a powerful method to extract the characteristic features from large molecular-line data in an unbiased way. In particular, PCA-3D treating the spatial and velocity information simultaneously is found to be very useful to disentangle complex molecular distributions in disk-forming regions of the two Class 0 protostellar sources, L483 and B335. We here discuss the characteristic features of the molecular line distributions derived from them. In particular, we focus on the difference between nitrogen-bearing and oxygen-bearing species, NH_2CHO, and $HCOOH$.

9.1 Nitrogen-bearing and Oxygen-bearing Species

Figures 9.1(a), (b), and (c) are biplots showing the contributions of the principal components for each molecular-line distribution derived from PCA-3D for L483 on the PC1-PC2, PC1-PC3, and PC2-PC3 planes, respectively. The yellow and blue plots represent the nitrogen-bearing and oxygen-bearing organic molecules, respectively. In Figures 9.1(a) and (b), the PC1 contributions of the oxygen-bearing molecules tend to be slightly larger than those of the nitrogen-bearing molecules. Moreover, the oxygen-bearing organic molecules except for CH_3OH ($18_{3,16}-17_{4,13}$, A) show small contributions of PC2 and PC3. On the contrary, the contributions of PC2 and PC3 are larger for the nitrogen-bearing molecules except for CH_3CN than those for the oxygen-bearing molecules. This result reveals a spatial differentiation of the nitrogen-bearing and oxygen-bearing molecular-line emission in the disk/envelope system of L483. In principle, distributions of molecular lines can be different due to the excitation effect, as shown in the H_2CO line case for IRAS 15398−3359 (Chapter 7). Although we cannot see this trend in the lower excitation CH_3OH lines (E_u =50 K: #1, E_u =61 K: #2, E_u =46 K: #4, and E_u =190 K: #6) for L483, only the very high excitation line of CH_3OH ($18_{3,16}-17_{4,13}$, A; E_u =447 K: #13) shows a relatively high contribution of PC2. The dust temperature is supposed to be

70–130 K (Oya et al., 2017; Jacobsen et al., 2019), whereas the H_2 density is roughly estimated to be 10^8 cm^{-2} or higher from the H_2 column density (4.9–9.5)×10^{23} cm^{-2} (Oya et al., 2017) and the assumed size of the hot region (~100 au). Although the LTE condition is almost fulfilled, the line with high E_u such as CH$_3$OH ($18_{3,16}$−$17_{4,13}$, A) is expected to appear in a compact hot region around the protostar. This is the reason for its relatively high PC2 value.

Judging from the large contribution of PC1, the distributions of the oxygen-bearing molecules slightly extend along the disk/envelope direction. On the other hand, the nitrogen-bearing molecules with the small PC1 and large PC2 contributions have compact distributions with the high-velocity components. A larger velocity width for a more compact distribution found in PC2 is physically reasonable, because the rotation/infall velocity is expected to increase as approaching to the protostar.

Such a spatial differentiation of the nitrogen-bearing and oxygen-bearing molecular-line emission is also seen in the disk/envelope system of B335. Figure 9.2(a) is a biplot showing the contributions of the principal components for each molecular-line distribution derived from PCA-3D for B335 on the PC1-PC2 plane. The blue, cyan, and light blue plots represent, deuterated CH$_3$OH (CH$_2$DOH, CHD$_2$OH, and CH$_3$OD), CH$_3$OH, and the other oxygen-bearing organic molecules, respectively. The yellow plots indicate the nitrogen-bearing molecules. The PC2 contributions of the nitrogen-bearing molecules tend to be larger than those of the oxygen-bearing ones except for HCOOH (#19, #21, and #24), indicating the compact distribution of the nitrogen-bearing ones. Thus, the positive and negative PC2 contributions reflect the different distributions between the nitrogen-bearing and oxygen-bearing molecules. The details for HCOOH are discussed in Section 9.2.

In Figure 9.2(a), a systematic difference between CH$_3$OH and its deuterated species can be seen. The deuterated species tend to have a larger negative contribution of PC2, indicating a more extended distribution with a narrower linewidth than CH$_3$OH. Although their extended features can be recognized by eye in the moment 0 maps (Figure 8.3), we can show it by PCA definitively. The slight difference among the oxygen-bearing molecules is seen on the PC1-PC2 plane (Figure 9.2(a)), where the CH$_3$OH lines have a larger contribution of PC1 and the CH$_2$DOH lines have the negative contribution of PC2.

The chemical differentiation between the nitrogen-bearing and oxygen-bearing complex organic molecules (COMs) have been reported for low-mass and high-mass star-forming regions on various scales (e.g., Wyrowski et al., 1999; Bottinelli et al., 2004a,b; Kuan et al., 2004; Beuther et al., 2005; Fontani et al., 2007; Calcutt et al., 2018; Oya et al., 2018; Csengeri et al., 2019). This still remains as an important issue to be solved for astrochemistry. Recently, important observational results stepping forward to solve this problem has come out. Csengeri et al. (2019) conducted the ALMA observation toward the high-mass protostellar source, G328.2551-0.5321, and reported that the nitrogen-bearing COMs including NH$_2$CHO and C$_2$H$_5$CN are concentrated around the protostar, while the oxygen-bearing COMs such as CH$_3$OH and C$_2$H$_5$OH are present around the centrifugal barrier of the infalling gas. They argue that the production of the nitrogen-bearing COMs is related to the protostellar heating, while that of the oxygen-bearing COMs

is to the accretion shock heating of the infalling gas. If this picture could be applied to low-mass protostellar sources, the nitrogen-bearing COMs would have more compact distributions than the oxygen-bearing COMs. This is consistent with our results of PCA-3D. Thus, we reveal such differentiation in the disk/envelope system of the low-mass protostellar sources L483 and B335, while the size scale is much smaller than the G328.2551-0.5321 case.

Note that the SiO emission also traces a shock in L483, but it is caused by the outflow. Indeed, SiO does not have any correlation with the oxygen-bearing molecules. On the other hand, the different distributions in L483 are also seen in the PC3 values for some molecules such as C_2H_5CN and HC_3N (Figure 9.1(c)). It should be noted that C_2H_5CN shows PC2 and PC3 similar to SiO (Figure 9.1(c)). This similarity might tell us a clue to solve the origin of C_2H_5CN. To go further, we need to observe other lines of this molecule for confirmation of the above trend.

9.2 NH$_2$CHO and HCOOH

An important result from the PCAs for L483 and B335 is on the distribution of NH_2CHO. This molecule containing a peptide-like bond (N$-$C=O) is thought to be a mother molecule for prebiotic evolution, and hence, various observational, experimental, and theoretical works for the molecule have been reported (e.g., Saladino et al. 2012; Barone et al., 2015; López-Sepulcre et al., 2015, 2019; Quénard et al., 2018; Martín-Doménech et al., 2020). Detections of NH_2CHO toward star-forming regions (e.g., Bisschop et al., 2007a; Yamaguchi et al., 2012; Kahane et al., 2013; Mendoza et al., 2014; Gorai et al., 2020; Colzi et al., 2021) as well as comets of the solar system (Bockelée-Morvan et al., 2000; Biver et al., 2014; Goesmann et al., 2015) imply inheritance of this molecule from protostellar cores to planetary systems.

As described in Section 8.4, for L483, the NH_2CHO ($12_{11,1}-11_{11,0}$ and $12_{0,12}-11_{0,11}$) lines are well correlated with PC2 (Figure 8.7(b)). This means that they have a compact distribution with the high-velocity component. A compact distribution of NH_2CHO can also be confirmed in the map presented by Jacobsen et al. (2019). Figures 8.2 (s) and (u) of Chapter 8 represent the line profiles of NH_2CHO ($12_{11,1}-11_{11,0}$ and $12_{0,12}-11_{0,11}$) toward the continuum peak, respectively. They both have a slight dip at the systemic velocity and a redshifted peak around ~9 km s^{-1}, as seen in the PC2 spectrum of PCA-3D, although the slight difference is seen between the two lines. Such a spectral line feature of the NH_2CHO ($12_{0,12}-11_{0,11}$) line is consistent with that reported in Oya et al. (2017). The compact distribution of NH_2CHO is not likely the excitation effect, because the upper state energies (E_u) of the NH_2CHO lines are comparable to those of the low-excitation CH$_3$OH lines. For B335, the NH_2CHO ($12_{0,12}-11_{0,11}$) line has a large correlation for PC1 and PC2, which can reproduce the compact distribution with the high-velocity component (Section 8.7). It was previously reported that this line has a broad spectral line width without a strong absorption feature around the systemic velocity (Imai et al., 2016, 2019), which means the high-velocity components. Thus, we conclude that NH_2CHO resides in the inner part of the rotating disk/envelope structure with the

observations. In general, the NH_2CHO distribution has been suggested to be compact in other sources: e.g., HH212 (Lee et al., 2017), G328.2551-0.5321 (Csengeri et al., 2019), G10.6 (Law et al., 2021).

Various chemical pathways for NH_2CHO have been proposed including gas-phase (Quan & Herbst, 2007; Garrod et al., 2008; Halfen et al., 2011; Barone et al., 2015; Skouteris et al., 2017) and grain-surface processes (Charnley, 1997; Raunier et al., 2004; Fedoseev et al., 2016). Mendoza et al. (2014) and López-Sepulcre et al. (2015) reported a correlation between the abundance of NH_2CHO and HNCO based on their survey observations toward various star-forming regions from low-mass to high-mass ones. The abundance relationship was also reported with the ALMA observations (Coutens et al., 2016; Allen et al., 2020) and was supported by theoretical calculation (Quénard et al., 2018). These works suggest some chemical relations between the two species. Hydrogenation of HNCO has been proposed as one possible formation process leading to NH_2CHO on dust grains (López-Sepulcre et al., 2015; Quénard et al., 2018), although Quénard et al. (2018) noted that the power-law correlation between the two species can be seen, even if NH_2CHO is not formed from HNCO through hydrogenation on dust grains. Thus, the chemical link to HNCO would be a key to resolve the formation route of NH_2CHO.

In our study, a relation between HNCO and NH_2CHO is also seen in PCA-3D for both sources. Indeed, both HNCO and NH_2CHO are closely located on the PC1-PC2 biplot of Figure 9.1 for L483. Similarly, their close association is seen in the PC1-PC2 biplot of Figure 9.2 for B335. However, the microscopic processes for the NH_2CHO formation are still controversial. We need laboratory and theoretical works on the formation process of NH_2CHO in the gas phase and on dust grains.

On the other hand, a similar trend of HCOOH to the nitrogen-bearing molecules, NH_2CHO HNCO, and HC_3N, which can be seen in the PCA-3D for B335, is another important result. HCOOH, the simplest organic carboxylic acid, has been observed in the gas phase towards high-mass and low-mass star-forming regions (Woods et al., 1983; Liu et al., 2001; Bisschop et al., 2007a; Vastel et al., 2014; Lefloch et al., 2017; Oya et al., 2017; Favre et al., 2018; Csengeri et al., 2019) as well as the cold dark interstellar cloud (Irvine et al., 1990) and the comets of planetary system (Biver et al., 2014). Csengeri et al. (2019) also reported the compact distribution of HCOOH and the nitrogen-bearing species, which is essentially consistent with our result.

Although the chemical route of HCOOH has also been investigated experimentally (Ioppolo et al., 2011) and theoretically (Tielens & Hagen, 1982; Garrod & Herbst, 2006; Garrod et al., 2008; Vasyunin et al., 2017), the formation process and the chemical link to the nitrogen-bearing species are puzzling. Our results suggest that they are liberated from dust grains or formed in the gas phase in the region closer to the protostar than the oxygen-bearing COMs. It should be noted that it seems to be not only the temperature for the liberation of these molecules formed on grain mantles during the protostellar core phase. As described in Chapter 5, we derived the temperature distribution around the protostar within the radius of ~10 au, whose result suggests the possibility of the shock accretion heating in the outer envelope. The temperature of the outer envelope is derived to be almost 170 K, which is higher than that of the inner envelope, ~100 K. However, HCOOH and

NH$_2$CHO does not appear in the gas phase at the outside of the radius of ~6 au even though these desorption temperatures are comparable to those of CH$_3$OH, as shown in Table 9.1 (Oya et al., 2019). In other words, the other factors rather than the temperature are responsible for these molecules to be observed in the gas phase. It may be the high-density condition, the protostellar radiation, or both of them. If we can extract the common characteristic distribution of these molecules in various sources with the PCA, we will have an important clue to the formation processes of NH$_2$CHO and HCOOH. To understand the chemical process in the disk/envelope system during the early stage of star formation, systematic observations of more molecular lines for other Class 0/I protostars with higher angular resolution and higher signal-to-noise ratio are awaited.

Table 9.1: Desorption Energies and Desorption Temperatures of Molecular Species

Molecular Species	Desorption Energy[a] $E_{\rm des}/k_{\rm B}$ (K)	Desorption Temperature[b] $T_{\rm des}$ (K)
C	800	15
S	1100	20
CO	1150	21
O	1600	30
CS	1900	35
H$_2$CO	2050	37
CCH	2137	39
SO	2600	47
H$_2$CS	2700	49
H$_2$S	2743	50
OCS	2888	53
SiO	3500	64
HCOOCH$_3$	4000	73
H$_2$O	4800	87
CH$_3$OH	4930	90
HCOOH	5000	91
SO$_2$	5330	97
NH$_2$CHO	5556	101

[a] Desorption energy are taken from Kinetic Database for Astrochemistry (KIDA; Wakelam et al. (2012), http://kida.obs.u-bordeaux1.fr/).
[b] The temperatures are derived from the desorption energy with the equation $k_B T_{\rm des} = E_{\rm des}/55$. Taken from Oya et al. (2019).
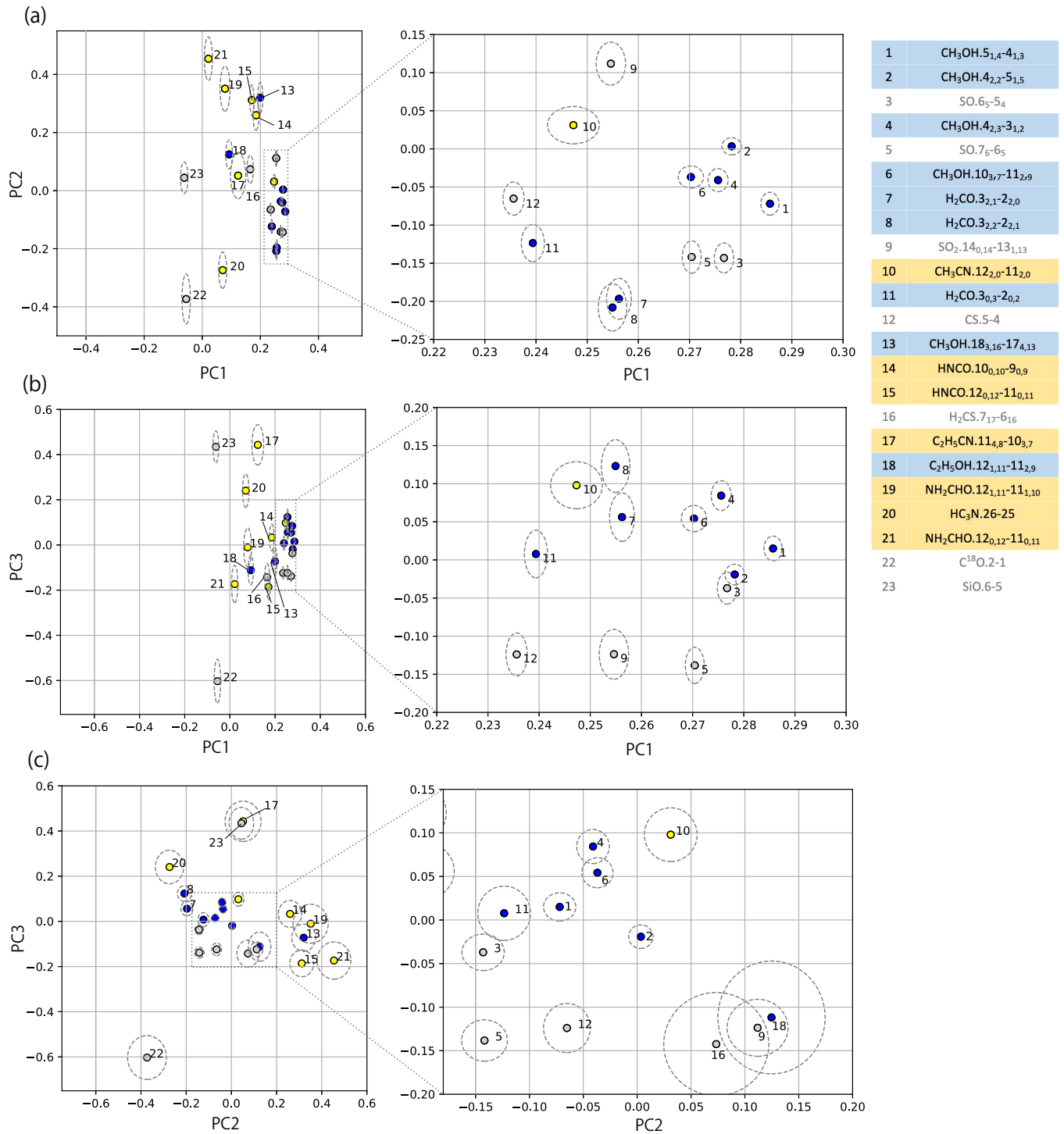
Figure 9.1: (a-c) Biplots of the contributions for the principal components in PCA-3D for each molecular-line distribution in L483 on the PC1-PC2, PC1-PC3, and PC2-PC3 planes. The dashed ellipses represent the uncertainties (Section 6.3). The numbers represent the molecular lines listed in the attached table. Blue and yellow represent the oxygen-bearing and nitrogen-bearing organic molecules, respectively.
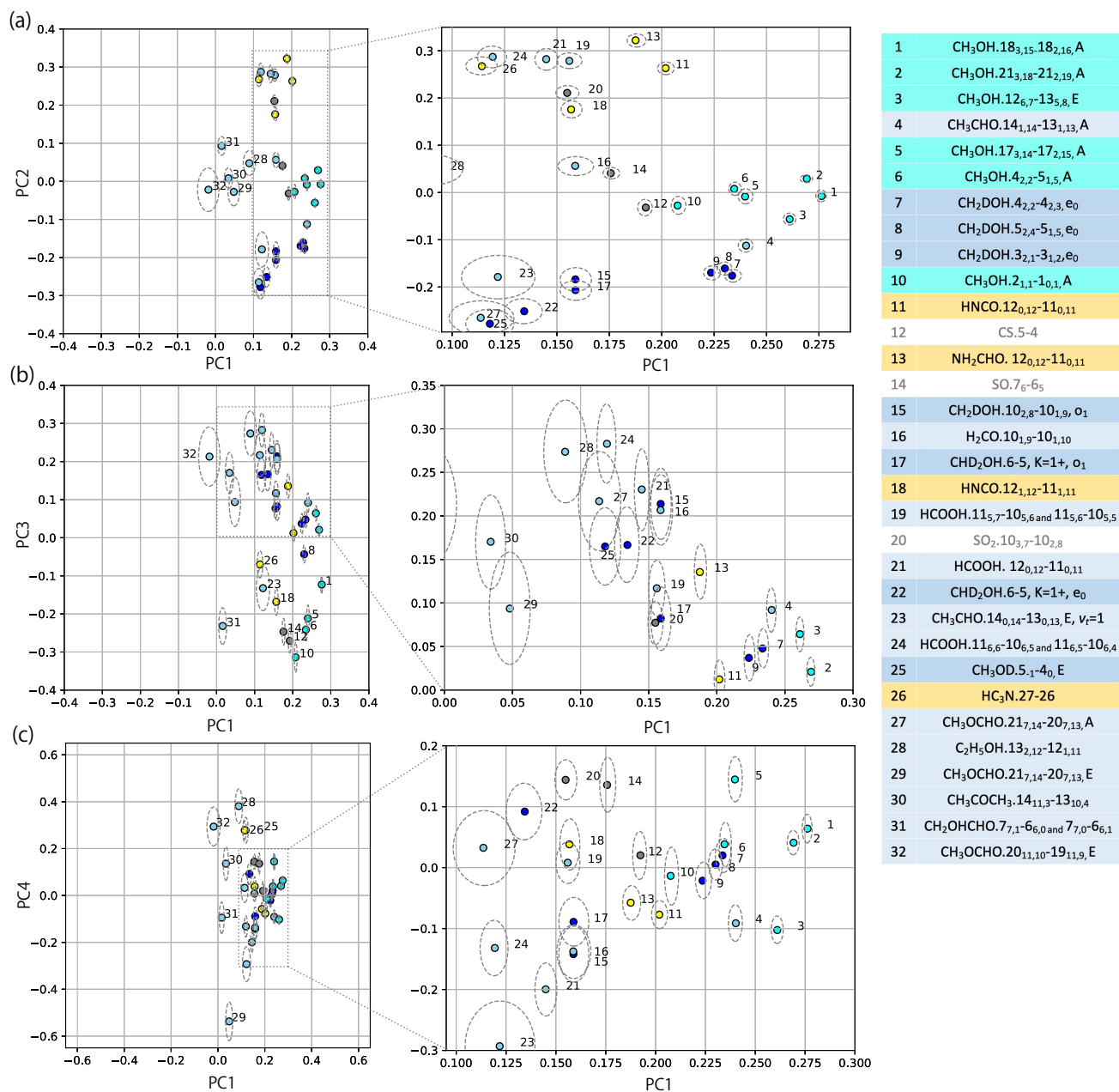
Figure 9.2: (a, b, c) Biplots of the contributions for the principal components in PCA-3D for each molecular-line distribution in B335 on the PC1-PC2, PC1-PC3, and PC1-PC4 planes. The dashed ellipses represent the uncertainties (Section 6.3). The numbers represent the molecular lines listed in the attached table. Blue, cyan, and light blue plots represent deuterated CH_3OH (CH_2DOH, CHD_2OH, and CH_3OD), CH_3OH, and the other oxygen-bearing molecules, respectively. Yellow plots indicate the nitrogen-bearing organic molecules.

Chapter 10
Conclusion

Focusing on the early stage of low-mass star formation, we have studied the physical and chemical structures around the three protostellar sources with ALMA at a high resolution (0."03-0."5). New pictures of the early stage, some of which are unexpected, have been derived. These results have provided us with a novel insight into physical and chemical processes in the beginning of low-mass star formation, which will eventually contribute to understandings of the origin of the solar system as one of the huge building blocks. Also, we still have some puzzles to be addressed in the future.

10.1   Summary of This Thesis

Major results of this thesis are summarized below. They consist of the two parts, physics and chemistry.

Physical Structure

(1) Our study on IRAS 15398−3359 described in Chapter 3 reveals that the rotationally supported disk begins to form at the earliest stage of low-mass star formation. The protostellar mass is comparable to or even lower than the mass of the first core expected theoretically, and the disk structure has a similar mass to the protostar. Since the protostar is still embedded in the thick envelope gas, the low protostellar mass means its youth. Hence, this result suggests the co-evolution of disks and stars. The protostar and the disk covered by a thick envelope whose mass is larger by an order of magnitude would make the disk structure unstable.

(2) In this very low-mass protostellar source, we find the large reorientations of the outflow during $\sim 10^3$ -10^4 yr from the birth of the protostar (Chapter 4). The detection of the SiO emission extending over 10^3 -10^4 au scale with the narrow line width is clear evidence for the past outflow activity. The outflow reorientation may be related to non-uniform internal angular momentum distribution in the molecular cloud core. Detection of the third outflow in this source further supports this picture.

(3) High-resolution observations of B335 at a few au scale enable us to resolve the inner envelope structure within the radius of 10 au around the protostar (Chapter

5). We find that the temperature does not monotonously decrease as the increasing distance from the protostar, but locally increases at a certain radius in the envelope. We propose that the gas accreting toward the protostar can cause a shocked region at this radius, resulting in the local temperature increase.

Chemical Structure

(1) Protostellar envelope/disk systems have complex chemical structures. We have employed Principal Component Analysis (PCA), as a powerful method to characterize and classify the molecular distributions systematically (Chapter 6). This is the first attempt to employ this method to protostellar sources. We find that the field range for PCA should be determined by a scientific purpose (Chapter 7), and PCA for the cube data is the best way to fully characterize the chemical differentiation (Chapters 8 and 9). PCA enables us to interpret the distribution and the kinematics of the various molecular lines simultaneously without any preconception.

(2) The characteristic features of organic molecular lines are extracted by PCA systematically. The distributions of the oxygen-bearing and nitrogen-bearing molecules are systematically different, where those of nitrogen-bearing molecules are more compact. This trend is similar to those suggested in other sources in previous works. Here, we clearly indicate it in an unbiased way. The correlation between NH_2CHO and HNCO is further confirmed, and this result will be a key to explore the possible relation in the formation processes of these two molecules.

(3) In B335, the distributions of the HCOOH lines are found to be more compact than those of the oxygen-bearing molecular ones. The compact distribution of HCOOH, which is similar to the distributions of nitrogen-bearing molecules, suggests a potential relation or similarity to the chemical pathways forming NH_2CHO and HNCO. It has ever been thought that these molecules are produced in the prestellar phase on the dust grains and are liberated into gas phase during the protostellar phase due to the protostellar heating and outflow shocks. However, the situation is not so simple. On the basis of the temperature structure presented in this thesis, the other factors rather than the temperature is responsible for the compact distributions, for example: the high-density condition and the protostar radiation. This result requires reconsideration of the formation of organic molecules.

As summarized above, the early stage of protostellar evolution does not proceed 'smoothly' both in physics and chemistry, but often reveals drastic and sporadic changes. The chemical phenomena are deeply related to the physical structure and their changes. Although the results presented in this thesis for the three protostellar sources need to be examined for other sources, they are raising new challenges for theories of star formation and molecular evolution. Thus, they will be an important clue to understanding the diversity of protostellar sources and eventually of planetary systems in the end.

10.2   Future Prospects

10.2.1   Does a Disk Have Any Relation to the Remnant of a First Hydrostatic Core?

As described in Chapter 3, we have found a rotating disk structure associated with the very low-mass protostar, IRAS 15398−3359. Such a disk structure is theoretically predicted to have a relation to the first hydrostatic core (e.g., Saigo et al., 2008; Bate, 2010; Inutsuka et al., 2010). According to these theoretical simulations, the rotating first core is flattened, and its size is as small as 10 au. Figure 10.1 indicates the evolution of protostellar objects in terms of mass after the beginning of contraction in the molecular cloud core (Inutsuka et al., 2010). They suggest that the remnant of the first core turns to be a rotating disk structure in the very early evolutionary phase. However, observational verifications of this process have not been done yet. In this thesis work, the detailed characterization of the disk structure has to be left for future works, because the ALMA data in our hands are not enough in spatial resolution and sensitivity.
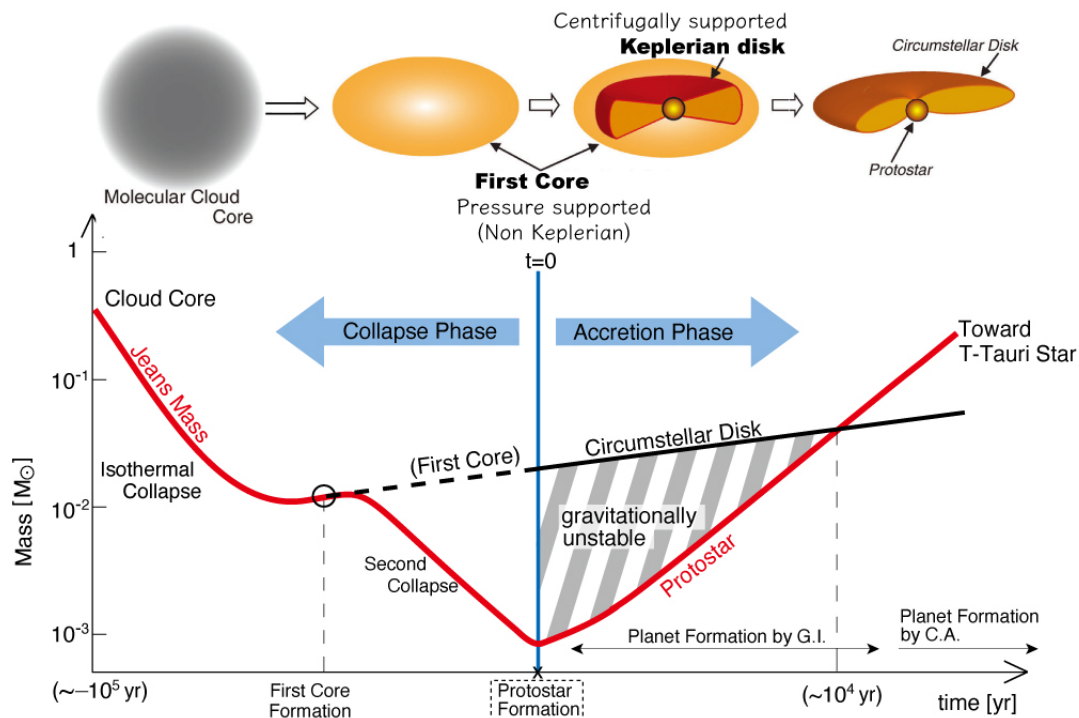

Figure 10.1: Schematic picture of the variation of the mass for the evolution of protostellar objects in the collapsing core. The blue vertical axis corresponds to the beginning of protostar formation. The object mass decreases at once after the birth of a first core, and a protostar grows with the circumstellar disk in the gas accretion phase. The first core is suggested to be the precursor of the circumstellar disk. Taken from (Inutsuka et al., 2010).

IRAS 15398−3359 has a protostellar mass as low as 0.007 $M_\odot$ (<0.01 $M_\odot$), indicating the very early stage. Hence, this source will provide us a chance to see the remnant of the first core, if the inside of the disk structure can be resolved at

a sufficient high resolution. In general, the first cores are supported by gas pressure, and hence, it will reveal non-Keplerian rotation, in contrast to the rotationally supported disks that show Keplerian rotation profiles. A close look at the rotation motion and the structure of the disk is important to assess its relation to the first core at higher resolution observations (<30 au) in the future.

10.2.2 Angular Momentum Distribution of a Protostellar Core

We have proposed that changes in the angular momentum within the protostellar core can cause the large episodic reorientations of the outflow of IRAS 15398−3359 (Chapter 4). While recent theories indicate that turbulent eddies in cores have different angular momenta (Misugi et al., 2019), we need to verify this situation with observations of the angular momentum distribution. If the multiple outflows from IRAS 15398−3359 are the result of accretion from a turbulent core, we expect that the core velocity structure should be complex.

The N_2H^+ and $H^{13}CO^+$ lines are known to trace cold and dense cores. Figures 10.2(a) and (b) show the moment 1 maps of N_2H^+ (J =1−0) and $H^{13}CO^+$ (J =3−2) line emission, respectively, observed toward IRAS 15398−3359 in the ALMA Large Program FAUST. While both distributions are round and extended over ~3000 au scales around the continuum peak, $H^{13}CO^+$ is slightly compact, tracing the inside of the core. Although the velocity gradient can be seen in both images, their directions look different from each other. This may imply that the angular momentum within the protostellar core depends on the distance from the protostar.
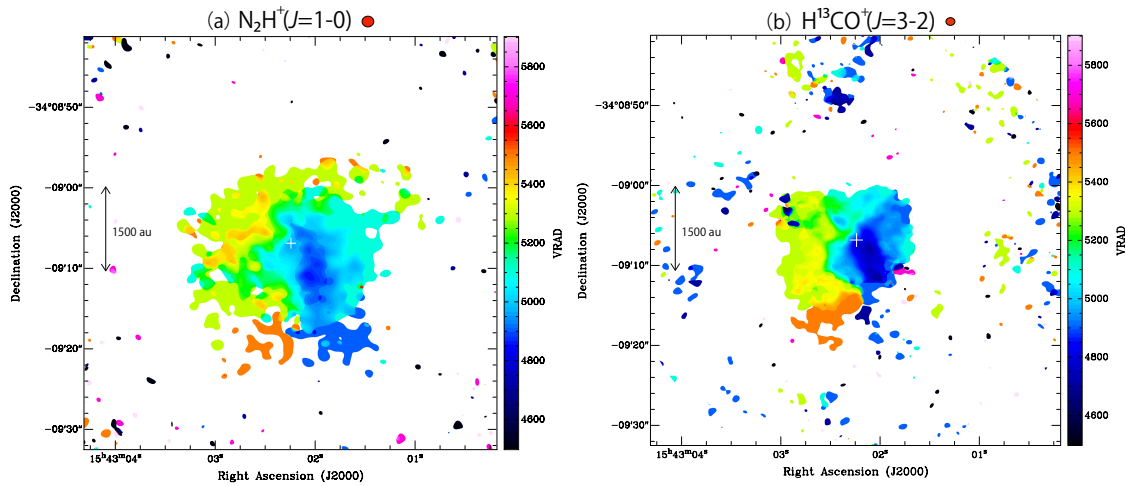

Figure 10.2: (a, b) Moment 1 maps of N_2H^+ (J =1−0) (a) and $H^{13}CO^+$ (J =3−2) (b) lines observed for IRAS 15398−3359. The cross marks represent the protostellar position. The circles after the name of the line represent the beam size. Velocity is shown in color. The directions of the velocity gradients are different from each other.

However, we cannot conclude it with these observational data. It is hard to determine accurately the angular momentum axis of the inside, based on the $H^{13}CO^+$ (J =3−2) line, because it also trace part of the primary outflow along the northeast to southwest direction. Ideally, the comparison should be made among the

molecular lines of a single molecular species with different critical densities, since the lower frequency lines trace gas with lower density. For instance, by using the H^{13}CO$^+$ (J =3−2 and J =1−0) lines, we can trace different parts of the core, allowing us to measure how the rotation of the core varies with the size. Such kinds of works have been reported for other sources (Pineda et al., 2019; Gaudel et al., 2020), but a careful look at the IRAS 15398−3359 case is interesting.

10.2.3 Exploring of Molecular Distributions around Protostars

Molecules around protostars probably have a relation to materials in the solar system. As mentioned in Chapter 1, some organic species found around protostars are also detected in the comet in the Rosetta mission (Goesmann et al., 2015). However, chemical routes of such molecules from protostellar sources to planetary systems are still controversial.

We can now study organic species at a small scale around protostars. High resolution observations with ALMA have recently revealed hybrid sources, which are a WCCC source containing hot corino nature (e.g., B335 and L483 Imai et al., 2016; Oya et al., 2017). In this regard, our observation with the FAUST project has very recently detected a few high excitation lines of CH$_3$OH and the faint emission of HCOOCH$_3$ in IRAS 15398−3359, indicating a hot corino nature, although it has long been identified as a WCCC source. Thus, detailed chemical characterization is necessary for other sources in order to reveal what organic molecules are inherited to planetary system and how much. For this purpose, the analysis with PCA is essential, as we have demonstrated in Part II of this thesis. Some specific features of organic molecular distributions could be a key to solve the evolutionary routes at the beginning stage.

More and more observations for other low-mass protostellar sources are needed, in order to discuss the chemical processes based on observations. As well, collaborations with molecular science and surface science are necessary to interpret observational results in a microscopic (molecular-based) way. This direction is an important toward our ground goal, understanding the origin of the solar system.

Acknowledgements

Bibliography

Agúndez, M., Cernicharo, J., de Vicente, P., et al. 2015, A&A, 579, L10

Agúndez, M., Cernicharo, J., & Guélin, M. 2015, A&A, 577, L5

Agúndez, M., Marcelino, N., Cernicharo, J., et al. 2018, A&A, 611, L1

Agúndez, M., Marcelino, N., Cernicharo, J., et al. 2019, A&A, 625, A147

Aikawa, Y., Furuya, K., Yamamoto, S., et al. 2020, ApJ, 897, 110

Aikawa, Y., Wakelam, V., Garrod, R. T., et al. 2008, ApJ, 674, 984

Aikawa, Y., Wakelam, V., Hersant, F., et al. 2012, ApJ, 760, 40

Albrecht, S., Winn, J. N., Marcy, G. W., et al. 2013, ApJ, 771, 11

Allen, V., van der Tak, F. F. S., López-Sepulcre, A., et al. 2020, A&A, 636, A67

Altwegg, K., Balsiger, H., & Fuselier, S. A. 2019, Annual Review of Astronomy and
    Astrophysics, 57, 113

Alves, F. O., Girart, J. M., Caselli, P., et al. 2017, A&A, 603, L3

Ambrose, H. E., Shirley, Y. L., & Scibelli, S. 2021, MNRAS, 501, 347

André, P. 1994, The Cold Universe, 179

Andre, P., Ward-Thompson, D., & Barsony, M. 1993, ApJ, 406, 122

Andre, P., Ward-Thompson, D., & Barsony, M. 2000, Protostars and Planets IV, 59

Andrews, S. M., Huang, J., Pérez, L. M., et al. 2018, ApJL, 869, L41

Aota, T., Inoue, T., & Aikawa, Y. 2015, ApJ, 799, 141

Arce, H. G., Santiago-García, J., Jørgensen, J. K., et al. 2008, ApJL, 681, L21

Arce, H. G., Mardones, D., Corder, S. A., et al. 2013, ApJ, 774, 39

Aso, Y., Ohashi, N., Aikawa, Y., et al. 2017, ApJ, 849, 56

Aso, Y., Ohashi, N., Saigo, K., et al. 2015, ApJ, 812, 27

Avery, L. W., Broten, N. W., MacLeod, J. M., et al. 1976, ApJL, 205, L173

Bachiller, R., Martin-Pintado, J., & Fuente, A. 1993, ApJL, 417, L45

Bachiller, R., & Pérez Gutiérrez, M. 1997, ApJL, 487, L93

Bachiller, R. 1996, Annual Review of Astronomy and Astrophysics, 34, 111.

Bacmann, A., Taquet, V., Faure, A., et al. 2012, A&A, 541, L12

Baraffe, I., & Chabrier, G. 2010, A&A, 521, A44

Barone, V., Latouche, C., Skouteris, D., et al. 2015, MNRAS, 453, L31

Bate, M. R., Tricco, T. S., & Price, D. J. 2014, MNRAS, 437, 77

Bate, M. R. 1998, ApJL, 508, L95

Bate, M. R. 2010, MNRAS, 404, L79

Beichman, C. A., Myers, P. C., Emerson, J. P., et al. 1986, ApJ, 307, 337

Benedettini, M., Viti, S., Codella, C., et al. 2007, MNRAS, 381, 1127

Benson, P. J. & Myers, P. C. 1989, Astrophysical Journal, Supplement, 71, 89

Bergin, E. A. & Tafalla, M. 2007, Annual Review of Astronomy and Astrophysics, 45, 339

Beuther, H., Zhang, Q., Greenhill, L. J., et al. 2005, ApJ, 632, 355

Bianchi, E., Chandler, C. J., Ceccarelli, C., et al. 2020, MNRAS, 498, L87

Bisschop, S. E., Fuchs, G. W., Boogert, A. C. A., et al. 2007, A&A, 470, 749

Bisschop, S. E., Jørgensen, J. K., van Dishoeck, E. F., et al. 2007, A&A, 465, 913

Biver, N., Bockelée-Morvan, D., Debout, V., et al. 2014, A&A, 566, L5

Bjerkeli, P., Jørgensen, J. K., Bergin, E. A., et al. 2016, A&A, 595, A39

Bjerkeli, P., Jørgensen, J. K., & Brinch, C. 2016, A&A, 587, A145

Bjerkeli, P., van der Wiel, M. H. D., Harsono, D., et al. 2016, Nature, 540, 406

Bjerkeli, P., Ramsey, J. P., Harsono, D., et al. 2019, A&A, 631, A64

Blake, G. A., Sutton, E. C., Masson, C. R., et al. 1987, ApJ, 315, 621

Bockelée-Morvan, D., Lis, D. C., Wink, J. E., et al. 2000, A&A, 353, 1101

Bodenheimer, P. 1995, Annual Review of Astronomy and Astrophysics, 33, 199

Born, M. & Wolf, E. 1959, 'Principles of Optics', Cambridge Univ. Press, p562

Bottinelli, S., Ceccarelli, C., Lefloch, B., et al. 2004, ApJ, 615, 354

Bottinelli, S., Ceccarelli, C., Neri, R., et al. 2004, ApJL, 617, L69

Brinch, C., & Jørgensen, J. K. 2013, A&A, 559, A82

Busch, L. A., Belloche, A., Cabrit, S., et al. 2020, A&A, 633, A126

Calcutt, H., Jørgensen, J. K., Müller, H. S. P., et al. 2018, A&A, 616, A90

Calmonte, U., Altwegg, K., Balsiger, H., et al. 2016, MNRAS, 462, S253

Cami, J., Bernard-Salas, J., Peeters, E., et al. 2010, Science, 329, 1180

Carrasco-González, C., Sierra, A., Flock, M., et al. 2019, ApJ, 883, 71

Caselli, P. & Ceccarelli, C. 2012, Astronomy and Astrophysics Reviews, 20, 56

Caselli, P., Benson, P. J., Myers, P. C., et al. 2002, ApJ, 572, 238

Caselli, P., Walmsley, C. M., Zucconi, A., et al. 2002, ApJ, 565, 331

Caselli, P., Hartquist, T. W., & Havnes, O. 1997, A&A, 322, 296

Caselli, P., Hasegawa, T. I., & Herbst, E. 1993, ApJ, 408, 548

Caselli, P., Pineda, J. E., Zhao, B., et al. 2019, ApJ, 874, 89

Caselli, P., Walmsley, C. M., Tafalla, M., et al. 1999, ApJL, 523, L165

Cazaux, S., Tielens, A. G. G. M., Ceccarelli, C., et al. 2003, ApJL, 593, L51

Ceccarelli, C., Caselli, P., Fontani, F., et al. 2017, ApJ, 850, 176

Cernicharo, J., Agúndez, M., Cabezas, C., et al. 2021, A&A, 649, L15

Cernicharo, J., Marcelino, N., Roueff, E., et al. 2012, ApJL, 759, L43

Chapman, N. L., Davidson, J. A., Goldsmith, P. F., et al. 2013

Chapman, N. L., Lai, S.-P., Mundy, L. G., et al. 2007, ApJ, 667, 288

Charnley, S. B. 1997, IAU Colloq. 161: Astronomical and Biochemical Origins and the Search for Life in the Universe, 89

Charnley, S. B., Tielens, A. G. G. M., & Millar, T. J. 1992, ApJL, 399, L71

Chen, X., Arce, H. G., Zhang, Q., et al. 2013, ApJ, 768, 110

Cheung, A. C., Rank, D. M., Townes, C. H., et al. 1968, Physical Review Letters, 21, 1701

Cheung, A. C., Rank, D. M., Townes, C. H., et al. 1969, Nature, 221, 626

Chou, T.-L., Takakuwa, S., Yen, H.-W., Ohashi, N., & Ho, P. T. P. 2014, ApJ, 796, 70

Codella, C., Bachiller, R., & Reipurth, B. 1999, A&A, 343, 585

Codella, C., Cabrit, S., Gueth, F., et al. 2014, A&A, 568, L5

Codella, C., Ceccarelli, C., Bianchi, E., et al. 2020, A&A, 635, A17

Codella, C., Lefloch, B., Ceccarelli, C., et al. 2010, A&A, 518, L112

Colzi, L., Rivilla, V. M., Beltrán, M. T., et al. 2021, A&A, 653, A129

Coutens, A., Jørgensen, J. K., van der Wiel, M. H. D., et al. 2016, A&A, 590, L6

Csengeri, T., Belloche, A., Bontemps, S., et al. 2019, A&A, 632, A57

Dame, T. M. & Thaddeus, P. 1985, ApJ, 297, 751

Dapp, W. B. & Basu, S. 2010, A&A, 521, L56

Dapp, W. B., Basu, S., & Kunz, M. W. 2012, A&A, 541, A35

De Simone, M., Codella, C., Ceccarelli, C., et al. 2020, A&A, 640, A75

Douglas, A. E. & Herzberg, G. 1941, ApJ, 94, 381

Drozdovskaya, M. N., van Dishoeck, E. F., Jørgensen, J. K., et al. 2018, MNRAS, 476, 4949

Drozdovskaya, M. N., van Dishoeck, E. F., Rubin, M., et al. 2019, MNRAS, 490, 50

Duan, Y.-B., Ozier, I., Tsunekawa, S., et al. 2003, Journal of Molecular Spectroscopy, 218, 95

Dunham, M. M., Allen, L. E., Evans, N. J., et al. 2015, Astrophysical Journal, Supplement, 220, 11

Dutrey, A., Semenov, D., Chapillon, E., et al. 2014, Protostars and Planets VI, 317

Dzib, S. A., Loinard, L., Ortiz-León, G. N., et al. 2018, ApJ, 867, 151

Endres, C. P., Schlemmer, S., Schilke, P., et al. 2016, Journal of Molecular Spectroscopy, 327, 95

Enoch, M. L., Corder, S., Dunham, M. M., & Duchêne, G. 2009, ApJ, 707, 103

Evans, N. J., Di Francesco, J., Lee, J.-E., et al. 2015, ApJ, 814, 22

Evans, N. J., Dunham, M. M., Jørgensen, J. K., et al. 2009, Astrophysical Journal, Supplement, 181, 321

Ewen, H. I. & Purcell, E. M. 1951, Nature, 168, 356

Fateeva, A. M., Bisikalo, D. V., Kaygorodov, P. V., et al. 2011, Astrophysics and Space Science, 335, 125

Favre, C., Fedele, D., Semenov, D., et al. 2018, ApJL, 862, L2

Favre, C., Vastel, C., Jimenez-Serra, I., et al. 2020, A&A, 635, A189

Fedoseev, G., Chuang, K.-J., van Dishoeck, E. F., et al. 2016, MNRAS, 460, 4297

Feigelson, E. D. & Montmerle, T. 1999, Annual Review of Astronomy and Astrophysics, 37, 363

Feng, S., Codella, C., Ceccarelli, C., et al. 2020, ApJ, 896, 37

Fontani, F., Pascucci, I., Caselli, P., et al. 2007, A&A, 470, 639

Francis, L., Johnstone, D., Herczeg, G., et al. 2020, Astronomical Journal, 160, 270. doi:10.3847/1538-3881/abbe1a

Frerking, M. A., Langer, W. D., & Wilson, R. W. 1982, ApJ, 262, 590. doi:10.1086/160451

Fuller, G. A., Lada, E. A., Masson, C. R., et al. 1995, ApJ, 453, 754

Furuya, R. S., Kitamura, Y., & Shinnaga, H. 2006, ApJ, 653, 1369

Gaczkowski, B., Preibisch, T., Stanke, T., et al. 2015, A&A, 584, A36

Garrod, R. T. & Herbst, E. 2006, A&A, 457, 927

Garrod, R. T. & Widicus Weaver, S. L. 2013, Chemical Reviews, 113, 8939

Garrod, R. T., Widicus Weaver, S. L., & Herbst, E. 2008, ApJ, 682, 283

Gaudel, M., Maury, A. J., Belloche, A., et al. 2020, A&A, 637, A92

Goesmann, F., Rosenbauer, H., Bredehöft, J. H., et al. 2015, Science, 349, 2.689

Goldreich, P., & Lynden-Bell, D. 1965, MNRAS, 130, 97

Goldreich, P. & Kwan, J. 1974, ApJ, 189, 441

Gorai, P., Bhat, B., Sil, M., et al. 2020, ApJ, 895, 86

Gratier, P., Bron, E., Gerin, M., et al. 2017, A&A, 599, A100

Gueth, F., Guilloteau, S., & Bachiller, R. 1996, A&A, 307, 891

Gueth, F., Guilloteau, S., & Bachiller, R. 1998, A&A, 333, 287

Gusdorf, A., Riquelme, D., Anderl, S., et al. 2015, A&A, 575, A98

Högbom, J. A. 1974, Astronomy and Astrophysics, Supplement, 15, 417

Hacar, A., Tafalla, M., Forbrich, J., et al. 2018, A&A, 610, A77

Halfen, D. T., Ilyushin, V., & Ziurys, L. M. 2011, ApJ, 743, 60

Hama, T. & Watanabe, N. 2013, Chemical Reviews, 113, 8783

Hara, C., Kawabe, R., Nakamura, F., et al. 2020, arXiv:2010.06825

Hartmann, L., Cassen, P., & Kenyon, S. J. 1997, ApJ, 475, 770

Hartmann, L. 2009, Accretion Processes in Star Formation: Second Edition, by Lee Hartmann. ISBN 978-0-521-53199-3. Published by Cambridge University Press, Cambridge, UK, 2009.

Hasegawa, T. I., Herbst, E., & Leung, C. M. 1992, Astrophysical Journal, Supplement, 82, 167

Hayashi, C. 1961, Publications of the ASJ, 13, 450

Hayashi, C. 1966, Annual Review of Astronomy and Astrophysics, 4, 171.

Henyey, L. G., Lelevier, R., & Levée, R. D. 1955, Publications of the ASP, 67, 154

Herbst, E. & Leung, C. M. 1989, Astrophysical Journal, Supplement, 69, 271

Herbst, E. & van Dishoeck, E. F. 2009, Annual Review of Astronomy and Astrophysics, 47, 427

Hirano, N., Ho, P. P. T., Liu, S.-Y., et al. 2010, ApJ, 717, 58

Hirano, N., Kameya, O., Kasuga, T., et al. 1992, ApJL, 390, L85

Hirano, N., Kameya, O., Nakayama, M., et al. 1988, ApJL, 327, L69

Hirano, N., Liu, S.-Y., Shang, H., et al. 2006, ApJL, 636, L141

Hirano, S., Tsukamoto, Y., Basu, S., et al. 2020, ApJ, 898, 118

Hirota, T., Ohishi, M., & Yamamoto, S. 2009, ApJ, 699, 585

Hirota, T., Sakai, N., & Yamamoto, S. 2010, ApJ, 720, 1370

Hsieh, T.-H., Murillo, N. M., Belloche, A., et al. 2018, ApJ, 854, 15

Hsieh, T.-H., Hirano, N., Belloche, A., et al. 2019, ApJ, 871, 100

Hueso, R., & Guillot, T. 2005, A&A, 442, 703

Hull, C. L. H. & Zhang, Q. 2019, Frontiers in Astronomy and Space Sciences, 6, 3

Imai, M., Oya, Y., Sakai, N., et al. 2019, ApJL, 873, L21

Imai, M., Sakai, N., Oya, Y., et al. 2016, ApJL, 830, L37

Inutsuka, S.-i., Machida, M. N., & Matsumoto, T. 2010, ApJL, 718, L58

Inutsuka, S. 2012, Progress of Theoretical and Experimental Physics, 2012, 01A307

Ioppolo, S., van Boheemen, Y., Cuppen, H. M., et al. 2011, MNRAS, 413, 2281

Irvine, W. M., Friberg, P., Kaifu, N., et al. 1990, A&A, 229, L9

Jørgensen, J. K. 2004, A&A, 424, 589

Jørgensen, J. K., Müller, H. S. P., Calcutt, H., et al. 2018, A&A, 620, A170

Jørgensen, J. K., van der Wiel, M. H. D., Coutens, A., et al. 2016, A&A, 595, A117

Jørgensen, J. K., Visser, R., Sakai, N., et al. 2013, ApJL, 779, L22

Jacobsen, S. K., Jørgensen, J. K., Di Francesco, J., et al. 2019, A&A, 629, A29

Jiménez-Serra, I., Martín-Pintado, J., Rodríguez-Franco, A., et al. 2004, ApJL, 603, L49

Jiménez-Serra, I., Martín-Pintado, J., Rodríguez-Franco, A., et al. 2005, ApJL, 627, L121

Jiménez-Serra, I., Caselli, P., Martín-Pintado, J., et al. 2008, A&A, 482, 549

Jiménez-Serra, I., Caselli, P., Tan, J. C., et al. 2010, MNRAS, 406, 187

Jiménez-Serra, I., Martín-Pintado, J., Caselli, P., et al. 2009, ApJ, 695, 149

Johansen, A. & Lambrechts, M. 2017, Annual Review of Earth and Planetary Sciences, 45, 359

Jolliffe, I. T. 1986, Springer Series in Statistics

Kahane, C., Ceccarelli, C., Faure, A., et al. 2013, ApJL, 763, L38

Kaifu, N., Ohishi, M., Kawaguchi, K., et al. 2004, Publications of the ASJ, 56, 69

Kaifu, N., Suzuki, H., Ohishi, M., et al. 1987, ApJL, 317, L111

Kawasaki, Y., Koga, S., & Machida, M. N. 2021

Keene, J., Hildebrand, R. H., Whitcomb, S. E., et al. 1980, ApJL, 240, L43

Kojima, T., Kroug, M., Takeda, M., et al. 2009, Applied Physics Express, 2, 102201

Kristensen, L. E., van Dishoeck, E. F., Bergin, E. A., et al. 2012, A&A, 542, A8

Kroto, H. W., Heath, J. R., Obrien, S. C., et al. 1985, Nature, 318, 162

Kuan, Y.-J., Huang, H.-C., Charnley, S. B., et al. 2004, ApJL, 616, L27

López-Sepulcre, A., Balucani, N., Ceccarelli, C., et al. 2019, ACS Earth and Space Chemistry, 3, 2122

López-Sepulcre, A., Jaber, A. A., Mendoza, E., et al. 2015, MNRAS, 449, 2438

López-Sepulcre, A., Watanabe, Y., Sakai, N., et al. 2016, ApJ, 822, 85

Lada, C. J. & Wilking, B. A. 1984, ApJ, 287, 610

Ladd, E. F., Adams, F. C., Casey, S., et al. 1991, ApJ, 366, 203

Larson, R. B. 1969, MNRAS, 145, 271

Law, C. J., Zhang, Q., Öberg, K. I., et al. 2021

Lee, C.-F. 2011, ApJ, 741, 62

Lee, C.-F., Codella, C., Li, Z.-Y., et al. 2019, ApJ, 876, 63

Lee, C.-F., Hirano, N., Zhang, Q., et al. 2014, ApJ, 786, 114

Lee, C.-F., Li, Z.-Y., Ho, P. T. P., et al. 2017, ApJ, 843, 27

Lee, C.-F., Li, Z.-Y., Ching, T.-C., Lai, S.-P., & Yang, H. 2018, ApJ, 854, 56

Lee, C.-F., Stone, J. M., Ostriker, E. C., et al. 2001, ApJ, 557, 429

Lefloch, B., Bachiller, R., Ceccarelli, C., et al. 2018, MNRAS, 477, 4792

Lefloch, B., Castets, A., Cernicharo, J., et al. 1998, ApJL, 504, L109

Lefloch, B., Ceccarelli, C., Codella, C., et al. 2017, MNRAS, 469, L73

Li, Z.-Y., Krasnopolsky, R., & Shang, H. 2013, ApJ, 774, 82.

Lim, J., Hanawa, T., Yeung, P. K. H., et al. 2016, ApJ, 831, 90

Lindberg, J. E., Jørgensen, J. K., Brinch, C., et al. 2014, A&A, 566, A74

Liu, S.-Y., Mehringer, D. M., & Snyder, L. E. 2001, ApJ, 552, 654

Lombardi, M., Lada, C. J., & Alves, J. 2008, A&A, 480, 785

Lommen, D., Jørgensen, J. K., van Dishoeck, E. F., & Crapsi, A. 2008, A&A, 481, 141

Looney, L. W., Mundy, L. G., & Welch, W. J. 2000, ApJ, 529, 477

Lopes, S., Fausto, R., & Khriachtchev, L. 2018, Journal of Chemical Physics, 148, 034301

Lundgren, A., 2013, ALMA Cycle 2 Technical Handbook Version 1.1, ALMA

Machida, M. N. & Basu, S. 2019, ApJ, 876, 149

Machida, M. N., Hirano, S., & Kitta, H. 2020, MNRAS, 491, 2180

Machida, M. N. & Hosokawa, T. 2013, MNRAS, 431, 1719

Machida, M., & Hosokawa, T. 2013, Protostars and Planets VI Posters

Machida, M. N., Inutsuka, S.-. ichiro ., & Matsumoto, T. 2008, ApJ, 676, 1088

Machida, M. N., Inutsuka, S.-i., & Matsumoto, T. 2011, ApJ, 729, 42

Machida, M. N., Inutsuka, S.-I., & Matsumoto, T. 2011, Publications of the ASJ, 63, 555

Machida, M. N., Matsumoto, T., & Inutsuka, S.-i. 2016, MNRAS, 463, 4246

Marcelino, N., Cernicharo, J., Agúndez, M., et al. 2007, ApJL, 665, L127

Martín-Doménech, R., Öberg, K. I., & Rajappan, M. 2020, ApJ, 894, 98

Masson, J., Chabrier, G., Hennebelle, P., et al. 2016, A&A, 587, A32

Masunaga, H. & Inutsuka, S.-. ichiro . 2000, ApJ, 531, 350

Masunaga, H., Miyama, S. M., & Inutsuka, S.-i. 1998, ApJ, 495, 346

Matsumoto, T., Machida, M. N., & Inutsuka, S. 2017, ApJ, 839, 69

Matsumoto, T. & Tomisaka, K. 2004, ApJ, 616, 266

Maureira, M. J., Arce, H. G., Dunham, M. M., et al. 2020, MNRAS, 499, 4394

Maureira, M. J., Pineda, J. E., Segura-Cox, D. M., et al. 2020, ApJ, 897, 59

Maury, A. J., André, P., Testi, L., et al. 2019, A&A, 621, A76

Maury, A. J., Belloche, A., André, P., et al. 2014, A&A, 563, L2

McGuire, B. A. 2021, arXiv:2109.13848

McKellar, A. 1940, Publications of the ASP, 52, 187

McMullin, J. P., Waters, B., Schiebel, D., et al. 2007, Astronomical Data Analysis Software and Systems XVI, 127

Meier, D. S., & Turner, J. L. 2005, ApJ, 618, 259

Mellon, R. R. & Li, Z.-Y. 2009, ApJ, 698, 922

Mendoza, E., Lefloch, B., López-Sepulcre, A., et al. 2014, MNRAS, 445, 151

Mestel, L. 1963, MNRAS, 126, 553

Mikami, H., Umemoto, T., Yamamoto, S., et al. 1992, ApJL, 392, L87

Misugi, Y., Inutsuka, S., & Arzoumanian, D. 2019, ApJ, 881, 11

Miura, H., Yamamoto, T., Nomura, H., et al. 2017, ApJ, 839, 47

Mowat, C., Hatchell, J., Rumble, D., et al. 2017, MNRAS, 467, 812

Mukhopadhyay, I. 2016, Infrared Physics and Technology, 75, 139

Muller, C. A. & Oort, J. H. 1951, Nature, 168, 357.

Murillo, N. M., Lai, S.-P., Bruderer, S., Harsono, D., & van Dishoeck, E. F. 2013, A&A, 560, A103

Murillo, N. M., Harsono, D., McClure, M., et al. 2018, A&A, 615, L14

Myers, P. C. & Benson, P. J. 1983, ApJ, 266, 309

Myers, P. C., Linke, R. A., & Benson, P. J. 1983, ApJ, 264, 517

Observing with ALMA-A Primer: Doc 8.1, ver. 2 in 2021

Ohashi, S., Codella, C., Sakai, N., et al. 2022, arXiv:2201.07334

Ohashi, N., Saigo, K., Aso, Y., et al. 2014, ApJ, 796, 131

Okoda, Y., Oya, Y., Sakai, N., et al. 2018, ApJL, 864, L25

Okoda, Y., Oya, Y., Sakai, N., et al. 2020, ApJ, 900, 40

Olofsson, S. & Olofsson, G. 2009, A&A, 498, 455

Onishi, T., Mizuno, A., Kawamura, A., et al. 2002, ApJ, 575, 950

Ortiz-León, G. N., Loinard, L., Dzib, S. A., et al. 2018, ApJL, 869, L33

Oya, Y., López-Sepulcre, A., Sakai, N., et al. 2019, ApJ, 881, 112

Oya, Y., Moriwaki, K., Onishi, S., et al. 2018, ApJ, 854, 96

Oya, Y., Sakai, N., Lefloch, B., et al. 2015, ApJ, 812, 59

Oya, Y., Sakai, N., López-Sepulcre, A., et al. 2016, ApJ, 824, 88

Oya, Y., Sakai, N., Sakai, T., et al. 2014, ApJ, 795, 152

Oya, Y., Sakai, N., Watanabe, Y., et al. 2017, ApJ, 837, 174

Oya, Y., Sakai, N., Watanabe, Y., et al. 2018, ApJ, 863, 72

Oya, Y., Watanabe, Y., López-Sepulcre, A., et al. 2021, ApJ, 921, 12

Oya, Y. & Yamamoto, S. 2020, ApJ, 904, 185

Palla, F. 1999, Star Formation 1999, 6

Palla, F., & Stahler, S. W. 1991, ApJ, 375, 288

Park, Y.-S., Panis, J.-F., Ohashi, N., et al. 2000, ApJ, 542, 344

Payne, M. J., & Lodato, G. 2007, MNRAS, 381, 1597

Penston, M. V. 1969, MNRAS, 144, 425

Pickett, H. M., Poynter, R. L., Cohen, E. A., et al. 1998, Journal of Quantitiative
    Spectroscopy and Radiative Transfer, 60, 883

Pineda, J. E., Maury, A. J., Fuller, G. A., et al. 2012, A&A, 544, L7

Pineda, J. E., Segura-Cox, D., Caselli, P., et al. 2020, Nature Astronomy, 4, 1158

Pineda, J. E., Zhao, B., Schmiedeke, A., et al. 2019, ApJ, 882, 103

Podio, L., Codella, C., Lefloch, B., et al. 2017, MNRAS, 470, L16

Punanova, A., Caselli, P., Feng, S., et al. 2018, ApJ, 855, 112

Quénard, D., Jiménez-Serra, I., Viti, S., et al. 2018, IAU Symposium, 332, 415

Quan, D. & Herbst, E. 2007, A&A, 474, 521

Raunier, S., Chiavassa, T., Duvernay, F., et al. 2004, A&A, 416, 165

Redaelli, E., Alves, F. O., Santos, F. P., et al. 2019, A&A, 631, A154

Reipurth, B., Yu, K. C., Heathcote, S., et al. 2000, Astronomical Journal, 120, 1449

Rivilla, V. M., Jiménez-Serra, I., Martín-Pintado, J., et al. 2021, Proceedings of the
    National Academy of Science, 118, 2101314118

Rubin, M., Altwegg, K., Balsiger, H., et al. 2019, MNRAS, 489, 594

Rygl, K. L. J., Benedettini, M., Schisano, E., et al. 2013, A&A, 549, L1

Sai, J., Ohashi, N., Saigo, K., et al. 2020, ApJ, 893, 51

Saigo, K., & Tomisaka, K. 2006, ApJ, 645, 381

Saigo, K., Tomisaka, K., & Matsumoto, T. 2008, ApJ, 674, 997

Saito, S., Kawaguchi, K., Yamamoto, S., et al. 1987, ApJL, 317, L115

Sakai, N., Hanawa, T., Zhang, Y., et al. 2019, Nature, 565, 206

Sakai, T., Sakai, N., Foster, J. B., et al. 2013, ApJL, 775, L31

Sakai, N., Sakai, T., Hirota, T., et al. 2008, ApJ, 672, 371

Sakai, N., Sakai, T., Hirota, T., et al. 2009, ApJ, 697, 769

Sakai, N., Sakai, T., Hirota, T., et al. 2010, ApJ, 722, 1633

Sakai, N., Sakai, T., Hirota, T., et al. 2014a, Nature, 507, 78

Sakai, N., Oya, Y., Higuchi, A. E., et al. 2017, MNRAS, 467, L76

Sakai, N., Oya, Y., López-Sepulcre, A., et al. 2016, ApJL, 820, L34

Sakai, N., Oya, Y., Sakai, T., et al. 2014b, ApJL, 791, L38

Sakai, N., Sakai, T., & Yamamoto, S. 2006, Publications of the ASJ, 58, L15

Sakai, N. & Yamamoto, S. 2013, Chemical Reviews, 113, 8981

Saladino, R.,   Botta, G., Pino, S., et al. 2012, Chemical Society Reviews, 41, 5526

Saruwatari, O., Sakai, N., Liu, S.-Y., et al. 2011, ApJ, 729, 147

Schilke, P., Walmsley, C. M., Pineau des Forets, G., et al. 1997, A&A, 321, 293

Scibelli, S. & Shirley, Y. 2020, ApJ, 891, 73

Shirley, Y. L., Evans, N. J., Rawlings, J. M. C., et al. 2000, Astrophysical Journal, Supplement, 131, 249

Skouteris, D., Vazart, F., Ceccarelli, C., et al. 2017, MNRAS, 468, L1

Smith, M. D., Suttner, G., & Yorke, H. W. 1997, A&A, 323, 223

Snyder, L. E. & Buhl, D. 1971, ApJL, 163, L47

Snyder, L. E., Buhl, D., Zuckerman, B., et al. 1969, Physical Review Letters, 22, 679

Soma, T., Sakai, N., Watanabe, Y., et al. 2018, ApJ, 854, 116

Spezzano, S., Caselli, P., Bizzocchi, L., et al. 2017, A&A, 606, A82

Stahler, S. W., Shu, F. H., & Taam, R. E. 1980, ApJ, 241, 637

Stutz, A. M., Rubin, M., Werner, M. W., et al. 2008, ApJ, 687, 389

Sugimura, M., Yamaguchi, T., Sakai, T., et al. 2011, Publications of the ASJ, 63, 459

Suzuki, H., Yamamoto, S., Ohishi, M., et al. 1992, ApJ, 392, 551

Tachihara, K., Dobashi, K., Mizuno, A., Ogawa, H., & Fukui, Y. 1996, Publications of the ASJ, 48, 489

Tafalla, M., Myers, P. C., Mardones, D., et al. 2000, A&A, 359, 967

Takaishi, D., Tsukamoto, Y., & Suto, Y. 2020, MNRAS, 492, 5641

Takakuwa, S., Kamazaki, T., Saito, M., et al. 2007, Publications of the ASJ, 59, 1

Takakuwa, S., Saigo, K., Matsumoto, T., et al. 2017, ApJ, 837, 86

Taquet, V., Bianchi, E., Codella, C., et al. 2019, A&A, 632, A19

Tielens, A. G. G. M. & Hagen, W. 1982, A&A, 114, 245

Tobin, J. J., Bourke, T. L., Mader, S., et al. 2019, ApJ, 870, 81

Tobin, J. J., Dunham, M. M., Looney, L. W., et al. 2015, ApJ, 798, 61

Tobin, J. J., Hartmann, L., Chiang, H.-F., et al. 2012, Nature, 492, 83

Tobin, J. J., Kratter, K. M., Persson, M. V., et al. 2016, Nature, 538, 483

Tobin, J. J., Looney, L. W., Li, Z.-Y., et al. 2016, ApJ, 818, 73

Tobin, J. J., Looney, L. W., Wilner, D. J., et al. 2015, ApJ, 805, 125

Tobin, J. J., Looney, L. W., Li, Z.-Y., et al. 2018, ApJ, 867, 43

Tobin, J. J., Sheehan, P. D., Megeath, S. T., et al. 2020, ApJ, 890, 130

Tomida, K., Okuzumi, S., & Machida, M. N. 2015, ApJ, 801, 117

Tokuda, K., Onishi, T., Matsumoto, T., et al. 2016, ApJ, 826, 26

Tokuda, K., Onishi, T., Saigo, K., et al. 2014, ApJL, 789, L4

Tokuda, K., Onishi, T., Saigo, K., et al. 2017, ApJ, 849, 101

Tomisaka, K. 2002, ApJ, 575, 306

Toomre, A. 1964, ApJ, 139, 1217

Tothill, N. F. H., Löhr, A., Parshley, S. C., et al. 2009, Astrophysical Journal, Supplement, 185, 98

Tsukamoto, Y. 2016, Publications of the Astron. Soc. of Australia, 33, e010

Tsukamoto, Y., Iwasaki, K., Okuzumi, S., et al. 2015, ApJL, 810, L26

Tsukamoto, Y., Iwasaki, K., Okuzumi, S., et al. 2015, MNRAS, 452, 278

Tsukamoto, Y., Okuzumi, S., Iwasaki, K., Machida, M. N., & Inutsuka, S.-i. 2017, Publications of the ASJ, 69, 95

Tsukamoto, Y., Okuzumi, S., Iwasaki, K., et al. 2018, ApJ, 868, 22

Tucker, J. R. & Feldman, M. J. 1985, Reviews of Modern Physics, 57, 1055

Turner, B. E. 1991, Astrophysical Journal, Supplement, 76, 617

Ungerechts, H., Bergin, E. A., Goldsmith, P. F., et al. 1997, ApJ, 482, 245

van der Tak, F. F. S., Black, J. H., Schöier, F. L., et al. 2007, A&A, 468, 627

van der Wiel, M. H. D., Jacobsen, S. K., Jørgensen, J. K., et al. 2019, A&A, 626, A93

van Dishoeck, E. F., Herbst, E., & Neufeld, D. A. 2013, Chemical Reviews, 113, 9043

van Gelder, M. L., Tabone, B., Tychoniec, Ł., et al. 2020, A&A, 639, A87

van Kempen, T. A., van Dishoeck, E. F., Hogerheijde, M. R., & Güsten, R. 2009, A&A, 508, 259

van 't Hoff, M. L. R., van Dishoeck, E. F., Jørgensen, J. K., et al. 2020, A&A, 633, A7

Vastel, C., Ceccarelli, C., Lefloch, B., et al. 2014, ApJL, 795, L2

Vasyunin, A. I., Caselli, P., Dulieu, F., et al. 2017, ApJ, 842, 33.

Vazzano, M. M., Fernández-López, M., Plunkett, A., et al. 2021, A&A, 648, A41

Velusamy, T., Langer, W. D., & Thompson, T. 2014, ApJ, 783, 6

Wakelam, V., Ceccarelli, C., Castets, A., et al. 2005, A&A, 437, 149

Wakelam, V., Herbst, E., Loison, J.-C., et al. 2012, Astrophysical Journal, Supplement, 199, 21

Ward-Thompson, D., Zylka, R., Mezger, P. G., & Sievers, A. W. 2000, A&A, 355, 1122

Watanabe, N. & Kouchi, A. 2002, ApJL, 571, L173

Watanabe, Y., Nishimura, Y., Harada, N., et al. 2017, ApJ, 845, 116

Watanabe, Y., Sakai, N., López-Sepulcre, A., et al. 2017, ApJ, 847, 108

Watanabe, Y., Sakai, N., Sorai, K., Ueda, J., & Yamamoto, S. 2016, ApJ, 819, 144

Watson, D. M. 2020, Research Notes of the American Astronomical Society, 4, 88

Weinreb, S., Barrett, A. H., Meeks, M. L., et al. 1963, Nature, 200, 829

Williams, J. P., & Cieza, L. A. 2011, Annual Review of Astronomy and Astrophysics, 49, 67

Wilson, R. W., Jefferts, K. B., & Penzias, A. A. 1970, ApJL, 161, L43

Winn, J. N. & Fabrycky, D. C. 2015, Annual Review of Astronomy and Astrophysics, 53, 409

Woods, R. C., Gudeman, C. S., Dickman, R. L., et al. 1983, ApJ, 270, 583

Wurster, J., & Li, Z.-Y. 2018, Frontiers in Astronomy and Space Sciences, 5, 39

Wurster, J., Price, D., & Ayliffe, B. 2014, MNRAS, 444, 1104

Wurster, J., Price, D. J., & Bate, M. R. 2016, MNRAS, 457, 1037

Wyrowski, F., Schilke, P., Walmsley, C. M., et al. 1999, ApJL, 514, L43

Xue, Y., Suto, Y., Taruya, A., et al. 2014, ApJ, 784, 66

Yıldız, U. A., Kristensen, L. E., van Dishoeck, E. F., et al. 2015, A&A, 576, A109

Yamaguchi, T., Takano, S., Watanabe, Y., et al. 2012, Publications of the ASJ, 64, 105

Yamamoto, S., Saito, S., Kawaguchi, K., et al. 1987, ApJL, 317, L119

Yamamoto, S. 2017, Introduction to Astrochemistry: Chemical Evolution from Interstellar Clouds to Star and Planet Formation, Astronomy and Astrophysics Library. ISBN 978-4-431-54170-7. Springer Japan, 2017.

Yen, H.-W., Koch, P. M., Takakuwa, S., et al. 2015, ApJ, 799, 193

Yen, H.-W., Koch, P. M., Takakuwa, S., et al. 2017, ApJ, 834, 178

Yen, H.-W., Takakuwa, S., Koch, P. M., et al. 2015, ApJ, 812, 129

Yen, H.-W., Takakuwa, S., Ohashi, N., et al. 2013, ApJ, 772, 22

Yen, H.-W., Zhao, B., Koch, P. M., et al. 2021, ApJ, 916, 97

Zamponi, J., Maureira, M. J., Zhao, B., et al. 2021, MNRAS, 508, 2583

Zapata, L. A., Fernández-López, M., Rodríguez, L. F., et al. 2018, Astronomical Journal, 156, 239

Zhang, Y., Higuchi, A. E., Sakai, N., et al. 2018, ApJ, 864, 76

Zhang, Y., Tan, J. C., Tanaka, K. E. I., et al. 2019, Nature Astronomy, 3, 517

Zhao, B., Caselli, P., Li, Z.-Y., et al. 2016, MNRAS, 460, 2050

Zhao, B., Caselli, P., Li, Z.-Y., & Krasnopolsky, R. 2018, MNRAS, 473, 4868

A&A: Astronomy & Astrophysics
ApJ: Astrophysical Journal
ApJL: Astrophysical Journal, Letters
MNRAS: Monthly Notices of the Royal Astronomical Society